Failing Under Pressure: Exploring the Frictional-Viscous transition in Cold Subduction Zones

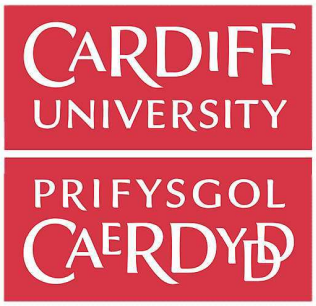

Sara De Caroli

Thesis submitted for the degree of Doctor of Philosophy at Cardiff University

21/12/2023

Abstract

The rheology of epidote-blueschists deforming along the prograde path in the subduction zone downdip the seismogenic zone, and along the retrograde path in shear zones guiding exhumation, is poorly documented. In SW Japan, in the Ryukyu arc, the Tomuru block-in-matrix metabasites represent an exhumed subduction complex that registers prograde deformation at epidote-blueschist conditions (T $\sim$ 400 ℃ and P $\sim$ 8-9 kbar) and offers a natural laboratory to understand how microstructure and deformation mechanisms influence bulk rheology and fault behaviour along the plate interface during the prograde path. In the block-in-matrix complex, deformation occurred by progressively increasing strain from greenschist and epidote-blueschist blocks to epidote-blueschist matrix, reflected by increase in foliation development. Both blocks and matrix deform through distributed viscous creep by diffusive mass transfer under low shear stress, estimated at 11-28 MPa. Overall, microstructural studies indicate that the viscosity contrast between blocks and matrix must have been relatively low, but not negligible. The structural and mechanical heterogeneity during deformation results in epidote-blueschists likely accommodating plate creep at the P-T conditions of deformation. Retrograde blueschists exposed in the Lento unit (Alpine Corsica) register deformation during exhumation from blueschist to greenschist facies. Microstructural analyses indicate that bulk rheology during exhumation was governed by frictional-viscous flow, with the frictional component being accommodated by cataclasis if actinolite and epidote and frictional sliding along chlorite foliae, while the viscous component was accommodated by pressure solution of chlorite, albite, actinolite, and epidote, with minor dislocation creep of actionlite. Fluid-driven retrograde reactions accompany exhumation from blueschist to greenschist facies and lead to reaction and textural weakening, thus reducing rock strength. These mechanisms are important in limiting the stress magnitudes in retrograde shear

zones, likely favouring fault creep in subduction zones if fluids are available to drive retrograde reactions.

Acknowledgements

I would like to thank my supervisors Åke Fagereng and Tom Blenkinsop for their guidance and support, the amount of learning I have done by working with them has been truly immesurable. Åke first took a chance on me by bringing me on this PhD project and allowing me to see the world and be part of something quite amazing. His support in navigating the challenging waters of the past four years has been something I will forever be grateful for. Tom has joined the supervisory team a little later along the way, but his help and support has been fundamental in the past two years, and I consider myself lucky to have had the chance to collaborate with him.

Thank you to my other two supervisors, Kohtaro Ujiie and Francesca Meneghini. Kohtaro organised fieldwork in Japan, which lead to me studying some of the most beautiful rocks I have ever seen, and gave me a chance to explore Japan in a trip that I can certainly say changed my life for good. I will always cherish the things I learnt from him during in field work and the post-field chats in front of a cold glass of awamori in tropical Ishigaki with his team and Francesca. Francesca not only brought me to beautiful Corsica, but was a great support throughout my PhD both scientifically and personally.

3 years of this project were funded by the College of Physics and Engineering at Cardiff University. This project received funding by the European Research Council (ERC) under the European Union's Horizon 2020 research and innovation programme (grant agreement No 715836 'MICA") to cover research costs, SEM, field work, conferences, and other costs of my PhD.

My sincere thanks go to Tony Oldroyd for preparing the best thin sections, for showing me all the labs machinery and for opening the doors any time I would lock myself out of the SEM room. Duncan Muir taught me how to properly use the SEM and patiently taught me how to work on the EBSD during those strange

Covid restriction times, and I could not be more thankful to have had such a good teacher.

Outside of academia, the number of people who deserve my sincere, big "Thank you!" is very, very long. To i miei amici from back home: Ari, Miri, Alberto, Cu, Marika, che ve lo dico a fare, grazie sempre e per sempre per il supporto costante da tutta, spesso tanta, vita. It makes the heart at ease knowing that no matter the distance, some people will always be with you.

When I first moved to Cardiff I never thought I would meet the amazing great friends I met. Thank you to Gabi, without our walks and talks and movie marathons I would have never survived the pandemic, you give the best pep talks someone could wish for and you are a gift that I will always cherish. Esther, who is the best housemate and an even better friend, I will never ever thank you enough for the support and the adventures of the past two years, you are truly a friend for life. To Grace, the bright voice of reason I always gravitate to, a thank you for the support on my dark days.

My university life would have never been the same without Erin and Ana, the way you have supported me is the reason I made it to the end of my PhD. Thank you Y'All for being the best AGU conference buddy, and to Ana, for the office chats and the nights out dancing. To Sophie, with whom I drank so many coffees and who has always unknowingly been a great guide during my PhD.

To Abi and Roberto, the best geology buddies I could have asked for.

Last, but not least, to my parents, thank you for raising me stubborn, Ma e Pa, grazie, sempre.

Contents

List of Figures

List of Tables

Chapter 1

Thesis outline

1.1 Main Research Questions

The overall aim of this thesis is to understand the deformation style of epidote-blueschist rocks during prograde and retrograde deformation in the context of subduction zones. To address this, this thesis focuses on the data from samples collected during field work in Ishigaki Island (Ryukyu Arc – SW Japan), where epidote-blueschist rocks record prograde deformation, possibly on the subduction interface, from greenschist to epidote-blueschist facies (T $\sim$ 400 ℃ and P $\sim$ 8-9 kbar; Imaizumi and Ishizuka, 1988), and from Lento (Corsica), where greenschist facies metabasites register exhumation from blueschist facies (T = 400 $\pm$50 ℃ and P = 0.80 $\pm$ 0.20 GPa; Levi et al., 2007) to greenschist facies conditions through deformation by duplex structures in the accretionary wedge.

To understand how epidote-blueschist rocks deform in the subduction context, the thesis aims to address these questions:

Q1: Which structural fabrics (i.e., foliations, fractures, syn-tectonic veins) characterise epidote-blueschist rocks in subduction zones?

Q2: What is the bulk rheology of epidote-blueschists in the subduction context?

Q3: How does the metamorphic path influence epidote-blueschist rheology?

1.2 Thesis outline

This thesis comprises three main parts: (1) A general introduction to provide the background for the scientific topics addressed, giving an overview of subduction interface structure, seismic style and rheology of the rocks deforming in subduction zones, with focus on deformation mechanisms and microstructures; (2) A geologic setting chapter, illustrating the specific contexts where research has been conducted; (3) a Methods chapter describing how research has been conducted, with the tools and the type of analyses taken; (4) Three scientific chapters outlining the work conducted on prograde and retrograde epidote-blueschists (Chapters 5-6-7); (5) A general discussion, focusing on how the data described and interpreted in the scientific chapters can provide answers to the main research questions and, finally (6) a brief chapter where the main conclusions are outlined, with points for future research.

Among the main scientific chapters, Chapter 5 focuses on which deformation mechanisms are active in epidote-blueschist rocks in the Tomuru block-in-matrix metabasites (Ishigaki Island, Ryukyu arc, SW Japan) through microstructural analyses on epidote-blueschist blocks and matrix. Chapter 6 expands on the data interpreted in the previous chapter, and it focuses on the structural style of the Tomuru block-in-matrix metabasites, through field-scale observations and microstructural analyses on both greenschist blocks and epidote-blueschist blocks and matrix, to understand which deformation mechanisms guide bulk rheology of a heterogeneous complex. The structural data is accompanied by calculation of

differential stress to understand the stress levels during deformation on the plate interface. Finally, geochemical data is used to compare bulk composition of greenschists and epidote-blueschists of Tomuru block-in-matrix. Chapter 7 focuses on the microstructures in the greenschists from the Lento unit (Alpine Corsica, Corsica), in order to understand which mechanisms are responsible for deformation of retrograde blueschists.

Chapter 5 is derived from a manuscript accepted for publication in Journal of Structural Geology. Sara De Caroli is the lead author of the manuscript, with Åke Fagereng, Kohtaro Ujiie, Francesca Meneghini, Tom Blenkinsop and Duncan Muir as the co-authors. Sara De Caroli undertook field work, microstructural analysis and wrote the manuscript. Åke Fagereng helped with field work and provided scientific guidance and constructive comments during stages of writing. Tom Blenkinsop helped with scientific guidance and constructive comments of the manuscript. Kohtaro Ujiie helped with the field work and with scientific guidance during sample collection and manuscript review. Francesca Meneghini helped on field work and provided constructive comments on the manuscript. Duncan Muir helped with SEM-EBSD analyses.

Chapter 6 presents original work derived from field work conducted in Ishigaki in October 2022, once travel was permitted in Japan after 3 years of lockdown. Sara De Caroli undertook field work and microstructural analysis. Åke Fagereng and Tom Blenkinsop provided scientific supervision and constructive comments. Kohtaro Ujiie helped with field work and provided scientific guidance for the work. Francesca Meneghini helped with field work. XRF analysis was carried out by Phil Janney at the University of Cape Town and Duncan Muir helped with SEM-EBSD analyses.

Chapter 7 presents original work derived from field work conducted in Corsica in November 2021, when travel was permitted in Corsica after lockdown. Sara De

Caroli undertook field work and microstructural analyses. Åke Fagereng helped with field work and scientific supervision. Francesca Meneghini helped with field work and provided scientific guidance and constructive comments. Tom Blenkinsop provided scientific supervision and constructive comments. Duncan Muir helped with SEM-EBSD data collection, Maria Di Rosa helped with field work.

Chapter 2

Introduction

2.1 Subduction plate boundary structure

Subduction zones are characterised by a complex internal structural architecture, with a lower plate and an overriding plate separated by the subduction plate interface, also referred to as megathrust fault, which represents a zone of concentrated deformation, characterised by a series of gently dipping, simultaneously active fault surfaces, generally anastomosing into creating a shear zone (Fisher and Byrne, 1987; Cloos and Shreve, 1996; Kimura et al., 2012; Rowe et al., 2013; Fagereng et al., 2018). The position of the subduction megathrust along active subduction zones is delineated by the distribution of seismicity, as more than 85% of global seismic moment released is estimated to occur along convergent plate boundaries (Pacheco et al., 1993). The thickness of active plate boundaries is not univocally defined, as seismological observations on the depth limit are unclear, however, through observations on drilling sites and on exhumed plate boundaries, Rowe et al. (2013) estimated the thickness of a typical plate boundary to be in the range of 100-350 m throughout the seismogenic zone.

On the plate interface, the area on which earthquakes can nucleate is defined as

the seismogenic zone, identified by the distribution of macroseismic activity (Hyndman et al., 1997) (Fig. 2.1). The updip limit of the seismogenic zone is suggested to be controlled by the 150 ℃ isotherm, at the temperature limit where clay minerals start to destabilise and where several other diagenetic processes take place (e.g., Moore and Saffer, 2001; Hyndman et al., 1997). As the seismogenic zone is correlated with a regime where shearing is accommodated mostly by frictional sliding and cataclasis, the downdip limit is defined by the passage from a frictional regime to a quasi-plastic regime, where aseismic shearing is accommodated by continuous, ductile deformation in mylonitic belts (Sibson, 1984). Several factors control the depth of regime transition, the primary ones being temperature, composition of the crust, strain rate, effective stress, geothermal gradient and water content. In a quartz-feldspathic crust, the prime factor controlling this depth is the onset of crystal plasticity in quartz, which happens at temperatures above 350 ℃, where dislocation creep becomes the predominant deformation mechanism (Sibson, 1984; Blanpied et al., 1995; Scholz, 1998). Also, an increase in geothermal gradient, or a decrease in strain rate will cause the frictional to quasi-plastic transition to move upward (Sibson, 1984).

The plate interface updip of the seismogenic zone is characterised by a transition zone that separates it from stable sliding at shallow levels. There, along some margins, slow earthquakes (See Section 2.4.1) can propagate (Wallace et al., 2016). At depth, the seismogenic zone transitions downwards into a zone of aseismic creep, the seismic-aseismic transition occurs in the depth range of 25-40 km, corresponding to temperatures in the range of 350-500 ℃ (Peacock et al., 2011; Tichelaar and Ruff, 1993) (Fig. 2.3). This transition zone downdip of the seismogenic zone is regarded to be the source of episodic tremor and slow slip (See Section 2.4.1) (Hirose et al, 1999; Dragert et al., 2001, Obara, 2002), the origin of which is still uncertain.

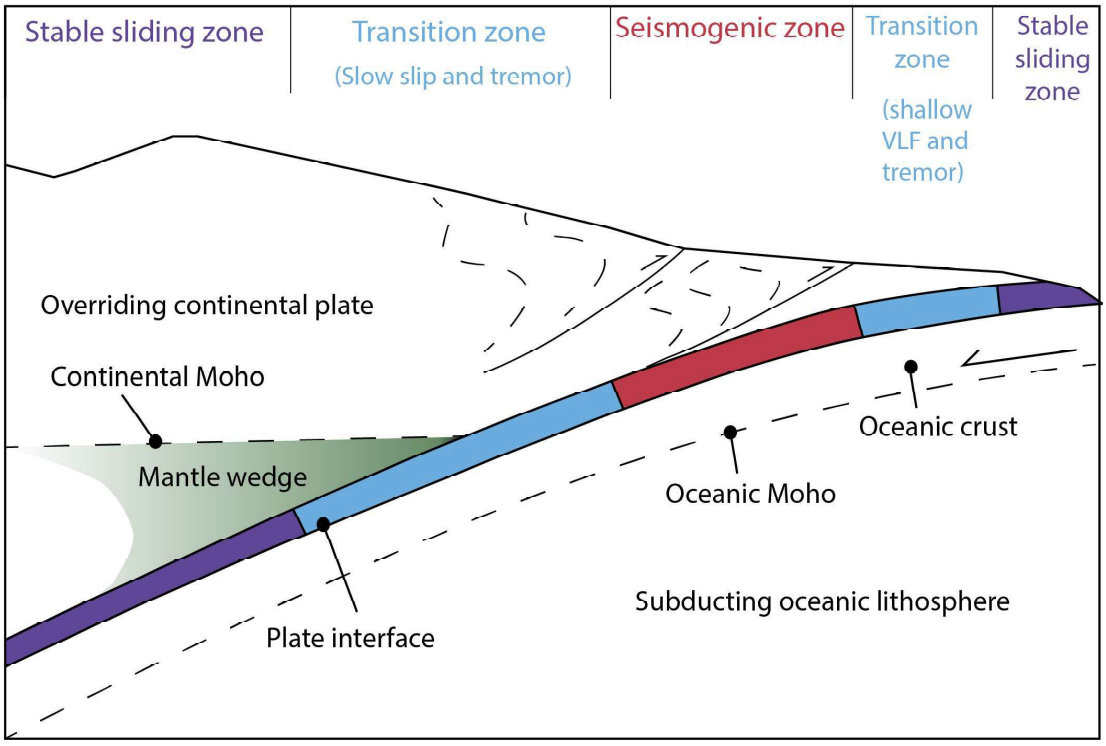

Figure 2.1: Schematic subduction zone setting. The plate interface is divided into domains with characteristic seismic behaviour, from the stable aseismic sliding zone to transitional zone to seismogenic zone. modified from the cross section of the Nankai subduction zone in Obara and Kato (2016).

2.2 Fluid circulation in the subduction interface

Fluids entering the subduction zones in the incoming oceanic plate include pore water contained in intergranular/fracture porosity in the sediment and igneous crust, and fluids liberated from dehydration reactions (Saffer and Tobin, 2011). Subduction of the oceanic crust involves a significant amount of volatile-rich rocks entering the subduction megathrust, Peacock (1990) models that for a 2.5 km thick basalt layer, at least 2 wt.% H_2O and 0.1 wt.% CO_2 is bound in minerals, for a general 4 x 10^{11} kg3 of volatile mass subducted per year contained in hydrous minerals such as prehnite, chlorite and amphibole forming as a result of hydrother-

mal circulation and high temperature-low pressure metamorphism at mid-ocean ridges.

At shallow levels, in the upper few km of the subduction interface, the main fluid release is from pore compaction. With increasing depth, pressure increase leads to loss of porosity, and as pore water is lost, metamorphic dehydration reactions become the dominating process in releasing fluids (Saffer and Tobin, 2011). During metamorphism, grain reorganisation and recrystallisation can transfer the lithostatic load to the newly expelled fluid phase, as suggested by the presence of syn-metamorphic veins and by modelling studies suggesting that devolatisation occurs under fluid overpressure (Connolly, 2010).

The locus of fluid overpressure is a function of permeability, a parameter which is space and time dependent, as it is function of the complex architecture of subduction zones and the range of lithologies involved in the megathrust. Syn-metamorphic veins and high stratal disruption have been documented to be restricted in the footwall of the subduction megathrust in examples from different convergent margins (Fisher and Byrne, 1987; Kondo et al., 2005; Rowe et al., 2009), suggesting that the plate interface can act as a permeability barrier, which may be inferred by the presence of foliation-parallel veins observed in exhumed subduction complexes, indicating fluids flow parallel to the shear zone fabrics, but likely not across. However, released fluids can locally migrate into the overlying forearc crust where they can remain present as a fluid phase or be consumed by retrograde metamorphic reactions (Peacock, 2009), through shear zones that guide exhumation, or in splay faults (i.e., shear zones that guide exhumation of the Lento unit, See Section 3.2).

Fluid release from dehydration reactions is episodic, as it depends on specific dehydration reactions involving specific mineral phases (Fagereng and Diener, 2011; Condit et al., 2020), however means of seismic imaging show how

overall, fluid pressure in the subduction interface changes as a function of depth, with shallow and deep aseismic or conditionally seismic zones that are at extreme over-pressure (near lithostatic), and with a seismogenic locked zone in between, characterised by lower fluid pressure (Fig. 2.2, Saffer and Tobin, 2011; Shelly et al. 2006). Fluid overpressure has been directly correlated with the plate interface seismic architecture, in particular, overpressure has been correlated to the shallow and deep aseismic and transitional zones, while the area with lower fluid pressure has been correlated with the seismogenic zone through means of tomographic imaging around the source region of slow slip and tremor (Matsubara et al., 2009). Moreover, Audet et al. (2009) connected the region of high pore fluid pressure and low effective stress to areas where metamorphic dehydration reactions happen at depth.

At the grain scale, the presence of an aqueous fluid promotes diffusive mass transfer mechanisms (see Section 2.6.2), particularly pressure solution, which can be an effective deformation mechanism to accommodate deformation on the plate interface at depth, where blueschist rocks are stable (e.g., Wassmann and Stockert, 2013). This mechanism has been interpreted to favour stable plate creep (Condit and French, 2022; Fagereng and den Hartog, 2017; Gratier and Gamond, 1990).

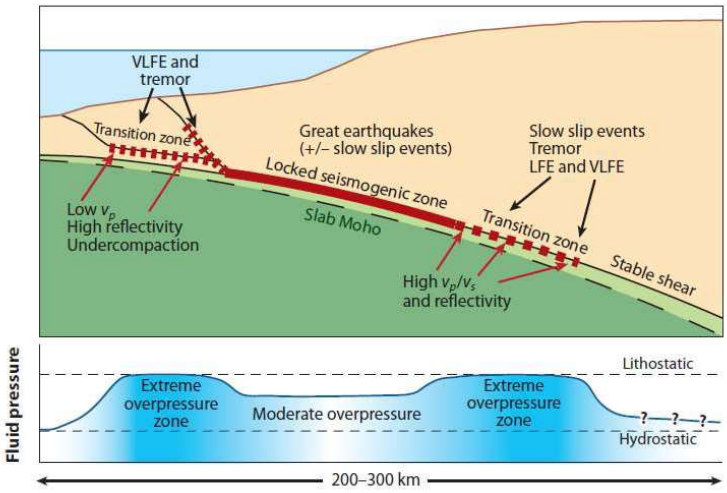

Figure 2.2: Correlation between subduction zone seismic domains and fluid overpressure. The seismogenic zone corresponds to an area or moderate overpressure, versus the transition zones, where overpressure is much higher. From Saffer and Tobin (2011).

2.3 Blueschist metamorphism in subduction zones

Subduction zones are characterized by low geothermal gradients, in the order of less of 10 ℃/km, compared to 25-35 °C/km in continents and ocean basins (Ernst, 1973; Cloos and Shreve, 1988). This is because the cold oceanic crust and sedimentary cover subduct under the warmer continental crust, decelerating the rate at which temperature rises with depth and rising pressure. The typical thermal structure of subduction zones regulates metamorphic reactions that lead up to HP/LT metamorphic facies associations (Miyashiro, 1961). In particular, blueschist facies metamorphic rocks represent evidence of plate convergence, as these rocks are generally found in quite narrow and discontinuous belts in the arc-ward side of Mesozoic and Cenozoic subduction complexes (Cloos and Shreve, 1988; Ernst, 1973; Oxburgh and Turcotte, 1971). Blueschist rocks can be subdivided into lawsonite-blueschists (sodic amphibole + lawsonite) and epidote-blueschists (sodic amphibole + epidote + quartz, e.g., Evans, 1990). These two sub-facies are stable

in similar P range, but in distinct T ranges, with lawsonite-blueschists stable in T $\sim$ 200-360 ℃ and epidote-blueschists are stable at T $\sim$ 360-500 ℃ (Peacock, 1992) (Fig. 2.3). During subduction, blueschist facies rocks can undergo further dehydration at higher P and destabilise in eclogite facies rocks (Fig. 2.3). Once subduction ceases, destabilization of blueschist rocks can happen by decompression, where blueschist rocks can be replaced by greenschists and epidote-amphibolite facies mineral assemblages through fluid-assisted retrograde re-hydration reactions (Evans, 1990).

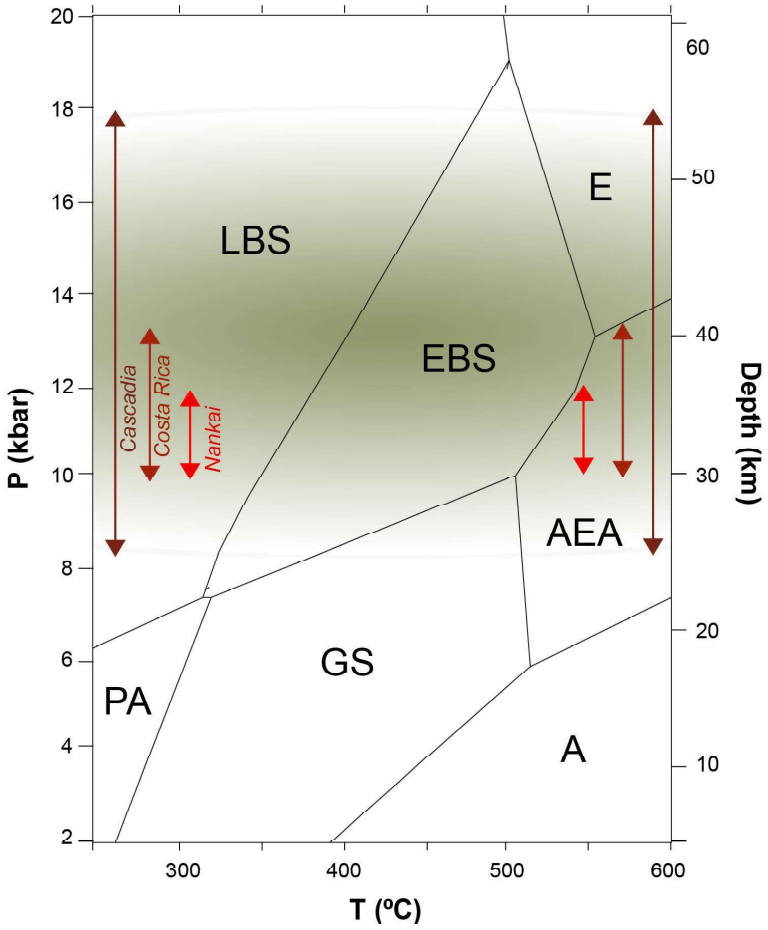

Figure 2.3: Phase relations of metabasites. PA: Pumpellyte- actinolite facies; GS: greenschist facies; EBS: epidote-blueschist facies; LBS: lawsonite-blueschist facies; E: eclogite facies; AEA: actinolite-epidote-amphibolite facies; A: amphibolite facies. In green, the depth range of deep slow slip and tremor (ETS) generally observed in subduction zones, with depth ranges for Nankai (Kano et al., 2019), Costa Rica (Davis et al., 2011) and Cascadia (Luo and Liu, 2021). Modified from Evans (1990).

2.4 Slip styles along the plate interface

Observations with geodetic and seismic means have recorded how a wide range of seismic and aseismic signals contributes to plate deformation (Peng and Gomberg, 2010; Schwartz and Rokosky, 2007). In this realm, slip rates can vary widely from plate convergence values (cm/year) during aseismic creep, to circa 1 m/s during earthquake rupture. Earthquakes accommodate displacement at rates in the order of one meter per second, as a result of frictional instabilities along fault surfaces (Brace and Byerlee, 1966; Sibson, 1977), where seismic slip happens through fast frictional sliding, while aseismic creep approximates plate convergence rate and is the dominant slip style at depth below the seismogenic zone, where viscous deformation mechanisms dominate rheology. Between these end members, slow earthquakes can occur with intermediate slip rates (Peng and Gomberg, 2010).

2.4.1 Slow earthquakes

Slow earthquakes comprise a range of phenomena, from slow slip events (SSEs), low frequency earthquakes (LFEs) and tectonic tremor (e.g., Beroza and Ide, 2011; Peng and Gomberg, 2010; Schwartz and Rokosky, 2007). SSEs are geodetically observed aseismic signals that occur when slip on fault surfaces does not reach dynamic velocities (Linde, 1996; Rogers and Dragert, 2003). In fact, slow slip proceeds at intermediate slip rates and can endure for months and years (in the order of mm-cm per year), not reaching dynamic velocities able to radiate seismic waves, and so fault movement generating earthquakes is inhibited (Peng and Gomberg, 2010; Bürgmann, 2018).

Structurally, SSEs have been commonly observed in the areas up-dip and down-dip of the seismogenic zone. However, they have also been detected along the length of the seismogenic zone, where fault surfaces show a patchwork of seismic

styles, changing from completely locked patches to continuously slipping zones, hence leading to the interpretation that in subduction zones lithospheric deformation is accommodated by a complex interplay of seismic slip and aseismic creep along the plate interface (Schwartz and Rokosky, 2007).

Slow slip events are often detected with deep non-volcanic tremor, a weak, extended seismic signal with low frequency (1 – 10 Hz) and no clear body wave arrivals that have been observed as a phenomenon with long time duration, from hours to weeks (Obara, 2002; Obara et al., 2004). Other seismic signals are involved into the spectrum of slow, long duration fault displacement events, and they include very low frequency earthquakes (VLFEs), anomalous events with very low frequency energy of 10 – 20 seconds and little or no frequency content (Obara and Ito, 2005), and low frequency earthquakes (LFEs) (Shelly et al., 2006). LFEs are weak seismic signals enriched in low frequencies (1 – 5 Hz) interpreted as extended tremor, that are recorded to be generated at 30 – 35 km depth on the subduction interface (Shelly et al., 2006; Shelly et al., 2007). LFEs within the tremor signal are thought to be generated directly by shear slip on the plate interface, during aseismic transients, as slip accelerates because of geometric or physical irregularities of the plate interface (Ide et al., 2007; Shelly et al., 2006). They can thus represent seismic signal accompanying slow slip events, which are otherwise too weak to generate detectable seismic signals. The association of slow slip and tremor, firstly observed in Cascadia (e.g., Rogers and Dragert, 2003), is referred to as 'episodic tremor and slip' (ETS) (Obara et al., 2004; Peng and Gomberg, 2010; Takagi et al., 2016).

2.4.2 Mechanisms of slow slip

Mechanisms generating slow slip events are still not clear, however, as slow slip events are spatially and temporally connected with large earthquakes (Obara and

Kato, 2016), it is crucial to understand which mechanisms can contribute to their propagation. Based on tomographic images of seismic velocities in subductions zones such as Cascadia and Nankai (Audet et al., 2009; Kodaira et al., 2004), slow slip events are inferred to occur near or within a low velocity layer, characterised by anonymously high Vp/Vs values (compressional to shear velocity ratio), commonly interpreted as near-lithostatic pore-fluid pressure and inferred low shear stress. These properties are consistent with numerical simulation of episodic slow slip and tremor-triggering properties that require a weak megathrust downdip of the seismogenic zone (Rubinstein et al., 2010).

Given the lithological complexity of the subducting plate, where mixing of strong and weak materials is common, the geological heterogeneities of the plate interface are thought to play an important role in controlling aseismic instabilities (Fagereng and Sibson, 2010; Skarbek et al., 2012). In fact, most crustal fault zones are made of mixed material comprising elements with a competency contrast that can result in mixed continuous-discontinuous deformation, which can be identified in the rock record as brittly deformed, more competent lenses or blocks embedded in a ductilely deformed matrix (Collettini et al., 2011; Fagereng and Sibson, 2010). At the grain scale, the proportion of rigid and weaker material can control deformation response. With low volume fraction of the weak lithology shear is localised in a thin zone, strain rate is increased and discontinuous/brittle deformation is inferred to be predominant, whereas with a high volume fraction of the weak lithology, shear can be accommodated in a wider area, shear strain is distributed and ductile matrix flow favoured (Fagereng and Sibson, 2010; Handy, 1990;1994). Rigid blocks would therefore act as asperities where brittle fractures can nucleate, accommodating shear discontinuities, whereas matrix-predominant regions would deform aseismically. Combined fracture and viscous flow of shear zones comprising strong and viscous materials could therefore generate stress tran-

sients that can resemble slow slip (Hayman and Lavier, 2014). The occurrence of slow slip events near the edge of seismogenic regions has led to the suggestion that a transition in frictional properties controls the location of slow slip (Schwartz and Rokosky, 2007). In the framework of rate and-state friction (see Section 2.6.1), SSEs have been suggested to arise along the base of the seismogenic zone due to a velocity-dependence of rate and state friction parameters, so that a material becomes stable once a critical velocity is reached. In particular, the change of frictional behaviour from velocity-weakening to velocity-strengthening, where faults can be considered conditionally stable, has been inferred as a possible mechanism for the nucleation of slow slip.

In the source of slow earthquakes, however, the microstructural record of the rocks potentially hosting slow slip cannot be implied by geophysical and geodynamic methods. As previously mentioned, metamorphic dehydration reactions are specifically important for understanding the deep ETS source, as they can set an important source of rheological heterogeneity, such as change in viscosity, shear stress and deformation mechanism active. Fluids are important in allowing deformation by pressure solution, which can enable deformation at very low shear stresses (Wassmann and Stöckhert, 2013), thus possibly favouring slow earthquake propagation. At depths below the seismogenic zones, dehydration from blueschist to form eclogite can increase viscosity and lead up to combined viscous – brittle shear, potentially resembling episodic tremor and slip (Behr et al., 2018). There is still however uncertainty on what is the rheology of high pressure rocks at depths below the seismogenic zone but before the onset of pervasive eclogitisation. In this sense, in order to understand ETS source, is fundamental to understand the rheology of blueschist rocks (Question 2), considering parameters such as which deformation mechanisms contribute to blueschist deformation style and how the metamorphic path influences rheology and slip style (Question 3).

2.5 Rheology of the lithosphere

Rocks that undergo deformation on the subduction plate boundary are typically a mélange of heterogeneous rock compositions, with a range of rheological properties that evolve with progressive deformation and metamorphism (Fagereng and Sibson, 2010; Raymond, 1984). Rheology is the study of the quantitative response of rocks to deformation, that is the change in shape and orientation as response to external stress. Rheology describes material properties through constitutive equations that relate stress and strain or strain rate (Bingham, 1929; Bürgmann and Dresen, 2008; Reiner 1964) and is the function of environmental, lithological and mechanical factors such as mineralogy, grain size, fluid content, chemistry, strain rate, T, P and shear stress (Knipe, 1989).

Rock deformation behaviour can vary between ductile and brittle deformation, these are purely descriptive terms that refer to the structures that can form in the rock. Brittle deformation refers to the development of discontinuous structures (i.e., fractures, faults), it is a pressure-dependent process because fracturing or frictional slip along grain boundaries or discrete fault planes is not affected greatly by temperature changes (Rutter, 1986; Schmid and Handy, 1991). Brittle deformation at the grain-scale may lead to ductile deformation at the larger scale, as brittle and ductile behaviour are scale-dependent (Passchier and Trouw, 2005). Ductile deformation leads to the development of continuous elements (i.e., foliations, lineations) and can result from fracturing, frictional, and viscous processes. The term viscous is used to describe mechanisms that produce strengths dependend on strain rate. Viscous deformation is described as a function of strain rate and stress, typically given as shear stress (τ) or as differential stress (σ). Strain rate ($\dot{\epsilon}$) can be defined as the speed at which rocks deform, for viscous creep τincreases as differential stress increases, and in the case of viscous rheology, the strain rate/stress relationship varies from linear to exponential. When strain rate

increases linearly with stress, the rock behaviour is defined as linear or Newtonian, whereas when strain rate increases exponentially with differential stress, rock behaviour is defined as non-Newtonian or power law (e.g., Schmid, 1982). Newtonian flow represents diffusive mass transfer deformation mechanisms, whereas power law represents dislocation creep (see Section 2.6.2) (Tsenn and Carter, 1987).

In a viscous system, when differential stress does not vary, rocks will deform at a constant strain rate, this is referred to as steady state flow. Most rocks do not show steady state flow during the entire history of deformation, during progressive deformation they can in fact experience strain hardening or strain softening. Strain hardening refers to increasing rock strength with strain rate, which in general refers to the increased work necessary to deform a rock and can lead to brittle fracturing of the rock volume. Contrarily, strain softening results in decreasing strength with strain rate, it generally refers to the less work necessary to deform a rock and can lead to localisation of deformation in shear zones (See Section 2.8).

2.5.1 Strength profiles

Modelling of lithosphere strength generally represents crustal rheology as a two-mechanism strength profile (Fig. 2.4A), where the upper parts of the crust are modelled using a brittle-frictional rheology, whereas the lower parts are described by viscous flow, generally using power law creep equations describing dislocation creep of quartz (Brace and Kohlstedt, 1980). As mentioned in the previous section, brittle failure is pressure-dependent, becoming more efficient with depth, and therefore brittle behaviour is generally modelled by a straight line, whereas at higher temperatures, ductile behaviour is dominant, which reduces crustal strength with depth, so that ductile behaviour is modelled by a curve (Sibson, 1977, Scholz, 1988). The two regimes are separated by a region of brittle-ductile (or frictional-viscous) transition (Byerlee, 1968; Schmid and Handy, 1991), which is generally

regarded as occupying a 5 – 20 km depth range in the lithosphere.

The two-mechanism strength model offers an overview of rheological behaviour of the lithosphere, however it is a very simplified model, as the strength of the lithosphere can vary based on tectonic environment over time. Another factor to take in consideration for fault strength is the presence of fluids, as they can cause fault weakening, with consequent shallowing of the brittle-ductile transition (Fig. 2.4B) (Imber et al., 2001; Winstch et al., 1995). In particular, Bos and Spiers (2002) identify the brittle-ductile region behaviour to be pressure-solution controlled, where mechanical behaviour is both normal stress and rate-sensitive. In this light, the deformation mechanisms active in rocks can shed light on what factors control rheology and fault/shear zone strength.

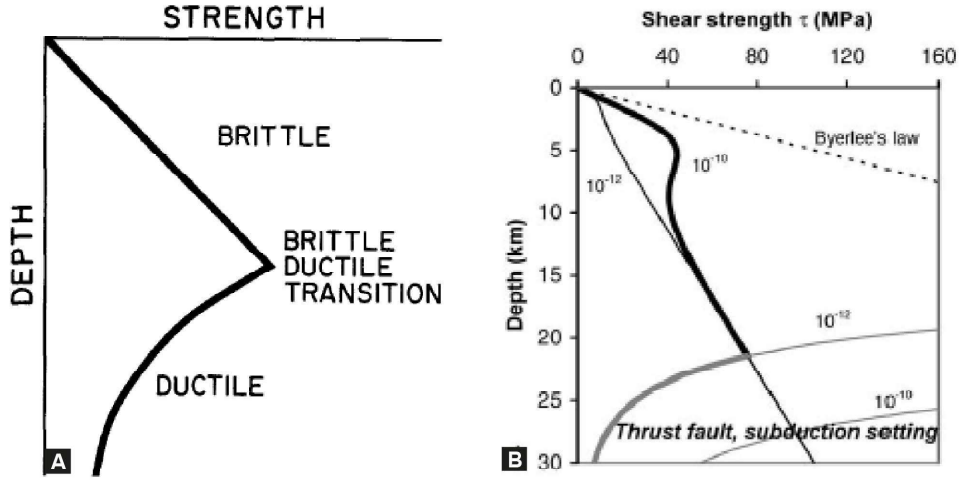

Figure 2.4: Strength-depth curves. A) Two-mechanism model from Scholz, 1988. B) Model considering pressure solution from Niemeijer and Spiers, 2005.

2.5.2 The subduction interface

Understanding of the dynamics of subduction-related deformation and seismicity requires knowing the rheological behaviour and properties of the plate interface. This requires focusing on the effects of temperature and pressure, but also on the

interaction of the interface with the mantle and overriding plate, as well as the lithological complexity of the interface and fluid circulation. The interaction of all of these parameters makes the description of the bulk rheological properties of the subduction megathrust particularly difficult.

One central topic in subduction zone dynamics, which allows to put into context rock rheology and deformation style, is the strength of subduction megathrusts. Stress state and strength of the interface is particularly important because it gives the framework of the dynamics of subduction as well as the mechanical framework to which different lithologies deform and to where deformation is localised. Global distribution of earthquakes demonstrates that deformation localises along plate boundaries, while the interior of the plates remain relatively undeformed, meaning that strain is localised at the interface. This, in turn, implies that subduction megathrusts are intrinsically weaker compared to their interiors. Thermal inversion analysis and geodynamic modelling show that plate interfaces generally have low shear stresses, in the order of 10 - 35 MPa (Beall et al., 2020; Duarte et al., 2015). These values may be influenced by different parameters, from variations in frictional strength, previous seismicity, fluid pressure, slab dynamics, and possibly plate age and sediment thickness (Beall et al., 2020; Duarte et al., 2015; Ruff, 1989). A well-used conceptual model requires the presence of weak subducting sediments on top of the mechanically strong oceanic crust to allow the plate interface to creep at low shear stresses (Shreve and Cloos, 1986), as seismic observations suggest the presence of a kilometres-thick creeping layer at the top of the deeply subducted oceanic lithosphere, which would act as a low-viscosity layer favouring plate creep (Tichelaar and Tuff, 1993). However the thickness of the sediment layer is not necessarily high, as dehydration and compaction during subduction can lead to more than 50% volume reduction by the time sediments get buried to 10 km depth (Moore and Vroliik, 1992). Moreover, the thickness of sediments is

variable between margins, and the oceanic crust is topographically rough in many creeping margins (Wang and Bilek, 2011) meaning that creep occurs despite the presence of seamounts and horsts with thin sediment cover, suggesting that creep of the oceanic crust does not necessarily need for a continuous layer of lubricating subducting sediments.

The only direct record of plate interface strength is contained in the microstructural and structural record of lithogies exhumed in the context of subduction zones. Therefore understanding the deformation mechanisms that guide the deformation style of exhumed subduction complexes can be correlated to the stress state of the plate interface.

2.6 Deformation mechanisms

Rocks strain as a response to stress. The mechanisms in which rocks deform depend on a series of factors, however a first distinction can be made by temperature and pressure dominant mechanisms. In the uppermost few kilometres of the crust, low temperature and low confining pressure conditions favour frictional deformation in the form of sliding along discontinuities, whereas at higher depth, temperature and confining pressure increase favouring deformation by viscous processes. The latter are temperature-dependent processes and they comprise a series of grain size-dependent mechanisms such as diffusive mass transfer and dislocation creep. Other factors are also important in guiding which deformation mechanisms can be active in rocks, such as composition, grain size, availability of fluids, strain rate and differential stress (Knipe, 1989). One single deformation mechanism can be active during deformation, however, rocks with heterogeneous components can deform typically by different deformation mechanisms, both frictional and viscous, active simultaneously (Knipe, 1989), for example with some rigid mineral deforming by

frictional mechanisms surrounded by others deforming by viscous processes, or the same mineral can deform by different mechanism in the same rock volumes, if grain size and/or fluid pressure distribution is heterogeneous. The physical conditions under which each deformation mechanism is dominant are illustrated in deformation mechanisms maps, which relate grain size, temperature, differential stress and strain rate in fields where one mechanism can be favoured over the another (Fig. 2.5). Deformation mechanisms are computed from mineral flow laws, which allow to identify T-stress domains where one specific mechanism is dominant in laboratory deformation experiments. Deformation mechanism maps therefore can be a useful instrument in assessing the conditions at which rock microstructure form, but careful handling should be taken as naturally deformed samples often show complex microstructures that cannot simply be put into a single mechanism field. For example, in shear zones, size reduction through brittle fracturing or crystal plasticity during strain localisation promotes grain-size sensitive deformation mechanisms such a diffusion creep, so there can be a switch from dislocation creep to diffusive mass transfer deformation (White et al., 1980).

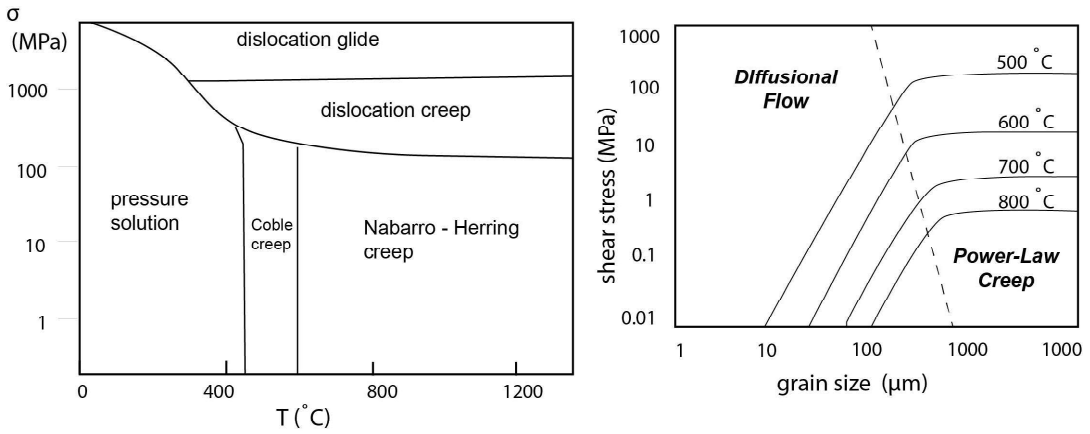

Figure 2.5: Left - Deformation mechanism map for quartz (from Rutter, 1986). Different deformation mechanisms are active at different T-stress conditions. Right - Deformation mechanism map for wet plagioclase. The dashed line indicates the passage from diffusional flow, which is dominant at small grain size, to power law creep, dominant at larger grain sizes (Rybacki and Dresen, 2004).

2.6.1 Fracturing and frictional sliding

At low confining pressure, stress causes elastic energy to be stored in rocks up until when the rocks reach their elastic limit and rupture, causing release of energy as seismic waves during earthquakes. This deformation is accompanied by loss of cohesion, and as a result, faults and fractures develop. Earthquake development or aseismic frictional slip on fault surfaces depends on rock frictional coefficient (Scholz 1998), where rock strength is controlled by the frictional properties of the rocks, following Amontons's law (Byerlee, 1978):

$$\tau = C0 + \mu * \sigma_n \tag{2.1}$$

Where shear stress (τ) is dependent on friction (μ) and differential stress (σ_n) and a coefficient depending on rock type (C0). Friction (μ) is dependent on confining pressure and has been measured in ranging generally from 0.6 (P $<$ 200 MPa) and

0.8 (P > 200 MPa), with shear stress increasing linearly with normal stress (Byerlee, 1978). The friction coefficient is largely independent of rock type (Byerlee, 1978), although the presence of phyllosilicates or clay minerals can lower significantly the value of friction. Another factor that significantly affects rock strength is rock fabric. Collettini et al. (2009) demonstrated how well-foliated rocks have significant lower friction coefficient (reduction of by values of 0.45-0.2) than rocks of similar composition but different fabric.

Since Byerlee (1978) rate-and-state friction laws have been used to better describe fault behaviour in generating stable or unstable slip by correlating the friction coefficient with the rate of deformation and state variables. The most commonly applied rate and state law is known as the Dieterich-Ruina law (Dieterich, 1979; Ruina, 1983), given as (Scholz, 1998):

$$\tau = \left[\mu_0 + a \ln\left(\frac{V}{V_0}\right) + b \ln\left(\frac{V_0 \theta}{D_c}\right)\right] \sigma_n \tag{2.2}$$

where V is slip velocity, V_0 is a reference velocity, μ_0 is the steady-state friction (when V=V_0), a and b are material parameters, and D_c is the critical slip distance. The state variable θ evolves according to:

$$\frac{\partial \theta}{\partial t} = 1 - \frac{V \sigma}{D_c} \tag{2.3}$$

where t is time and D_c is the critical slip distance over which μ evolves until it reaches steady-state. The parameter (a-b) controls frictional stability and can be expressed as:

$$(a - b) = \frac{\partial \mu}{\partial \ln V} \tag{2.4}$$

This means that if (a-b) is positive, then friction increases with slip velocity, consequently, rock is inherently stable and this behaviour is defined as velocity-

strenghtening. If (*a*-*b*) is negative, then friction decreases as slip velocity increases and the material is said to be velocity-weakening. It is inferred that velocity-strengthening behaviour promotes stable sliding and fault creep, while velocity-weakening behaviour promotes unstable sliding and earthquake nucleation. Earthquakes may propagate into velocity-strengthening material only if slip velocity is sufficiently high (Scholz, 1998).

2.6.2 Viscous deformation

There are several flow laws that empirically describe viscous flow, the simplest constitutive equation that embraces the different viscous mechanisms can be written in the form of

$$\varepsilon \;=\; A\, d^{-m}\sigma^{n} \;\; e^{(-Q/RT)} \tag{2.5}$$

Where $\dot{\epsilon}$ is strain rate (s), A is a material-dependent constant, d is grain size (μm), σ is stress (MPa) with m and n as respective sensitivity exponents, Q is activation energy for the material, R is the gas constant and T is temperature (K) (e.g., Rybacki and Dresen, 2004; Tsenn and Carter, 1987; Weertman, 1968). The equation highlights how grain size is a parameter that potentially determines strain rate variation. In this key, viscous deformation can be divided by grain size sensitive deformation, where m > 0, and grain size insensitive deformation, where m =0. Grain size sensitive deformation has $n = 1$, where deformation is guided by Newtonian flow and strain rate increases linearly with stress (Tsenn and Carter, 1987), whereas in grain size insensitive deformation, $n > 1$, deformation is guided by power-law and strain rate increases exponentially with stress.

Grain size sensitive creep

Grains size sensitive creep embraces diffusive mass transfer processes, which involve

strain associated with redistribution of material during deformation by diffusion processes. The term involves both solid-state diffusion creep and fluid assisted solution transfer (Knipe, 1989).

Diffusion creep works by migration of vacancies through the crystal lattice. When migration of vacancies happens within the crystal lattice, the mechanism is referred to Nabarro-Herring creep (intragranular diffusion) (Nabarro, 1948; Herring, 1950), whereas if diffusion of vacancies happens at the crystal boundaries, the process is referred to as Coble creep (intergranular diffusion or grain boundary diffusion) (Coble, 1963; Wheeler, 1992) (Fig. 2.6). Diffusion creep induces deformation by transfer of material (atoms) away from areas of high intergranular normal stress to areas of low intergranular normal stress. The driving force of this type of deformation is the presence of geochemical potential gradients within the crystal solids (Kerrich and Allison 1978; Wheeler, 1987). Diffusion creep is likely to be more effective in fine-grained materials, where the diffusion path is relatively short and where the differential stress levels are low enough to inhibit crystal plasticity (Knipe, 1989). Finally, diffusion creep mechanisms can and do happen without a fluid phase, however, the presence of fluids promotes diffusive mass transfer by accelerating the reaction and transport rate (Rutter, 1983).

When a fluid phase is present, the process is referred to as solution transfer (e.g., Wassmann and Stockert, 2013). This process involves dissolution at grain boundaries through a fluid phase, transport and precipitation in a new location. (Fig. 2.6). Typically, dissolution at grain boundaries happens at a high angle to the shortening direction, where normal stress is higher, and precipitation in a direction at low angle to normal stress, as the solubility of a mineral in an aqueous solution is higher where normal stress is higher (Gratier et al., 2013, Paterson, 1973). New phases can be transported locally, at grain boundaries, or at long distance, precipitating in strain shadows or veins (Fig. 2.9).

Both solid-state diffusion creep and dissolution-precipitation creep are favoured when grain sizes are small, and where stress is relatively low. Solid-state diffusion creep is active at higher temperatures than dissolution-precipitation creep, when temperature in a deforming rock is relatively high with respect to the melting temperature of constituent minerals (Passchier and Trouw, 2005).

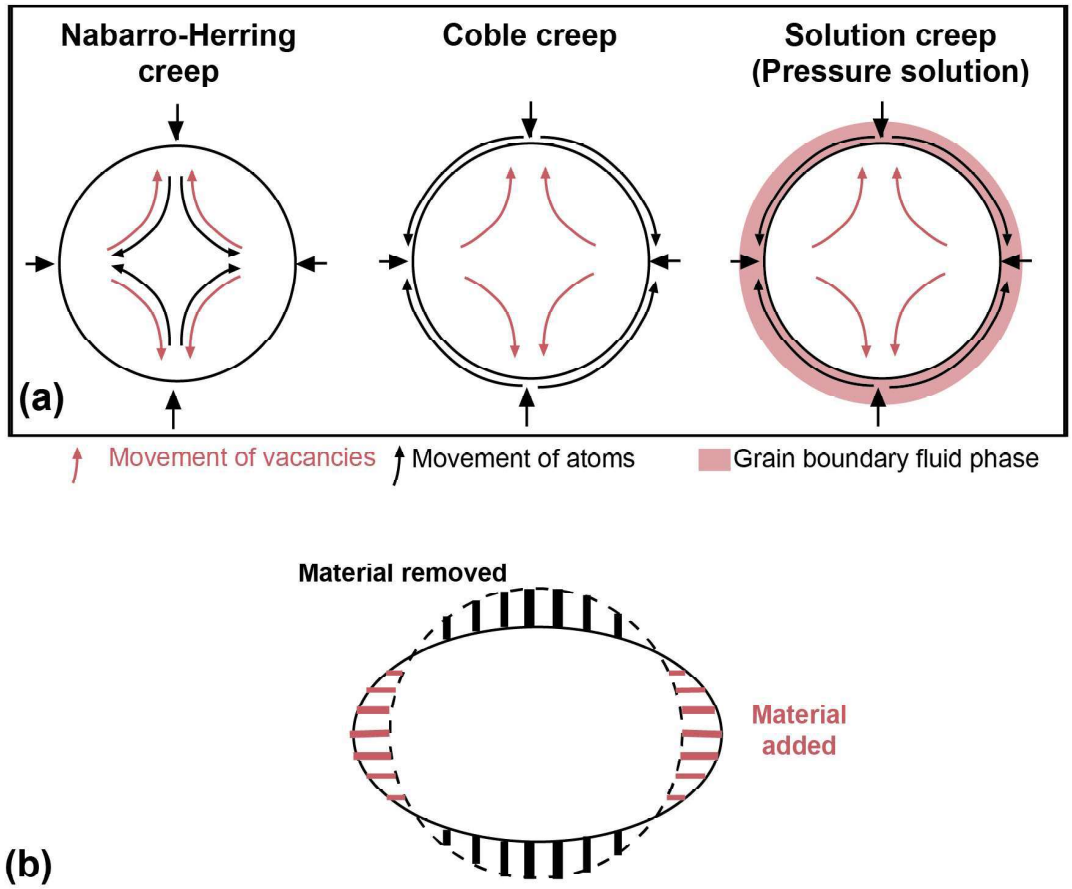

Figure 2.6: Diffusion mass transfer mechanisms. a) in Nabarro-Herring creep the movement of atoms remains within the crystal lattice, while in Coble creep atoms move at grain boundaries. During pressure solution, deformation happens at grain boundaries if a fluid phase is present. b) Change of shape related to deformation by diffusive mass transfer, where material is removed in the direction of applied stress and re-deposited in the direction of minimum stress. From Wojtal et al., 2022.

Grain size insensitive creep

In power law creep, deformation occurs by movement of lattice defects without brittle fracture, but while in diffusion creep lattice atoms are missing or are misplaced, in power law creep the lattice is distorted (Knipe, 1989), with the direction and minimum amount of displacement indicated by the Burgers vector. These defects are three-dimensional features referred to as line defects (dislocations, e.g., Wojtal et al., 2022). There are two types of line defects, screw dislocations and edge dislocations (Fig. 2.7). The screw dislocations exist where part of a crystal is displaced over one lattice distance from the other portion, whereas edge dislocations result from pulling apart two portions of the crystal and inserting an extra 'half lattice plane' (Passchier and Trouw, 2005). For screw dislocations, the Burgers vector is parallel to the line defect, whereas for edge dislocations, it is perpendicular to the dislocation line (Figure 2.7). The plane defined by an edge dislocation line and its perpendicular Burgers vector is known as glide plane, and, in the presence of sufficient applied shear stress, the dislocation line moves the Burgers vector across its glide plane, one lattice length at a time. This type of dislocation movement is referred to as dislocation glide (Wojtal et al., 2022). When the Burgers vector is coupled with the slip plane, it identifies a crystal slip system. Each mineral can have different slip systems active simultaneously, or they are active at different times, depending on the orientation and magnitude of the stress field in each grain. Moreover, dominant slip system for any mineral can change depending on T,P, and water content (Wojtal et al., 2022). Dislocations moving in specific slip systems cause the formation of a lattice preferred orientation (LPO).

As different slip systems get activated, dislocations can interfere with each other, getting tangled when they cross one another. At low temperatures and very high strain rates, distortion of aggregates by dislocation movement can occur without recovery or recrystallisation, as the low temperature hinders thermally activated mechanisms such as dislocation climb to occur. At these conditions, the

dominant deformation mechanism is expected to be dislocation glide, also referred to as low-temperature plasticity (Frost and Ashby, 1982; Kranjic et al., 2017; Tsenn and Carter, 1987). Experimental data shows that at high stress levels there is an exponential dependence of strain rate upon stress, greater than the one predicted by power law (Kranjic et al., 2017). Low temperature plasticity requires higher differential stresses for glide to occur, which can even surpass the differential stress necessary to cause brittle failure, therefore for ductile deformation to proceed, mechanisms that work against strain hardening need to operate. One effective mechanism that allows dislocations to pass by obstructions is dislocation climb, by which dislocations can effectively move to up or down their glide planes (Passchier and Trouw, 2005). This mechanism is operated by diffusion of vacancies, and it is hence thermally activated. The combination of glide and climb processes constitutes dislocation creep.

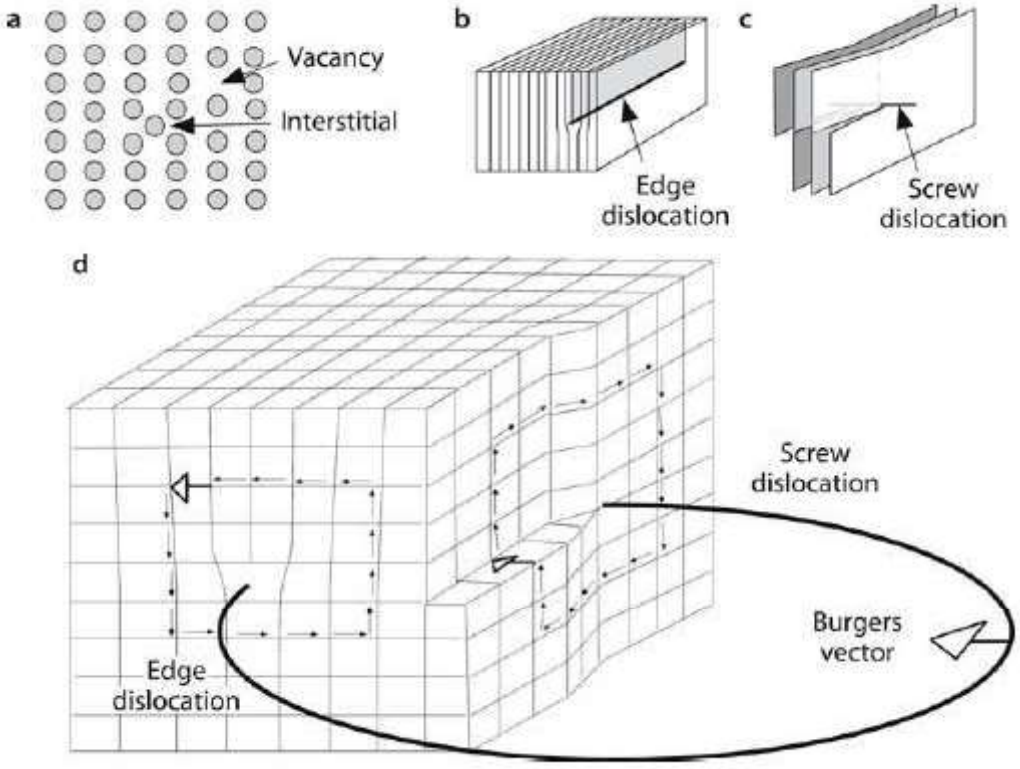

Figure 2.7: Crystal lattice and dislocations. A) schematic crystal lattice, with location of vacancies or interstitial atoms. b) edge and c) screw dislocations. d) Burgers vector direction when edge dislocations or screw dislocation are active. From Passchier and Trouw, 2005.

By enabling dislocations to untangle and move, climb eliminates the need for higher differential stresses to continue ductile deformation. Similarly, processes that reduce work hardening fall under the categories of recovery and recrystallisation. The term recovery covers mechanisms that lower the internal strain energy of crystals, which is at minimum when the lattice is free of dislocations, by reducing dislocation density (i.e., the total length of dislocations per volume, Passchier and Trouw, 2005). This situation can be achieved by climb or by the formation of tilt boundaries, also defined as low-angle boundaries. The movement of dislocations into tilt boundaries divides distorted single crystals into separate regions, relatively

undistorted, called subgrains. Another effective method to reduce internal strain energy is by recrystallisation. This process involves the reordering of the crystal microstructure through the change in grain size, orientation and shape of the crystal (Hirth and Tullis, 1992). The driving processes behind recrystallisation is the difference in internal energy between relatively strain free subgrains and highly strained neighbouring regions, therefore recrystallisation operates by grain boundary migration. There are three types of recrystallisation mechanisms, depending on temperature and stress regimes, which are defined as bulging, subgrain rotation and grain boundary migration recrystallisation (e.g., Hirth and Tullis, 1992; Stipp et al., 2002, Stipp et al., 2010).

Hirth and Tullis (1992) experimental data on quartz microstructure propose bulging recrystallisation (BLG, Regime 1) as dominantly active at low temperature and high stress and strain rates conditions, where recrystallisation is accommodated by grain boundary migration in the form of bulging of portions of deformed crystals (Fig. 2.8). Due to the low temperature conditions, climb is not effective, as it is dependent on diffusive processes that require higher temperatures (Lloyd and Freeman, 1994). With increase in temperature and/or decrease of strain rate, climb becomes more rapid and thus effective in accommodating recovery. Recrystallisation can occur by progressive subgrain rotation (SGR, Regime 2), where dislocations arrange into subgrain boundaries (Fig. 2.8) (Hobbs, 1968; Guillope and Poirier, 1979). With a further increase in temperature or decrease in strain rate (Regime 3), both of which result in decrease of flow stress, crystals deform by grain boundary migration (GBM) (Fig. 2.8). Given the higher temperature conditions, climb is still effective as recovery mechanism, therefore SGR is active in conjunction with GBM. Recrystallisation is achieved by subgrain rotation and once the grains have formed, they can become highly mobile and bulge (Lloyd and Freeman, 1994). Overall, dislocation creep requires higher stress to be activated,

compared to diffusion mass transfer (Tsenn and Carter, 1987).

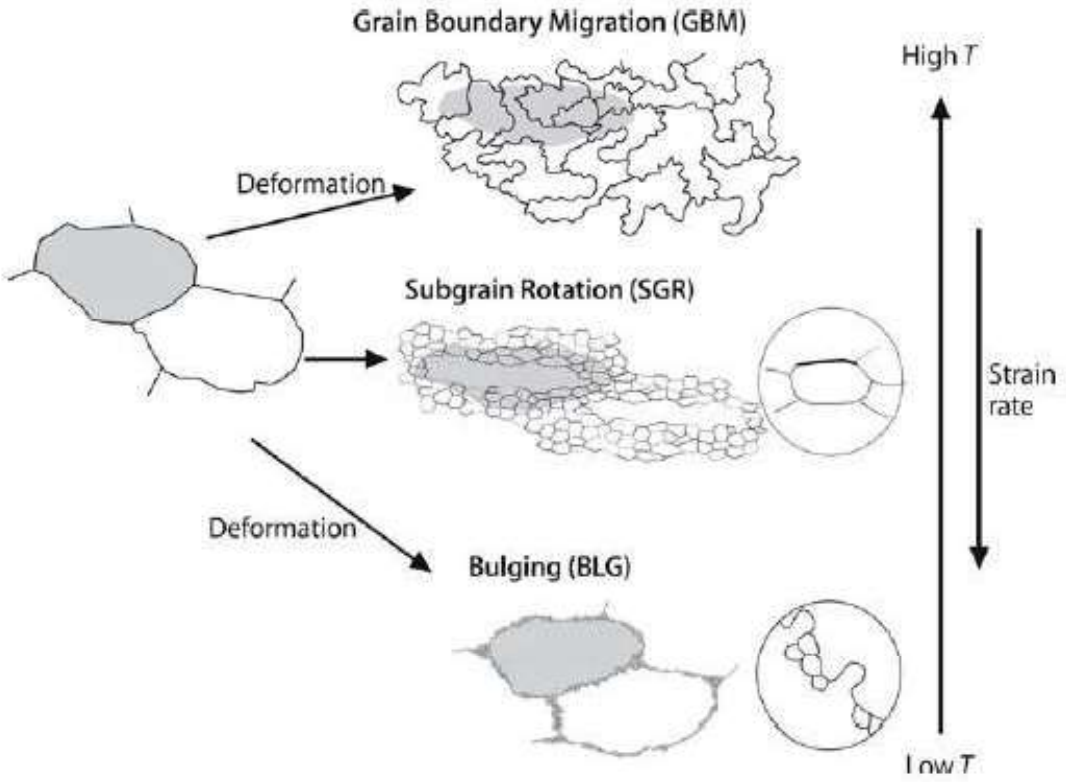

Figure 2.8: Dislocation creep regimes. From increasing T and decreasing strain rate, dislocation creep regimes are identified as bulging, subgrain rotation and grain boundary migration. From Passchier and Trouw, 2005.

Grain boundary sliding

When polycrystalline aggregates deform by diffusive mass transfer or dislocation creep, mineral grains must move past each other so to not create voids, with the movement taking place at their mutual interface (Langdon, 2006). When grain sizes are small, most of the deformation of the aggregate occurs with change of shale to enable grain movement past their neighbours, with each grain experiencing relatively small strain compared to the whole aggregate. (Wojtal et al., 2022). As, some distortion of grain shapes is necessary for the grains to move past each other,

the change of shape of each individual mineral can be accommodated by diffusive mass transfer or by dislocation creep. The net changes in shapes can be sufficiently small that the aggregate exhibits weak or no shape preferred orientation or even a weak CPO.

2.7 Microstructures

Microstructure refers to the arrangement of mineralogical and fabric elements within a rock. Minerals parameters such as grain size, shape and crystal lattice configurations (lattice distortion, LPO or lack thereof), change depending on temperature, pressure, shear stress, strain rate and fluid availability (Knipe, 1989). In this sense, microstructures register the physical conditions, kinematics and mechanisms of deformation, therefore they are a fundamental tool to understand rock rheology during tectonic events. In polymineralic rocks, the coexistence of microstructures with fabric-forming processes gives us clues about rock deformation history.

Diffusive mass transfer leaves behind microstructural evidence that is the consequence of movement of mass through the lattices of the grains, along the grain boundaries or along the interface between a fluid and the grains. When material gets removed from a source, it leaves behind evidence in the form of stylolitic contacts, truncated grain boundaries, or, especially in the case of solid-state diffusion, grain boundaries with no evidence of distortion or pressure solution (Fig. 2.9a). In the locations of deposition of new material, mass is added to existing grains in pressure shadows, where new material is identified by overgrowths, which often have fibrous habit, with their long axes parallel to the stretching direction (Fig. 2.9b). The internal structure of crystals that deform by diffusive mass transfer is characterised by lack of distortion in the crystal lattice, and minerals can show

compositional zoning, with change in composition from the centre to the rims, commonly in the direction parallel to extension. Moreover, as diffusion removes material from sites of high stress to deposit them in sites of low stress, the grains may develop a shape preferred orientation (SPO), with new crystals progressively align parallel to the stretching direction. SPO can be accompanied by LPO, as experimental data show that LPO can be formed by oriented grain growth and rigid grain rotation during deformation accommodated by diffusion creep of amphibole (Getsinger and Hirth, 1994) as well as by pressure solution in several naturally deformed samples (Menegon et al., 2008; Tulley et al., 2022).

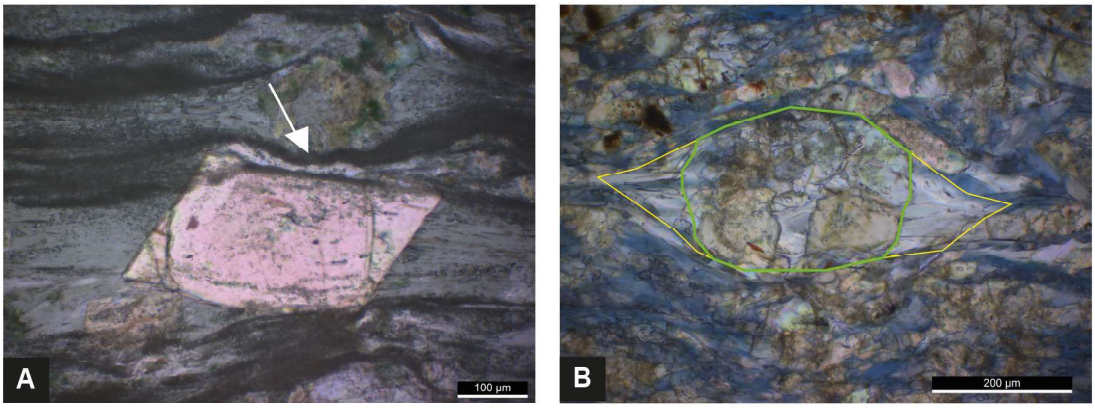

Figure 2.9: Examples of characteristic microstructures of diffusive mass transfer. A) truncation of epidote boundaries in a metabasalt from the Lento unit, the white arrows indicates the locus of dissolution of material. B) development of albite in epidote strain shadows, with mineral growth parallel to the lineation in an epidote-blueschist sample from the Tomuru metabasites.

For grain size insensitive mechanisms, diagnostic microstructures vary based on temperature-strain rate regimes described in Section 2.6.2. At the conditions where bulging recrystallisation is dominant, grains show undulose extinction, where different parts of the grains go extinct at different orientations in response of misorientations in the lattice causing extinction angles to change (Figs. 2.10a). Stipp et al. (2002) describe how recrystallised minerals are also characterised by sutured

grain boundaries, where recrystallised grains that form along the boundaries of larger porphyroclasts are about the same size as grain boundary bulges. Through Transmission Electron Miscoscopy (TEM) observations, grains show high density of tangled dislocations, which show no evidence for development of subgrains (Hirth and Tullis, 1992). At higher temperatures and lower strain rates, where climb is effective, recovery processes organise dislocations into subgrains by progressive subgrain rotation recrystallisation (Guillope and Poirier, 1979), and as grains continue to deform, subgrains develop larger angular misorientation compared to the host lattice (Fig. 2.10b). Once the angular distortion relative to the host grains exceeds 10°, the subgrains becomes effectively a new grain. The result is an aggregate with core-mantle texture (White, 1976), where 'core' refers to the deformed porphyroclasts and 'mantle' to the relatively strain-free subgrains and new grains developed at the edges of the porphyroclasts. Moreover, Stipp et al. (2002) observe that the porphyroclasts can form elongate ribbon grains, which can be completely polygonised, with subgrains at the core as well as the rims of the grains. At low strain rate conditions and high temperatures, where grain boundary migration is dominant, recrystallised grains exhibit irregular shape, commonly amoeboid, with lobate grain boundaries (Figs. 2.10c, 2.11). They have typically large to very large grains sizes compared to microstructures resulting from bulging. If grain boundary migration goes sufficiently far, the distorted cores of the grains can be replaced completely, creating a fully recrystallised rock. Grain deformation leads to reorientation of crystallographic direction which leads to the development of LPO (Knipe, 1989), however, as mentioned previously, LPO can be formed during diffusive mass transfer and therefore is not necessarily diagnostic of crystal plasticity.

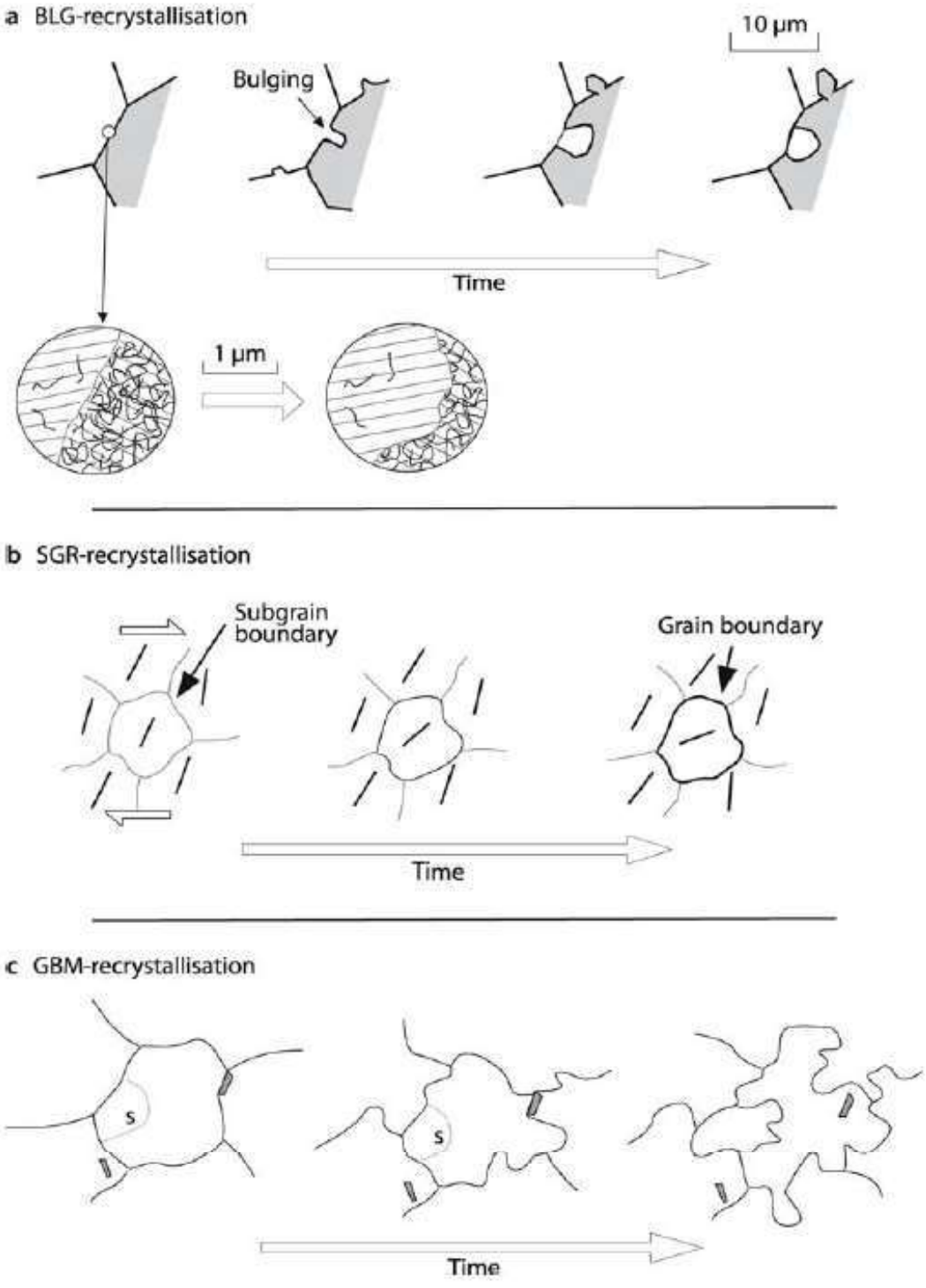

Figure 2.10: Schematic microstructures for dislocation creep. From Passchier and Trouw, 2005

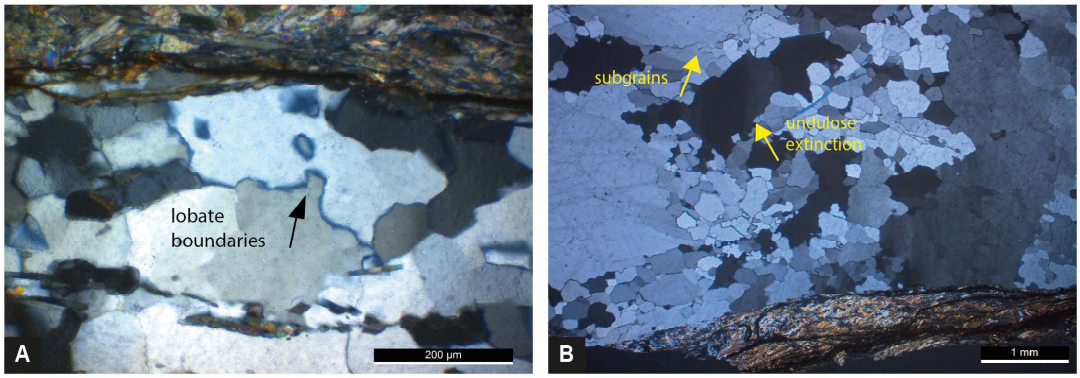

Figure 2.11: Examples of microstructures typical of dislocation creep in quartz grains. a) lobate boundaries identifying deformation by GBM in a quartz-rich vein from the Tomuru block-in-matrix metabasites; B) undulose extinction and subgrain formation during SGR – recrystallisation in a quartz-rich vein sample from the Tomuru metasediments.

2.8 Strain localisation in shear zones

Strain localisation represents mechanical weakening of rocks, which in turn can be defined as the reduction in stress at constant strain rate, or as the increase in strain rate at constant stress (e.g., White et al., 1980). Different factors can occur in promoting strain localisation in rocks, one of the main important factors is grain size reduction (Rutter and Brodie, 1988, Montesi and Hirth, 2003), which can possibly change the active deformation mechanism, from grain size insensitive creep to grain size sensitive diffusion creep, which in turn lowers the strength of the rock (De Bresser et al., 2001). Grain size reduction might be the result of fracturing, dynamic recrystallisation, as subgrains have smaller grain sizes than the original mineral, and of metamorphic reactions. The latter can contribute to strain localisation by forming smaller grains that are likely to promote diffusive mass transfer, of by producing soft, new strain-free grains with consequent increase in strain rate in the reaction products (White and Knipe, 1978). Metamorphic re-

actions can also create new grains that are weaker than the original ones, which constitutes reaction softening (e.g., Wintsch et al., 1995) for example by phyllosilicate production from stronger phases such as amphibole or feldspars, which is typical of retrograde metamorphism. Reaction softening and fault weakening is therefore typical of retrograde shear zones (Imber et al., 1997). New grains are observed to form in the orientation parallel to shear direction, with grains aligning to form interconnected networks, this way, shear zone strength can be significantly reduced (geometric weakening, e.g., Handy, 1990; Collettini et al., 2009). Finally, fluid circulation contributes to lowering shear zone strength by i) promoting diffusive mass transfer mechanisms, particularly enhancing dissolution-precipitation processes (Gratier et al., 2013) and grain boundary sliding (Langdon, 2006), ii) lowering effective stress by increasing fluid pressure, therefore lowering fracture strength of a rock and causing hydraulic fracturing and consequent weakening by reduced grain size and/or crystalplastic recovery and recrystallisation (White et al., 1980), iii) kickstarting metamorphic and metasomatic reactions that lead to the aforementioned reaction weakening.

The review just presented shows how the rheology of rocks deforming in subduction zones affects slip behaviour of faults. Particularly, the rheology of blueschist rocks is an interesting topic, since the T-P conditions of deformation are likely spatially coincident to the ETS source downdip of the seismogenic zone. However, literature describing epidote-blueschist rocks is scarce, as it typically focus along the lawsonite-blueschist to eclogite transition. We use Research Questions 1 to 3 to address epidote-blueschist rheology in subduction zones. Particularly, with Q1 we compare the deformation style of epidote-blueschists deforming along the prograde path (Chapter 6) and retrograde path (Chapter 7); with Q2 we focus on describing what elements govern epidote-blueschist rheology, in particular what are the deformation mechanisms active in epidote blueschists and greenschist (Chapter 5

and 6) and retrograde blueschists (Chapter 7). Finally, Q3 specifically addresses how the metamorphic path (prograde/retrograde) can affect rheology.

In order to understand epidote-blueschist rheology and answer the research questions, we study samples from two exhumed subduction complexes (see Chapter 3), the Tomuru block-in-matrix metabasites (Ishigaki, Ryukyu arc, SW Japan), which record prograde deformation at epidote-blueschist conditions, and the Lento unit metabasites (Lento, Alpine Corsica), which register retrograde deformation from blueschist to greenschist conditions. In order to address the rheological questions, we use microstructural and laboratory based analyses on metabasites deformed along the prograde and retrograde path (see Chapter 4).

Chapter 3

Geologic setting

3.1 Exhumed epidote-blueschists in the Ryukyu arc (Ishigaki, SW Japan)

The island of Ishigaki is part of the Yaeyama islands, set in the southwestern sector of the Ryukyu arc, east of Taiwan. Here the oceanic crust of the Philippine Sea plate subducts towards the NW at 12.5 cm/yr (Heki and Kataoka, 2008) under the Amurian plate along the Ryukyu trench (Lallemand et al., 1999) (Fig. 3.1a). Oblique convergence of 40° causes important right-lateral strike-slip faults in the upper plate (Lallemand et al., 1999). The Ryukyu arc is separated from the Nankai subduction zone by the Palau-Kyushu ridge, and these two tectonic areas have different geologic structures and plate structures, so that correlations between the two are difficult.

The stratigraphy of Ishigaki island comprises a metamorphic basement, consisting of Triassic Tomuru metamorphic rocks, the Jurassic Fusaki Formation and Eocene Miyara and Nosoko Formations, unconformably overlain by quaternary sediments (Kizaki, 1986; Nuong et al., 2008; Osozawa and Wakabayashi, 2012)

(Fig. 3.1b). The Tomuru metamorphic rocks, the subject of this study, crop out in km-scale anticlinal domes overlain by the sedimentary cover in the northern, central, and western areas of Ishigaki (Osozawa and Wakabayashi, 2012), and they consist of HP-LT mafic, pelitic and psammitic schists, the latter containing blocks of metamorphosed gabbros and serpentinites, interpreted as originating from the oceanic crust (Nuong et al., 2008). Two types of veins intersect these rocks, and can be classified by composition as quartz-rich and epidote-rich. Quartz-rich veins are abundant in the pelitic schists and at the contact between the mafic and pelitic lithologies and are parallel to subparallel to the main foliation. Quartz-rich veins are also present in the mafic schists, but are less abundant than in the pelitic schists. The epidote-rich veins are limited to the mafic schists, occur relatively scattered throughout the studied outcrops, and appear both parallel to and cross-cutting the main foliation.

The mafic schists have been divided into three groups based on their mineral assemblages, indicative of different metamorphic grades (Nuong et al., 2008). The lowest grade rocks contain glaucophane, pumpellyite, lawsonite and aragonite, while in the intermediate grade metabasites the pumpellyite, aragonite, lawsonite assemblage is replaced by glaucophane and epidote. In the north of Ishigaki island the highest-grade rocks crop out, containing barroisite in the mafic schists and garnet in the pelitic schists. The boundaries between the three groups of rocks are covered by later sedimentary rocks and cannot be directly observed. K-Ar phengite dating gives metamorphic ages ranging from 208-220 Ma for the highest grade metabasites to 188-205 Ma for the lowest grade metabasites. Based on the presence of aragonite, metamorphic conditions have been estimated at $\sim$ 400 ℃ and 8-9 kbar (Ishizuka and Imaizumi, 1988).

On the basis of these apparent radiometric dates, a unique correlation of these rocks to other HP metabasites in the adjacent tectonic regions to the Ryukyu

arc has not been possible and remains largely speculative to this day, as they have been correlated by different authors to different HP units, namely the Upper Paleozoic Sangun metmaorphic rocks of Japan and the Nagasaki metamorphic rocks of Kyushu (Faure et al., 1988), however, since exposed land along the Ryukyu Trench is scarce, basement correlations between the Ryukyu arc and the northern sectors are difficult and remain speculative.

The paragenesis of the blueschist rocks in this study is characterised by glaucophane, Fe-epidote and albite as the main foliation-forming minerals, along with minor quartz and titanite, and by the absence of lawsonite. This signifies metamorphic conditions at the epidote-blueschist facies, although we cannot exclude that some of the epidote was originally lawsonite during the progressive deformation recorded in the rocks. It is important to consider that epidote and lawsonite do not respond identically to deformation (Kim et al., 2013); however, the approach used in this study should have general applicability to understanding epidote-blueschist rheology, due to the preponderance of foliation-forming glaucophane in most blueschist rocks and given that it is generally abundant in our samples.

Two deformation stages are recognized. The first, D1, resulted in the main foliation S1 striking NNE-SSW with gentle to moderate dips to the NW (Fig 3.1c), and it is characterized by stretching lineations (L1, Fig. 3.1c) and shear structures with a general NW-SE trend and top-to-SE sense of shear (Osozawa and Wakabayashi, 2012). Peak HP-LT metamorphism is related to the D1 deformation stage based on the mineral paragenesis defining the main foliation S1, characterised by the presence of glaucophane, Fe-epidote and albite with minor quartz and titanite. A second deformation stage, D2, is recognized as folding the S1 schistosity with asymmetric open folds with NE vergence and axial planes dipping gently towards SW (Fig. 3.1b). The D2 transport direction is subparallel to NE-SW striking strike-slip faults, leading previous authors to hypothesise that the

exhumation might have been associated with a significant strike-slip component (Osozawa and Wakabayashi, 2012). The D2 stage is suggested to have accommodated exhumation, including the extrusion of the Tomuru rocks in the core of km-scale anticlinal domes, according to Osozawa and Wakabayashi (2012). Our microstructural observations are limited to the epidote-blueschist mafic schists of the Tomuru metamorphic rocks, sampled where D1 structures and S1 foliation dominate and the rocks are not markedly affected by D2 deformation.

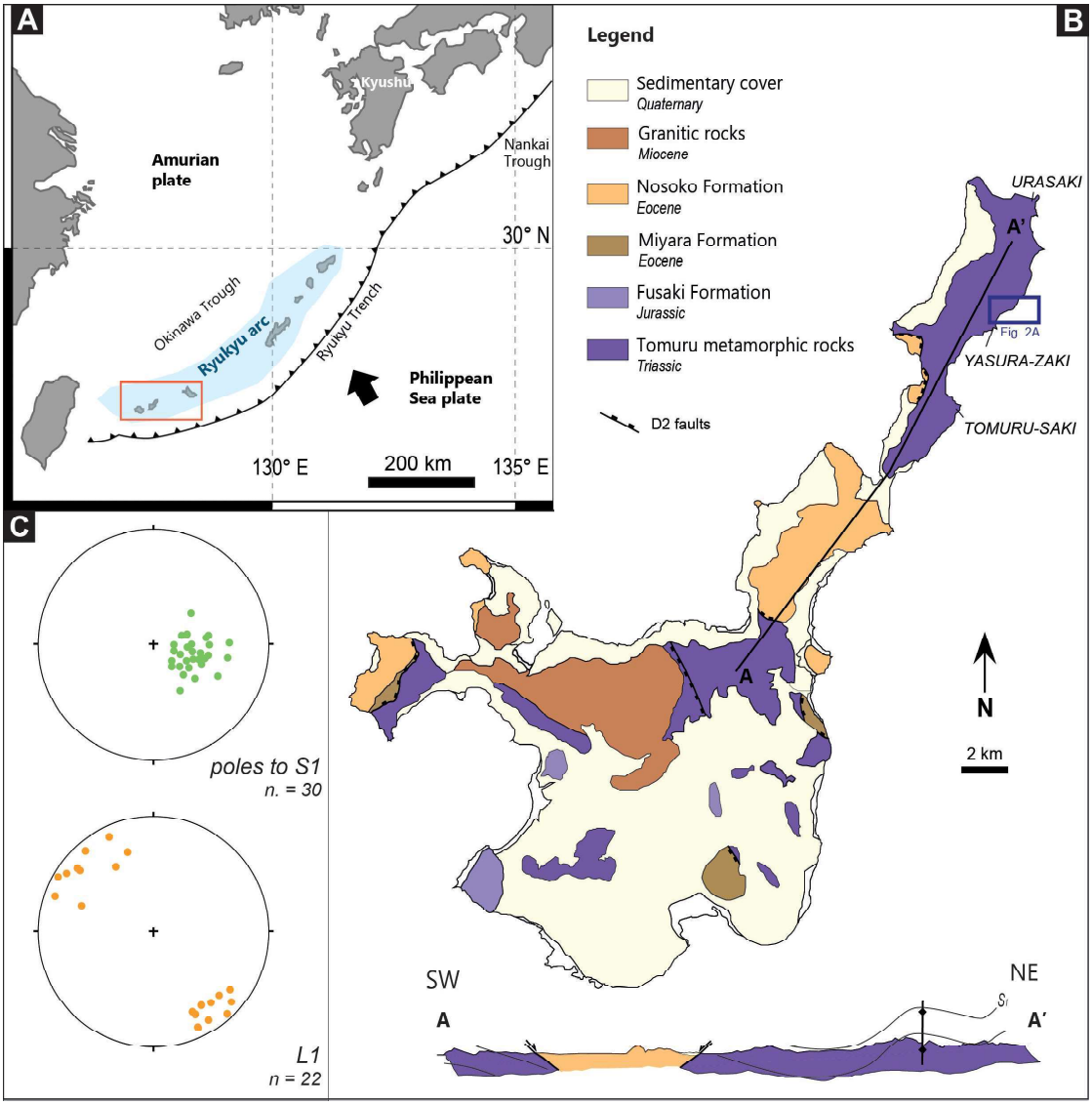

Figure 3.1: a) Tectonic setting of the Ryukyu arc, SW Japan. The Philippine Sea Plate subducts towards NW under the Amurian plate along the Ryukyu Trench. Contoured in red, the location of the Yaeyama Islands, where Ishigaki Island is located, in the southernmost sector of the Ryukyu arc; b) geologic map of Ishigaki Island and geologic profile (modified from Osozawa and Wakabayashi, 2013). Contoured in blue, the location of the analysed block-in-matrix epidote-blueschists; c) stereographic equal area projections of the main structures measured in the Tomuru epidote-blueschists, foliation S1 and mineral lineation L1 (n=number of measurements). S1 is generally NNE-SSW striking, with gentle to moderate dips to NW; L1 dips gently towards SE and NW.

3.2 Retrograde blueschists from the Lento unit, (Schistes Lustrés, Alpine Corsica)

The geologic setting of Corsica is characterised by a complex stack of tectonic units, with the Alpine Corsica, characterised by a stack of units of Mesozoic age, is thrust over the Hercynian Corsica, characterised by Carboniferous to Permian granitoids intruded by late Permian volcanics (Fig. 3.2) (Duran-Delga, 1984; Marroni and Pandolfi, 2003).

In analogy with the Western Alps, Alpine Corsica is characterised by a series of oceanic units derived from the Ligure-Piemontese oceanic basin and continental units from Adria and Europe margins (Duran-Delga, 1984; Marroni and Pandolfi, 2007; Molli and Malavielle, 2011). Starting in Late Cretaceous, oblique convergence between Europe and Adria resulted in the development of a subduction zone, possibly within the Ligure-Piemontese ocean. Several hypotheses involve either west-dipping or east-dipping slabs, or the result of a tectonic inversion from one to the other (Vitale Brovarone et al., 2013 and references therein). During intraoceanic convergence, the oceanic sequence of Alpine Corsica was metamorphosed and deformed through underthrusting and subsequent accretion (Marroni and Pandolfi, 2007). In the Eocene, intraoceanic subduction was followed by continental collision (Duran-Delga, 1984). During this stage the oceanic units were thrust westward into the continental margin, with the resulting structure being a double verging orogenic wedge, where the oceanic units occupy the uppermost structural levels.

Alpine Corsica deformation reflects the evolution from Late Cretaceous intraoceanic subduction of the Ligure-Piemontese oceanic lithosphere to the Eocene continental collision (Di Rosa et al., 2019; Malavielle et al., 1998; Marroni et al, 2004; Vitale Brovarone and Herwartz, 2013). Subduction of oceanic lithosphere

was accommodated through ductile deformation operating during D1 deformation phase. D1 structures involve S1 HP-LT foliation that is preserved in the most competent lithologies (e.g., Vitale Brovarone et al., 2013). D2 deformation phase reflects the early exhumation conditions and D2 fabrics and structures are the most prominent features in Alpine Corsica, these are characterised by isoclinal folding, S2 penetrative foliation at greenschist conditions and thrusts with top-to-NW sense of shear, which accommodate exhumation by tectonic extrusion (Di Rosa et al., 2017). Following D2, exhumation is guided by D3 deformation stage, characterised by top-to-NW shear zones with structures involving S3 foliation indicative of sub-greenschist facies deformation, typically registered in the less competent lithologies. Finally, D4 structures accommodate the very last stages of exhumation in the form of large scale, high angle normal faults. No recrystallisation has been associated with this stage.

Within Alpine Corsica, the Schistes Lustrés complex is composed of a series of lithostratigraphic units where the processes related to the intraoceanic subduction and subsequent continental collision are well recorded. Deformation stages record the tectonic evolution from Late Cretaceous subduction-related HP/LT metamorphism to subsequent Middle Eocene retrograde metamorphism during exhumation (Guyedan et al., 2017; Vitale Brovarone et al., 2013; Vitale Brovarone et al., 2014). The Schistes Lustrés complex has also been divided into units separated by their metamorphic grade, from the lowest structural level to the highest there are the i) lawsonite-eclogite and lawsonite blueschist units (Fig. 3.2), with jadeite-bearing blueschist to eclogite metamorphism, ii) the lawsonite-blueschist units, with high grade-blueschist facies overprint, and iii) the low-grade blueschist units, which include the Lento unit, strongly deformed under blueschist facies metamorphism (Levi et al., 2007; Vitale Brovarone et al., 2013).

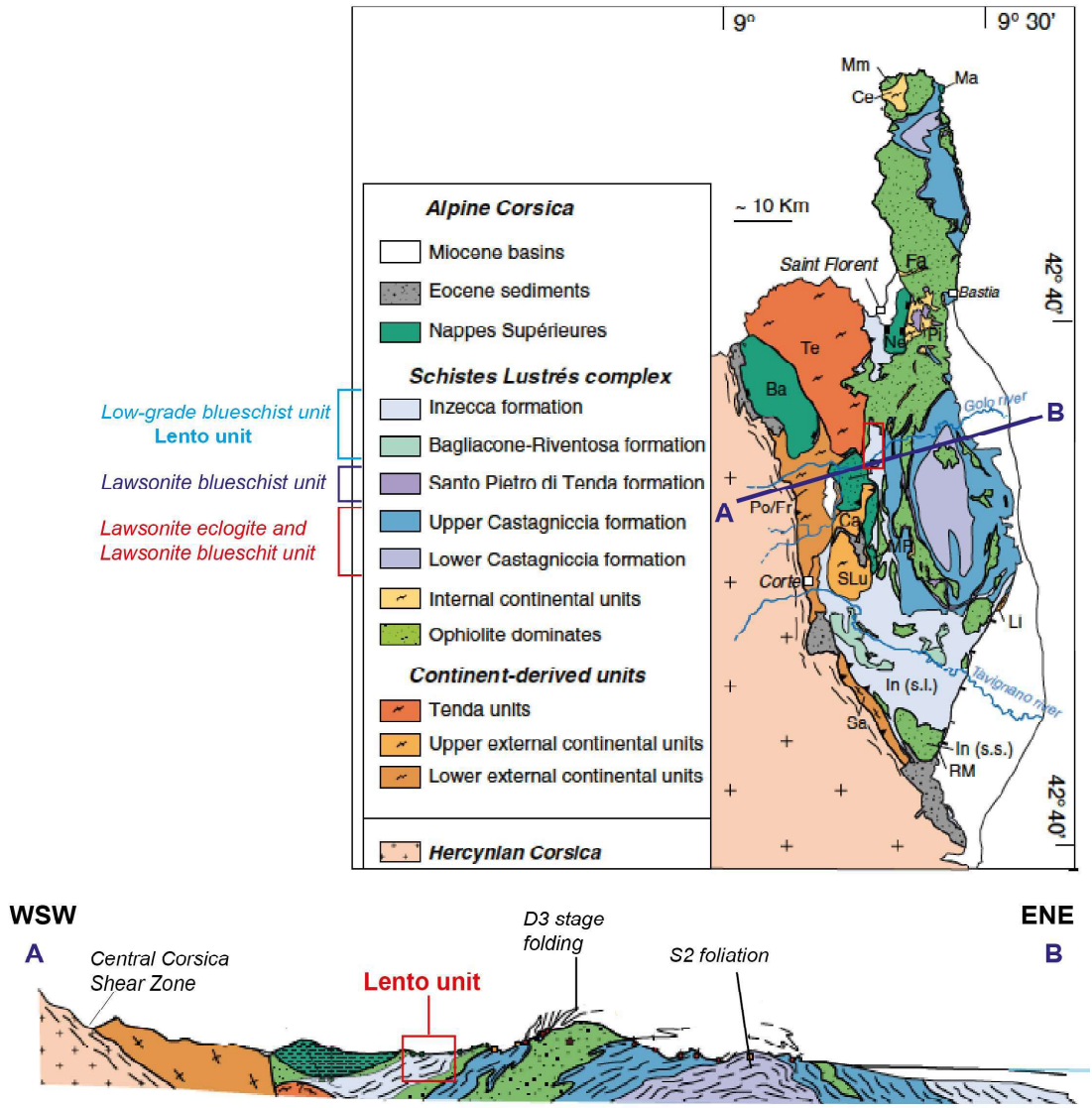

Figure 3.2: Tectonic setting of Alpine Corsica (from Vitale Brovarone et al., 2013). Alpine Corsica is characterised by a complex stack of units, here is reported the division by lithostratigraphic units and the corresponding metamorphic units. In red rectangle, both in the map and in the cross section, the location of the Lento unit, subject of this study. In the cross section are highlighted the two most prominent structural features of Alpine Corsica, the S2 foliation and D3-stage folding. Hercynian Corsica are divided by the Central Corsica shear zone.

The Lento unit, the subject of this study, is characterised by a Middle to Late Jurassic metaophiolite sequence consisting of a basement covered by a volcano-sedimentary complex followed by a sedimentary sequence. The basement is rep-

resented by metaserpentinites associated with metagabbros, both covered by a volcano-sedimentary sequence of metapillow lavas and metaophiolitic breccias. The metasedimentary succession includes a thin level of metaradiolarites and a thick succession of dm-thick layers of micaschist and marbles alternate with m-thick levels of calcschists, defined as the Erbajolo Formation.

The Lento unit registers four deformation stages, from subduction-related to exhumation-related deformation of Alpine Corsica (Fig. 3.3). D1 phase structures are poorly represented due to the intense transposition from the more pervasive D2 stage structures. It is recognised as non-cylindrical intrafoliar folds in marble layers and in metagabbros, or as a continuous foliation within microlithons at the microscale, with a HP paragenesis characterised by sodic amphibole, lawsonite and phengite, indicative of low-grade blueschist metamorphism (Levi et al., 2007). D2 phase structures are the most widespread, both in the ophiolitic basement and in the metasediment succession. D2 deformation is characterised by isoclinal folds, NW-verging, associated with a well-developed S2 foliation. At the microscale, the S2 foliation is characterised by the recrystallization of chlorite, Na-Ca amphibole, quartz, albite epidote and minor titanite. The S2 paragenesis is superimposed over the high-pressure S1 mineral assemblages.
D3 deformation stage is characterised by E-verging folds associated with a spaced S3 axial plane foliation, which occurs as disjunctive cleavage in the more competent units such as the metaophiolitic basement and marbles layers of the sedimentary succession, and as a crenulation cleavage in the micaschists and calcschists. At the microscale S3 foliation is found only in the micaschists, and it is characterised by quartz, calcite, chlorite and white mica. D4 structures occur as sub-vertical open folds that only slightly modify the structural setting. At the microscale, they are not associated with metamorphic assemblage, and they are found as a weak and widely space disjunctive cleavage. D1 phase structures and associated blueschist

metamorphism can be regarded as formed during accretion in a subduction zone during the Late Cretaceous (Lahondere et al., 1997; Levi et al., 2007). The post-D1 deformation is regarded to be related to the exhumation history of the Lento unit, developed until the Miocene, when the sediments seal all the deformation observed in the Schistes Lustrés (Brunet et al., 2000). D2 phase is interpreted to represent the first exhumation stage, which shortening event forming NW-verging folds linked to duplex formation in the accretionary prism (Levi et al., 2007). Microstructures of S1 and S2 paragenesis are interpreted to represent near isothermal transition from blueschist to greenschist facies conditions, with D2 structures being the subject of this study. D3 phase is connected to a further shortening event, producing E-verging structures, evolving at shallower levels than the previous D2 deformation stage, as interpreted form the low-grade sub greenschist metamorphic assemblages. Finally, D4 deformation structures are thought of originated from vertical shortening and folding of pre-existing structures. Since no metamorphic mineral assemblage has been recognised in association with D4 phase, it is interpreted to represent deformation during an even shallower tectonic event before the onset of extensional tectonics. D3 and D4 structures have been observed on the field but not considered for this study.

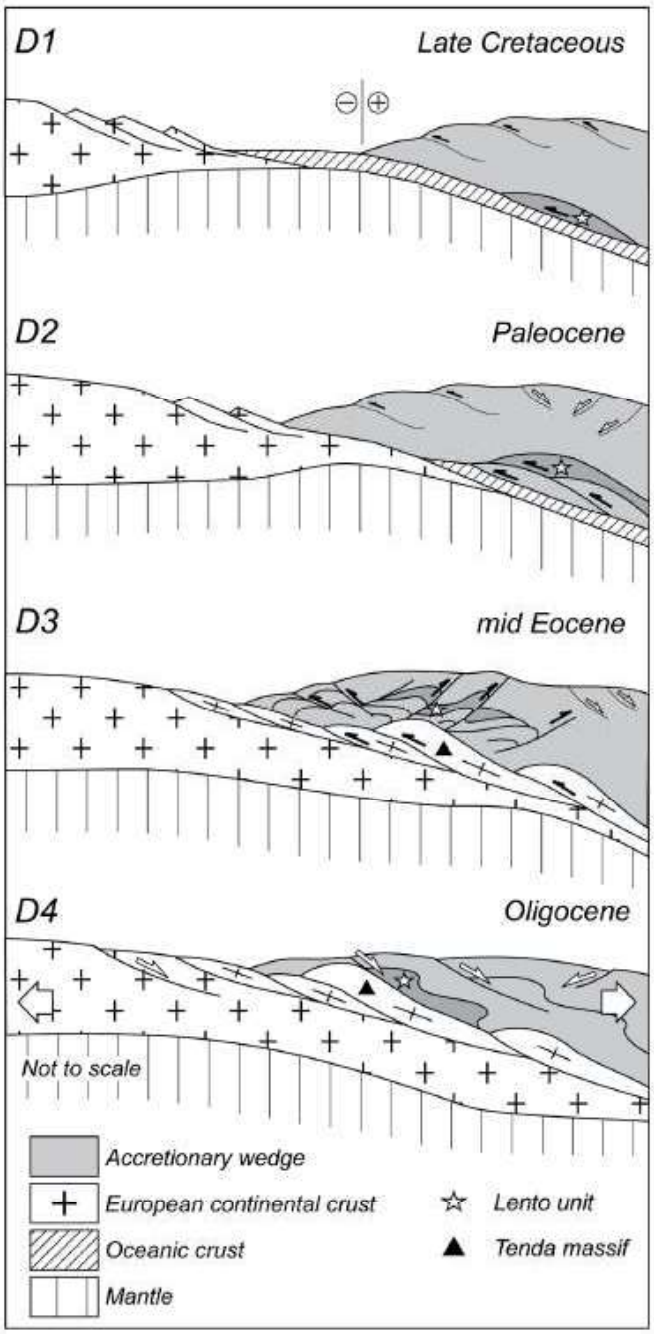

Figure 3.3: Geodynamic model of the Lento unit tectono-metamorphic history. D1: coherent underplating at 25-30 km, D2: transition from accretion to exhumation through Nw-verging thrusts and duplexes; D3: exhumation stage through horizontal shortening with E-verging thrusts; D4: final stage of exhumation, extensional event (from Levi et al., 2007).

Chapter 4

Methods

Chapter 5 data is based on a total of 11 samples of epidote-blueschist rocks were used for microstructural observations, and two representative samples were chosen for detailed microstructural analyses, each representing block and matrix of the epidote-blueschist Tomuru metamorphic rocks (see Table 6.1, Chapter 6). In Chapter 6, a total of 6 samples of greenschist blocks were used for microstructural observations. Included in the analyses in this chapter are 11 samples of epidote-blueschist rocks, already described in Chapter 5 (Table 6.1). Samples of greenschist and epidote-blueschists were collected where D1 structures and S1 foliation were the main feature and where rocks were not markedly affected by D2 structures. Chapter 7 is based on 17 samples (See Table 7.1, Chapter 7) of metabasites and metasediments were used for microstructural analysis. Samples were collected from the field where the main structural feature were the D2 structures and where overprint by subsequent structures (D3-D4) was undetected or marginal.

Hand-samples were cut along the kinematic XZ section of the finite strain ellipsoid, where the X-axis is parallel to the stretching lineation, defined in both samples by the preferred alignment of glaucophane and albite grains, and the Z-axis is perpendicular to foliation. Foliation-forming glaucophane, epidote and albite were

analysed on polished carbon-coated thin sections using the Zeiss Sigma HD Field Emission Gun scanning electron microscope (SEM) in the School of Earth and Environmental Sciences at Cardiff University equipped with two Oxford Instruments energy-dispersive spectroscopy detectors (EDS). EDS maps were obtained with 20kV beam current, 2µm step size and 40% dwell time. Electron backscatter diffraction (EBSD) patterns were acquired with a Nordlys Oxford Instruments detector and 20 kV accelerating voltage, 14 – 22 mm working distance and 0.5 – 2 µm step size on a 70°tilted sample. EBSD data were analysed using automated procedures in the MTEX toolbox (Bachmann et al., 2010) in MATLAB to obtain grain maps of block and matrix, mineral proportions, to carry out fabric analyses and to provide crystallographic orientation data for the principal foliation-forming components of the rocks.

EBSD maps are formed by moving a focused probe electrons though a grid on the sample surface in a scanning electron microscope. The electrons backscattered from the samples are collected by the detector to a photon sensitive imaging detector (charged coupled device camera) to form electron backscatter diffraction patterns. The sample is highly titled (70°) to increase the quality of the patterns obtained. Patterns are then processed from the camera to the processing computer through Aztec software, where the diffractions patterns are related to identification of specific mineral phases and crystal orientation data. The resulting EBSD map then contains data about the crystal species that characterise the rock sample, their grain boundaries, mineral crystallographic orientation and lattice characteristics. Good indexing of the different mineral phases results in a good quality EBSD map which is the key step into accurate rheological analysis and interpretation. The quality of the pattern and the EBSD map depends on a few factors, including the stepping size of the map, which is measured in μm and refers to the measure of the smallest length at which the probe scans the sample

surface, with smaller step sizes resulting in more accurate reading of the sample surface, although it significantly impacts the time of processing. Minerals with inclusions or that have poor database constraints can be poorly indexed with resulting higher percentage of 'non indexed' phases. This technically impacts the quantity of the information carried by an EBSD map, however not necessarily its quality, as the 'non-indexed' percentage could be made up of single pixels that add up to the overall section, which is common in larger maps. EBSD maps used in this thesis have 'non-indexed' percentages from 20- 40%, these values seem high overall, however they only limitely impact the phases used to constrain the samples rheology, as amphibole, epidote and albite are all well indexed and show well defined grain boundaries and are therefore useful to constrain their microstructural characteristics and overall rheology of the rocks.

4.1 Grain reconstruction and fabric analyses

Grain boundaries were digitised using the automated 'calcGrains' procedure through the MTEX toolbox with a 10°misorientation threshold to define single grains. Grain sizes of glaucophane, epidote and albite were determined by fitting ellipses to single grains and measured as the equivalent diameter derived from the grain area measured through an automated procedure in MTEX. Grain size results have been plotted in grain size histograms for each mineral analysed, along with mean and standard deviation. Mean grain size has been measured as the arithmetic mean, although geometric mean can be more precise, in these samples the difference between arithmetic and geometric mean are not dissimilar, as both are close to the peak value of the grain size histograms. SImilarly in MTEX, fabric analysis was carried out by measuring the grain aspect ratios, calculated as the ratio between long and short axes of fitted ellipses, and the grain orientations,

calculated as the angle of the fitted ellipse long axis to the stretching lineation (Sections 5.3.2; 6.3.3). Grain aspect ratios were plotted against grain orientations to show the degree of shape-preferred orientation of each mineral phase.

4.2 Misorientation maps and LPO plots

Orientation data for glaucophane, epidote and albite were used to compile internal misorientation maps (mis2mean) and lattice preferred orientation (LPO) plots (Sections 5.3.3; 6.3.3; 7.4). Mis2mean measures the intragranular misorientation as deviation from the grain mean misorientation value. It has been the preferred method used in this thesis as it can effectively show the quantity and shape of intragranular lattice distortion. The latter have been created based on the mean orientation of single grains. The mean orientation of each grain has been plotted on lower hemisphere, equal area projections. The M-index was calculated for each mineral, as a measure of LPO fabric strength from 0 for random fabrics to 1 for single crystal orientations and it is based on the distribution of misorientation angles (Skemer et al., 2005). It has been preferred to other fabric strength measuring indexes because it's less sensitive to the quantity of grains measured and therefore can allow more reliable and straightforward interpretation of the data.

4.2.1 Subgrain computing method

In Chapter 7 (see Section 7.4.1), subgrain boundary analysis was computed in order to understand which slip systems are active in actinolite grains and how compatible they are to deformation with crystal plasticity (e.g., Lloyd et al., 1997, Prior et al., 2002, Piazolo and Jaconelli, 2014). One sample of metagabbro was chosen to compute subgrain misorientation analysis using EBSD analysis. Actinolite grains were segmented considering grain as an area enclosed by grain boundaries with a

misorientation ¿10 ° and subgrain boundaries as boundaries with misorientation between 1.5° and 10° (e.g., Wheeler, 2001). Trace boundary analysis method is used to determine the 2D geometry of low-angle boundary and active slip systems. This method considers the dispersion of orientations around a rotation axis for an area surrounding the computed subgrain boundary, the rotation axis is identified in the pole figures as the direction with little or no dispersion (Lloyd and Freeman, 1994). In the case of a tilt boundary, the boundary plane must contain the 2D boundary trace and the rotation axis. The plane perpendicular to the rotation axis represents the slip system active during deformation.

4.3 Amphibole chemistry

Amphibole compositions were measured through EDS. Compositional maps were acquired using a 20 kV voltage and the instrument was calibrated using kaersutite as standard to measure amphibole composition. Our measurements of the standard remained within a standard deviation of 0.5 wt% (typically < 0.2 wt%) from the published values of the standard for all elements reported. Amphibole compositions were measured separately in cores and rims of grains from both the matrix and block. Mineral formula recalculation was carried out on the basis of 23 oxygens and 15 total cations. We plotted the recalculation made by the maximum of Fe^{3+}, obtained by following the Schumacher (1997) procedure for calculation of minimum, average and maximum Fe^{3+} in amphiboles. Mineral analyses and recalculation for amphiboles are reported in Tables 5.1 and 5.2 (Chapter 5), Tables 6.2 and 6.3 (Chapter 6) and Table 7.2 (Chapter 7) .

4.4 Geochemistry

Microstructural and field observations on Tomuru block-in-matrix metabasalts reveal only limited but significant fabric and petrographic differences between greenschist and blueschist facies rocks. In order to further investigate the differences in bulk composition the metabasalts and in order to characterise the affinity of the protolith, samples were analysed both from blueschist and greenschist facies rocks (Section 6.4). Analyses have been carried on bulk major and trace elements on both greenschists and epidote-blueschists.

4.4.1 XRF

Samples were cut, cleaned and subsequently crushed on an agate mill until finely powdered. Bulk rock major and trace elements were measured on a Panalytical Axios wavelength-dispersive XRF spectrometer at the Department of Geological Sciences at the University of Cape Town. Powdered samples were heated to 110℃ overnight to dry, with the samples being weighted before and after the process to record the water lost upon heating (H_20^-). Finally, the dried samples were heated to 800℃ for 4 hours and subsequently cooled and weighed to record the weight lost upon heating (loss on ignition – LOI). The samples were subsequently fused with a lithium borate flux to produce fused discs on which major element compositions were measured, and pressed powder briquettes from which trace element data were recorded. XRF analysis is reported in Table 6.4 (Chapter 6)

4.4.2 Isocon method

The isocon diagram (Grant, 1986) has been used in literature to visualise element concentration and mass changes between protolith and altered rocks. This method was based on Gresen's equations (Gresen, 1967) to aid the analysis of hydrother-

mal alteration, but several authors applied it to metamorphic terraines to understand the coexistence of metamorphic rocks with different metamorphic assemblages. Some authors specifically used it to analyse the coexistence of greenschists and blueschist rocks (Barrientos and Selverstone, 1993); Halama and Konrad-Schmolze, 2015).

4.4.3 Vein piezometry

Piezometry (following Cross et al., 2017) on quartz grains was used to calculate the mean recrystallised grain size of ductilely deformed quartz in quartz-rich veins sampled in the metabasites. The mean recrystallised grain size is used to obtain the range of values of differential stress (Section 6.5). Differential stress estimates derived from quartz piezometry were converted into shear stress values following Behr and Platt (2014):

$$\tau = \frac{(\sigma_1 - \sigma_3)}{\sqrt{3}} \tag{4.1}$$

Chapter 5

Deformation microstructures of low- and high-strain epidote-blueschist (Ryukyu arc, Japan)

Abstract

We present field and microstructural data from an exhumed subduction complex in the Ryukyu arc, Japan, where epidote-blueschist, Triassic, Tomuru metamorphic rocks with block-in-matrix structure crop out. With the aim to constrain epidote-blueschist rheology, we investigate fabric development and infer deformation mechanisms of blocks and matrix through microstructural analyses on the main fabric-forming minerals: glaucophane, epidote and albite. The blocks have a poorly developed, discontinuous foliation. In contrast, the matrix has a well-developed, continuous foliation. Glaucophane is the principal foliation-forming phase, arranged in interconnected layers that surround epidote and albite, which suggests

that glaucophane controls epidote-blueschist rheology. Deformation mechanisms inferred from petrographic and electron backscatter diffraction (EBSD) analysis are similar in blocks and matrix, with glaucophane deformed by diffusion creep accompanied by reaction-driven creep, albite by diffusion creep, and epidote by brittle fracture and incipient dislocation creep, based on degrees of internal misorientations, lattice preferred orientation (LPO) development and grain size. During deformation, shear stress must have been relatively low, which is implied by the predominance of diffusion and reaction creep as the dominant deformation mechanisms, and by the small viscosity contrast between blocks and matrix, reflected by their similarity in dominant deformation mechanism.

5.1 Introduction

In convergent margins, the subducting and overriding plates are separated by a kilometres-thick plate boundary shear zone, also referred to as subduction megathrust (Fig. 2.1). The subduction megathrust is typically thought of as a heterogeneously strained mélange of rocks, which have heterogeneous composition and a wide range of rheological properties that evolve with progressive deformation and metamorphism (Fisher and Byrne, 1987; Fagereng and Sibson, 2010; Rowe et al., 2013, Oncken et al., 2022). Subduction megathrust segments accommodate a variety of geophysically-observed fault slip styles varying from steady creep through a range of transient, slow earthquake phenomena to fast, episodic earthquake slip (Peng and Gomberg, 2010). The downdip limit for earthquake nucleation is controlled by the depth where rock behaviour changes from frictional to viscous (Brace and Kohlstedt, 1980; Chen and Molnar, 1983; Sibson, 1982; Scholz, 1988). This transition tends to occur at 350 – 450 ℃ or near the Moho, whichever is shallower (Hyndman et al., 1997). A spectrum of slow earthquakes generally occur downdip of the seismogenic zone (Peng and Gomberg, 2010; Schwartz and Rokosky, 2007; Obara and Kato, 2016; Behr and Bürgmann, 2021). This region is therefore host to multiple slip speeds, although the participating geological structures and accommodating mineral-scale deformation mechanisms are not well known (Kirkpatrick et al., 2021).

Viscous deformation in the crust occurs predominantly by diffusion creep and dislocation creep. Diffusion creep is the predominant deformation mechanism that prevails at low stress and small grain size in shear zones and implies a linear dependence of strain rate on stress (Tsenn and Carter, 1987) (Section 2.6.2 Grain size sensitive creep). In contrast, power-law creep, where rock behaviour is controlled by dislocation glide and climb, is an intragranular process independent of grain size, and with a non-linear relationship between strain rate and stress (Weertman,

1968) (Section 2.6.2., Grain size insensitive creep).

At fixed stress and strain rate, small grain sizes promote diffusive mechanisms, whereas larger grain sizes promote dislocation glide and/or climb. Moreover, grain size evolution, for example through grain growth or grain size reduction by metamorphism and/or metasomatism, relates to changes in flow strength and can move the energetically favourable mechanism between diffusion- and dislocation-controlled deformation (Rutter and Brodie, 1988; Montési and Hirth, 2003; Kilian et al., 2011, Lee et al., 2022, Ujiie et al., 2022). In addition, during deformation, syn-tectonic reactions can lead to oriented growth of crystals with changing composition, reflecting syn-kinematic changes in pressure and temperature through zoning (Wintsch and Yi, 2002; Wintsch and Yeh, 2013). Observations on natural and laboratory-deformed samples show that the new mineral phases form in orientations favourable to accommodate shear stress, with a preferred orientation parallel to foliation (Shea and Kroenenberg, 1993). Therefore, there can be a strong control of mineral reactions on the development of rock fabric, which in turn will lead to weakening (e.g., reaction creep; Wintsch et al., 1995; 2013).

Mafic oceanic rocks and seafloor sediments are the main lithologies involved in deformation along the subduction interface. In particular, blueschist rocks represent the remnants of oceanic crust that have been subducted to high pressure (P) -low temperature (T) metamorphic conditions (Miyashiro, 1961; Ernst, 1973) and are characterised by distinctive mineral assemblages with a foliation typically defined by glaucophane. The P-T range of blueschist stability (e.g., Peacock, 1992) coincides with metamorphic conditions at the depth-range typical of temporally coincident, episodic tremor and slow slip (ETS) in the transition zone downdip of the seismogenic zone (typically, but not exclusively, 30-50 km and in excess of 300°C) (Rogers and Dragert, 2003; Obara et al., 2004; Obara and Kato, 2016). In this depth and temperature range, tectonic displacement is accommodated by

geodetically and seismically detected ETS in some places, including segments of the well-instrumented Nankai and Cascadia margins (Obara, 2002; Rogers and Dragert, 2003; Peng and Gomberg, 2010). However, at similar inferred P-T conditions, some subduction zones (e.g., Central Cascadia, Schmalzle et al., 2014) show a combination of ETS and steady fault creep. At the Ryukyu Arc, short-term slow slip events occur with mobile source areas of low frequency earthquakes, which are temporally but not always spatially coincident with the slow slip (Nakamura, 2017; Suenaga et al., 2021). This variable behaviour is thought to reflect different rheology of the materials on the subduction interface, and consequently different deformation mechanisms active in the rocks deforming at that depth and temperature (Fagereng et al., 2014; Kotowski and Behr, 2019; Behr and Bürgmann, 2021, Kirkpatrick et al., 2021).

Glaucophane and sodic amphiboles (e.g., Leake et al., 1997) define blueschist fabric and are therefore an important control on subduction interface rheology downdip of the seismogenic zone. The mechanisms that govern their deformation are critical for understanding megathrust stress state and slip style; however, there is limited literature that analyses the deformation mechanisms prevalent in glaucophane. Previous studies on blue amphiboles relevant to the subduction thrust interface suggest dislocation creep as the dominant deformation mechanism in glaucophane deformation, on the basis of microstructural and intracrystalline misorientation data (Behr et al., 2018; Kim et al., 2013; Kotowski and Behr, 2019). However, Misch (1969) described microstructures indicative of synkinematic diffusion creep in Na-amphiboles, and recently Muñoz-Montecinos et al. (2023) described the role of dissolution-precipitation creep in accommodating Na-amphibole deformation in the region of subduction interface ETS.

In a broader range of P-T stability and tectonic environments, thus not limited to the HP-LT environments where glaucophane is stable, amphibole group

minerals have been interpreted to deform by a variety of deformation mechanisms in both naturally- and laboratory-deformed samples. Some authors suggest dominant dislocation creep represented by intracrystalline features such as subgrains and undulose extinction formed via glide and climb on (100)<001> at high temperatures (Brodie and Rutter, 1985; Reynard et al., 1989) or dislocation glide on (100)<001>(Skrotzki, 1990). In contrast, others highlight the importance of diffusion creep in the formation of amphibole fabric (Getsinger and Hirth, 2014) and, when a reactant aqueous phase is present, dissolution-precipitation creep (Berger and Stünitz, 1996; Condit and Mahan, 2018; Giuntoli et al., 2018; Muñoz-Montecinos et al., 2023; Lee et al., 2022; Tulley et al., 2020). Additionally, structures resulting from cataclastic flow have been observed in naturally deformed amphibolites at greenschist and amphibolite metamorphic conditions (Imon et al., 2004; Nyman et al., 1992) and at blueschist conditions (Muñoz-Montecinos et al., 2023).

We present data from an exhumed epidote-blueschist subduction complex of Triassic age on Ishigaki Island in the Ryukyu arc, Japan, which we interpret to represent a fossilized subduction shear zone that records deformation downdip of the seismogenic zone. We analyse and compare the deformation characteristics of higher- and lower-strain block-in-matrix epidote-blueschist rocks to understand rheology of subduction interfaces below the seismogenic zone, including the range of depth and temperature where ETS typically occur. First, we address the foliation development, through grain size analyses and mineral shape analyses of foliation-forming glaucophane, epidote and albite. Secondly, we determine which deformation mechanisms were active and whether they varied between blocks and matrix of similar composition but different fabrics.

5.2 Field observations

The mafic schists of the Tomuru metamorphic rocks crop out in a block-in-matrix structure characterised by epidote-blueschist facies mineral assemblages, with a fine-grained matrix embedding multi-dm sized blocks, including both epidote-blueschist and greenschist mineral assemblages (Fig. 5.2A). Throughout the rock volume, greenschist blocks and epidote-blueschist blocks are present in similar abundance.

The matrix contains a uniform fabric, characterised by a NE-SW striking sub-mm-spaced foliation that wraps around the blocks, and a well-developed NW-SE trending mineral lineation defined by the preferred alignment of glaucophane and albite, which is interpreted as a stretching lineation (Fig. 3.1, Section 3.1). The blocks, both greenschist and epidote-blueschist, generally have poorly foliated cores and well-foliated rims. At the outcrop scale, the only difference between epidote-blueschist blocks and matrix is the foliation development; there is no discernible difference in colour or mineralogy, and any grain size difference is minor. The cores show a mm-spaced internal foliation (Fig. 5.1D), which is aligned with the general NE-SW strike of the matrix, and a similar but less developed NW-SE trending mineral lineation as that seen in the matrix, whereas the rims present a fabric that is similar to that of the epidote-blueschist matrix, with a sub-mm spaced foliation, NE-SW striking (Fig. 5.1C,E).

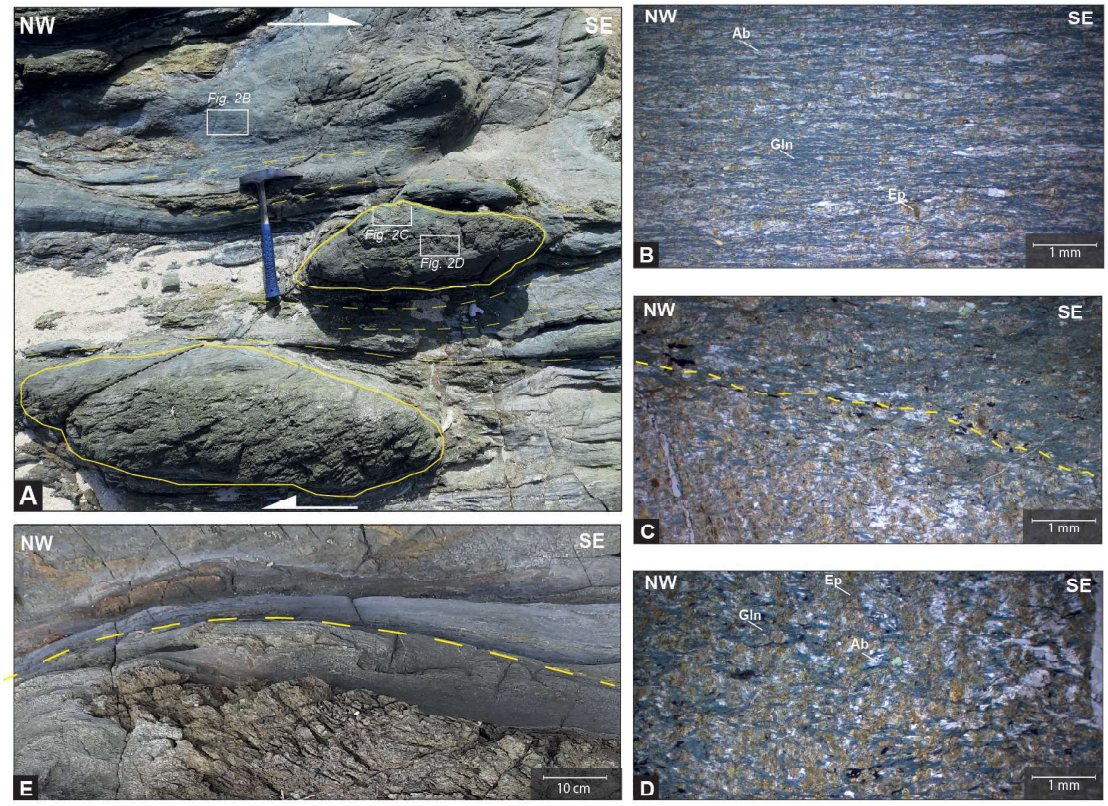

Figure 5.1: a) Mesoscale block-in-matrix structure of the Tomuru metamorphic rocks. Contoured in yellow, the epidote-blueschist blocks are embedded in a well-foliated epidote-blueschist matrix; b) photomicrograph of the well-foliated epidote-blueschist matrix analysed in this paper, where continuous layers of glaucophane alternate with domains of epidote, albite and minor quartz and titanite; c) photomicrograph of the epidote-blueschist block rim. The yellow dashed-line separates the poorly foliated fabric of the block core (bottom left of image) from the well-foliated fabric of the core rim (top right of image); d) photomicrograph of the poorly foliated epidote-blueschist block analysed in this paper. Glaucophane grains are not well interconnected and lie between epidote and albite grains. e) detail of the block margin (bottom left of image) in contact with the epidote-blueschist matrix (top right of image). Note how the block has a poorly foliated core and a well-foliated rim. Gln: glaucophane, Ep: epidote, Ab: albite

5.3 Microstructural analyses

5.3.1 Matrix and block microstructure

In this study, we focus on microstructures of the epidote-blueschist blocks and matrix rocks to consider the rheological differences causing the block-in-matrix structure to develop. Based on EBSD maps, the epidote-blueschist matrix contains a modal mineral assemblage of glaucophane (43%), epidote (27%), albite (18%), with minor white mica, quartz and titanite. The epidote-blueschist blocks have the same mineral assemblage as the matrix but lower glaucophane content, with epidote (45%), albite (24%), glaucophane (21%) and minor quartz and titanite. There are also greenschist blocks containing chlorite and Ca- rather than Na-amphibole in the area, these are considered in Chapter 6.

At the microscale, the matrix is characterised by continuous layers of glaucophane and minor white mica separating discontinuous domains of epidote, albite, quartz and minor titanite (Figs. 5.1B, 5.2A). Glaucophane long axes are generally parallel to the foliation, but locally are at a higher angle forming an oblique foliation consistent with a top to S/SE sense of shear. Glaucophane constitutes the main foliation and is also locally present in epidote strain shadows (Fig. 5.3C). Epidote, albite, quartz and titanite domains range in size from 100 µm to a few millimetrers and have a lenticular shape that is only rarely asymmetric, in those cases consistent with a top to S/SE sense of shear. Epidote grains, in particular, are fractured and accompanied by strain shadows with fine-grained overgrowths of albite and, locally, glaucophane (Fig. 5.3D,E). Blocks have the same mineral assemblage as the matrix and are characterised by discontinuous domains of glaucophane and minor white mica alternating with mm-sized lenses of epidote, albite, quartz and titanite (Fig. 5.1D). The cores of the blocks are not as well-foliated as the matrix, with discontinuous layers of glaucophane separating grains of epidote

and only locally domains of epidote and albite (Fig. 5.3A). Most of glaucophane grains occur with their long axes oblique to the foliation. Similar to the matrix, epidote grains are mostly fractured and present albite in their strain shadows (Fig. 5.3C). The rims of the blocks show the same fabric characteristics as the matrix, with continuous layers of glaucophane separating grains of epidote, albite and titanite (Fig. 5.3D).

Backscattered electron images show, in the matrix and blocks alike, that most glaucophane crystals are chemically zoned (Figs. 5.2B, 5.3B). Glaucophane cores are relatively rich in Ca and Mg and the rims are relatively rich in Na, with lower Ca and Mg content (Fig. 5.4A,B). EDS analyses show that the cores (Table 5.2) have mostly a winchite composition, while the rims (Table 5.1) have a predominant glaucophane composition (Fig. 5.4C,D). The concentric zonation pattern is more developed along the grain long axis and less developed parallel to the short axis, showing that the chemical change is evident in both directions, normal to- and parallel to the grain elongation. This concentric pattern is not systematic for all the grains, with a few of them presenting complex patterns that are not recognisable as core-to-rim variations nor as representing new grains. Tentatively this pattern could be related to chemical truncations within the crystals. Epidote and albite grains do not appear to be zoned.

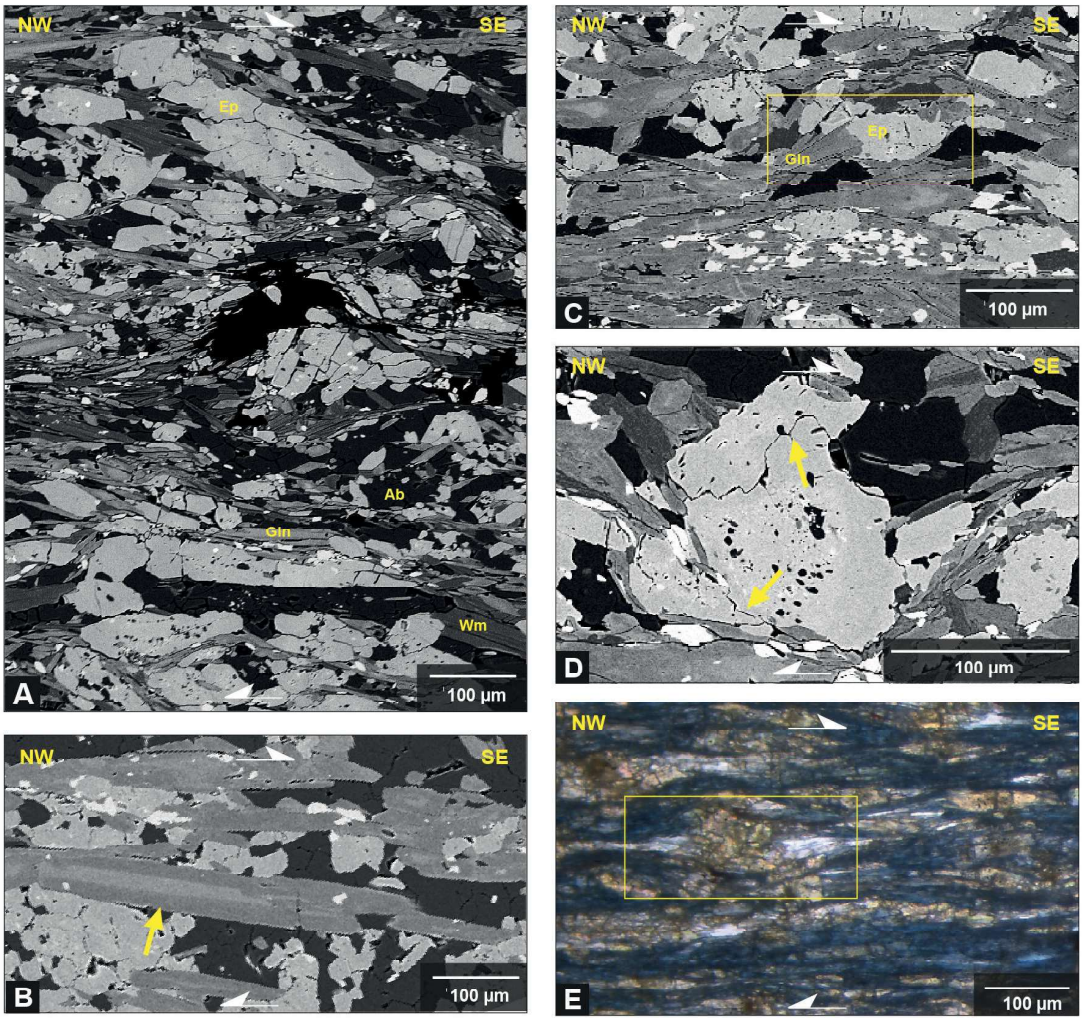

Figure 5.2: a) Backscattered electron (BSE) image of the representative microstructure for the epidote-blueschist matrix. Glaucophane grains are aligned with the foliation surrounding grains of epidote and albite; b) BSE image with detail of glaucophane grains aligned with the foliation. The zoning pattern is parallel to the long axis of the crystal and it is not truncated; c) BSE image of the microfabric of the matrix. In the yellow box the development of glaucophane grains in the strain shadows of epidote grains is noticeable; d) BSE image of large epidote porphyroclasts. Yellow arrows indicate fractures; e) optical microscope photomicrograph (crossed-polarised light) of matrix fabric. In the yellow box the presence of albite grains in the strain shadows of epidote is noticeable. Gln: glaucophane, Ep: epidote, Ab: albite

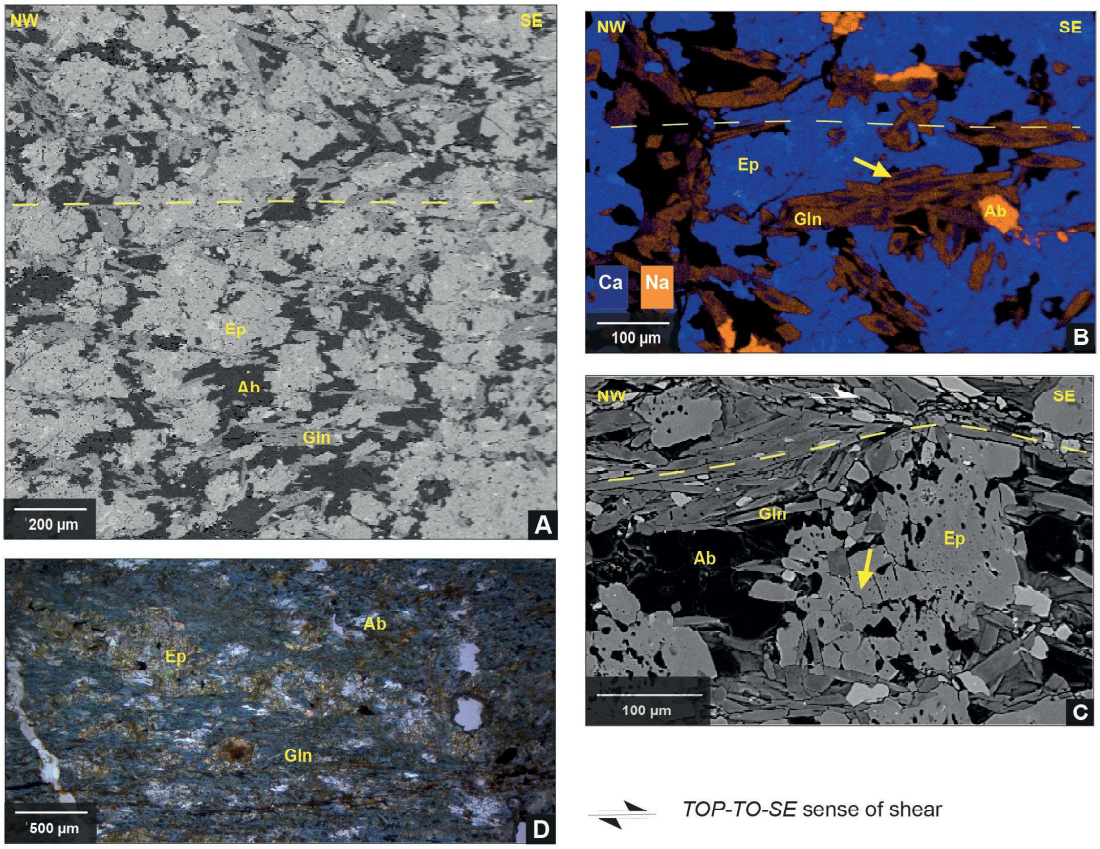

Figure 5.3: a) Backscattered electron (BSE) image of the representative microstructure of the epidote-blueschist blocks. The glaucophane grains form discontinuous layers and are not well aligned with the foliation (yellow dashed line); b) EDS map of the epidote-blueschist block microfabric. Yellow arrow indicates the glaucophane grains. The map shows the zoning of the grains, mostly parallel to the crystals' long axis. The cores of the grains are richer in Ca, whereas the rims are richer in Na. blue: Ca, Orange: Na; c) BSE image of epidote grain. Yellow arrow indicates fractures within the grain. Note how albite grains develop in the epidote strain shadows; d) photomicrograph of the fabric that characterises the rim of the epidote-blueschist block. Glaucophane grains form continuous layers, well aligned with the foliation. Gln: glaucophane, Ep: epidote, Ab: albite

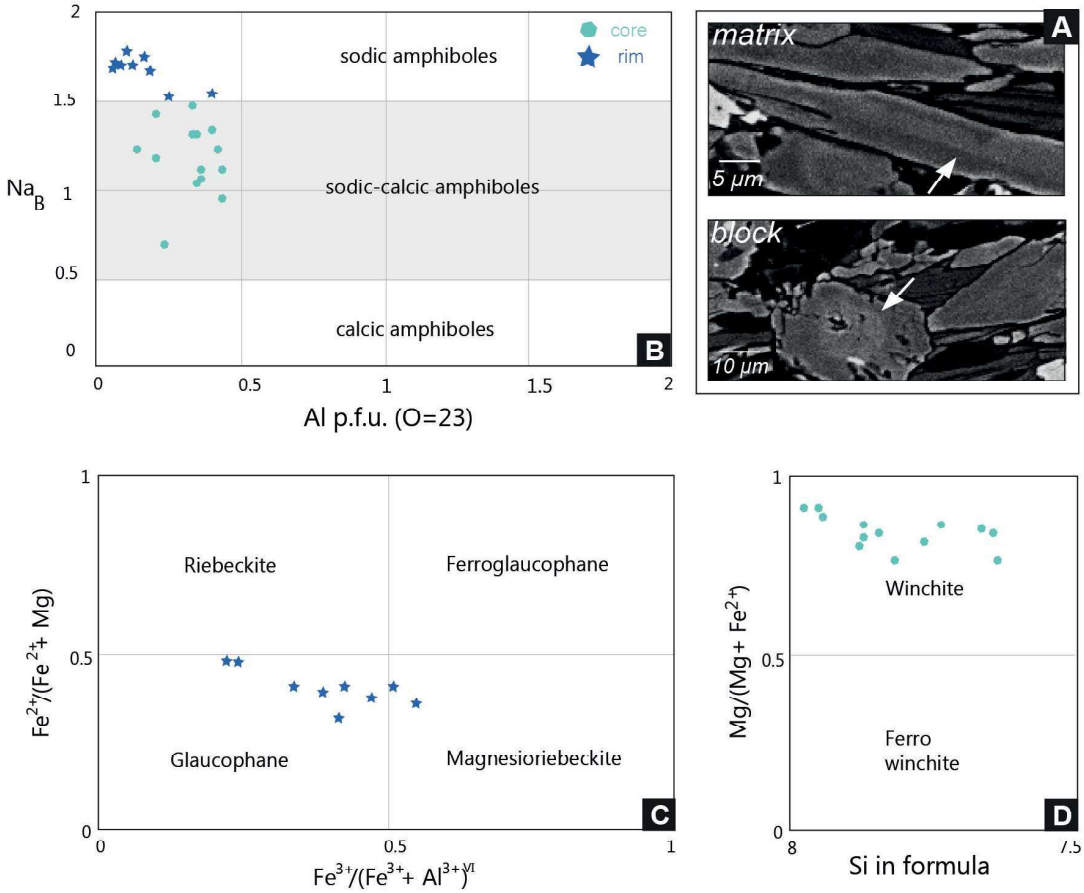

Figure 5.4: EDS analyses of foliation-forming amphiboles in Tomuru metamorphic rocks. a) Backscatter images showing the detail of chemical zoning in the blue amphiboles in the matrix and in the block. Arrows indicate the concentric core-to-rim zonations present. The grain cores, lighter grey, are rich in Ca, while the rims, darker grey, are rich in Na; b) plot of the variation of Na content over Al content in the cores and rims of amphiboles. The cores contain X_{NaB} ranging 0.6 – 1.5, the rims contain X_{NaB} ranging 1.5 – 1.72; c) Composition diagram for the amphibole rims, falling in the magnesioriebeckite – glaucophane field; d) composition diagram of the amphibole cores, plotting in the winchite field. Compositional plots from Leake et al., 1997.

5.3.2 Grain size analysis

In the epidote-blueschist matrix, glaucophane grain sizes range from a few microns to 50 µm (mean 10 µm) and aspect ratios vary from 1 to 9 (Fig. 5.5A,B). Epidote grains are up to 100 µm (mean 11 µm) and aspect ratios vary from 1 to 5 (Fig.

Table 5.1: Mineral analyses from amphibole grain rims. * Fe_2O_3 is total Fe. $X_{Fe2} = Fe_{2+}/(Fe_{2+}$ + Mg); $X_{Fe3} = Fe_{3+}/(Fe_{3+}$ + Al)VI; X_Mg = Mg/(Mg + Fe_{2+}). mrbk: magnesioriebeckite; gln: glaucophane; wnc: winchite.

	Rim analyses											
	mrbk	wnc	gln	wnc	gln	gln	gln	gln	gln	gln	gln	wnc
SiO2	55.07	55.49	56.94	55.88	54.48	56.14	57.01	58.03	56.24	57.32	56.52	51.33
TiO2	0.11	0.13	0.09	0.00	0.23	0.14	0.15	0.00	0.00	0.09	0.15	0.50
Al2O3	6.85	6.71	6.92	4.71	8.36	7.54	7.96	8.00	6.26	7.80	7.71	9.83
Fe2O3*	19.20	19.13	18.77	18.29	19.45	19.02	18.56	15.81	18.38	18.43	18.96	18.36
MnO	0.25	0.21	0.19	0.31	0.24	0.20	0.18	0.24	0.20	0.14	0.20	0.31
MgO	9.31	9.46	8.76	11.08	8.29	8.27	8.13	9.67	10.06	8.26	8.10	10.85
CaO	3.55	3.29	1.65	5.12	3.00	2.16	1.41	1.58	3.46	1.45	1.63	3.53
Na2O	5.54	5.43	6.39	4.53	5.83	6.45	6.36	6.63	5.26	6.45	6.57	4.77
K2O	0.14	0.11	0.07	0.08	0.14	0.08	0.27	0.00	0.17	0.07	0.07	0.47
Total	100.01	99.97	99.79	100.00	100.02	100.00	100.03	99.97	100.04	100.01	99.92	99.95
Si	7.67	7.86	7.89	7.80	7.60	7.81	7.92	7.94	7.79	7.94	7.84	7.15
Al	1.12	1.12	1.13	0.77	1.38	1.24	1.30	1.29	1.02	1.27	1.26	1.61
Ti	0.01	0.01	0.01	0.00	0.02	0.02	0.02	0.00	0.00	0.01	0.00	0.00
Mg	1.93	2.00	1.81	2.31	1.72	1.71	1.68	1.97	2.08	1.71	1.68	2.25
Fe2+	1.34	2.21	1.39	1.38	1.45	1.53	1.69	1.29	1.29	1.67	1.40	0.84
Mn	0.03	0.02	0.02	0.04	0.03	0.02	0.02	0.03	0.02	0.02	0.02	0.04
Ca	0.53	0.50	0.24	0.77	0.45	0.32	0.21	0.23	0.51	0.21	0.24	0.53
Na	1.50	1.49	1.72	1.23	1.58	1.74	1.71	1.76	1.41	1.73	1.77	1.29
K	0.02	0.02	0.01	0.01	0.03	0.01	0.05	0.00	0.03	0.01	0.01	0.08
Fe3+	0.90	0.05	0.78	0.75	0.82	0.68	0.47	0.52	0.84	0.47	0.79	1.30
Na_B	1.50	1.23	1.72	1.18	1.55	1.68	1.71	1.73	1.41	1.71	1.76	1.29
^{IV}Al	0.33	0.14	0.11	0.20	0.40	0.19	0.08	0.06	0.21	0.06	0.16	0.85
X*Fe2*	0.41	0.42	0.45	0.38	0.46	0.45	0.5	0.39	0.4	0.49	0.45	0.28
X*Fe3*	0.53	0.48	0.43	0.57	0.45	0.41	0.27	0.3	0.42	0.28	0.39	0.62
X*Mg*	0.59	0.57	0.56	0.62	0.54	0.53	0.49	0.6	0.51	0.51	0.54	0.72

Table 5.2: Mineral analyses from amphibole grain cores. * Fe_2O_3 is total Fe. $X_{Fe2} = Fe_{2+}/(Fe_{2+} + \mathrm{Mg})$; $X_{Fe3} = Fe_{3+}/(Fe_{3+} + \mathrm{Al})$VI; $X_Mg = \mathrm{Mg}/(\mathrm{Mg} + Fe_{2+})$. mrbk: magnesioriebeckite; gln: glaucophane; wnc: winchite.

	Core analyses											
	wnc	wnc	wnc	wnc	act	gln	wnc	wnc	wnc	wnc	wnc	wnc
SiO2	53.72	53.68	54.80	55.32	56.27	55.87	54.40	54.42	54.83	54.64	54.75	53.87
TiO2	0.23	0.15	0.21	0.12	0.00	0.40	0.10	0.09	0.12	0.00	0.13	0.13
Al2O3	4.87	4.92	5.99	5.62	1.65	7.03	6.24	4.79	4.61	4.31	6.49	5.76
Fe2O3*	19.04	19.81	18.69	18.10	14.14	18.19	18.43	19.26	18.42	18.88	18.38	18.35
MnO	0.33	0.27	0.27	0.27	0.46	0.26	0.25	0.34	0.31	0.33	0.26	0.30
MgO	11.27	10.73	10.39	10.95	15.27	9.75	10.61	10.86	11.60	11.57	10.41	11.03
CaO	6.81	6.32	4.59	4.60	11.02	2.72	5.12	5.80	6.06	6.28	4.47	6.06
Na2O	3.50	3.90	4.92	4.92	1.07	5.70	4.71	4.27	3.92	3.86	4.99	4.17
K2O	0.19	0.20	0.13	0.11	0.10	0.12	0.12	0.14	0.14	0.15	0.13	0.15
Total	99.96	99.98	100.00	100.02	100.00	100.05	99.99	99.97	100.02	100.02	100.01	99.83
Si	7.56	7.52	7.64	7.68	7.88	7.75	7.59	7.64	7.66	7.64	7.61	7.55
Al	0.81	0.81	0.99	0.92	0.27	1.15	1.03	0.79	0.76	0.71	1.06	0.95
Ti	0.02	0.02	0.02	0.01	0.00	0.04	0.01	0.01	0.01	0.00	0.01	0.01
Mg	2.37	2.24	2.16	2.27	3.19	2.02	2.21	2.27	2.42	2.41	2.16	2.31
Fe2+	1.35	1.05	1.26	1.15	1.42	1.42	1.22	1.30	1.24	1.18	1.18	1.25
Mn	0.04	0.03	0.03	0.03	0.06	0.03	0.03	0.04	0.04	0.04	0.03	0.04
Ca	1.03	0.95	0.69	0.68	1.65	0.40	0.76	0.87	0.91	0.94	0.67	0.91
Na	0.96	1.06	1.33	1.32	0.29	1.53	1.27	1.16	1.06	1.05	1.34	1.13
K	0.03	0.03	0.02	0.02	0.02	0.02	0.02	0.03	0.03	0.03	0.02	0.03
Fe3+	0.89	1.27	0.92	0.95	0.24	0.69	0.93	0.96	0.91	1.03	0.96	0.90
Na_B	0.96	1.05	1.31	1.32	0.29	1.53	1.24	1.13	1.06	1.05	1.33	1.09
^{IV}Al	0.44	0.33	0.36	0.32	0.12	0.25	0.41	0.36	0.34	0.36	0.39	0.45
X*Fe2*	0.34	0.32	0.37	0.33	0.31	0.41	0.35	0.36	0.33	0.33	0.35	0.35
XF*e3*	0.72	0.79	0.59	0.61	0.67	0.43	0.6	0.69	0.68	0.74	0.58	0.64
X*Mg*	0.65	0.68	0.63	0.7	0.69	0.58	0.64	0.63	0.66	0.67	0.65	0.65

5.5A,B). Albite size ranges from a few microns to 15 µm (mean 8 µm) with aspect ratios ranging from 1 to 5 (Fig. 5.5A,B). Although in general, glaucophane, epidote, and albite long axes orientations relative to the stretching lineation are scattered, the grains with the highest aspect ratios are aligned along the lineation suggesting that the matrix has a well-developed shape-preferred orientation (SPO) (Fig. 5.5B).

In the epidote-blueschist block, glaucophane grains have a broader grain size distribution compared to the matrix, ranging from a few microns up to 90 µm, but similar mean values (mean 13 µm), and aspect ratios of 1 to 7 (Fig. 5.5C,D). Epidote grains have a larger grain size than the matrix, with size up to 120 µm (mean 20 µm) and aspect ratios of 1 – 5 (Fig. 5.5C,D) and albite grains range in grain size from a few microns to 25 µm (mean 11 µm) and have aspect ratios ranging 1 to 3 (Fig. 5.5C,D). Here, there is a larger variation of orientation of glaucophane, epidote, and albite grains with respect to the lineation (Fig. 5.5D), and even the grains with the highest aspect ratios are not systematically aligned with the lineation, indicating that the epidote-blueschist blocks have a less developed SPO compared to the matrix.

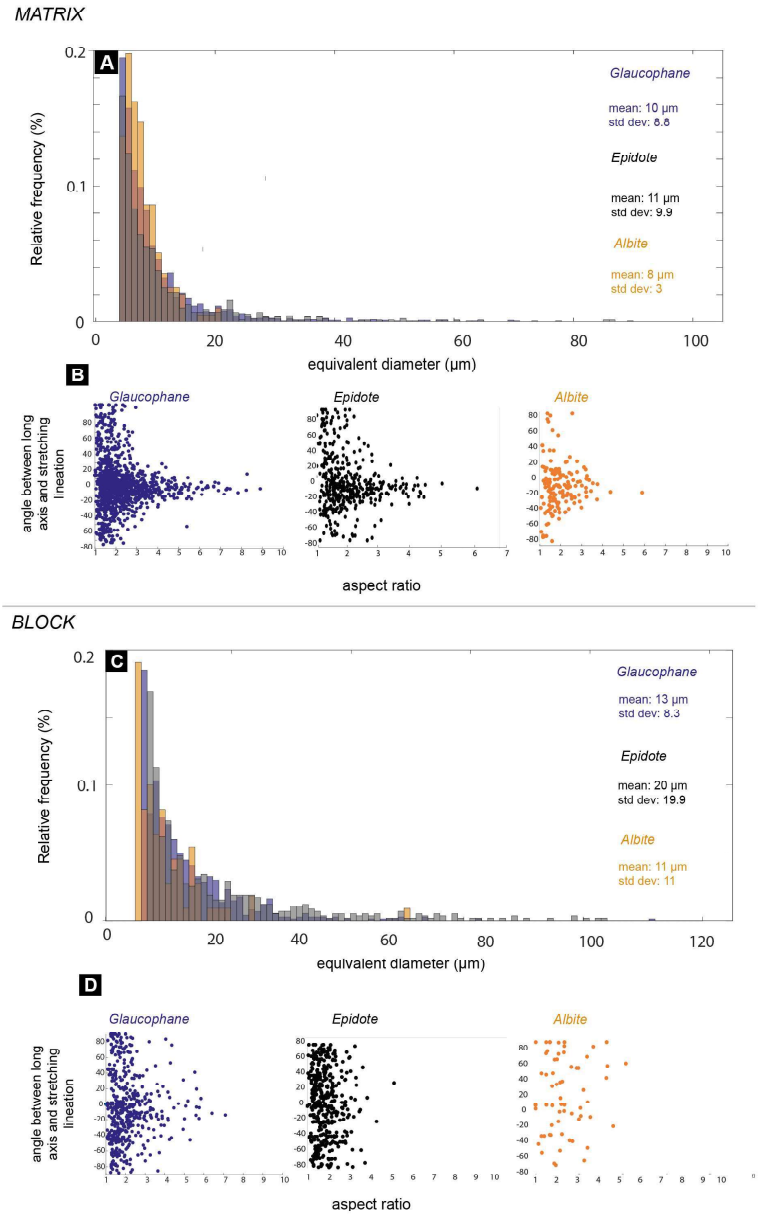

Figure 5.5: Grain size and fabric analysis of the foliation-forming minerals in the matrix and the block. a) composite grain size histograms of glaucophane, epidote and albite in the matrix. Size mean and deviation standard are reported for each mineral; b) grains aspect ratio versus angle to lineation plots for glaucophane, epidote and albite in the matrix. Point per grain analysis; c) composite grain size histogram of glaucophane, epidote and albite in the block, with size mean and deviation standard reported for each mineral; d) grain aspect ratio versus angle to lineation plots for glaucophane, epidote and albite in the block. Point per grain analysis.

5.3.3 EBSD analysis

Two matrix areas from the same thin section were analysed, as the microstructure of the matrix is heterogeneous, with glaucophane-rich (Fig. 5.6A,D,G) and epidote-rich portions (Fig. 5.6B,E,H). The glaucophane-rich portion is constituted for the most part by glaucophane (73% modal proportion; grain size up to 13 µm, mean 5 µm) with albite (8% modal proportion; grain size up to 23 µm) enveloping epidote domains (18%; 30 – 50 µm in size), whereas in the epidote-rich portion the glaucophane grains (32% ; mean grain size 5 µm) are less interconnected and lie between numerous grains of epidote of much larger grain size (60%; 75-100 µm size range); here albite (7%) has size up to 25 µm. In both matrix areas, EBSD analyses (Fig. 5.6A,B,C) show that foliation-forming glaucophane has very low misorientation angles (0-5°). The low degree and pattern of misorientations is not consistent with the formation of subgrains and does not suggest any significant crystal plasticity, with the highest misorientation angles corresponding to fractures within the grains (Fig. 5.6A,B). Moreover, the pattern of misorientation does not seem to be coincident with the chemical zoning of the glaucophanes. The glaucophane grains show a well-developed LPO, with poles to (100) sub-normal to foliation and <001> axes sub-aligned with the lineation both in the epidote-rich and glaucophane-rich portions (Fig. 5.6C). The glaucophane fabric strength has an M-index of 0.2.

EBSD analysis on epidote (Fig. 5.6D,E,F) shows different microstructures than glaucophane, both in magnitude and geometry of internal misorientation. Misorientation angles are greater (0-9°) and their pattern suggests misorientations along fractures in the larger grains with few local subgrains (Fig.5.6D,E). LPO is not particularly strong (M = 0.03), with poles to (100) having a scattered distribution, poles to (010) sub-parallel to foliation (Fig. 5.6F) and <001> axes sub-normal to lineation. Finally, albite grains show very low degrees of internal

misorientations (0-4°) (Fig. 5.6G,H), and very weak LPO (M =0.02), with no recognisable pattern (Fig. 5.6I).

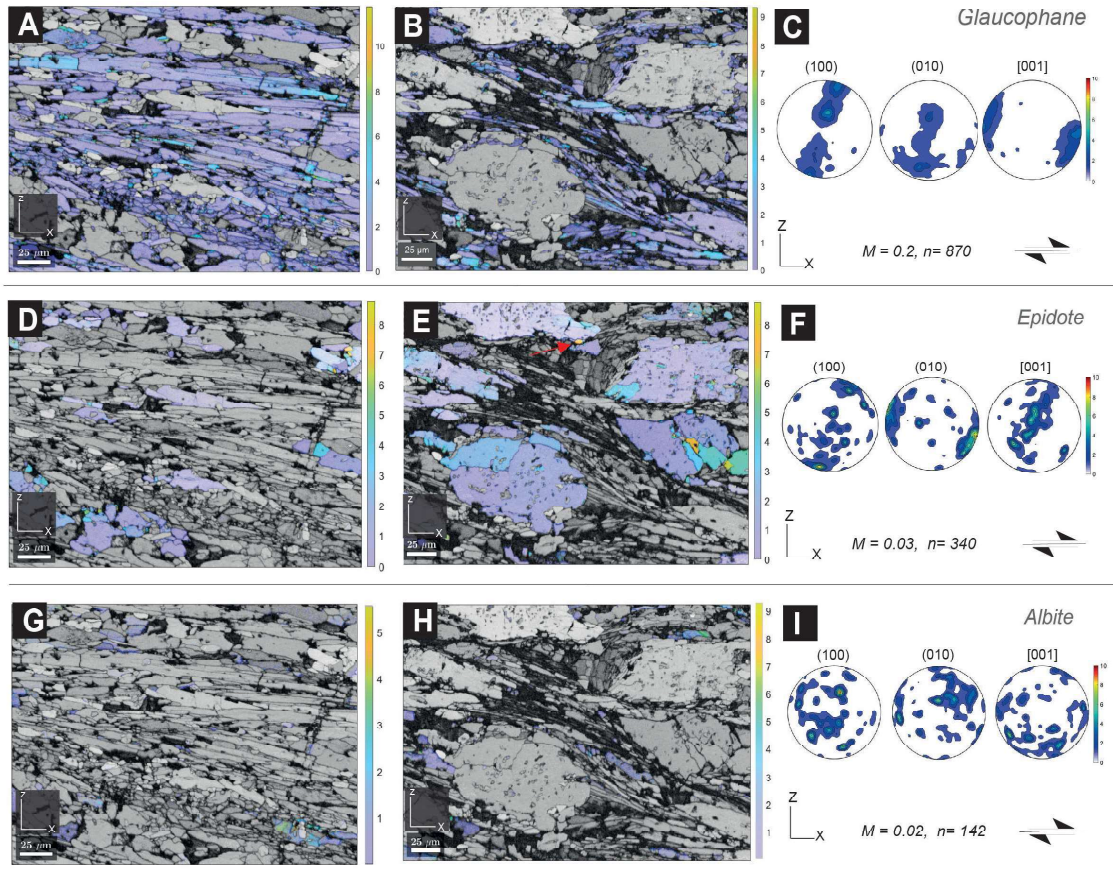

Figure 5.6: EBSD analyses on foliation-forming minerals in the matrix. a) and b) glaucophane misorientation maps (mis2mean) in the glaucophane-rich (a) and epidote-rich area (b) respectively. Colour bars indicate the angles of misorientations. c) glaucophane LPO plots, point per grain analysis, lower hemisphere projections. D) and e) epidote misorientation maps (mis2mean) in the glaucophane-rich (d) and epidote- rich area (e) respectively, white arrows indicate possible subgrains. f) epidote LPO plots, point per grain analysis, lower hemisphere projections. g) and h) albite misorientation maps (mis2mean) in the glaucophane-rich (g) and epidote-rich area (h) respectively. i) Albite LPO plots, point per grain analysis, lower hemisphere projections. M= Skemer index, n = number of grains.

The fabric in the epidote-blueschist block sample is not as heterogeneous as in the matrix (Fig. 5.7). Throughout the thin section, glaucophane grains are poorly connected and separate domains of coarser-grained epidote, albite and titanite.

Therefore, only one area, representative of the fabric, has been analysed. Here, similar to what was measured in the matrix, glaucophane shows low misorientation angles (0-7°), and the pattern of misorientations is not consistent with formation of subgrains (Fig. 5.7A), not coincident with the chemical zonations within the grains, and not aligned along fractures. LPO patterns show a more dispersed girdle than in the matrix, poles to (100) are sub-normal to the foliation and <001> axes are sub-parallel to the lineation with a more diffuse distribution. Here, the LPO is more scattered than in the matrix, with M-index = 0.07, substantially lower than the M-index for the epidote-blueschist matrix (Fig. 5.7A).

In the block, epidote grains show a higher degree of internal misorientation than the glaucophane, with angles locally up to 12°(Fig. 5.7B) and the pattern resembles subgrains only where misorientation angles are larger. There is no lattice-preferred orientation, with no alignment in the principal directions. The fabric strength is slightly lower than in the matrix (M = 0.02). Albite microstructures show a low degree of internal misorientation and weak LPO (M = 0.02) with poles to (100) showing a highly dispersed girdle and <001> axes highly scattered (Fig. 5.7C).

In the analysed samples, the M-index of fabrics in the epidote-blueschist matrix is low overall ($0.2 - 0.02$), but significantly higher than the M-index ($0.07 - 0.02$) of fabrics in the epidote-blueschist block. This comparison shows that the matrix has a better developed fabric than the blocks, consistent with mesoscale observations.

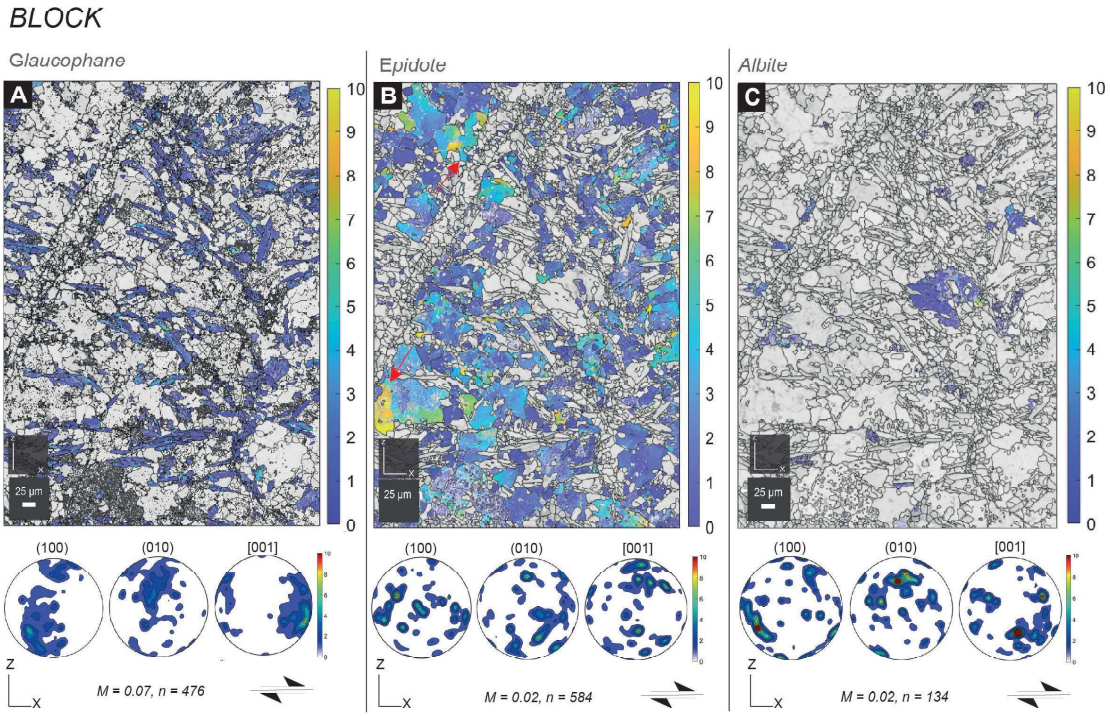

Figure 5.7: EBSD analysis on foliation-forming minerals in the block. a) misorientation map (mis2mean) for glaucophane and glaucophane LPO plots, point per grain analysis, lower hemisphere projections. b) Epidote misorientation map (mis2mean) and LPO plots, point per grain analysis, lower hemisphere projections. c) Albite misorientation map (mis2mean) and LPO plots, point per grain analysis, lower area projection. M= Skemer index, n = number of grains.

5.4 Discussion

5.4.1 Deformation mechanisms in the Tomuru epidote-blueschists

Our microstructural observations on samples of the Tomuru metamorphic rocks show that the epidote-blueschist matrix is characterised by two portions that differ in relative abundance of minerals and grain size of epidote (Fig. 5.6). The portion with high relative abundance of glaucophane and where epidote grain size is smaller represents a high strain domain of well-developed foliation and LPO (Fig. 5.6A,D,G). In contrast, the portion where epidote is more abundant and grain size is larger represents a relatively low strain domain of poorly developed foliation and poor LPO (Fig. 5.6B,E,H). In the relatively high strain domain, very low degrees of intracrystalline misorientations within the glaucophane grains, along with the absence of clear evidence of dislocation creep microstructures (e.g., undulose extinction, subgrains) exclude significant deformation by movement of dislocations. Moreover, the small grain size of glaucophane (mean: 10 µm) fits well with the grain size that is observed to effectively promote diffusive mechanisms in minerals in shear zones (Tsenn and Carter, 1987; Tullis and Yund, 1991; Stenvall et al., 2019). Concentric core-to-rim compositional variations in glaucophane grains, more developed along the long axes of the grains, parallel to the stretching lineation (Fig. 5.2B, 5.3B), are interpreted as the result of compositional changes acquired during subduction-related metamorphism, with increasing Na as pressure increases, as has been described in other high-pressure terranes (Nakamura and Enami, 1994). The geometry of zonation reinforces the interpretation that fabric-forming glaucophane grains deformed by diffusive mass transfer (e.g., Giuntoli et al., 2018) and were not the product of passive rotation and subsequent oriented growth. The presence of glaucophane grains in epidote strain shadow, although local, may suggest that there is contribution of pressure solution, although the ab-

sence of truncation of chemical patterns, as well as the absence of solution seams in these samples, suggests that contribution of pressure solution to deformation might not be significant, favouring the interpretation of predominant deformation by diffusion and reaction creep. The syn-deformation chemical changes within the amphibole grains, along with the well-developed shape preferred orientation, suggest that metamorphic reactions operating during diffusion-controlled deformation in glaucophane might have contributed to glaucophane fabric formation, by changing amphibole composition during progressive deformation, as pressure increased, and by aligning the glaucophane grains along foliation, in orientations favourable for them to effectively deform by diffusive mechanisms. Microstructural analysis on glaucophane fabric shows that a well-defined SPO developed during deformation by diffusion creep and reaction mechanisms can coexist with the development of a well-defined LPO, which is therefore not necessarily the product of dislocation creep in glaucophane.

Epidote microstructures show some differences from glaucophane: grains have a larger grain size, SPO is not well developed, and while the degree of internal misorientation is generally low, locally, epidote crystals have misorientation patterns suggesting development of subgrains (Figs. 5.6E, 5.7B). Although the LPO is less developed than in glaucophane, it is defined by a relatively dispersed girdle. These observations suggest that epidote grains might have experienced some very incipient, low strains by dislocation creep in the high strain domain. That said, the epidote grains are largely undeformed, and have behaved relatively rigidly with some fractures, so such local dislocation creep in epidote is not an important mechanism for bulk deformation of these rocks.

The albite crystals have small grain size, poorly developed SPO and LPO, and suggest deformation by diffusive mechanisms. The overgrowth in pressure shadows on epidote suggests that pressure solution was active during deformation of

albite, although the absence of chemical zonation, as well as evidence for truncation around albite grains, does not allow us to infer with certainty the importance of this component of diffusion. It is difficult to infer the degree to which reaction-driven creep contributed to form albite fabric, as there is no significant chemical zoning or strain localisation in the grains.

In the low strain domain, glaucophane and albite microstructures are comparable to those observed in the high strain domain, whereas epidote has higher degrees of internal misorientation, and, only locally, misorientations resemble subgrains, tentatively suggesting that dislocation creep played a minor role. However, LPO is very poorly developed, and the highest internal misorientations are limited to grains in epidote-rich domains (Fig. 5.6E,F) or to fractures within coarser epidote grains. These characteristics are likely indicative of dominantly passive grain rotation, with some intragrain deformation through fracturing, alongside incipient dislocation creep to small finite strains.

In summary, glaucophane grains have characteristics typical of diffusion creep, likely accompanied by reaction-driven creep, and similarly, albite deformed by a diffusive mechanism. In contrast, epidote deformation is characterised by passive grain rotation with intragrain fracturing and incipient dislocation creep. The geometry of the fabric, in which glaucophane forms interconnected layers that surround the epidote and albite grains, leads us to conclude that the predominant deformation mechanism controlling matrix rheology is diffusion and reaction creep in glaucophane. That a combination of diffusion and reaction can control amphibole deformation is not a new conclusion (e.g. Berger and Stünitz, 1996; Imon et al., 2004, Giuntoli et al., 2018; Soret et al., 2019; Lee et al., 2022; Muñoz-Montecinos et al., 2023), but a key point here is that such diffusion-reaction creep dominates at epidote-blueschist conditions in a block-in-matrix subduction interface shear zone, where blocks and matrix are defined by different viscosities during

diffusive deformation.

The heterogeneity within the matrix, with differences in fabric and strain of the glaucophane-rich and epidote-rich end-member domains at a millimeter scale, is equivalent to the difference between epidote-blueschist blocks and the matrix at multi-dm scale. In this sense, the blocks are similar to the low strain domains in the matrix, as their microstructures are comparable.

The difference between high and low strain portions of matrix and blocks at the mesoscale is potentially guided by glaucophane microfabrics. The presence of interconnected networks of glaucophane separating isolated domains of epidote and albite implies that strain is localised in the epidote-blueschist matrix, relative to the blocks. Moreover, diffusion creep accompanied by reaction creep as the predominant deformation mechanisms is indicative of a low stress domain. In the block, glaucophane does not form well-interconnected layers, and is located between more abundant and larger grains of epidote. Because epidote can be considered more competent than glaucophane, based on its relatively rigid and undeformed appearance, the block may have experienced higher stress despite the lower strain.

To better visualise these interpretations, a qualitative deformation mechanism map for glaucophane in our samples is shown in Figure 9. The plot illustrates the difference in fabric development between the blocks and the matrix: the matrix shows a well-defined foliation with glaucophane having well-developed SPO and LPO patterns, whereas the blocks retain a less pervasive foliation, with glaucophane having less well-defined SPO and LPO patterns (Fig. 5.8B). These small differences in fabric imply a relatively small competency contrast between the blocks and the matrix, thus lacking substantial viscosity gradients. However, the variation in grain size and fabric development also implies higher stress in the lower strain blocks, which is compatible with expectations from numerical models

of higher strain rate flow around more rigid blocks (Beall et al., 2019; Behr et al., 2021) – although again the viscosity contrast must have been relatively low for the blocks not to deform more (Beall et al., 2019). The difference in stress conditions must also be small enough to favour deformation by diffusion creep, accompanied by reaction-driven creep, in both block and matrix, as observed from the microstructures. Moreover, it can be argued that the small competency contrast inferred between block and matrix, along with the microstructural evidence, implies that the shear stress is too low to initiate deformation by dislocation creep, except in a few higher stress locations, favouring diffusive mechanisms instead.

5.4.2 Implications for stress on the plate interface and seismic style

Although there are no previous studies with detailed interpretation of the tectonic origin of Tomuru epidote-blueschists, the block-in-matrix structure with consistent asymmetry that characterizes the Tomuru metamorphic rocks represents shear zone structure typical of the melanges commonly characterising the subduction interface (Shreve and Cloos, 1986; Fagereng and Sibson, 2010; Kimura et al., 2012; Rowe et al., 2013) (Fig. 5.8A). Moreover, in the preserved epidote-blueschist mineral assemblage, zonation indicative of progressive growth during subduction allows us to interpret that the Tomuru epidote-blueschists were subject of high pressure and relative low temperature metamorphism during deformation, which is typical of subduction zones (Miyashiro, 1961; Ernst, 1973; Maekawa et al., 1993). Moreover, the epidote-blueschist blocks and matrix have the same mineralogy, and the change of fabric from the core to the rim of the blocks, suggests that the block-in-matrix fabric of the Tomuru metamorphic rocks forms as the consequence of different strain localization processes, from block to matrix, during subduction-related deformation. This strain localization is, at least in the final product, a

function of slightly finer grain size and a more interconnected glaucophane fabric, and thus more efficient diffusion and reaction creep. Several processes may have initiated these differences, including different grain size and/or fabric in the protolith, cataclastic grain size reduction, or metamorphic or metasomatic grain size and fabric evolution. We do not have the data to separate these options, but emphasize the importance of grain size and fabric, whatever their origin, as controls on strain localization in these epidote-blueschist rocks.

In terms of plate interface rheology, low stress conditions and high fluid pressure have been related to slow earthquakes (Kodaira et al., 2004; Audet et al., 2009; Fagereng et al., 2011; Ujiie et al., 2018). These conditions are also important if we consider the role fluids and stress levels have on which type of diffusion mechanism can be active on the plate interface. In the presence of a fluid phase, generally at low temperature and slow shear strain rates, dissolution-precipitation creep is considered to be dominant (Wassman and Stockert, 2012; Tulley et al., 2020; Malvoisin and Baumgartner, 2021), as opposed to solid-state diffusion, which happens at higher temperatures than dissolution-precipitation creep, and where diffusion occurs either along grain boundaries (Coble creep) or through the crystal lattice (Nabarro-Herring creep) (Rutter, 1976; Wheeler, 1992). In the Tomuru metamorphic rocks we might currently not be able to discern whether solid-state diffusion or fluid-assisted diffusion is predominant. Tomuru metabasites have fewer veins than exhumed subduction complexes such as the Coastal Makimine Mélange and Nagasaki Metamorphic Rocks in Kyushu, where fluid-related deformation is thought to be enhanced by local or nearby dehydration reactions (Tulley et al., 2022; Ujiie et al., 2022), or blueschist in the Zagros suture zone that preserve vein networks indicative of episodic fluid injection and brittle deformation (Muñoz-Montecinos et al., 2023). The presence of veins in this study suggests that fluids were present; however, more data to constrain the timing and deformation condi-

tions of the veins compared to the metabasites, are needed to clarify the amount to which veining contributed to deformation of the mafic rocks at epidote-blueschist facies conditions. Based on the data available, some fluid may have aided diffusion along grain boundaries and leading to overgrowths in pressure shadows, but likely not enough to create a pervasive dissolution-precipitation related foliation.

We can conclude with more certainty that local stress during deformation of the Tomuru epidote-blueschists must have been low enough to maintain diffusion and/or reaction creep as the predominant mineral-scale deformation mechanism in the interconnected glaucophane ± albite that controlled bulk-rock rheology. In order to change the predominant deformation mechanism from diffusion to dislocation creep, at fixed strain rate, pressure and temperature, stress should be locally and transiently elevated, especially when grain size is very small (Fig. 5.8C). To further quantify stresses, rheological relations need to be carefully defined by relating microstructures and fabric analysis with geologically realistic strain rates.

Examples of studies on rheology of natural blueschists are rare in literature, and the Tomuru epidote-blueschists differ when compared to some other natural examples. Some studies observe close association of blueschist rocks to eclogite, where the heterogeneity induced by the dehydration of glaucophane-rich blueschist to form higher viscosity eclogite causes local stress increases that could possibly promote dislocation creep in glaucophane (Behr et al., 2018). Other studies investigating fabrics of natural lawsonite blueschists interpret the formation of glaucophane during exhumation, as suggested by the change in chemical composition within the grains, with decrease of Na from core to rim (Kim et al., 2013). The authors suggest deformation by dislocation creep during exhumation and retrogressive metamorphism. Yet other studies point out the role of diffusive deformation mechanisms in amphibole-rich rocks, similarly to what we describe for the To-

muru metamorphic rocks; however, these authors highlight fracturing and fluid flow at grain boundaries to facilitate dissolution-precipitation creep as the bulk deformation mechanism for amphibole (Giuntoli et al., 2018; Muñoz-Montecinos et al., 2023), which partially differs from our observations where there is little evidence for fracturing/cataclasis accompanying the diffusion and reaction creep in glaucophane.

In terms of plate interface seismic style, the generally low inferred shear stress and the small inferred stress gradients between blocks and matrix could facilitate steady creep in the deep subduction interface, because transients are unlikely to develop if stresses and deformation mechanisms are both relatively constant in time and space. This inference is consistent with general low stress conditions, and although it is important to consider that deformation is potentially sensitive to local changes in strain rate or fluid pressure. Episodic tremor and slow slip require episodic transient stress changes to occur. To create conditions where the plate interface could move transiently rather than by steady creep, it would be necessary to impose a stress or strain rate change (e.g., Beall et al., 2019), for example through a nearby earthquake, larger competency contrast between blocks and matrix, or by transient weakening though fluid pressure pulses driven by dehydration reactions during prograde deformation. Such changes may occur if epidote-blueschist rocks are subducted deeper and epidote and glaucophane dehydrate, at temperatures exceeding 500 ℃ or more (dependent also on pressure, Fagereng and Diener, 2011). This can lead to a fluid pressure increase at the sort of depths at which slow slip occurs in the relatively cold Alaska subduction margin (e.g. Ohta, 2006; Li, 2016).

5.5 Conclusions

We quantified fabric development of an epidote-blueschist block-in-matrix association, showing that despite the same mineralogy, blocks and matrix preserve differences in fabric development. The blocks have poorly developed foliation and LPO compared to the matrix in which they are embedded. From microstructural analyses of the main foliation-forming minerals glaucophane, albite and epidote, both matrix and block rheology are controlled by diffusion and reaction creep of fabric-forming glaucophane, diffusion creep in albite, and with minor incipient dislocation creep and fracturing in relatively rigid epidote. The inferred fabric development and deformation microstructures suggest that during deformation on the plate interface, local stress levels were low to explain lack of significant deformation in the dislocation creep regime in any of the minerals.

Literature on natural blueschist deformation mechanisms is limited and our observations underline the importance of diffusive and reaction-driven creep processes governing fabric development of subducting epidote-blueschists, and at a bigger scale, plate interface rheology in the depth range for ETS below the thermally-controlled seismogenic zone. Our observations imply that at epidote-blueschist conditions, glaucophane-controlled deformation by distributed diffusion creep can occur at low stress, and influx of fluids or a transient stress increase is needed to change the rheology and generate instabilities. Further quantification of stresses, indispensable for accurate modelling of stability fields of deformation mechanisms, requires an amphibole flow law and its extrapolation to geological strain rates.

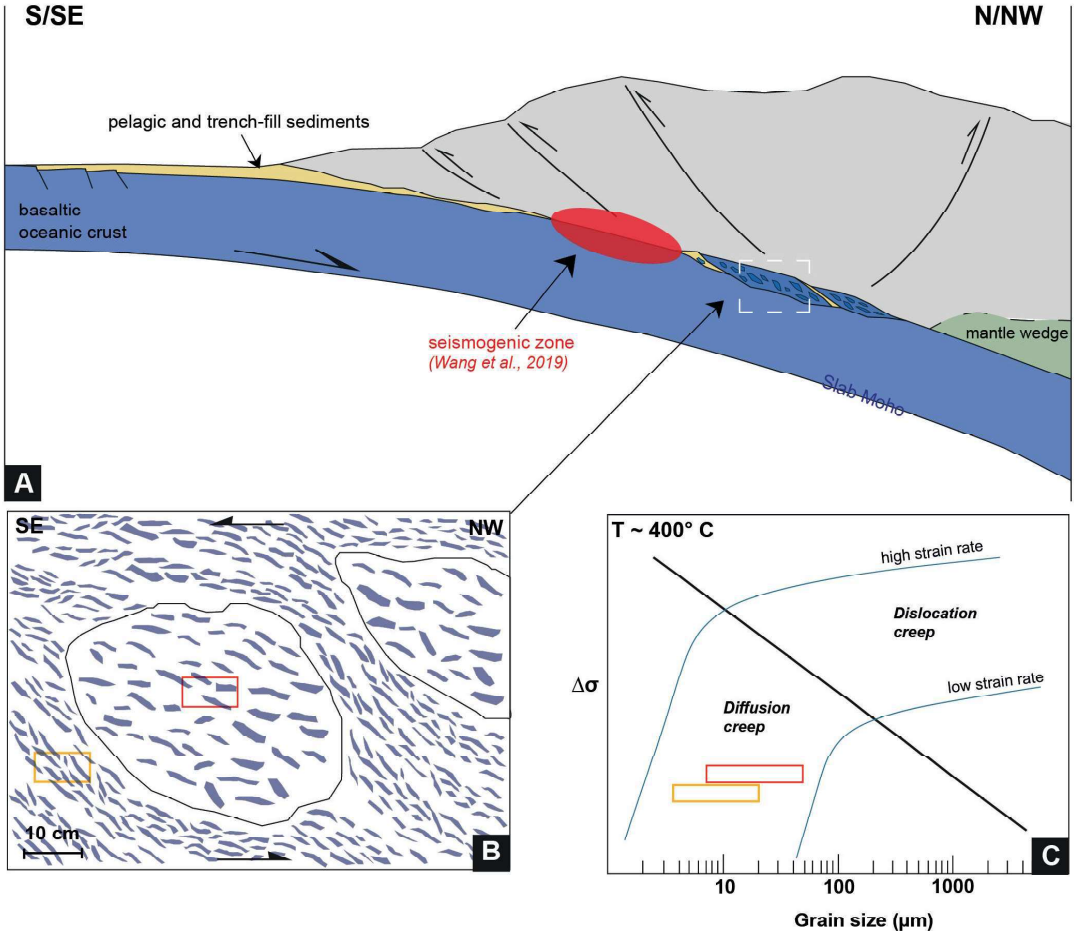

Figure 5.8: a) Qualitative cross section sketch of a convergent margin showing the approximate setting of exhumed Tomuru epidote-blueschists. In red, the location of the seismogenic zone interpreted by Wang et al, 2019. b) Schematic cartoon representative of the different foliation development of the block-in-matrix Tomuru blueschists. In blue, foliation drawn as glaucophane grains (not in scale). In yellow and red, the representation of matrix and block samples analysed. c) Qualitative sketch of an approximate deformation mechanism map for glaucophane, with the diffusion creep field being predominant at lower stress conditions. We chose to represent only dislocation creep as representative at higher stresses in our samples. Dislocation glide and/or cataclastic deformation may be possible at higher stresses, but that have not been shown because they are so far unknown in detail. Red box represents epidote-blueschist block, yellow box represents the matrix. The length of the boxes refers to the range in glaucophane grain size, the vertical position has been chosen arbitrarily within the field of diffusion creep, representing the interpreted higher stress in the block and lower stress in the matrix.

Chapter 6

Formation processes of epidote-blueschist block-in-matrix in the Ryukyu arc (SW Japan)

Abstract

Block-in-matrix complexes are internally fragmented bodies that are typically considered to register deformation in subduction zones. To explore block-in-matrix formation processes, we study the Tomuru block-in-matrix metabasites, an exhumed subduction complex in the Ryukyu arc (Ishigaki, SW Japan). The complex is characterised by blocks of different metamorphic assemblage, epidote-blueschist and greenschist, embedded in an epidote-blueschist matrix. Field-scale and microstructural observations show that the Tomuru block-in-matrix registers subduction-related deformation accommodating NW-verging subduction of the Philippean Sea Plate, through combined ductile and brittle deformation. This leads to the development of a NW-SE striking foliation, locally showing top-to-SE sense of shear, and NW-SE trending stretching lineation. Ductile fabrics are ac-

companied by brittle deformation accommodated through minor fracturing of the greenschist blocks and contained veining, through the development of syn-tectonic epidote-rich and quartz-rich veins. During deformation, Tomuru metabasites registered prograde metamorphism from greenschist to epidote-blueschist conditions, as both greenschists and epidote-blueschists, blocks and matrix, have prograde foliations, with amphiboles showing Na-rich rims. In the greenschist blocks, the foliation is characterised by actinolite, epidote, albite, chlorite and minor muscovite, whereas in the epidote-blueschists it is formed by glaucophane, epidote, albite and minor muscovite and titanite. Microstructural and EBSD analyses show that both the deformation mechanism leading to foliation development is distributed diffusive mass transfer, for the blocks and matrix alike, under low shear stress conditions. The coexistence of rocks with different metamorphic assemblage is not function of difference in bulk composition, as geochemical analyses showed that both rocks derive from MORB composition. The close association of greenschists and epidote-blueschists is likely to be ascribed to local differences in reaction kinetics as a function of grain size, strain and fluid circulation on the subduction interface. Moreover, fluid flow favours deformation mechanisms of diffusive mass transfer, such as dissolution-precipitation creep (c.f. Wassman and Stockert, 2013) and diffusion creep. Distributed linear-viscous creep governs bulk rheology of blocks and matrix of the Tomuru block-in-matrix complex and likely favours creep during subduction at epidote-blueschist conditions.

6.1 Introduction

6.1.1 Block-in-matrix structure in subduction zones

Block-in-matrix formations consist of mappable and internally fragmented bodies, containing a variety of relatively rigid blocks in a pervasively deformed matrix (Raymond, 1984; Silver and Beutner, 1980). Block in matrix formations, in the form of either mélanges or broken formations, are a typical feature of exhumed subduction-related terrains (Cowan, 1985; Shreve and Cloos, 1987). Block-in-matrix formation can include the interplay of mechanical and metamorphic processes. Mechanical processes involve layer-parallel extension as a mechanical response of flattening and volume loss on low angle shear zones (Fagereng, 2013; Wakita, 2012), which causes progressive stratal disruption, forming characteristic boudinage of relatively competent layers and small-scale normal faults. In some studied examples of mélanges developed on the subduction interface, shear is responsible for the presence of a penetrative foliation, accompanied by a lineation which is oriented parallel to the general tectonic transport direction, as it forms in response of shear along the subduction interface (e.g., Ujiie, 2002).

Deformation on the plate interface is accompanied by metamorphic reactions, as rocks reach higher T-P conditions following the prograde path during subduction. Dehydration reactions guiding prograde metamorphism liberate significant amount of fluids on the subducting slab (e.g., Peacock, 1990), and may therefore contribute to the style of deformation of high pressure rocks and influence bulk strength and consequently rheology and fault slip style on the subduction interface (Hobbs et al., 2010; Saffer and Tobin, 2011) (See Section 2.2). At depth in subduction zones, eclogitisation of blueschist rocks during prograde metamorphism sets up a source of rheological heterogeneity, where dehydration to form eclogite causes viscous hardening relative to the blueschists though a process of

reaction hardening (Behr et al., 2018), resulting in a blueschist matrix deforming by distributed dislocation creep, surrounding brittlely deformed eclogite blocks. This coupled brittle-viscous behaviour could potentially resemble episodic tremor and slow slip, as episodic transients could be generated by plastic failure of more competent, rigid blocks within a viscous matrix (Beall et al., 2019; Hayman and Lavier, 2014). Ridley and Dixon (1984) show how fluid pathways can favour the progressive deformation of blueschist metabasites during metamorphism in eclogite facies. Metamorphic reactions can also favour mechanisms of softening (Hobbs et al., 2010; White et al., 1980)(see Section 2.8), where syn-tectonic reactions can contribute to the development of new, strain-free grains, which typically develop (or rotate) in the direction favourable for slip, thus increasing concentration of deformation and allowing shear zone development. Moreover, metamorphic reactions and increased fluid pressure within the deforming rocks can lead to development of veins, which are a feature typical of exhumed subduction complexes (e.g., Fisher and Byrne, 1987; Fisher and Brantley, 1992).

6.1.2 Coexistence of high pressure metabasites in subduction zone block-in-matrix

In most subduction zones, block in matrix formations are generally characterised by mixing of metabasite and metasediment blocks in a sedimentary matrix, as a result of a deforming subducting oceanic crust with its sedimentary cover, as for example the well documented Shimanto complex in Japan (e.g., Kimura et al., 1991). Some examples of block-in-matrix formations with metabasite blocks embedded in a metabasite matrix have been documented as well, although limited in existing literature (e.g., Cycladic arc in Greece, Behr et al., 2018, Ridley and Dixon, 1984). Metabasites undergoing high-pressure low-temperature metamorphism during subduction, evolve in greenschist, blueschist and eclogite rocks as pressure and temperature increase. Devolatilisation reactions govern the stability field of metabasites (Evans, 1990) (See Section 2.3). In particular, greenschist assemblages destabilise in epidote-blueschists with release of water following Maruyama et al. (1986) equation:

$$9Chl + 50Ab + 6Act = 25Gln + 6Ep + 7Qtz + 14H2O. \quad (6.1)$$

Epidote-blueschists are characterised by stable Na-amphibole + epidote + quartz and can destabilise in eclogite at higher P-T (Evans, 1990). So that when a volume of rock undergoes prograde metamorphism during deformation, it would equilibrate homogeneously under specific P-T conditions as dehydration reactions guide facies evolution. However, this is not necessarily documented, as coexisting metabasites with greenschist, blueschist, and eclogite parageneses have been documented in block-in-matrix complexes, as documented in Chapter 5 in the Ryukyu arc, where greenschist and epidote-blueschist rocks coexist in the Tomuru block-in-matrix.

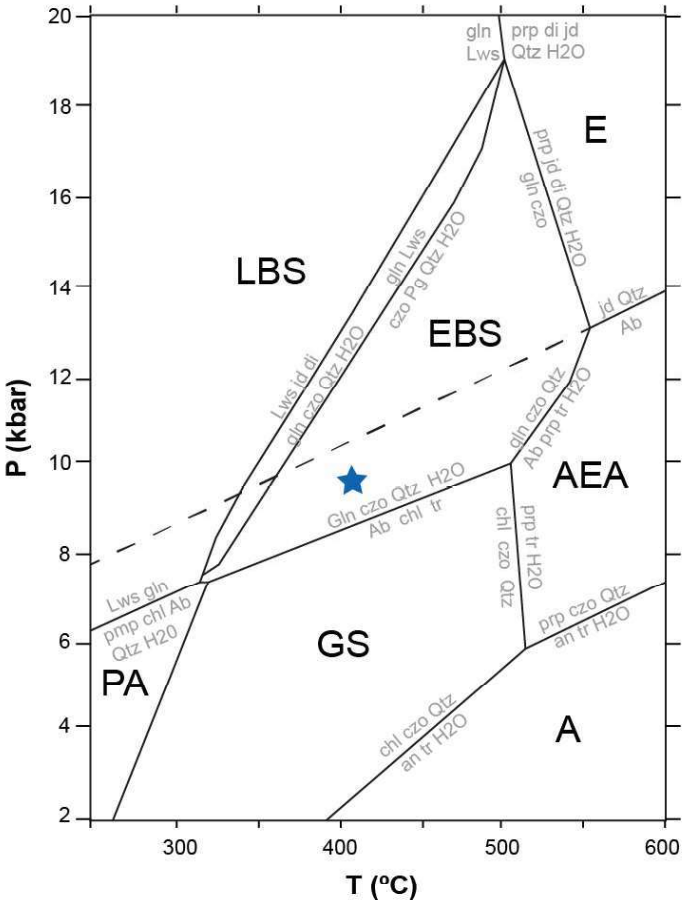

Figure 6.1: Phase diagram showing the stability fields of blueschist rocks (from Evans, 1990). Fields are separated by lines indicating the mineral reactions that guide facies evolution. Blue star indicates T-P conditions of the Tomuru epidote-blueschists (See Chapter 3, Section 3.1). PA: pumpellyite-actinolite; GS: greenschist; LBS: lawsonite-blueschist; EBS: epidote-blueschist; E: eclogite; A: amphibolite; AEA: Albite-epidote amphibolite.

Blueschist rocks have been frequently observed coexisting with greenschists and with eclogites in subduction-related metamorphic terrains such as the Cyclades in Greece (Matthew and Schiedstedt, 1984; Brocker et al. 1990, Behr et al., 2018), the Coastal Cordillera in Chile (Halama and Schmolze, 2015), in the Western Alps (Pognante and Kienast, 1987) and in Brittany in France (Barrientos and Selverstone, 1993). Previous studies provide no universal cause behind the coexistence of blueschists and these other metamorphic assemblages, but generally,

they have been ascribed to i) tectonic juxtaposition of units that equilibrated at different P-T paths, ii) bulk composition differences within the same protolith, and iii) different fluid content in the protolith. Blueschist and eclogite coexistence has generally been described as the product of metamorphic mixing caused by tectonic juxtaposition in the subduction channel (Pognante and Kienast, 1987; Bousquet, 2009), where the two different lithologies would present different metamorphic assemblage as a record of different P-T paths during prograde metamorphism. The blueschists and eclogites would then be accreted on the subduction channel and exhumed together. An alternative explanation invokes that eclogites are derived by dehydration during prograde metamorphism of the blueschists. In this way, the rocks derive from the same protolith undergoing low-T high-P deformation along a unique P-T path, and they maintain distinct mineral assemblages as a result of differences in bulk compositions in the protolith (Behr et al., 2018). Ridley and Dixon (1984) highlight that the coexistence of blueschist and eclogite metamorphic assemblages can be related to different fluid pathways during progressive deformation from blueschist to eclogite facies, where the equilibration under eclogite conditions is dependent on the degree and intensity of strain.

Coexistence of blueschists with greenschists has been explained as the product of different bulk composition of the same magmatic protolith (Baziotis and Mposkos, 2011), with the result that different bulk compositions can crystallise different facies-index minerals, i.e., actinolite for greenschists and glaucophane for blueschists, even when the rocks undergo the same P-T path during subduction deformation and subsequent retrogression (Dungan, 1983; Baziotis and Mposkos, 2011). Another factor that has been inferred to contribute to the presence of greenschist assemblages and blueschists is the overprinting by fluids during retrograde metamorphism of a single protolith (Matthews and Schliestedt, 1984; Schliestdt and Matthews, 1987; Broker, 1990; Barrientos and Selverstone, 1993; Halama and

Konrad-Schmolke, 2015). During retrogression, the nature of the fluids infiltrating the blueschists can be varied, some authors describe the greenschist bands as the result of selective infiltration of syn-metamorphic fluids in the blueschist bodies during deformation in the subduction channel (Barrientos and Selverstone, 1992). Other studies highlight the possibility of external fluid sources derived from adjacent tectonic units that selectively infiltrate the blueschists (Schliestedt and Matthews, 1987; Broker, 1990). Finally, Halama and Konrad-Schmolze (2015) suggest that the coexistence of the two distinct metamorphic assemblages could be the result of a combination of compositional variability in the bulk rock composition and subsequent retrograde overprint by layer-parallel selective fluid infiltration. Fluids, therefore, can play a crucial role in the formation of heterogeneous subduction complexes, whether they are generated during prograde metamorphism through dehydration reactions of the subducting materials, or whether they are migrating updip from a deeper source (Saffer and Tobin, 2011).

6.1.3 Oceanic crust strength during subduction

As previously described (see Section 2.5) subduction interfaces are intrisically weak in respect to the relatively underformed overriding and subducting plates. Heat flow data and modelling revealed in fact that megathrusts shear stresses are low (< 35 MPa; Duarte et al., 2015).

Frictional experiments on fresh basaltic rocks show high frictional strength ($\mu \sim 0.75$; He et al., 2007) and velocity-weakening behaviour, moreover viscous creep of dry diabase at shear stresses <200 MPa requires temperatures of > 650 ℃ assuming a moderate strain rate (Mackwell et al., 1998). These high strengths are incompatible with the inferred low strengths of creeping plate interfaces at the base of the seismogenic zone (Hardebeck and Loveless, 2018), however, recent literature showed that the oceanic crust alone can be sufficiently weak to accomodate plate

creep at low inferred shear stress at greenschist-amphibolite conditions at the base of the seismogenic zone (Tulley et al., 2020), thus lacking the need of a continuous layer of lubricating sediments along with the oceanic crust. This can be considered valid until the onset of pervasive eclogitisation at greater depths, where the oceanic crust is expected to have significantly increased viscosity (Behr et al., 2018). At depth where blueschist facies rocks are stable, the behaviour of blueschists is poorly documented. Sawai et al. (2016) performed shear experiments on lawsonite blueschists, showing that they have an apparent friction coefficient μ ranging 0.5 - 0.6 at 300-400 ℃ and display velocity weakening behaviour at 400 ℃, suggesting that the oceanic crust at blueschist conditions can potentially be mechanically strong, leading to instability and possibly earthquake nucleation.

There is little knowledge in literature as to how greenschist to blueschist coexistence can happen in prograde settings, as opposed to the well documented retrograde ones. In this chapter we investigate the hypotesis that the heterogenous Tomuru block-in-matrix is the result of progressive deformation on the subduction interface, following the metamorphic and structural evolution from greenschist facies to epidote-blueschist facies conditions on the prograde path. Moreover, we consider how this structural heterogeneity can affect rheology on the plate interface at greenschist to epidote blueschist conditions, as mostly documented heterogenous complexes studied in literature are deformed at higher depths on the subduction interface, at the blueschist ot eclogite transition. Finally, we investigate whether glaucophane-rich subducting metabasites at epidote-blueschist conditions can accomodate plate creep at geological strain rates.

We use microstructural and geochemical data to understand what processes contribute to the formation of the Tomuru block-in-matrix complex from a protolith of oceanic-affinity during deformation on the subduction interface at epidote-blueschist conditions. We highlight which factors favour the coexistence of green-

schist and epidote-blueschist assemblages and discuss how the deformation style and metamorphic history does influence bulk rheology of rocks deforming at epidote-blueschist conditions.

6.2 Outcrop heterogeneity of block-in-matrix Tomuru metabasalts

Tomuru metabasalts crop out in three different locations in the north of Ishigaki Island, Tomuru, Yasura-zaki and Urasaki, where they are in tectonic contact with well-foliated, intensely veined micaschists (Figs. 6.2, 6.3A). Tomuru metabasites vary in structure, fabric and metamorphic assemblage. In Tomuru (Fig. 6.2A), the metabasites have a block-in-matrix structure, with greenschist blocks embedded in an epidote-blueschist matrix (Fig. 6.3B). These form a 30 m thick, NW-SE oriented body in tectonic contact with fine-grained, well-foliated greenschists that lack the block-in-matrix structure. The tectonic contact is characterised by a meter-thick high strain zone, where the greenschist blocks gradually change in shape from spherical to ellipsoidal (Figs. 6.3B,C), and their internal fabric from isotropic, with no distinguishable foliation at the macroscale, to well-foliated, denoting a gradual increase in strain. The tectonic contact is oriented NW-SE and parallel to the main foliation in the greenschists and in the block-in-matrix metabasites. The epidote-blueschist matrices show a pervasive sub-horizontal SE-trending lineation, formed by the preferred orientation of glaucophane and albite grains. The well-foliated greenschists are in turn in tectonic contact with metasediments (Fig. 3A). These rocks are quartz-rich micaschists, well-foliated, characterised by a mm-spaced foliation, striking NW-SE, parallel to the tectonic contact with the metabasites.

In Yasura-zaki (Fig. 2B), Tomuru metamorphic rocks are represented solely

by block-in-matrix metabasites (Fig. 6.3D,E). They are characterised by coarser-grained greenschist blocks in a fine-grained epidote-blueschist matrix like the rocks in Tomuru, however, here they differ by a higher degree of strain. The blocks, of multi-dm size, are very well foliated and lenticular in shape, showing an asymmetry that indicates top-to NW and locally, top-to-SE sense of shear. The main foliation both in the matrix and in the blocks is striking NW-SE with moderate dips towards SW. In Urasaki (Fig. 6.2C), the metabasites, are represented by fine-grained greenschist rocks, poorly foliated, with foliation striking NNE-SSW and dipping gently towards WNW, that appear in tectonic contact with Eocene metasediments (Fig. 6.3F). It is worth mentioning that here epidote-blueschist rocks are not found as extensive outcrops in contact with the green metabasites or as blocks within a greenschist matrix.

At the mesoscale, the greenschist blocks vary in size, from multi-cm to meter-scale within the same outcrop, and shape, from spherical to lenticular. When the greenschist blocks are not asymmetric, their internal foliation is either very poorly defined, whereas when blocks are asymmetric, they tend to have a pervasive NW-SE oriented foliation that is generally parallel to the one in the matrix. Lineation trends gently towards SE. The contact between the greenschist blocks with the epidote-blueschist matrix can be locally sharp, with a very distinct line between block and matrix, however it is very common to observe gradational contacts, where the cores of the blocks, green and coarser-grained, transition to blue and finer-grained rims that present the same colour and pervasive foliation as the epidote-blueschist matrix (Fig. 6.3A).

Locally, there is evidence of brittle deformation in the block-in-matrix metabasites. The blocks present mineralised quartz-rich veins that tend to be parallel to, or at low angle to the foliation (Fig. 6.3E). Quartz-rich veins are also sporadically present in the epidote-blueschist matrix, typically close to the tectonic

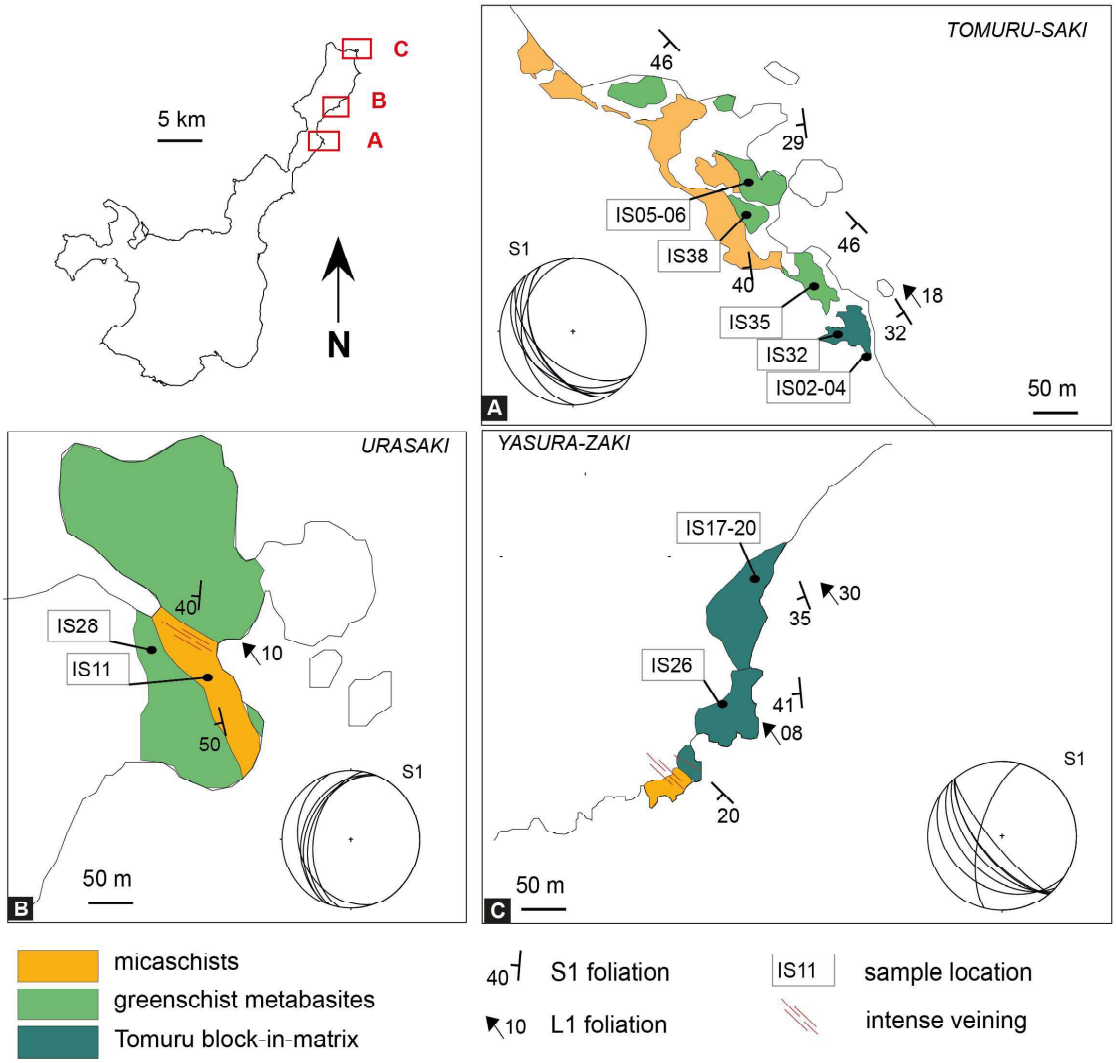

Figure 6.2: Geological maps of the Tomuru metamorphic rocks. A) Tomuru section. Quartz-rich micaschists are in tectonic contact with Tomuru block-in-matrix and Tomuru greenschist rocks. S1 has NW-SE strike and dips at medium angle towards SW. L1 is NW-trending with gentle plunge. C) Yasura-zaki section. Tomuru block in matrix metabasites are in tectonic contact with micaschists. S1 is NW-SE striking with dips at a moderate angle towards SW. L1 is NW-trending and sub-horizontal. B) Urasaki section. Tomuru metabasites are in tectonic contact with metasediments. S1 is oriented NNE-SSW with gentle dips towards WNW and L1 is NW-trending with gentle to moderate plunges.

Table 6.1: Sample list from Ishigaki. EBS: epidote-blueschist, GS: greenschist

Outcrop	Sample	Name	Description	Latitude	Longitude
Tomuru	IS02	EBS matrix	coarse grained	N 24.53369	E 124.30708
	IS03	EBS matrix	fine grained, well-foliated	N 24.53370	E 124.30709
	IS04	Contact block/matrix	Contact portion between GS block and EBS matrix	N 24.53371	E 124.30710
	IS05	GS matrix	fine grained, well-foliated	N 24.53345	E 12430713
	IS06	GS block	fine-grained, poorly foliated	N 24.53346	E 12430714
	IS07	GS matrix	fine grained, well-foliated	N 24.53347	E 12430715
	IS32	EBS matrix	well-foliated	N 24.53368	E 124.30707
	IS35	Quartz-rich vein	vein in metabasites, top-to-SE sense of shear	N 24.53368	E 124.30707
	IS38	Quartz-rich vein	vein in micaschists, top-to-SE sense of shear	N 24.53369	E 124.30708
Yasura zaki	IS17	EBS block	fine grained, foliated	N 24.56001	E 124.32193
	IS18	EBS block	fine grained, foliated	N 24.56002	E 124.32194
	IS19	EBS matrix	fine grained, well-foliated	N 24.56003	E 124.32195
	IS20	EBS matrix	fine grained, well-foliated	N 24.56004	E 124.32196
	IS25	EBS matrix	coarse grained, foliated	N 24.55771	E 124.31676
	IS26	EBS block	coarse grained, poorly foliated	N 24.58801	E 124.33990
Urasaki	IS10	GS metabasite	coarse grained, poorly foliated	N 24.604518	E 124.339688
	IS11	Metapelite	well-foliated	N 24.604518	E 124.339688
	IS28	GS foliated block	fine grained, foliated	N 24.604518	E 124.339688

contact with the metasediments, where they appear boudinaged and parallel to the main foliation (Fig. 6.4D), locally presenting top-to -SE and top-to-NW asymmetry (Fig. 6.4E). The epidote-blueschist blocks and matrix present epidote-rich veins that are generally parallel to the main foliation and that are not found in the greenschist blocks. They have thickness varying from a few mm to a few cm and lengths up to meter-scale. Locally they are folded, but they do not show asymmetry or any sign of shear displacement (Figs. 6.4B,C).

The quartz-rich micaschists are intensely veined, with two systems of quartz-rich veins. The most pervasive one is characterised by multi cm-spaced quartz veins, usually varying in thickness from a few mm to a few cm, parallel to the main foliation (Fig.6.4F). Their length varies from the cm-sale to the outcrop scale, and locally show top-to-SE and top-to NW asymmetry. They are commonly boundinaged or show pinch-and-swell structure. The second system is characterised by sparse quartz-rich veins crosscutting the main foliation at a high angle.

6.3 Microstructural analyses

6.3.1 Petrography of greenschist blocks and micaschists

Blocks show a textural gradient from the core to the rim, microstructural analyses were carried out separately from samples taken from the core, green and coarse-grained at the mesoscale, and the edge of the green blocks, finer grained and bluer in colour. The fabric of these rocks shows some variability, locally, the cores of the greenschist blocks are poorly foliated (Fig. 6.5A), with discontinuous chlorite and actinolite separating large grains of epidote, typically fractured. Blocks can also be massive (Fig. 6.5B), constituted in large part by epidote, with only locally thin layers of chlorite. Locally, epidote grains are fractured, presenting chlorite growth in the infillings, or epidote layers are boudinaged. The majority of greenschist

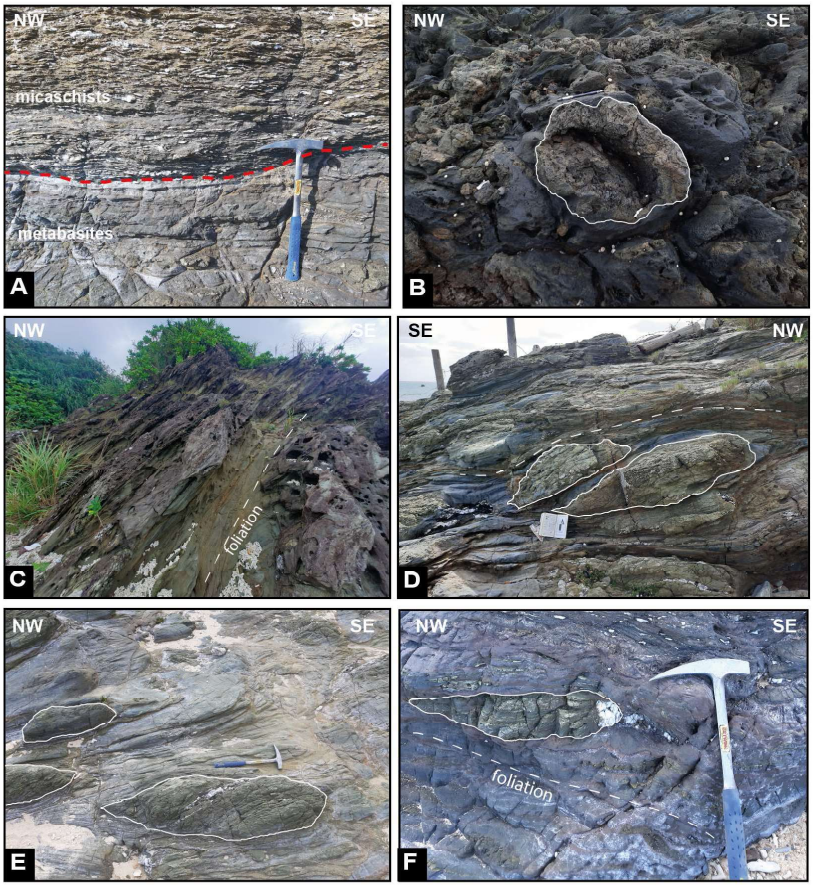

Figure 6.3: A) Tomuru outcrop. Tectonic contact between micaschists and greenschist metabasites, NW-SE striking and parallel to the internal foliation of the two units. The micaschists are well-foliated, intensely veined rocks, with a sub-mm spaced continuous foliation. The metabasites vary in aspect, in the figure, they are well-foliated, with mm-spaced foliation; B) Tomuru outcrop. Round, coarse grained, massive greenschist blocks embedded in fine-grained, well-foliated epidote-blueschist matrix. Contoured in white, one of the blocks resembles a pillow lava. C) Tomuru outcrop. Higher strained zone, the greenschist blocks have very elongated shapes and are almost undistinguishable from the matrix. D) and E) Yasura-zaki outcrop. Lenticular shaped greenschist blocks embedded in the epidote-blueschist matrix, showing with top-to-NW and top-to-SE asymmetry respectively. Here, the greenschist blocks are well-foliated and have quartz-rich veins parallel to the foliation. F) Urasaki outcrop. Greenschist metabasites, poorly foliated, with greenschist blocks with massive fabric (contoured in white).

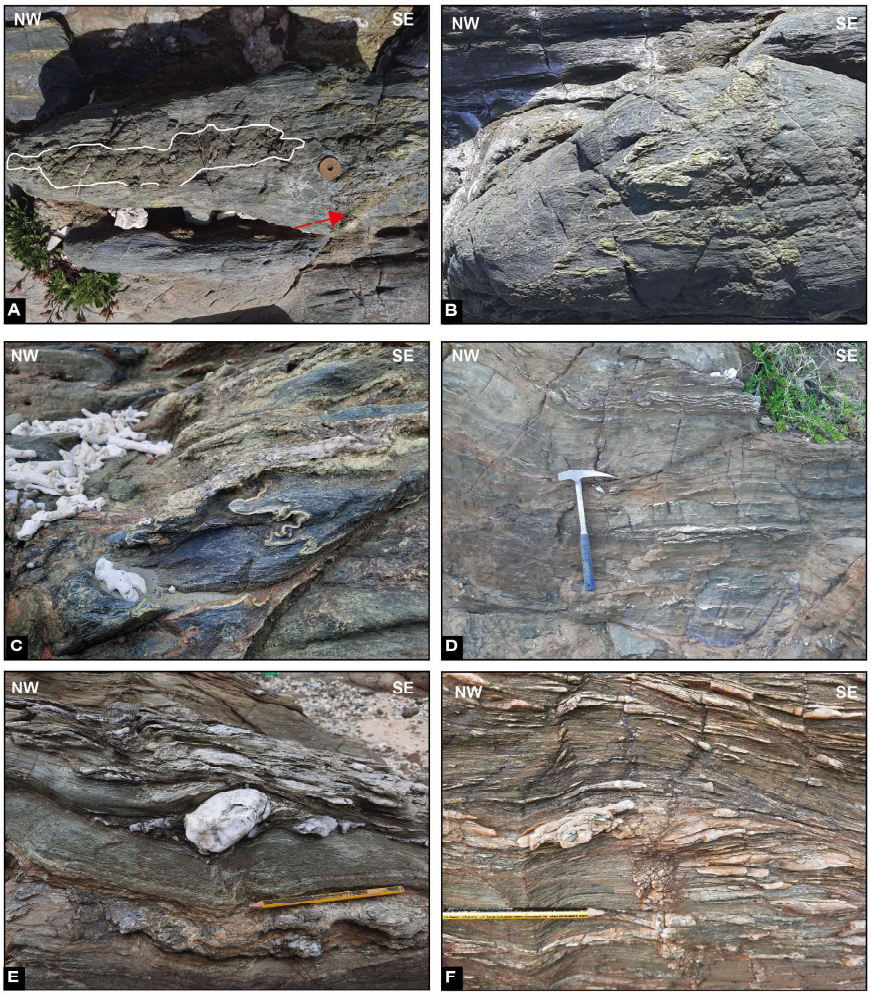

Figure 6.4: A) Yasura-zaki, detail of an epidote-blueschist block. Contoured in white, the core of the block is represented by coarse-grained, massive greenschist that transitions to a blue and well foliated rim. Note the presence of green epidote veins in the blue rim; B) and C) detail of the epidote-rich veins developed in the epidote-blueschist block in A). C) Tomuru, detail of epidote veins folded in an epidote-blueschist matrix; D) Urusaki, foliation-parallel quartz-rich veins in the metabasites. They have length that varies from meter scale to outcrop scale and have irregular spacing throughout the outcrop; E) Tomuru, detail of quartz-rich vein in metabasites showing top-to-SE asymmetry; F) Tomuru, foliation-parallel quartz veins in the metasediments. They have thickness varying from mm- to cm-scale and they have cm-scale frequency.

blocks analysed, however, are foliated, with a foliation defined by actinolite (17-21%), chlorite (6-10%) and muscovite (2-7%) separating domains of epidote (17-19%), albite (7-10%) and minor titanite (1-5%) (40% non-indexed grains through EBSD analysis) (Fig. 6.5C). Epidote grains have size up to 200 µm and they are typically fractured, albite grains have size up to 100 µm, and they are present both as single grains along the foliation, or in lenticular domains with epidote and titanite (Fig. 6.5D). Chlorite is relatively abundant in these samples, it has small grain size, with long axes up to 50 µm and is found predominantly in epidote strain shadows or in the main foliation with actinolite (Fig. 6.5C). Actinolite grains, with size up to 100 µm, form more or less continuous layers separating epidote and albite grains. Only locally, actinolite is present in epidote strain shadows (Fig. 6.5E). Amphiboles grains are locally zoned, with concentric geometry. Compositional variations show Ca-rich cores and increasing quantity of Na and Al at the rims (Figs. 6.5F, 6.6A). The composition at the cores has been identified as actinolite, while the composition at the rims has been identified as winchite or as barroisite (Fig. 6.6B,C).

The contact between the blocks and the matrix (Fig. 6.7) is parallel to the main foliation recognised on the field and oriented NNW-SSE. At the microscale, the passage from block to matrix is evident by an abrupt change in colour, which is the consequence of the change in mineral assemblage of the greenschist block core, containing a foliation predominantly rich in actinolite and chlorite, and the epidote-blueschist matrix, containing a foliation rich in glaucophane (see epidote-blueschist matrix description in Chapter 5). EDS map of the contact shows details about the differences between the foliation-forming amphiboles in the two different portions (Fig. 6.7E). In close proximity of the contact, the blue matrix is characterised by glaucophane, which corresponds to the analyses at the optical microscope and at the mesoscale. In the green portion however, the amphibole, green at the optical

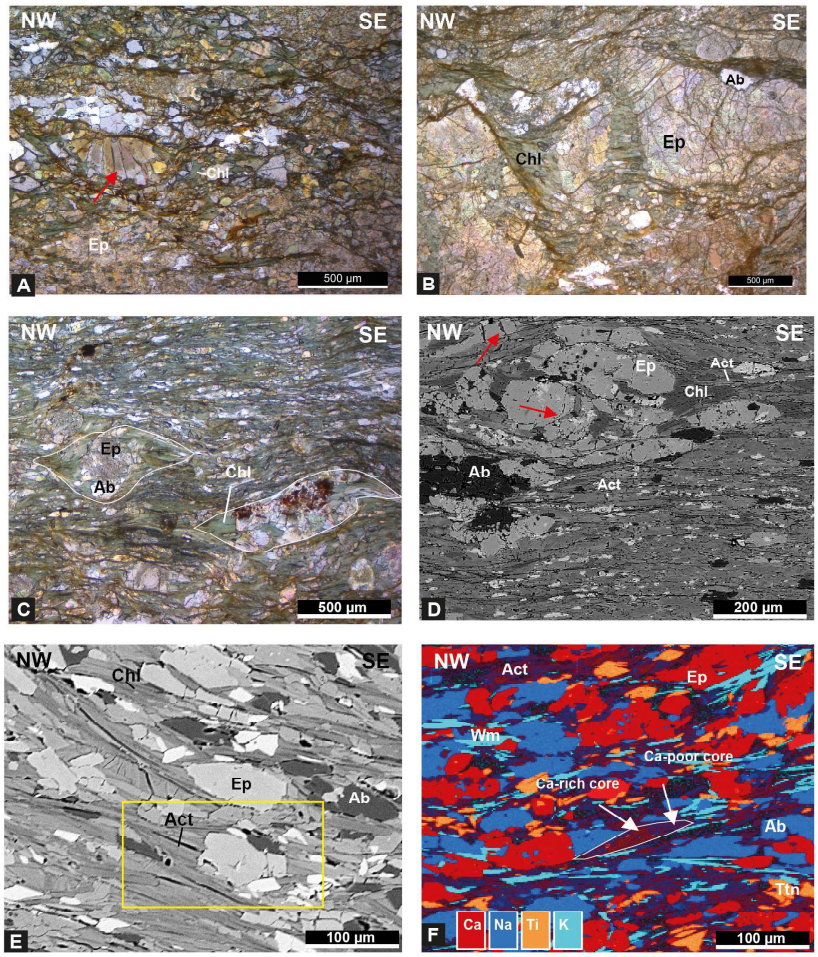

Figure 6.5: A) photomicrograph of poorly foliated core of greenschist blocks, foliation is poorly developed, characterised by discontinuous layers of chlorite and actinolite separating grains of epidote and albite. In red, fractures within epidote grains (plane polarised light); B) photomicrograph of massive core of greenschist blocks, epidote are fractured and chlorite is present in the infilling (plane polarised light); C) photomicrograph of the fabric representative of foliated greenschist blocks. The foliation is defined by alignment of actinolite and chlorite separating domains of epidote and albite, contoured in white, chlorite developes in the epidote strain shadows, showing top-to-SE asymmetry (plane polarised light); D) BSE image of foliated greenschist microstructure. Epidote grains are fractured, chlorite is present in the strain shadows (red arrows indicate fractures); E) BSE image of greenschist foliation. Continuous layers of actinolite and chlorite grains separate epidote and albite. In yellow box, actinolite grains develop in epidote strain shadows; F) EDS map of representative greenschist block. Contoured in white, an actinolite grain shows compositional variations from the core, rich in Ca and the rims, richer in Na.

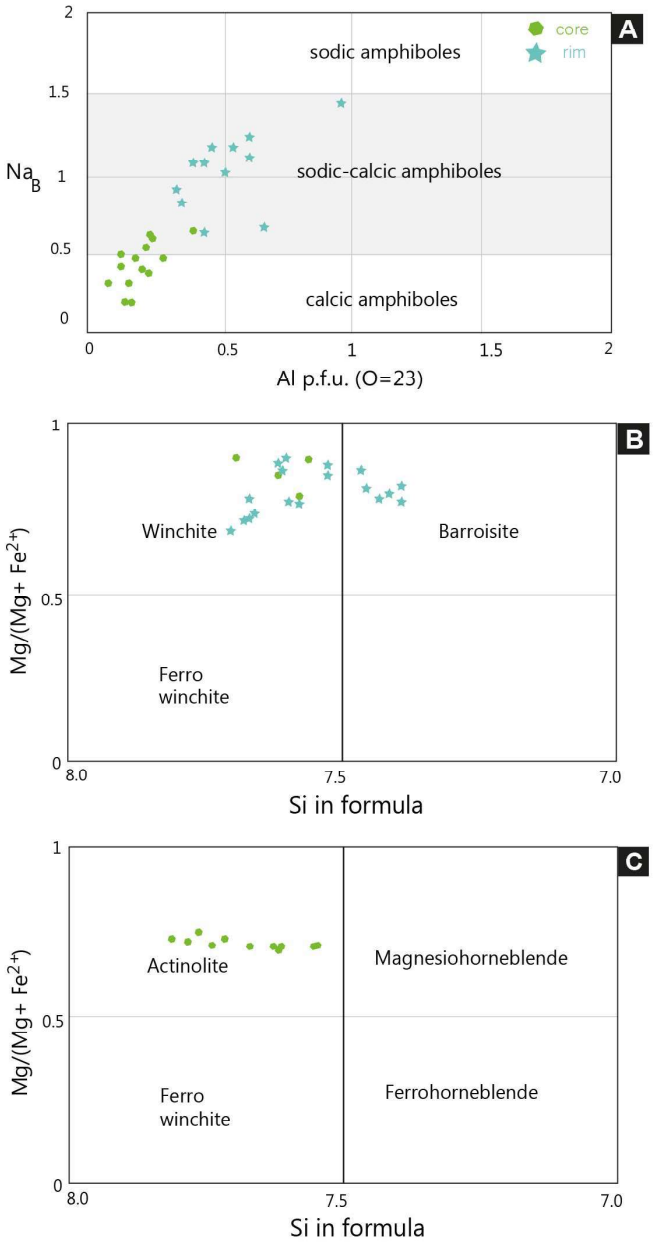

Figure 6.6: Amphibole chemistry (analyses in Table 6.1) A) Compositional variations of amphiboles in the greenschist blocks, showing increase of Na and Al2O3 content from the cores (green circles) and the rim (blue stars). B) Classification diagram of amphiboles rims, of winchite and barroisite composition, (classification diagram of Na-Ca amphiboles from Leake et al., 1997). C) Classification diagram of amphiboles cores, of actinolite composition, (classification diagram of Ca-amphiboles from Leake et al., 1997).

Table 6.2: Mineral analyses from amphibole grains cores. * Fe_2O_3 is total Fe. $X_{Fe2} = Fe_{2+}/(Fe_{2+} + \text{Mg})$; $X_{Fe3} = Fe_{3+}/(Fe_{3+} + \text{Al})$VI; $X_Mg = \text{Mg}/(\text{Mg} + Fe_{2+})$. act: actinolite; barr: barroisite; wnc: winchite.

	Core analyses														
	whc	act	barr	whc	barr	barr	act	act	act	act	act	act	act	act	barr
SiO2	54.95	55.86	53.38	55.47	52.83	53.30	55.38	54.46	53.77	53.76	55.89	55.43	56.04	55.94	52.34
TiO2	0.09	0.11	0.10	0.00	0.16	0.11	0.10	0	0.11	0.32	0	0	0	0	0.11
Al2O3	4.00	2.27	4.74	2.60	6.87	6.26	2.73	4.19	3.85	4.83	2.04	2.48	2.59	2.7	6.88
Fe2O3*	14.97	13.52	15.86	14.37	16.23	15.93	13.16	14.35	15.27	15.76	12.6	12.47	13.42	13.94	17.98
MnO	0.26	0.30	0.29	0.29	0.32	0.33	0.30	0.27	0.28	0.34	0.28	0.25	0.28	0.26	0.48
MgO	14.29	16.00	13.84	15.37	12.38	12.66	15.77	14.42	14.35	13.17	16.13	16.09	15.52	15.14	11.35
CaO	8.69	10.22	9.10	9.89	7.54	8.00	11.25	10.14	10.08	8.77	12.03	12.04	10.67	10.46	6.81
Na2O	2.59	1.60	2.50	1.89	3.48	3.25	1.24	2.05	2.1	2.92	0.92	1.1	1.35	1.46	3.82
K2O	0.12	0.12	0.19	0.10	0.20	0.19	0.10	0.12	0.19	0.14	0.11	0.14	0.13	0.1	0.24
sum	99.96	100.00	100.00	99.97	100.00	100.03	100.04	100.00	100.00	100.01	100.00	100.00	100	100	100.01
Si	7.62	7.76	7.45	7.71	7.37	7.44	7.71	7.60	7.54	7.55	7.80	7.75	7.80	7.77	7.33
Al	0.65	0.37	0.78	0.43	1.13	1.03	0.45	0.69	0.64	0.80	0.34	0.41	0.42	0.44	1.14
Ti	0.01	0.01	0.01	0.00	0.02	0.01	0.01	0.00	0.01	0.03	0.00	0.00	0.00	0.00	0.01
Cr		0.00		0.00											
Mg	2.96	3.31	2.88	3.18	2.57	2.63	3.27	3.00	3.00	2.76	3.36	3.35	3.22	3.14	2.37
Fe2+	0.98	1.09	1.01	1.02	1.05	1.12	1.15	1.18	1.19	1.35	1.28	1.30	1.25	1.13	1.07
Mn	0.03	0.04	0.03	0.03	0.04	0.04	0.04	0.03	0.03	0.04	0.03	0.03	0.03	0.03	0.06
Ca	1.29	1.52	1.36	1.47	1.13	1.20	1.68	1.52	1.51	1.32	1.80	1.80	1.59	1.56	1.02
Na	0.70	0.43	0.68	0.51	0.94	0.88	0.33	0.55	0.57	0.80	0.25	0.30	0.36	0.39	1.04
K	0.02	0.02	0.03	0.02	0.03	0.03	0.02	0.02	0.03	0.03	0.02	0.02	0.02	0.02	0.04
Fe3+	0.76	0.48	0.84	0.65	0.84	0.74	0.38	0.50	0.60	0.50	0.19	0.16	0.31	0.49	1.03
NaB	0.70	0.43	0.64	0.51	0.87	0.80	0.32	0.48	0.49	0.68	0.20	0.20	0.36	0.39	0.98
AlVI	0.28	0.13	0.23	0.13	0.50	0.47	0.16	0.29	0.18	0.68	0.14	0.16	0.23	0.21	0.47
XFe3	0.73	0.79	0.78	0.83	0.63	0.61	0.71	0.63	0.77	0.77	0.58	0.50	0.58	0.70	0.69
XFe2	0.25	0.25	0.26	0.24	0.29	0.30	0.26	0.28	0.28	0.28	0.28	0.28	0.28	0.27	0.31
XMg	0.75	0.75	0.74	0.76	0.71	0.70	0.74	0.72	0.72	0.72	0.72	0.72	0.72	0.73	0.69

Table 6.3: Mineral analyses from amphibole grains rims. * Fe_2O_3 is total Fe. $X_{Fe2} = Fe_{2+}/(Fe_{2+} + \text{Mg})$; $X_{Fe3} = Fe_{3+}/(Fe_{3+} + \text{Al})$VI; $X_Mg = \text{Mg}/(\text{Mg} + Fe_{2+})$. act: actinolite; wnc: winchite.

	Rim analyses										
	whc	whc	whc	whc	whc	whc	whc	whc	whc	whc	act
SiO2	54.86	54.71	54.20	54.81	54.59	54.43	55.02	54.44	54.77	54.02	56.08
TiO2	0.11	0.00	0.09	0	0.12	0.13	0	0.13	0.14	0	0
Al2O3	3.84	3.72	5.65	4.79	4.25	5.17	4.66	4.84	4.8	4.89	1.69
Fe2O3*	14.48	14.97	15.10	14.17	17.23	16.42	17.5	18.02	16.76	17.1	12.22
MnO	0.31	0.29	0.26	0.27	0.24	0.33	0.4	0.45	0.41	0.54	0.74
MgO	14.87	14.58	13.42	14.11	12.34	12.49	11.85	11.73	11.99	12.57	16.58
CaO	9.11	9.52	7.97	9.03	7.84	7.97	6.16	5.96	7.01	7.2	11.37
Na2O	2.28	2.03	3.10	2.55	3.24	2.94	4.18	4.2	3.98	3.51	1.22
K2O	0.15	0.16	0.18	0.27	0.16	0.14	0.13	0.13	0.14	0.16	0.1
sum	100.00	99.98	99.97	100.00	100.01	100.02	99.9	99.9	100	99.99	100
Si	7.61	7.62	7.52	7.61	7.66	7.60	7.68	7.60	7.68	7.53	7.79
Al	0.63	0.61	0.92	0.78	0.70	0.85	0.77	0.80	0.79	0.80	0.28
Ti	0.01	0.00	0.01	0.00	0.01	0.01	0.00	0.01	0.01	0.00	0.00
Cr	0.00	0.00									
Mg	3.08	3.03	2.77	2.92	2.58	2.60	2.47	2.44	2.51	2.61	3.43
Fe2+	1.00	1.07	0.99	1.08	1.37	1.26	1.16	1.11	1.40	0.98	1.00
Mn	0.04	0.03	0.03	0.03	0.03	0.04	0.05	0.05	0.05	0.06	0.09
Ca	1.35	1.42	1.18	1.34	1.18	1.19	0.92	0.89	1.05	1.08	1.69
Na	0.61	0.55	0.83	0.69	0.88	0.80	1.13	1.14	1.08	0.95	0.33
K	0.03	0.03	0.03	0.05	0.03	0.02	0.02	0.02	0.03	0.03	0.02
Fe3+	0.68	0.67	0.76	0.56	0.65	0.66	0.88	1.00	0.56	1.01	0.42
NaB	0.61	0.55	0.82	0.66	0.82	0.80	1.08	1.11	0.95	0.92	0.31
AlVI	0.24	0.23	0.44	0.40	0.37	0.45	0.44	0.40	0.48	0.33	0.06
XFe3	0.74	0.75	0.63	0.58	0.64	0.59	0.66	0.71	0.54	0.75	0.87
XFe2	0.24	0.26	0.26	0.27	0.35	0.33	0.32	0.31	0.36	0.27	0.22
XMg	0.76	0.74	0.74	0.73	0.65	0.67	0.68	0.69	0.64	0.73	0.78

microscope, does not present the typical compositional pattern of the cores of the green blocks, with Ca-Na compositional zoning, but it is mostly sodic, with glaucophane composition. In both portions close to the contact, chlorite is present in a higher quantity that what is found in the green blocks or the blue matrix.

The micaschists are characterised by a foliation defined by discontinuous layers of white mica and chlorite, separating domains of quartz (Fig. 6.8A). In the micaschists it is possible to observe folding related to exhumation-related stage D2 (Osozawa and Wakabayashi, 2013).

6.3.2 Vein petrography

In the Tomuru epidote-blueschists, a system of epidote-rich veins is present both in the blocks and in the matrix. They are generally parallel to the foliation, but locally appear folded with their axial surface parallel to the foliation, which could be interpreted as intrafolial folds (Fig. 6.9A). They are generally blocky with mineralogy consisting mostly of epidote grains, and only locally presenting minor quantity of albite and quartz grains (Fig. 6.9B). Epidote grains range in size between 20 µm and 150 µm, and commonly do not show preferred alignment, albite grains are present as small clusters or as unoriented single grains, similar in size to the epidote grains, and finally, quartz grains, when present, are either isolated unoriented single grains or small clusters of grains, with size up to 100 µm. Locally, the epidote-rich veins present few glaucophane grains, with size up to 50 µm.

In the metabasites, foliation-parallel quartz-rich veins are generally blocky and their mineralogy is characterised of quartz grains with minor epidote, albite and, locally, glaucophane (Fig. 6.9C). Quartz grains range in size from 50 µm to 200 µm and are ductilely deformed, presenting irregular grain boundaries and undulose extinction (Fig. 6.9D). Epidote grains are generally present in small clusters, with

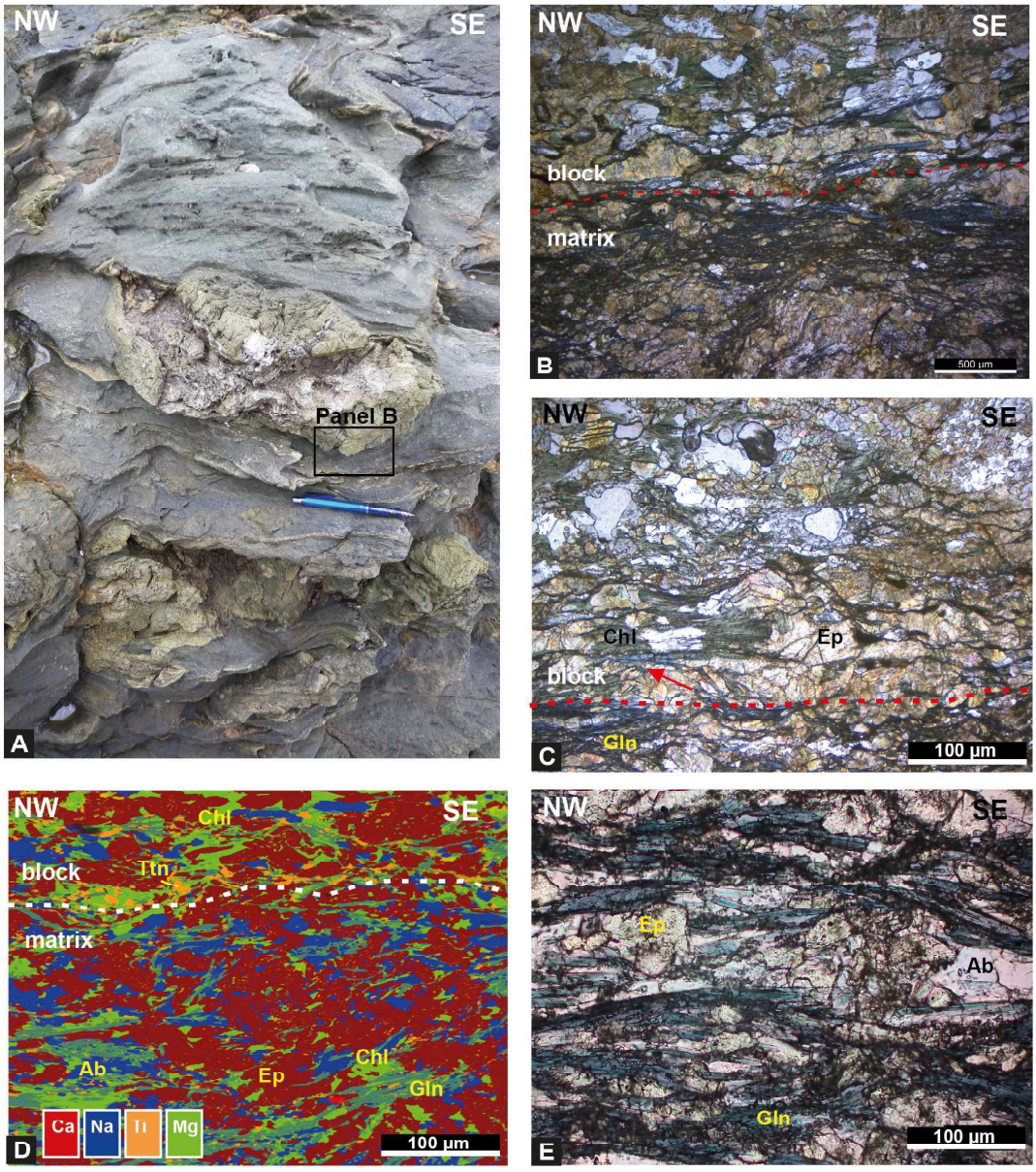

Figure 6.7: A) Contact between greenschist block and blueschist matrix in Tomuru. B) photomicrograph of the contact (plane polarised light); C) photomicrograph of the green block detail, where the foliation is characterised by Ep and Chl (plane polarised light) D) photomicrograph of the epidote-blueschist matrix (plane polarised light); E) EDS map of the contact. White dashed line separates the greenschist block (top) and epidote-blueschist matrix (bottom).

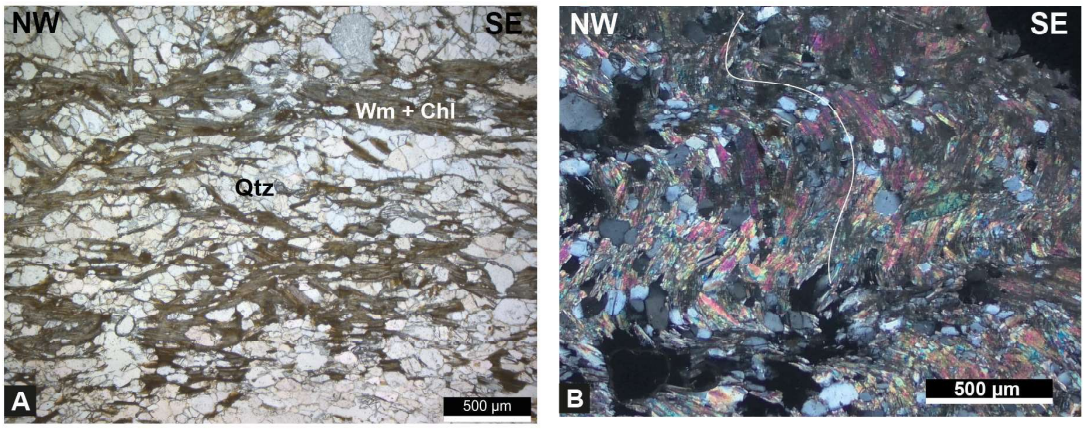

Figure 6.8: Micaschist microstructure. A) micaschist foliation is defined by discontinuous layers of white mica and chlorite separating quartz domains (plain polarised light); B) open folds folding the S1 foliation (cross polarised light).

single grains having size up to 100 µm, they are only locally slightly elongated parallel to the foliation. Albite grains, when present, have size up to 50 µm, and are present as isolated grains. Finally, glaucophane grains, with size up to 100 µm, are present generally as isolated grains, with long axes parallel to the vein walls and metabasite foliation.

Foliation-parallel, quart-rich veins found in the micaschists have the similar features to the ones in the metabasites, with blocky texture characterised by quartz grains and minor white mica (Fig. 6.9E). Glaucophane grains are not present in the veins we sampled. Quartz grains have larger grain size (100 – 500 µm) and are ductilely deformed, with irregular grain boundaries, undulose extinction and subgrains.

6.3.3 Fabric and EBSD analyses on the greenschist blocks

In the greenschist blocks, fabric-forming minerals have been identified as actinolite, epidote and albite. Actinolite is fine grained, with size ranging from a few µm to 90 µm (mean 15 µm) and aspect ratios ranging 1 – 8 (Fig. 6.10A,B). Epidote

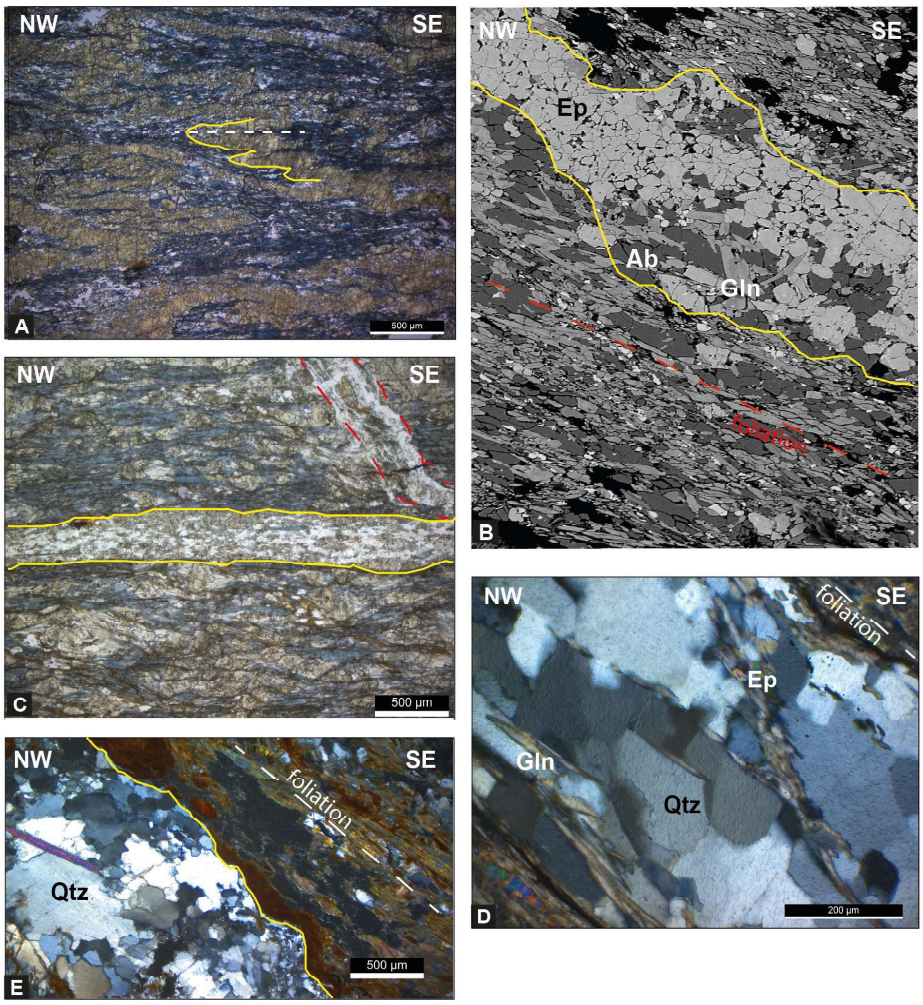

Figure 6.9: A) photomicrograph of foliation-parallel, epidote-rich veins in an epidote-blueschist matrix. In this sample, veins have a sub-mm to mm thickness and are mm-spaced. Locally, they appear folded (yellow curve) with their axial surface parallel to the foliation (white line) (plane polarised light); B) BSE image of epidote-rich vein in an epidote-blueschist matrix. The foliation-parallel vein is characterised by epidote with minor albite, quartz and glaucophane; C) photomicrograph of foliation parallel quartz-rich vein (contoured in yellow) in an epidote-blueschist matrix. Contoured in red, a quartz-rich vein crosscutting the foliation (plane polarised light). D) photomicrograph of of quartz-rich vein in an epidote-blueschist matrix. They are characterised by quartz, epidote and minor glaucophane. Quartz is ductilely deformed, with undulose extinction and irregular boundaries (cross polarised light); E) photomicrograph of quartz-rich vein in micaschists. Quartz grains are ductilely deformed, presenting undulose extinction, irregular boundaries and subgrains (cross polarised light).

grains are larger, with size up to 150 µm (mean 26 µm) and aspect ratios varying from 1 to 5 (Fig. 6.10B,C). Finally, albite grains show a similar size and shape distribution as the epidote grains, with size up to 150 µm (mean 22 µm) and aspect ratios ranging 1 to 6 (Fig. 6.10D,E). Even though most of the highest aspect ratio grains are aligned along the stretching lineation, there is significant scattering of long axis orientation, where the majority of the grains are not aligned to the stretching lineation, suggesting that the greenschist blocks do not have a shape preferred orientation (SPO) that is as well developed as the epidote-blueschist matrix analysed in the previous chapter.

EBSD analyses show that foliation-forming actinolite has generally low misorientation angles (0°-6°), with the highest misorientation angles being very localized where the actinolite grains are edged between grains of either epidote or albite (Fig. 6.11A). The pattern of misorientations does not suggest high degrees of crystal plasticity, a misorientation profile on an actinolite grain oriented with lineation shows that within the crystal misorientations are negligible and consistent through the entire length of the crystal (Fig. 6.12). LPO patterns are well defined, with poles to (100) subnormal to lineation and <001> axes aligned with lineation.

EBSD analyses on epidote show some similarities with the range and pattern of misorientations in actinolite, but different LPO patterns. In epidote, misorientation angles are low (0°-6°) with the highest misorientations very localized to a few spots, generally along fractures, which would imply only minor crystal plasticity. LPO patterns show significant scattering of <001>axes along lineation and a random distribution of poles to (100) (Fig. 6.11B). Albite shows even lower misorientation angles than actinolite and epidote (0°-4°), indicating almost no crystal plasticity and the LPO patterns have a random distribution (Fig. 6.11C).

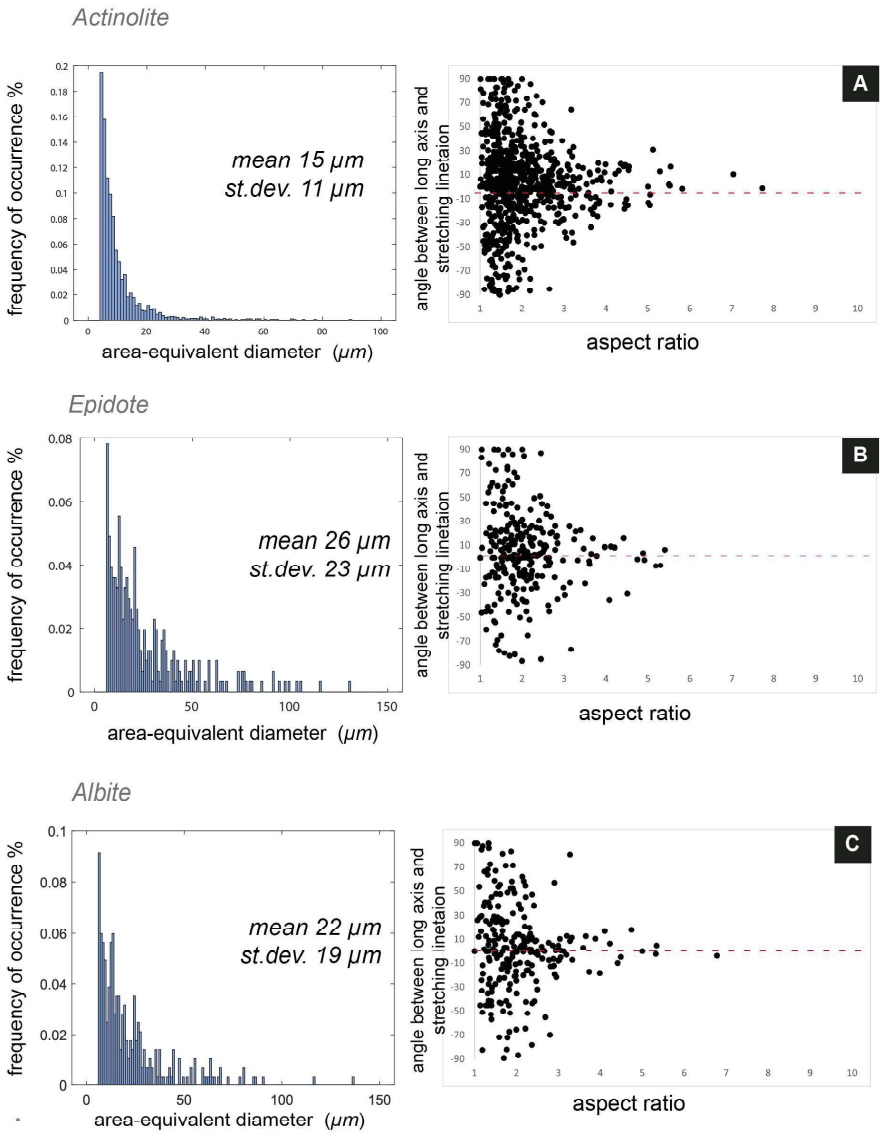

Figure 6.10: Point per grain analysis of foliation-forming minerals. A) grain size histogram based on equivalent diameter of amphibole grains. B) diagram representing shape preferred orientation of amphibole. C) grain size histogram based on equivalent diameter of epidote grains. D) diagram representing shape preferred orientation of epidote. E) grain size histogram based on equivalent diameter of albite grains. F) diagram representing shape preferred orientation of albite.

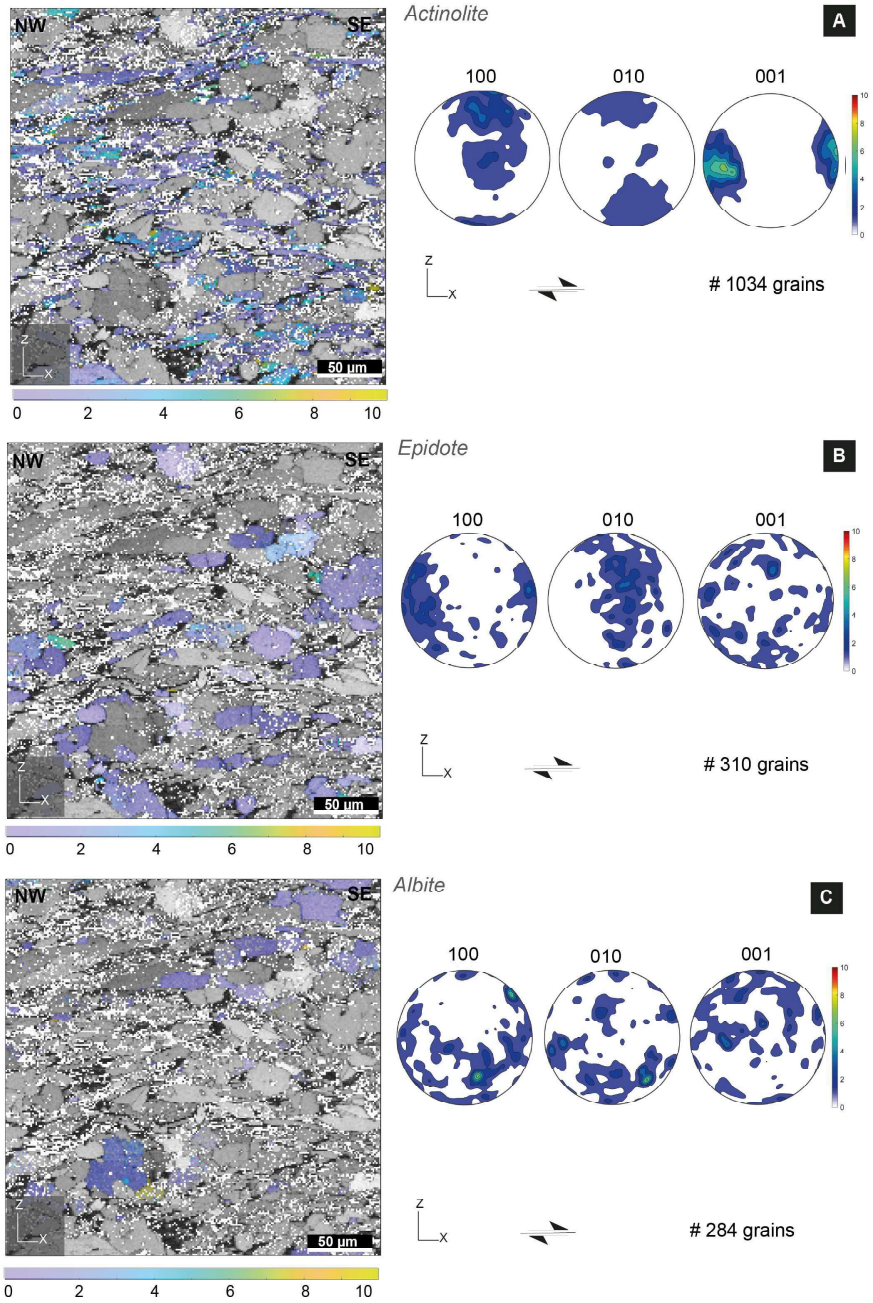

Figure 6.11: A) Misorientation map (coloured grains represent amphibole) and LPO contours for amphibole. Point per grain analysis, lower hemisphere projection. B) Misorientation map (coloured grains represent epidote) and LPO for epidote. Point per grain analysis, lower hemisphere projection. C) Misorientation map (coloured grains represent albite) and LPO contours for albite. Point per grain analysis, lower hemisphere projection.

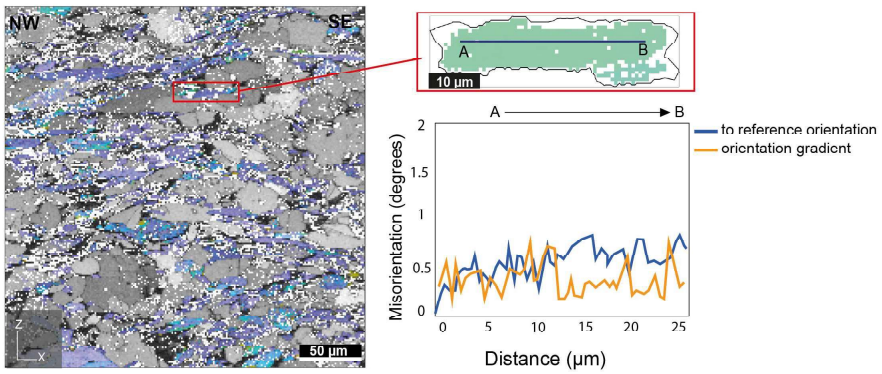

Figure 6.12: Misorientation profile of actinolite in Tomuru greenschist. The profile shows low and consistent values of misorientation from point A to B across the crystal length.

6.4 Metabasite characterisation

Whole-rock XRF analyses of major and trace elements (Table 6.2) were carried on both blocks and matrices of the Tomuru metabasites. Immobile elements have been used to classify these rocks as with low-grade high-pressure metamorphism, element mobility can be a considerable problem and lead to misclassification (Pearce, 1996).

Zr/Ti against Nb/Y plot is used to classify rocks by their alkalinity and stage of differentiation (Winchester and Floyd, 1977; Pearce, 1996). In this diagram all the metabasites analysed, both epidote-blueschist and greenschist facies samples, and from all the three outcrops of Tomuru, Yasura-zaki and Urasaki, plot on the basalt field (Fig. 6.13A). They have a similar Zr/Ti ratio, relatively close to the andesite and basaltic andesite field, which indicates they a have similar differentiation stage, while the Nb/Y ratio is wider, indicating they vary slightly in degree of alkalinity.

To discriminate between tectonic environments, basalt compositions were plotted on a V-Ti plot (Shervais, 1982) to distinguish between IAB (island arc basalts), MORB (mid-ocean ridge basalts) or OIB (ocean island basalts). All samples plotted on the MORB field, indicating that all these rocks were generated in the same tectonic environment (Fig. 6.13B). To further investigate the characteristics of

epidote-blueschist facies and greenschist facies rocks, spider diagrams were plotted based on trace elements detected by XRF. Normalised to N-MORB, both green amphibolite rocks and blueschist blocks show a similar multi-element patter, with a relatively high enrichment in Th and a flat pattern of the other trace elements, almost close to 1:1 ratio (Fig. 6.13C,D). The isocon plot (Fig. 6.13E) shows that there is limited mobility between greenschist and epidote-blueschists, as most of the oxides shown are close to the 1:1 ratio line.

Table 6.4: XRF analyses of greeenschist and epidote-blueschists.

	IS-02	IS-03	IS-05	IS-06	IS-10	IS-17	IS-18	IS-19	IS-20	IS-25	IS-26	IS-28	IS-32
Major elements (wt. %)													
SiO2	50.44	49.79	46.68	48.63	47.63	52.33	51.25	51.64	48.00	46.22	56.97	48.88	50.03
TiO2	1.80	1.84	1.77	1.89	2.07	1.24	1.38	1.36	1.65	2.15	1.60	1.63	1.84
Al2O3	16.05	16.08	16.01	15.97	14.90	14.60	14.54	14.78	15.14	13.96	12.56	14.03	15.99
Fe2O3	11.51	11.67	11.42	11.53	14.31	11.17	12.16	11.88	13.61	15.76	11.16	12.70	11.84
MnO	0.10	0.14	0.17	0.16	0.28	0.18	0.21	0.17	0.20	0.19	0.15	0.19	0.11
MgO	3.85	3.42	6.51	3.27	4.38	2.20	3.33	3.01	4.12	4.56	2.10	5.56	4.08
CaO	7.91	11.16	9.01	9.78	9.62	15.38	11.24	10.87	11.27	11.49	13.03	11.79	7.81
Na2O	4.48	4.33	3.01	4.31	1.35	1.06	3.79	3.73	3.48	2.67	1.36	2.64	4.16
K2O	1.50	0.39	1.14	0.44	0.73	0.01	0.12	0.27	0.42	1.02	0.02	0.23	1.77
P2O5	0.26	0.37	0.21	0.27	0.17	0.15	0.20	0.10	0.19	0.22	0.24	0.19	0.27
SO3	<0.01	<0.01	<0.01	<0.01	<0.01	<0.01	<0.01	<0.01	<0.01	<0.01	<0.01	<0.01	<0.01
Cr2O3	0.04	0.05	0.04	0.04	0.01	0.04	0.04	0.04	0.04	0.01	0.01	0.02	0.06
NiO	0.02	0.04	0.02	0.02	0.01	0.04	0.03	0.02	0.03	0.01	0.01	0.01	0.15
H2O-	0.17	0.04	0.24	0.92	0.44	0.20	0.51	0.67	0.28	0.04	0.05	0.03	0.34
LOI	1.51	1.05	2.89	1.74	3.75	1.23	1.37	1.27	1.74	1.42	0.86	1.65	1.79
Sum	99.61	100.33	99.09	98.93	99.64	99.78	100.16	99.79	100.14	99.70	100.10	99.52	100.21
Trace elements (ppm)													
Zn	103	106	99	91	134	66	98	79	106	140	65	101	124
Cu	38	45	54	55	89	37	50	50	54	24	28	30	46
Ni	104	89	118	109	67	130	169	153	179	62	34	60	96
Mo	<5	<5	<5	<5	<5	<5	<5	<5	<5	<5	<5	<5	<5
Nb	3	5	4	4	3	<3	<3	<3	<3	<3	<3	<3	4
Zr	125	124	126	130	138	89	107	109	123	143	98	94	130
Y	36	44	41	44	46	41	43	41	46	51	42	46	38
Sr	116	168	123	145	206	178	152	165	146	118	217	120	118
Rb	41	17	31	17	38	9	11	14	20	31	9	14	48
U	<5	<5	<5	<5	<5	<5	<5	<5	<5	<5	<5	<5	<5
Th	7	8	8	7	7	9	9	8	8	7	7	7	6
Pb	<3	3	<3	<3	3	<3	4	<3	<3	3	<3	3	<3
Co	43	48	47	44	55	43	58	56	59	58	21	47	45
Mn	807	1135	1421	1241	2430	1671	1711	1350	1611	1513	1147	1589	804
Cr	307	317	327	300	109	242	303	302	351	72	43	121	322
V	318	295	300	303	394	379	335	340	355	465	378	362	340
F	659	666	712	617	956	607	693	599	707	769	652	752	674
S	38	48	8	87	175	94	176	82	91	19	23	17	127
Cl	635	244	302	836	1141	709	1123	986	740	115	93	176	877
Sc	30	30	33	32	40	32	38	33	37	38	33	43	30
Ba	195	128	171	148	168	63	99	113	144	154	86	96	227

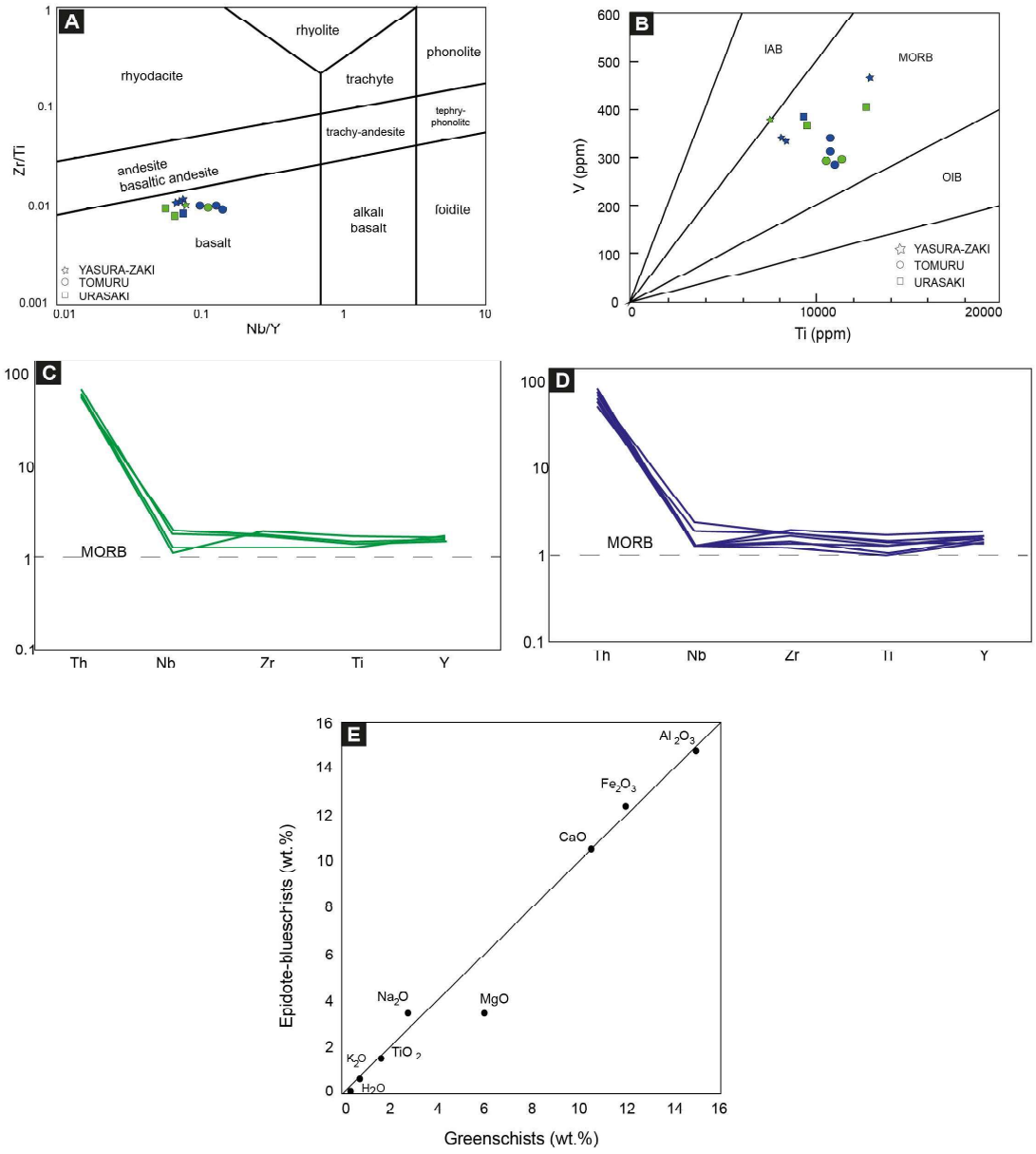

Figure 6.13: Metabasite characterisation diagrams. Blue indices represent blueschist rocks, green indices represent greenschist rocks. A) Zr/Ti vs Nb/Y discrimination diagram. B) V – Ti discrimination diagram. C) Trace element spider diagram for greenschist rocks. Normalisation to N-MORB composition. D) Trace element spider diagram for epidote-blueschist rocks normalised to N-MORB composition; E) Isocon plot with element distribution between greenschists and epidote-blueschists. Black line indicates the 1:1 ratio between oxides.

6.5 Shear stress calculation

Ductilely deformed quartz veins are present both in the metasediments and in the metabasites. In the metabasites, their geometry, parallel to the main foliation, along with the presence of glaucophane suggests that veins formed at the same condition at the glaucophane-rich foliation. As quartz deformed by dislocation creep, the vein microstructure should reflect the stress conditions during deformation, and ultimately the stress conditions of deformation of metabasites during foliation development. These stresses can be considered an upper bound on the strength of metabasalts, as quartz veins are often boudinaged or show pinch-and-swell structures, which implies they are stronger that both the greenschist and epidote-blueschist host metabasites. Quartz microstructures indicate that quartz deformed by dislocation creep, likely by grain boundary migration recrystallisation, as evidenced by lobate grain boundaries and relatively large grain size (Fig. 6.14A). Using an EBSD-based method (Cross et al., 2017) (Fig. 6.13B-F) we calculated a recrystallised quartz grain size of 83 $\pm$ 48.2 µm from foliation-parallel quartz-rich veins in the metabasites (Fig. 6.14F). Quartz grains were separated in relict and recrystallised based on the grain orientation spread (GOS) threshold value (Fig. 6.14D). Grain size of both recrystallised and relict grains (Fig. 6.14E) was obtained from the GOS based grain segmentation. Finally, the mean recrystallised grain size (RMS, Fig. 6.14E) is used to obtain differential stress values through the piezometer from Cross et al. (2017), which range from 19 to 48 MPa, indicating shear stress values of 11-28 MPa, calculated following (Behr and Platt, 2014). It was not possible to use this method on quartz veins in the metasediments, as quartz grains were pinned by numerous grains of albite, therefore unsuitable for piezometry.

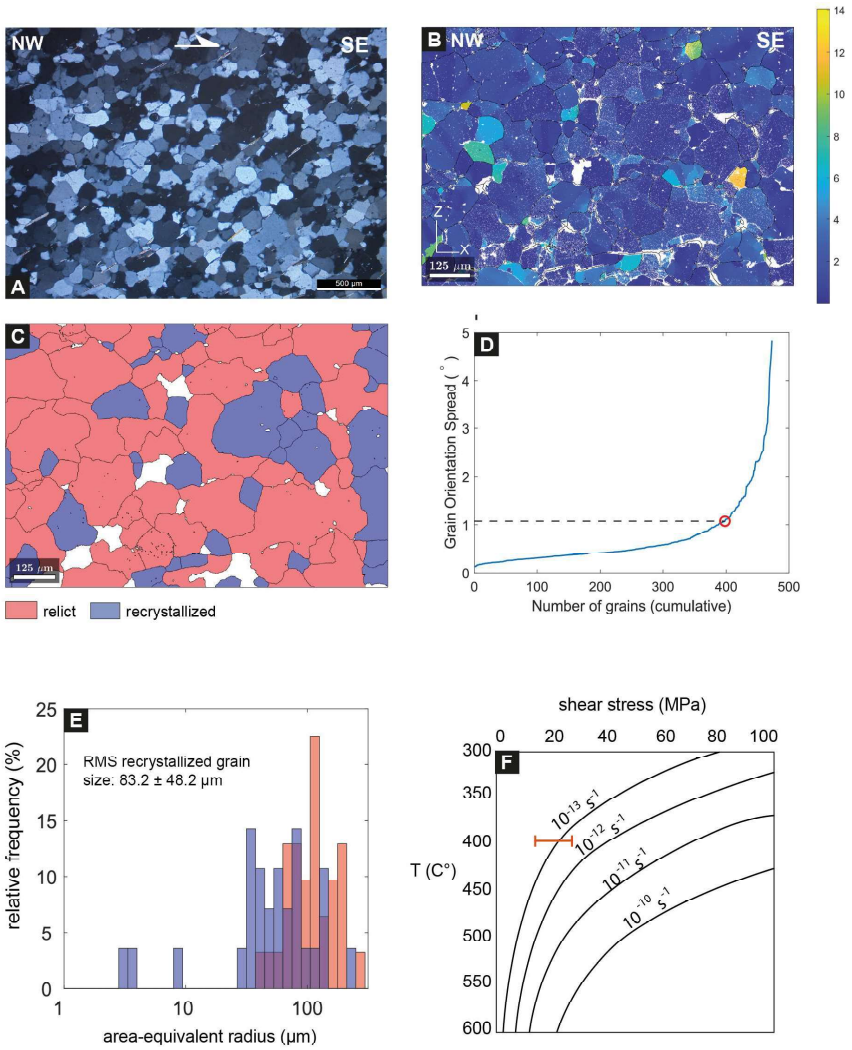

Figure 6.14: A) Cross-polarised photomicrograph of quartz microstructure from a quartz-rich vein sample in the metabasites. Quartz grains show irregular boundaries, locally lobate, with undulose extinction; B) Grain orientation spread (GOS) map of quartz grains; C) grain map showing relict (red) and recrystallised (blue) quartz grains. The difference between the two was based on the knee of the curve that correlates the GOS to the number of grains analysed; D) curve relating number of grains analysed with the GOS. The knee of the curve (red circle) represents the orientation threshold used to separate relict from recrystallised grains; E) Log10 grain size histogram of quartz grains, separated in relict (red) and recrystallised (blue). F) T-shear stress diagram showing strain rate curves from Hirt et al. (2001) flow law. In red, the values of shear stress analysed in our samples, which correspond to strain rate of 10^{-13} s^{-1}

6.6 Discussion

6.6.1 Metamorphic and structural history of the Tomuru block-in-matrix complex

Block-in-matrix Tomuru metabasites are characterised by the coexistence of greenschist and epidote-blueschist rocks, based on the different mineral assemblage defining two distinct metamorphic facies (Maruyama, 1986; Evans, 1990) (Fig. 6.1). Greenschist rocks contain a stable mineral association of Ca-rich amphibole (actinolite-winchite) + chlorite + epidote + albite and minor muscovite and titanite, whereas epidote-blueschist rocks are characterised by sodic amphibole (glaucophane – magnesioriebeckite) + epidote + albite and minor muscovite and titanite. Both the greenschist and epidote-blueschist elements of the block-in-matrix have prograde foliations and lack retrograde overprint. This is evident in the zonation of amphiboles in the greenschists and epidote-blueschists (Fig. 6.15B), where there is systematic enriching in Na and Al from the core to the rims (actinolite to winchite composition in the greenschists, and winchite to glaucophane/magnesioriebeckite composition in the epidote-blueschists). This pattern has been interpreted as evolution of amphibole composition during progressive HP metamorphism (Maruyama et al., 1986; Otsuki and Banno, 1990). The block-in-matrix association therefore registers prograde metamorphism from greenschist facies to epidote-blueschist facies. As the grains with prograde compositional zoning are systematically aligned along foliation and lineation, prograde metamorphism that guides greenschist to epidote-blueschist facies evolution is coeval with foliation formation and, consequently, with deformation on the subduction interface, as the orientation of the main foliation in the metabasites, NW-SE striking, with top-to-SE sense of shear indicators, is coherent with deformation during NW-verging subduction of the Philippean Sea Plate (See also Chapter 5).

During subduction, the structural evolution of the block-in-matrix metabasites is characterized by combined ductile and brittle deformation. Ductile deformation leads to the development of the penetrative NW-SE striking foliation contained both in the metabasites and micaschists, and the NW-SE trending stretching lineation (Section 3.1, Fig. 3.1). Ductile deformation is accompanied by vein formation, epidote-rich veins geometry, either parallel to the foliation or forming intrafolial folds, suggests that they formed at the time of foliation development during subduction-related deformation. Quartz-rich veins geometry, parallel to foliation in both the greenschist blocks and the epidote blueschist matrix, and their mineral assemblage, with glaucophane grains, indicates that they formed during subduction-related deformation, and therefore they are likely coeval to the epidote-rich veins (Fig. 6.14D). They are in fact found in the neck of greenschist blocks and parallel to foliation in the epidote-blueschist matrix and locally contain glaucophane grains (See Section 6.3.2, Fig. 6.9). There is no sufficient data presently to interpret the origin of silica-saturated fluids that form quartz-rich veins in the metabasites.

The degree of stratal disruption involved in forming the structure of Tomuru block-in-matrix metabasites is unclear, as the Tomuru block-in-matrix is a highly fragmented body, although it cannot be excluded that at least some parts of the structural heterogeneity observed derives from inherited structures. In fact in Tomuru some greenschist blocks texture resembles the morphology of pillow lavas embedded by a fine grained matrix (Section 6.3.1, Fig. 6.3B).

Given the parallelism of foliation in the micaschists and metabasites, that the contact between the micaschists and the metasediments is parallel to the internal foliation of both lithological units, and that both present foliation-parallel quartz-rich veins, the coupling of metabasites and metasediments is interpreted to happen during subduction (Fig. 6.15D). The two rock units would then likely be exhumed

together, as suggested by Osozawa and Wakabayashi, 2012, through large scale open folding (Fig. 6.15E).

6.6.2 Deformation mechanisms active in the Tomuru greenschist blocks

Deformation mechanisms active in epidote-blueschist blocks and matrix of the Tomuru metabasalts have been described in depth in Chapter 5, therefore, here we describe the deformation mechanisms active in greenschist blocks only.

Microstructure and fabric analyses on foliated greenschist blocks show that these rocks are characterised by a finely spaced foliation defined by more or less interconnected layers of actinolite and minor chlorite separating epidote and albite grains. Actinolite is characterised by relatively well-defined SPO and well-defined LPO, with <001> axes parallel to lineation and poles to (100) parallel to foliation. Differently, epidote and albite fabrics show a poorly defined SPO and weak LPO, where the grains have <001> axes poorly aligned with the lineation and poles to (100) and (010) in a random distribution. Consequently, most of the strain partitioning linked to foliation formation is related to actinolite.

Misorientation maps reveal that for the three minerals, internal plasticity is limited. Actinolite shows higher misorientations (6° - 8°) mostly when edged between larger grains of epidote or albite. The very low intracrystalline misorientations, along with the absence of clear evidence for dislocation creep in the microstructure, suggest that actinolite deforms by diffusive mass transfer. The geometry of zoning, with compositional variations from Ca-rich cores to Na-rich rims parallel to lineation lacks evidence of truncation, therefore it is not clear whether pressure solution creep contributed to actinolite deformation. Epidote grains have generally low internal misorientations, with the highest values (6°-10°) corresponding to crystal fractures and, only locally, areas that resemble subgrains, suggesting that

epidote grains deform mainly by cataclasis and passive grain rotation, possibly with some incipient dislocation creep. Finally, albite microstructure show very little intragrain misorientations and random LPO, which indicates that crystal plasticity is not effective as deformation mechanism in albite and that it likely deforms by diffusive mass transfer (e.g., Rybacki and Dresen, 2004).

Distributed deformation by diffusive mass transfer governs rheology of the Tomuru greenschist metabasites. The presence of epidote-rich veins in the epidote-blueschist matrix and blocks (See Section 6.2, Fig. 6.4; see also Chapter 5) might be related to localised, fluid-assisted deformation processes within a distributed deformation regime. During metamorphism from greenschist to epidote-blueschists, discrete amounts of fluids and Ca are released in the system, due to the change in composition from actinolite-winchite to glaucophane-magnesioriebeckite. Ca-rich fluids would then likely precipitate and form epidote-rich veins (Fig. 6.15C).

6.6.3 Stress levels in the Tomuru block-in-matrix metabasites

In the Tomuru metabasites, at 400 ℃, shear stress ranges 11 – 28 MPa, these values were compared to quartz rheology curves from Hirth et al. (2001) and indicate strain rate of $\sim 10^{-13}\ s^{-1}$ (Fig. 6.14E). These values are similar to the average bulk strain rate estimates for large-scale shear zones (Fagereng and Biggs, 2019). At same strain rate conditions, flow laws for dry basalt (Mackwell et al., 1998) require high temperatures for rocks to deform at shear stresses of less than 200 MPa. The estimations on quartz strength in veins deformed within Tomuru metabasalts suggest that deformation happened at shear stresses one order of magnitude lower, to values that are similar to those implied for subduction interfaces worldwide (Duarte et al., 2015), suggesting that metabasites at epidote-blueschist conditions can accomodate megathrust deformation at geological strain rates. The presence

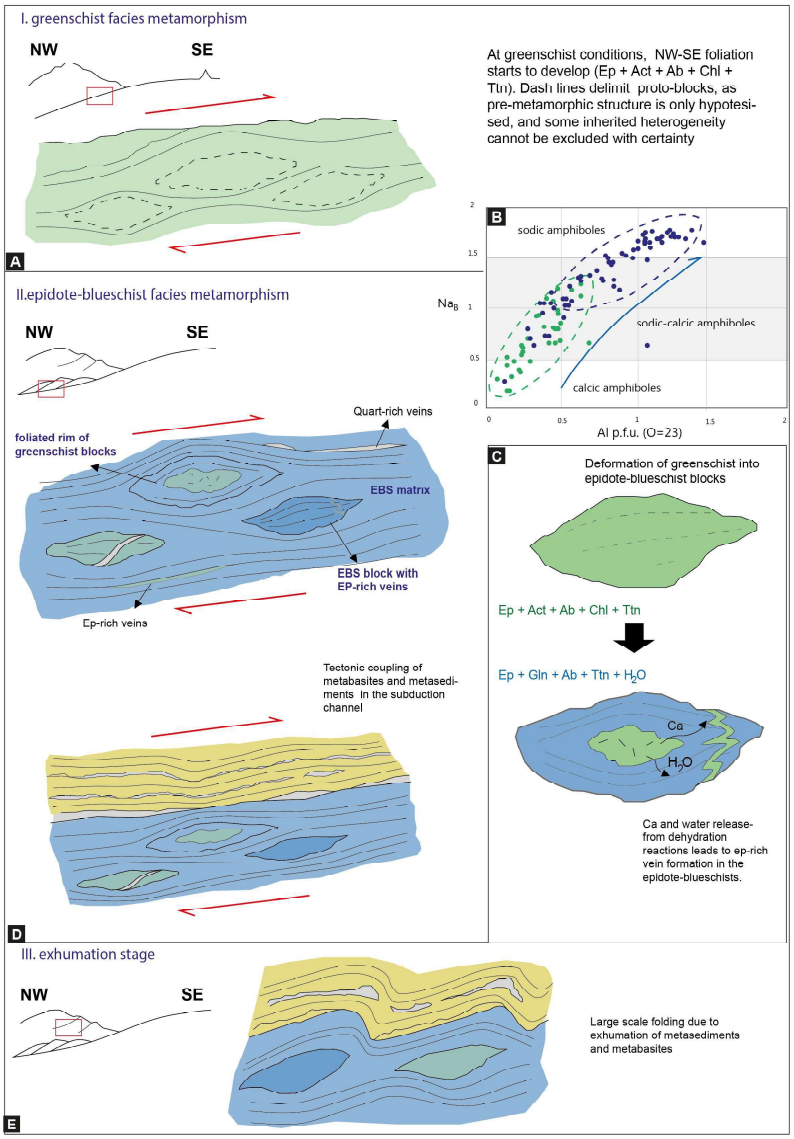

Figure 6.15: Deformation cartoon of Tomuru metabasites. A) During a first stage of subduction, metabasites would go through greenschist metamorphic condition and develop a greenschist-facies foliation; B) Diagram showing the progressive enrichment in Na and Al2O3 in amphiboles from the greenschist rocks to the epidote-blueschists; C) interpretation of the deformation processes of greenschists into epidote-blueschists, with formation of epidote-rich veins ; D) interpreted structure of the Tomuru block-in-matrix metabasites during subduction at epidote-blueschist conditions. The coupling with metasediments happened at this stage as evidenced by presence of foliation-parallel quartz veins; E) coupled metasediments and metabasites are exhumed together (Osozawa and Wakabayashi, 2012) through large scale folding

of interconnected layers of amphibole and, likely, fluid saturated conditions during dehydration of greenschists into epidote-blueschists, promoted deformation by diffusive mass transfer while also accommodating ductile deformation at low shear stress. Low shear stress conditions for creep in metabasites has also been reported in other subduction-contexts (Tulley et al., 2020), although at different T-P conditions and in rocks with abundant interconnected layers of phyllosilicates, which are not abundant in the Tomuru rocks.

6.6.4 Heterogeneity during prograde metamorphism

The structure of the Tomuru block-in-matrix metabasites shows the progressive evolution from greenschist to epidote-blueschist facies, accompanied by deformation by diffusive mass transfer of blocks and matrix during deformation on the subduction megathrust. Given this metamorphic and structural history, is it interesting to understand what factors contribute to the metamorphic and structural heterogeneity that we observe on the field, considering that previous literature concerning epidote-blueschist and greenschist coexistence in subduction terrains observes deformation in retrograde settings, where fluid deriving from an external source selectively infiltrates the blueschists, causing retrogression into greenschist assemblages (Barrientos and Selverstone, 1993; Baziotis and Mposkos, 2011).

In Ishigaki, greenschists and epidote-blueschists closely coexist in the field, with both elements appearing in the same outcrops, embedded by the matrix. The two metamorphic associations have both major and trace element compositions indicating that they derive from the same protolith of N-MORB composition, meaning that they must have been generated in a mid-ocean ridge from a primitive asthenospheric source (e.g., Pearce, 1996; Sun and McDonough, 1989). Ti/V ratio can be used to define the possible tectonic setting of the protoliths of metabasites, and Tomuru metabasites show ratios varying from 24 to 37 following the diagram

of Shervais (1982), once again confirming MORB affinity (Fig. 6.13). Moreover, the geochemical mobility between greenschists and epidote-blueschists is limited, therefore, the causes of this metamorphic association cannot be related to difference in bulk chemistry composition.

A possible explanation can be related to diffusion reaction kinetics, as there is progressive metamorphic evolution from greenschist to epidote-blueschists, both deforming by bulk diffusive mass transfer. As deformation has a catalytic effect on reaction kinetics, technically equilibrium can be reached during high strain deformation (Yund and Tullis, 1980; Ridley and Dixon, 1984), but when reaction rate is low compared to the rate of change of the physical conditions of metamorphism, low rates result in incomplete reactions and disequilibrium (Loomis, 1976, Koons et al., 1987), with relict phases in the rock microstructure. In the Tomuru block-in-matrix, the presence of both complete reactions in some areas,, where the elements are equilibrated under the same peak metamorphic assemblage (i.e., epidote-blueschist blocks with the same metamorphic assemblages as the matrix), and areas where reactions appear incomplete, where relicts are present (i.e., blocks preserving greenschist metamorphic assemblages only in the core, and have rims with the same mineralogy and fabric of epidote-blueschist matrix) can be guided by different reaction kinetics.

Grain size affects reaction kinetics by speeding up reactions when grain size is small, so that diffusive mass transfer is more effective. Grain size difference is relatively important in the Tomuru rocks, as some of the greenschist blocks are massive or have a large grain size (See Section 6.3.1), some resembling pillow lavas. However, most of the blocks have grain size comparable to the matrix, therefore grain size alone is not satisfactory in justifying the presence of disequilibrium products. Reaction kinetics that lead to the incomplete metamorphization of greenschist rocks into epidote-blueschists are likely the result of the complex in-

terplay of grain size with strain and fluid content, as described in literature (e.g., Tullis and Yund, 1980; White and Knipe, 1978; Yund and Tullis, 1980).

Tomuru metabasites show difference in fabric development, with progressive strain localisation from the core of the blocks, massive or relatively foliated, to the rims, well-foliated with similar fabric and mineralogy to the epidote-blueschists matrix (Fig. 6.15B,C). Difference in strain have also been documented between epidote-blueschist blocks and matrix (See Chapter 5). Therefore, the matrix has higher strain conditions than both greenschist and epidote-blueschist blocks. High strain and relatively small grain sizes maintain reaction rates high, promoting strain localisation during progressive metamorphism (e.g., White, 1975). Strain localization in the matrix likely happens by geometric softening during diffusive mass transfer, by forming well-interconnected layers of glaucophane grains, which are well-aligned with the foliation and lineation, and where metamorphic reactions aid strain softening by forming relatively strain-free new phases and by increasing diffusion rates during reaction (e.g., White et al., 1980).

Finally, fluids deriving from prograde dehydration reactions complete the deformation context of these rocks. They promote deformation by diffusive mass transfer and enhance rate of reactions, which in turn allows to concentrate deformation and allow shear zone development (Ridley and Dixon, 1984; White and Knipe, 1978).

In the case of Tomuru block-in-matrix, the prograde metamorphic association is preserved and does not get obliterated by subsequent exhumation stages. Previous literature indicates that exhumation of epidote-blueschists in Ishigaki was guided by strike slip faults (Osozawa and Wakabayashi, 2013), however the authors do do not specify how the Tomuru block-in-matrix prograde deforamtion could survive exhumation. Previous literature on greenschist-blueschist coexistence offers some options as to how blueschists can be preserved. Some state that in order for

their coexistence to be preserved, the rocks have to go through the same P-T path during retrogression as their prograde one (Ernst, 1988); other suggest that blueschists preservation without thermal overprint is plausible when exhumation is rapid (Peacock, 1992). Finally, some authors suggest that blueschists mineral assemblages are not necessarily easily destroyed by thermal overprinting, but they are easily altered by infiltration overprinting (Barrientos and Selverstone, 1993; Baziotis and Mposkos, 2011), which requires fluids infiltrating blueschist rocks and causing more or less localised retrogression to greenschist assemblages. These authors suggest therefore that in the absence of external aqueous fluids, blueschists can be preserved even through exhumation.

6.6.5 Implications for rheology during deformation on the subduction megathrust

In the Tomuru block-in-matrix metabasites, deformation on the subduction interface is accommodated by combined ductile and brittle deformation. Ductile deformation fabrics (i.e., foliation and lineation) are predominant over brittle deformation fabrics (i.e., fractures, veins), as evidenced by the relatively contained presence of veins, thus suggesting that at the depth where epidote-blueschists are stable, block-in-matrix bulk rheology is governed mostly by distributed viscous deformation within blocks and matrix, with localised areas of fluid assisted deformation, and by only minor brittle deformation.

Microstructural and fabric analyses suggest that deformation of greenschists and epidote-blueschists was guided by similar deformation mechanisms, where bulk shearing flow is accommodated by diffusive mass transfer active at low shear stresses, as measured through recrystallised quartz-vein piezometry (Section 6.5). Consequently, as previously described in Chapter 5, the viscosity contrast between blocks and matrix is relatively low, even considering the greenschist blocks. There-

fore, at the depth where epidote-blueschists are stable, the Tomuru block-in-matrix show clear metamorphic heterogeneity that likely does not translate into strong mechanical heterogeneity.

The strong predominance of distributed viscous creep in controlling bulk rheology in these rocks likely dampens the frictional failure of the more competent blocks and thus mantains block-in-matrix bulk strength relatively low. This has implications for seismicity on the subduction interface, as distributed viscous creep deformation in shear zone has been associated with stable, aseismic sliding (Condit and French, 2022). Fluids expelled by dehydration reaction could have also contributed to overpressure and hydraulic fracturing linked to the epidote-rich vein system, which can be distinctly found only in the epidote-blueschist rocks however the scale of veining is contained, therefore, it is debatable whether stress transients can be generated and consequently for tremor to propagate in the Tomuru block-in-matrix. This data suggests that Tomuru epidote-blueschists are likely to show predominantly velocity-strengthening rather than velocity-weakening behaviour, in contrast to shear experiments on lawsonite blueschists by Sawai et al. (2016).

6.7 Conclusions

Tomuru block-in-matrix metabasites (N-MORB) register prograde metamorphic evolution during deformation on the plate interface at epidote-blueschist conditions. Subduction-related deformation is accommodated by combined ductile and brittle deformation (with significantly more ductile strain), with development of NW-SE striking foliation and NW-SE trending lineation and syn-tectonic veins (epidote-rich and quartz-rich). This style of deformation is typical of exhumed subduction complexes registering deformation on the subduction megathrust (e.g., Raymond, 1984; Wakita, 2012).

The metamorphic heterogeneity between greenschist facies blocks and epidote-blueschist facies blocks and matrix is acquired during program metamorphism, and is the product of grain size, strain development and fluid flow in governing diffusion reaction kinetics. These variables influence the speed and effectiveness of reactions, causing either complete equilibration or disequilibrium in reaction products. This leads to present day structure, where and epidote-blueschist and greenschists are closely crop out in the field, the latter representing the relict product of disequilibrium. Both blocks and matrix deform by similar deformation mechanisms, where bulk rheology is governed by distributed viscous creep via diffusive mass transfer at low shear stress conditions. This suggests that the viscosity contrast between blocks and matrix is relatively low. Consequently, the Tomuru block-in-matrix do not show strong mechanical heterogeneity. This leads to the interpretation that at depth in the subduction zone, where epidote-blueschists are stable, transients leading to tremor might not easily generate when viscosity contrast is low and bulk rheology is governed by distributed diffusion mass transfer.

Chapter 7

Deformation style of retrograde blueschists from the Lento unit (Schistes Lustrés, Alpine Corsica)

Abstract

Metabasites from the Lento unit (Schistes Lustrés, Alpine Corsica) crop out as cartographic-scale blocks within a metasedimentary matrix. They register deformation stages that accompany subduction at blueschist conditions up to exhumation along the retrograde path at greenschist conditions. Metabasites consist of metabasalts and metagabbros, which have a greenschist facies foliation, but differ by fabric intensity and chlorite content. The metabasalts have a well-developed foliation defined by interconnected layers of chlorite separating grains of actinolite, epidote, albite and porphyroclasts replaced by pumpellyite. Metagabbros have a weakly developed foliation characterised by discontinuous layers of actinolite and chlorite separating more or less continuous layers of epidote and albite. Microstructural and EBSD analyses indicate that bulk rheology of metabasites during

exhumation was governed by frictional-viscous flow, with the frictional component being accommodated by cataclasis of epidote and actinolite and frictional sliding along chlorite foliae. The viscous component is accomodated by pressure solution of chlorite, albite, actinolite, and epidote with minor dislocation creep of actinolite. Fluid-driven retrograde reactions accompanying exhumation from blueschist to greenschist facies caused reaction and textural weakening, thus reducing rock strength. These mechanisms are important in limiting the stress magnitudes and enhancing strain localisation in retrograde shear zones, likely favouring fault creep in the accretionary prism.

7.1 Introduction

Phyllosilicate-rich rocks are commonly observed in faults that have been active at retrograde conditions (e.g., Collettini et al., 2019). Data on exhumed shear zones formed at depths close to the brittle-ductile transition preserve evidence of weakening mechanisms (Collettini and Holdsworth, 2004; Imber et al., 1997; Jefferies et al., 2006). An efficient mechanism that promotes weakening of shear zones and retrogression is fluid influx (Faulkner et al., 2010; Hickman et al., 1995; Sibson, 1994).

Retrogression refers to the onset of retrograde mineral reactions that destabilise metamorphic rocks after peak metamorphism as a consequence of change in tectonic regime, such as exhumation through uplifting and cooling in subduction zones and is generally restricted to discrete zones of deformation like shear zones (Etheridge and Cooper, 1981). Contrary to prograde settings, where the deforming lithologies constitute the primary fluid source (Peacock, 1990), rocks in retrograde settings do not produce local fluids, as they would have previously

dehydrated during prograde metamorphism. Consequently, for retrogressive reactions to happen, an external fluid source is necessary (e.g., Etheridge et al., 1983). In the accretionary prism, in a retrograde context, possible external fluid sources include fluids migrating upwards from the viscous lower crust of the lower plate (Kennedy et al., 1997). In this context, fluids have a direct effect on lithological changes that lead to reducing rock bulk strength. In fact, fluid-driven retrograde reactions can lead to the formation of weaker phases, like phyllosilicates such as chlorite and white mica, generally at the expense of stronger mineral phases, such as feldspars and amphibole (Imber et al., 1997; Jeffries et al., 2006; McAleer et al., 2017, Wintsch and Yeh, 2013). The mineralisation of weak phyllosilicates causes reaction and textural softening (White and Knipe, 1978; Wintsch et al., 1995), where phyllosilicates precipitate in continuous layers with systematic orientation, generally parallel to shear direction. This coupled mechanical and chemical processes considerably reduce the rock bulk strength to approach the strength of a single crystal (Shea and Kronenberg, 1993). Moreover, fluid influx contributes to increased fluid pressure, which has been linked to fault strength and stability (e.g., Blanpied et al., 1991; Hubbert and Rubey, 1959; Segall and Rice, 1995). Fluid overpressure and consequent and low effective normal stress have been linked to facilitating tectonic tremor, SSEs, LFE and VLFE (e.g., Ito and Obara, 2006). Fluid flow facilitates grain-size sensitive deformation mechanisms such as diffusion creep and dissolution-precipitation creep (Menegon et al., 2015; McKlay, 1977; Rutter, 1976; Stenvall et al., 2019), which contribute to maintaining fault strength low. In particular, observation on microstructures from retrograde shear zones and experimental data identify microstructures typical of frictional-viscous flow (sensu Bos and Spiers, 2002), where frictional and viscous mechanisms occur together. Viscous flow is accommodated by a fine grained mylonitic matrix, rich in anastomosing network of phyllosilicates surrounding more rigid microlithons, commonly

consisting of stronger minerals (Bos and Spiers, 2002; Fagereng and den Hartog, 2017). Deformation mechanisms supporting viscous flow in the matrix have been recognised as coupled pressure solution and frictional sliding on phyllosilicate foliae (Bos and Spiers, 2002; Niemeijer and Spiers, 2005). The effective strength of rocks deforming by frictional viscous flow is therefore controlled by phyllosilicate frictional strength and dissolution-precipitation rates, hence by normal stress, pore fluid pressure, grain size, composition, strain rate and orientation of sliding surfaces (Bos and Spiers, 2002; Niemeijer and Spiers, 2005).
Laboratory measurements on phyllosilicates (e.g., micas and clay) and phyllosilicate-rich rocks are considered to be frictionally weak, with coefficient of friction generally $\mu < 0.4$, chlorite in particular exhibits coefficients of frictions ranging from 0.25 -0.6 (Morrow et al., 2000; Moore and Lockner, 2004; Ikari et al., 2011). Conversely, most other minerals, such as framework and chain silicates are frictionally strong, with $\mu = 0.6 - 0.85$ (Byerlee, 1968; Blanpied et al., 1995).

Phyllosilicate-rich shear zones therefore play a dominant role in controlling fault strength and stability, as phyllosilicate growth has been proposed to cause frictional weakening and tend to promote velocity strengthening behaviour, a requirement for fault slip stability, particularly at low sliding velocities (Collettini et al., 2019; Fagereng and Ikari, 2020; Imber et al., 1997; Okamoto et al., 2019). Increase in phyllosilicate content has been linked to guiding the transition from seismogenic slip to aseismic creep, in creeping sections on the San Andreas fault (Fagereng and Diener, 2011; Holdsworth et al., 2011; Lockner et al., 2011; Moore and Rymer, 2007; Schleicher et al., 2012). Moreover, phyllosilicate minerals that form during metamorphism of hydrated oceanic crust at greenschist, blueschist and amphibolite facies conditions (Fagereng et al., 2018) deform at low shear stresses, are interpreted to produce enough weakening to reduce the bulk rock strength of the oceanic crust during subduction (Tulley et al., 2020) thus allowing subduction

at plate creep rates.

In this chapter, we aim to understand which are the deformation mechanisms active in the retrograde Lento blueschists at the larger scale, and in particular, we point attention at understanding which mechanisms guide amphibole deformation in a retrograde setting, where fluid influx, role of metamorphic reactions and stress-strain conditions can be significantly different from the prograde settings, as this particular topic can be often overlooked in literature. Moreover, we investigate how the process of textural and reaction softening can lead to strain localisation during exhumation and its effect on fault stability.

Here are reported observations on retrogressed blueschists of the Lento Unit (Schistes Lustrés, Alpine Corsica), where map-scale blocks of metabasites register deformation stages from the prograde path at blueschist conditions (T = 400 ± 50 ℃ and P = 0.80 ± 0.20 GPa, Levi et al., 2007) to exhumation within the accretionary prism at greenschist facies conditions. Through microstructural analyses we describe the deformation mechanisms that guide strain localisation during retrogression at greenschist facies, and how the strain localisation mechanisms affect the rheology of retrogressed blueschists during exhumation. Microstructural observations are limited to metabasalts and metagabbros, where S2 structures are preponderant and where there is no overprinting by later D3 and D4 structures (see Chapter 3, Section 3.2).

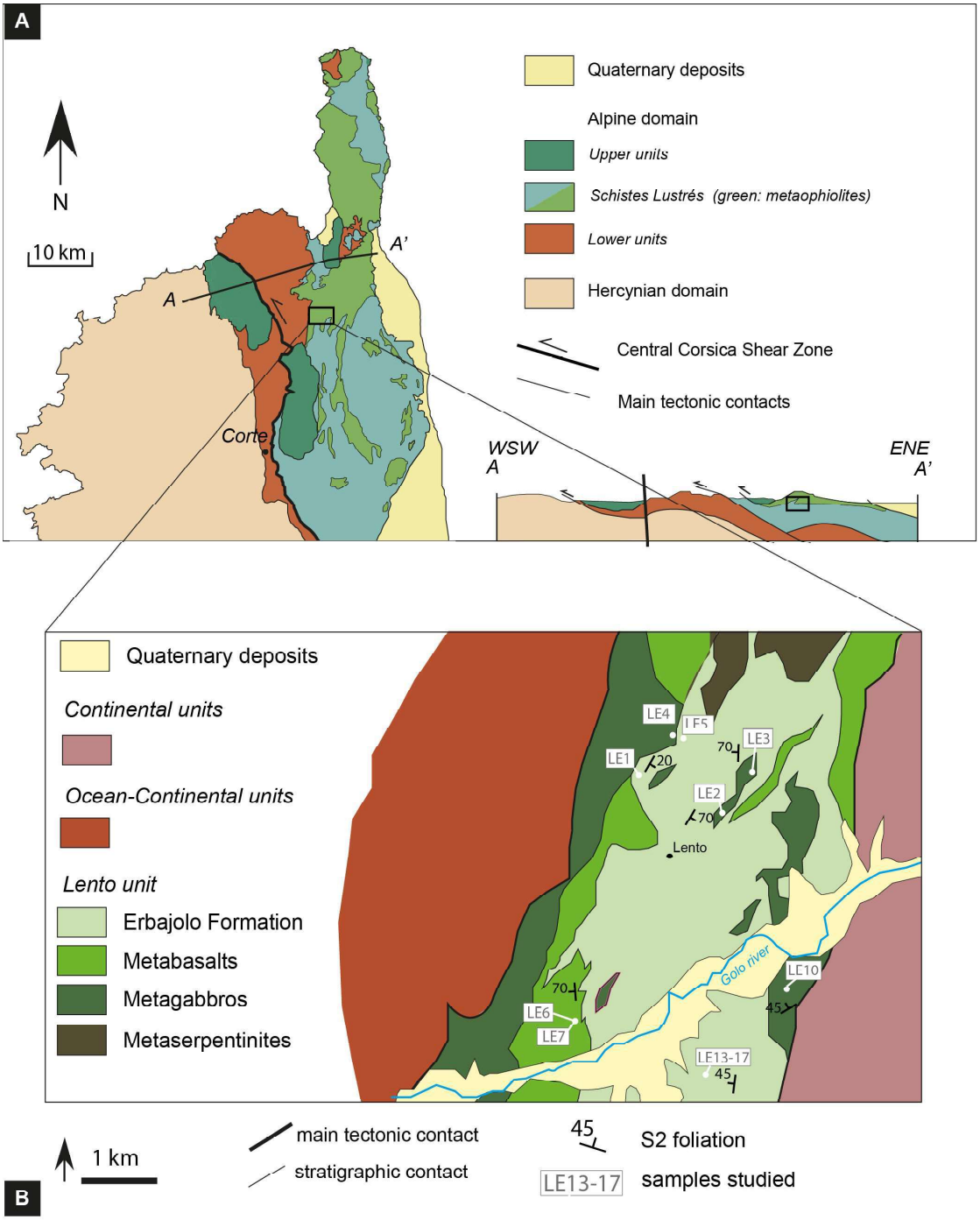

Figure 7.1: A) Tectonic setting of Alpine Corsica (modified from Brovarone et al., 2014) with detail of the Lento unit. Geologic map from Levi et al., 2007.

Table 7.1: Sample list from the Lento unit.

Sample	Name	Description
LE1	metagabbro	
LE2	metagabbro	fine-grained, poorly foliated
LE3	metagabbro	coarse-grained, poorly foliated
LE4	metagabbro	coarse-grained, poorly foliated
LE5	micaschist	well-foliated
LE6	metabasalt	fine-grained, well foliated
LE7	metabasalt	coarse-grained, foliated
LE10	metagabbro	medium-coarse grained, poorly foliated
LE13	calcschist	fine-grained, well foliated
LE14	phillitic schist	well-foliated
LE15	metabasalt	fine-grained, well foliated
LE16	metagabbro	fine-grained, poorly foliated
LE17	metabasalt	medium-coarse grained, foliated

7.2 Field observations

The Lento unit metabasites consist of metabasalts and metagabbros cropping out as lense-shaped bodies from tens of meters to km in size surrounded by the calc-micaschists of the Erbajolo Formation (Fig. 7.2A). In 3D, these bodies are elongated along NE-SW direction and dip towards NW and SE.

The metabasalts, of intense blue colour, have small grain size and are characterised by a continuous pervasive foliation, finely spaced, defined by the alignment of amphibole and chlorite (Fig. 7.2B). Locally, some green lenses are present, they are fine-grained and have an internal foliation that is parallel to the one in the rest of the metabasites. Despite the blue colour, the metabasalts are systematically retrogressed to greenschist facies rocks, in fact the main structural features are the pervasive S2 foliation, NE-SW striking with moderate to steep dips towards NW and SE, and the L2 lineation, SW-trending with gentle to moderate plunges, highlighted by the preferred alignment of amphibole and chlorite grains (Fig. 7.1E). Metabasalts are characterised by quartz-rich and calcite-rich veins, at high angle with the main foliation, which likely formed post-S2 deformation (Fig. 7.2F).

The metagabbros are coarse-grained and poorly foliated rocks, characterised by domains of plagioclase and epidote separated by discontinuous layers of amphibole and chlorite (Fig. 7.2C). Like the metabasalts, these rocks do not retain stable blueschist paragenesis and are retrogressed to greenschist facies assemblages. The discontinuous foliation is NE-SW striking with gentle to moderate dips towards SE and NW and recognised as S2. The lineation is not well defined in these rocks, and when recognisable it is characterised by the preferred alignment of amphibole and chlorite grains, it trends NW with gentle plunges (Fig. 7.2E). The schists surrounding the metabasite bodies are well-foliated rocks, characterised by a pervasive foliation where continuous layers of white mica and chlorite separate polymineralic layers of quartz, feldspar and calcite (Fig. 7.2D). The foliation,

recognised as S2, is NE-SW striking with moderate to steep dips towards NW and SE. The lineation here is defined by the preferred alignment of white mica and chlorite, NW-trending with gentle plunges.

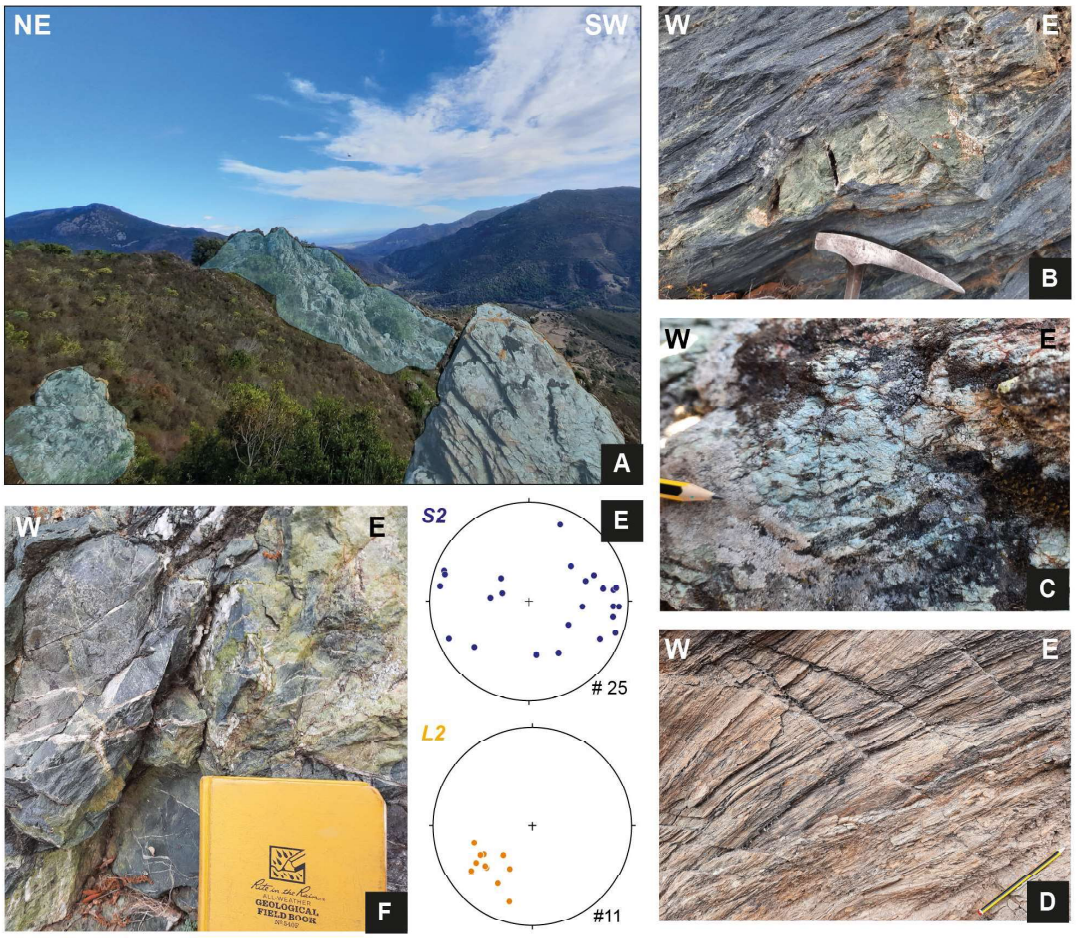

Figure 7.2: A) outcrops of metagabbro lenses, hundreds of metres in size (highlighted in blue), surrounded by the calc-micaschists of the Erbajolo Formation; B) Well-foliated fine grained blue metabasalt with green lens. Foliation is oriented NE-SW. Despite the blues colour, the metabasalts are retrogressed to greenschist facies paragenesis; C) Detail of metagabbro texture, the foliation is poorly developed, with discontinuous layers of amphibole and chlorite (dark) separating layers of epidote and albite. Foliation is oriented NE-SW; D) Calc-micaschist of the Erbajolo Formation, showing a pervasive foliation oriented NE-SW; E) Stereographic plot of S2 foliation poles and L2 lineations. Lower hemisphere, equal area projection; F) Aspect of calcite-rich veins in the metabasalt crosscutting the folation at a high angle.

7.3 Microstructure

Metabasalts are well-foliated rocks, with mm- scale layering of chlorite, actinolite and minor muscovite and titanite separating lenticular porphyroclasts extensively replaced by pumpellyite and quartz, ranging in size from hundreds of microns to 1 millimetre and, locally, grains of epidote and albite, with size up to 500 µm (Fig. 7.3A,B). Chlorite is the most abundant foliation-forming mineral, it is fine grained, with size of long axes ranging from a few microns up to 50 µm, and well-oriented along lineation and foliation, with crystal long axes parallel to shear direction. Chlorite is also present in both pumpellyite and quartz porphyroclasts and large epidote strain shadows (Fig. 7.3C,E,F) both as mineral phase and as replacement of glaucophane and muscovite along grains rims (Fig. 7.3D). Chlorite grain boundary are typically straight, however they locally are irregular (Fig. 7.3E,F). Actinolite grains range in size from 100 µm up to 300 µm, they form discontinuous layers, aligned with the foliation, or are present as isolated grains (Fig. 7.4A). Locally, actinolite grains preserve a core with Na-amphibole composition (Fig. 7.3A, Fig. 7.5), both at a high angle to the foliation or in porphyroclasts strain shadows, where the amphibole is substituted by chlorite (Fig.7.3B). In thin section, however, zoned actinolite is not commonly found in these rocks. Actinolite grains locally have undulose extinction (Fig. 7.4B) and are generally intensely fractured with fractures both parallel to- and at high angle to the grains long axes (Fig. 7.4C). Muscovite grains have a grain size similar to chlorite, up to 50 µm and form isolated, discontinuous levels often replaced by chlorite. Epidote grains have a size ranging from 100 µm to 500 µm, they are either forming isolated grains embedded in the chlorite-rich foliation, or domains with albite. They are commonly fractured, and locally show irregular grain boundaries at the edges, in the direction perpendicular to shear direction (Fig. 7.4D). Albite typically forms aggregates ranging in size from 100 µm to 500 µm. They can be asymmetrical, with top to

NW sense of shear, and present inclusions of chlorite and titanite and, locally, of pumpellyte and quartz porphyroclasts (Fig. 7.4E). Single albite crystals have size of circa 50 µm, they are not zoned and commonly show irregular grain boundaries (Fig. 7.4E). Metabasalts are characterised by abundant dissolution seams rich in clay, oriented along the foliation, close to chlorite layers, as well as at the margins of larger porphyroclasts and epidote grains (Figs. 7.3D, 7.4D). Locally, porphyroclasts asymmetry and oblique foliation are representative of a top-to-NW sense of shear (Fig. 7.4F). The paragenesis of the foliation, with chlorite, actinolite and minor muscovite, and the observed sense of shear indicators, allow to interpret it as S2 foliation (e.g., Levi et al., 2007). There is no microstructural evidence of an earlier S1 foliation in the metabasalts.

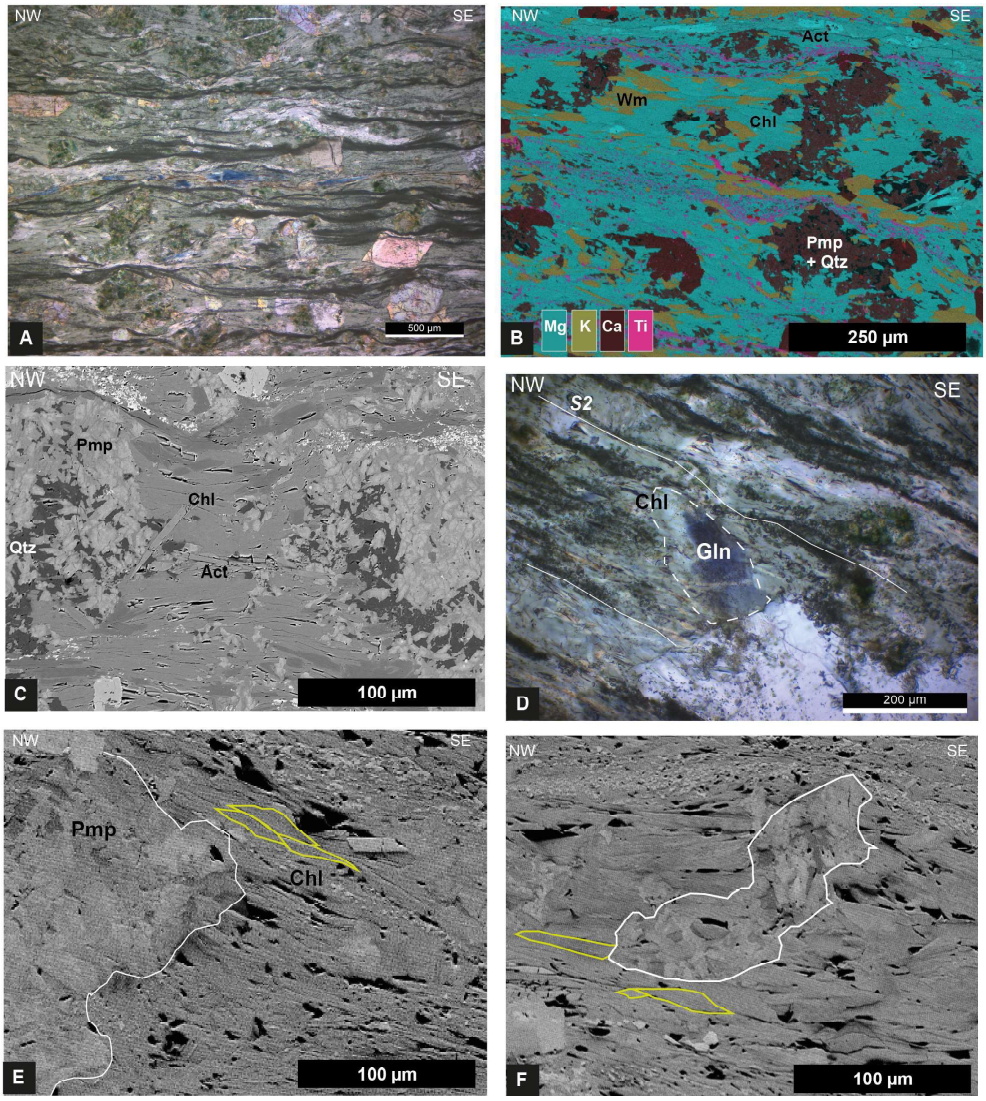

Figure 7.3: A) microphotograph of metabasalt. Continuous layers of chlorite and actinolite separate larger grains of epidote and polycrystalline porphyroclasts of pumpellyite, quartz and chlorite; B) EDS map of the foliation; C) BSE image detail of porphyroclast with chlorite-rich and actinolite strain shadows; D) photomicrograph of glaucophane grain (blue) preserved as it is replaced by chlorite at the rim. Note how it is at a high angle to the chlorite-rich foliation S2; E) FSE image of chlorite grains close to the top of pumpellyte-rich porphyroclasts. The grain boundaries are irregular; F) FSE image of chlorite grains in pumpellyte-rich porphyroclasts. Chlorite grains have both straight boundaries and irregular boundaries

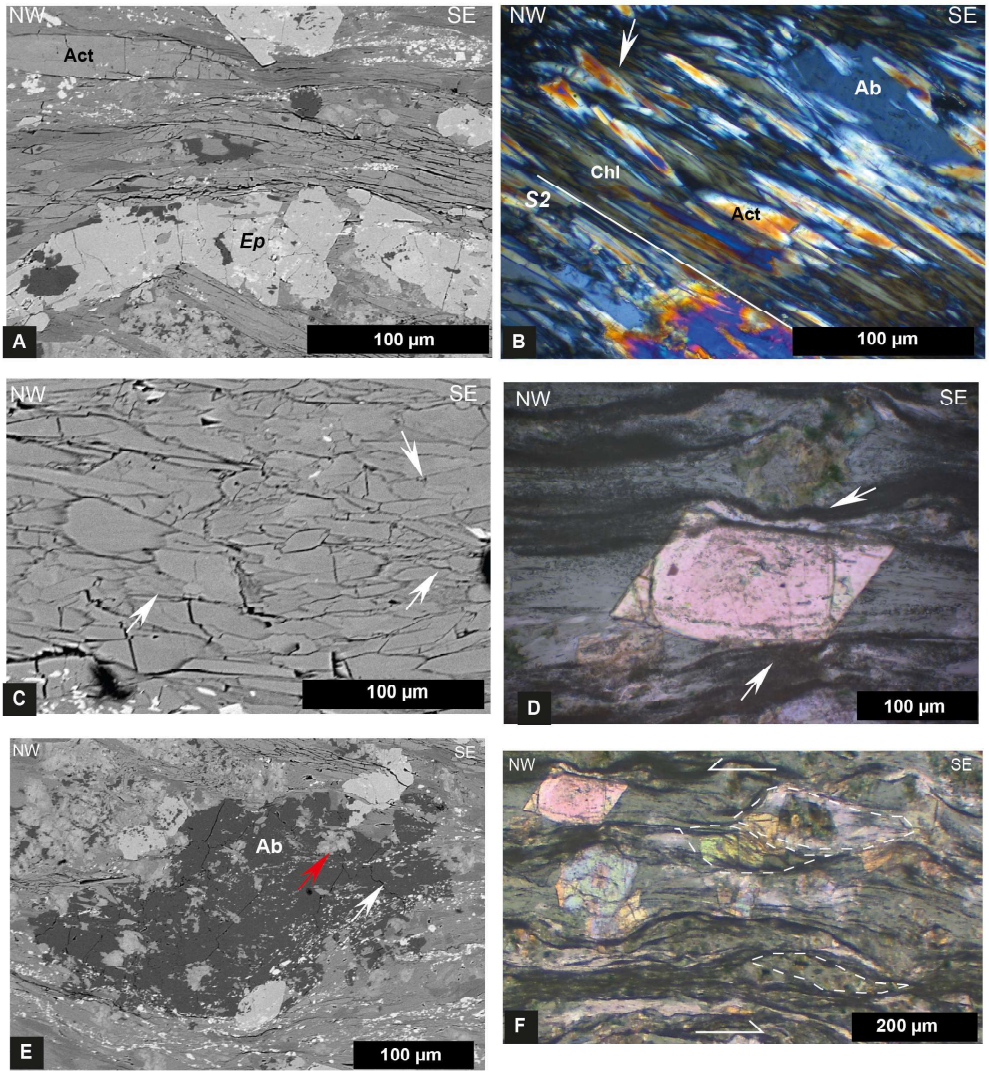

Figure 7.4: A) BSE image of large actinolite grains showing both fractures at a high angle to the grain long axis and at low angle to the long axis. Large grains of epidote are fractured; B) photomicrograph of ctinolite and chlorite grain aligned along the foliation. White arrow indicates actinolite undulose extinction (cross polarised light); C) BSE image of actinolite grains showing fractures. White arrows indicate some fractures at low angle to the grain long axis; D) photomicrograph of detail of solution seam at the margins of the epidote grain and the porphyroclasts (plane polarised light); F) BSE image of albite aggregate with inclusions of pumpellyte-rich porphyroclasts (red arrow), chlorite and titanite. Single albite grains have irregular boundaries (white arrow); G) photomicrograph of lenses and porphyroclasts asymmetry indicates top-to-NW sense of shear (plane polarised light).

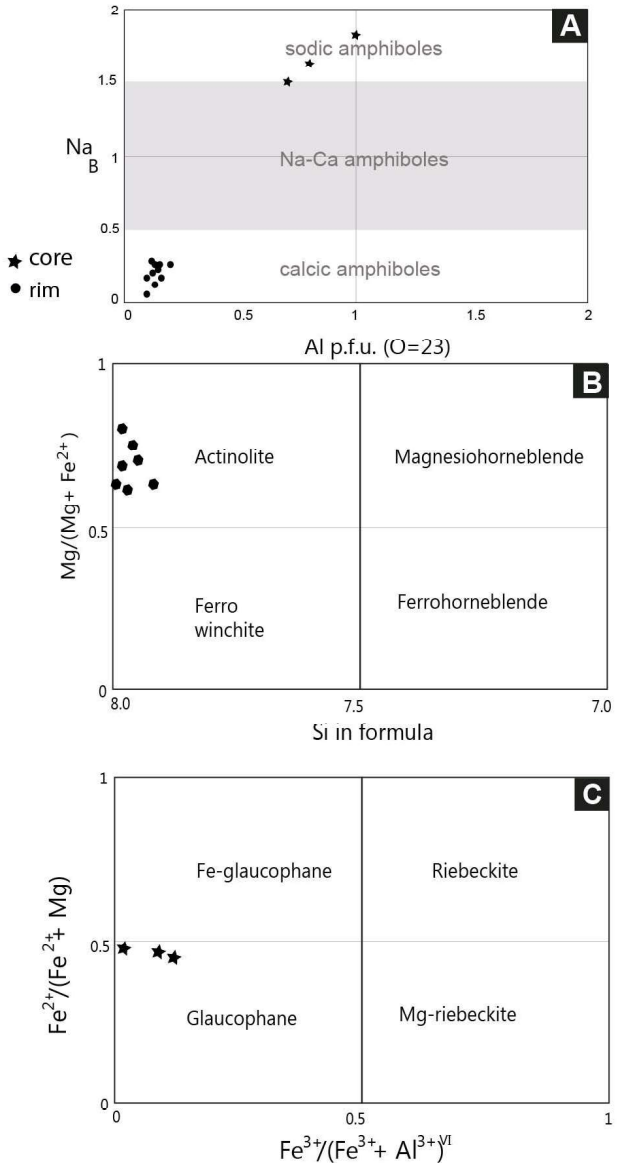

Figure 7.5: Classification of amphiboles from Lento metabasites based on 23 oxigens (following Leake et al., 1997). A) variation of Na_B and Al per formula unit (p.f.u). the core analyses plot show high values of Na_B, corresponding to glaucophane compositions in C. Rim analyses show low values of Na_B , corresponding to actinolite compositions in B. Analyses in Table 7.1

Metagabbros are poorly foliated rocks, characterised by discontinuous sub-mm layering of actinolite with minor muscovite and chlorite layers, separating layers and lenses rich in albite and epidote (Fig. 7.6A). Locally, actinolite layers

Table 7.2: Mineral analyses from amphibole grains. * Fe_2O_3 is total Fe. $X_{Fe2} = Fe_{2+}/(Fe_{2+} + \text{Mg})$; $X_{Fe3} = Fe_{3+}/(Fe_{3+} + \text{Al})$VI; $X_Mg = \text{Mg}/(\text{Mg} + Fe_{2+})$. act:actinolite; gln: glaucophane.

	Core analyses											Rim Analyses		
	LE6							LE10			LE12	LE6		
	Act	Act	Act	Act	Act	Act	Act	Act	Act	Act	Act	Gln	Gln	Gln
SiO2	57.81	57.39	57.78	57.84	57.61	57.19	57.53	58.55	58.84	59.02	58.01	58.99	58.53	58.48
TiO2	0	0	0	0	0	0	0	0	0	0	0			
Al2O3	0.67	0.97	1.11	0.82	0.88	1.13	0.96	0.86	0.64	0.68	0.82	6.11	4.82	4.14
Fe2O3	10.45	11.89	11.71	10.77	10.75	11.82	11.63	7.85	7.07	6.94	8.98	17.41	17.79	18.08
MnO	0.27	0.22	0.26	0.27	0.34	0.26	0.21	0.24	0.21	0.25	0	0.18	0.2	0.27
MgO	17.89	16.97	17.11	17.64	17.73	17.15	17.23	19.77	20.31	20.32	19.17	9.72	10.5	10.89
CaO	12.28	11.6	11.05	12.03	12.15	11.44	11.57	11.7	12.23	11.99	12.77	0.84	1.78	2.53
Na2O	0.63	0.97	0.98	0.63	0.54	1.01	0.87	0.94	0.7	0.8	0.25	6.74	6.16	5.62
K2O	0	0	0	0	0	0	0	0	0	0	0	0	0	0
Total	100	100.01	100	100	100	100	100	99.91	100	100	100	99.99	99.78	100.01
Si	7.97	7.95	8.01	8.00	7.97	7.91	7.97	7.97	8.00	8.02	7.95	8.20	8.18	8.19
Al	0.11	0.16	0.18	0.13	0.14	0.18	0.16	0.14	0.10	0.11	0.13	1.00	0.79	0.68
Ti	0.00	0.00	0.00	0.00	0.00	0.00	0.00	0.00	0.00	0.00	0.00	0.00	0.00	0.00
Cr		0.00	0.00	0.00	0.00	0.00	0.00	0.00	0.00	0.00	0.00	0.00	0.00	0.00
Mg	3.68	3.50	3.53	3.64	3.66	3.54	3.56	4.01	4.12	4.12	3.92	2.01	2.19	2.27
Fe2+	1.06	1.18	1.32	1.23	1.18	1.11	1.20	0.73	0.74	0.78	0.92	2.01	1.96	2.05
Mn	0.03	0.03	0.03	0.03	0.04	0.03	0.02	0.03	0.02	0.03	0.00	0.02	0.02	0.03
Ca	1.82	1.72	1.64	1.78	1.80	1.70	1.72	1.71	1.78	1.75	1.87	0.13	0.27	0.38
Na	0.17	0.26	0.26	0.17	0.14	0.27	0.23	0.25	0.18	0.21	0.07	1.82	1.67	1.53
K	0.00	0.00	0.00	0.00	0.00	0.00	0.00	0.00	0.00	0.00	0.00	0.00	0.00	0.00
Fe3+	0.14	0.20	0.04	0.02	0.06	0.26	0.15	0.16	0.07	0.01	0.10	0.01	0.12	0.06
NaB	0.17	0.26	0.26	0.17	0.14	0.27	0.23	0.25	0.25	0.17	0.07	1.81	1.65	1.51
IVAl	0.08	0.11	0.18	0.13	0.11	0.10	0.12	0.11	0.11	0.10	0.08	1.00	0.79	0.68
XFe3	0.63	0.65	0.19	0.11	0.35	0.73	0.54	0.59	0.59	0.40	0.56	0.01	0.13	0.09
XFe2	0.22	0.25	0.27	0.25	0.24	0.24	0.25	0.15	0.15	0.15	0.19	0.50	0.47	0.47
XMg	0.78	0.75	0.73	0.75	0.76	0.76	0.75	0.85	0.85	0.85	0.81	0.50	0.50	0.53

isolate microlithons rich in albite and muscovite (Fig. 7.6B). Actinolite grains range in grain size from 100 µm up to 500 µm, they form discontinuous levels and are typically replaced by chlorite. Commonly, actinolite grains are not zoned, except when they preserve cores with Na-amphibole composition (Fig. 7.6C). Grains are commonly fractured, with fractures commonly parallel to the grain long axes (Fig. 7.6D). Chlorite grains are very fine grained, with long axes size ranging from a few microns to 50 µm (Fig. 7.6D). They commonly have long axes parallel to the foliation, although the minute grain size does not allow for more precise observations. Epidote grains have size up to 250 µm, they form isolated porphyroclasts surrounded by albite and actinolite. They typically show inclusions of albite, chlorite and actinolite and are fractured (Fig. 7.6F). Albite grains have size of 50 µm in average and constitute continuous layers or lenses with epidote. They are typically not zoned and present grain boundaries that vary from straight to irregular (Fig. 7.6E). There is no microstructural evidence in the metagabbros of sense of shear indicators, however, the foliation paragenesis, characterised by the association of actinolite muscovite and chlorite, along with its mesostructural orientation, allow to interpret it as S2 foliation (e.g., Levi et al., 2007). The foliation recognised in the microlithons, defined by the preferred orientation of muscovite grains, at a high angle to the S2 foliation, is interpreted as an earlier foliation, likely S1, although there is no high-pressure mineral phase associated with it that can univocally distinguish it (Fig. 7.6B).

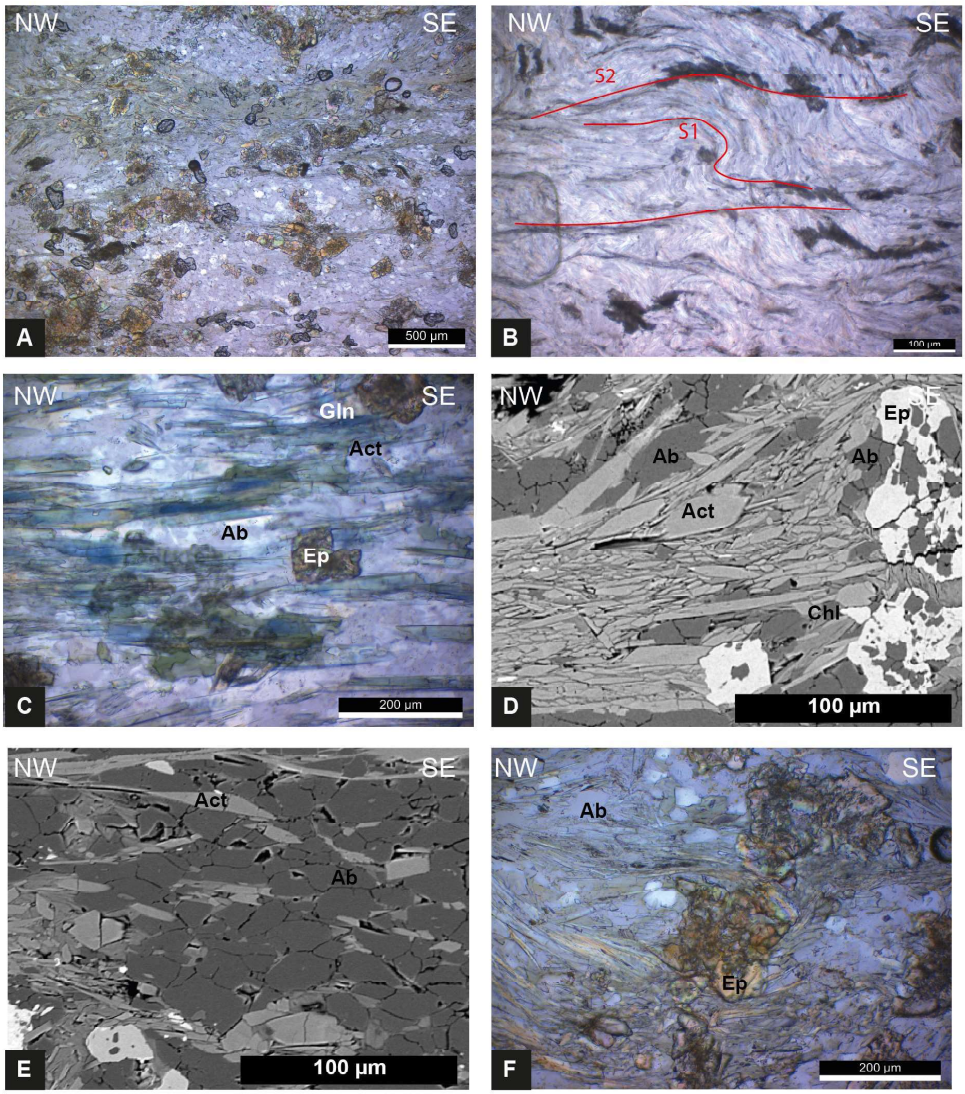

Figure 7.6: A) photomicrograph of poorly foliated fabric of metagabbro, with layers of muscovite and chlorite separating domains of albite and epidote (plane polarised light); B) photomicrograph of structural relationship between S2 foliation, defined by discontinuous levels of chlorite and actinolite separating microlithons of albite and muscovite. The foliation internal to the microlithons, S1, is defined by the preferred alignment of muscovite grains (plane polarised light); C) photomicrograph of actinolite grains with preserved Gln cores, red arrow shows growth of chlorite at the rims of some amphiboles (plane polarised light); D) BSE image of actinolite grains show fractures and structures resembling subgrains parallel to the grains long axes. Between actinolite grains, there is fine grained chlorite; E) BSE image of albite grains show irregular contacts; F) photomicrograph of epidote grains in metagabbros, they are fractured, showing albite growth in the strain shadows.

7.4 Fabric and intracrystalline deformation analysis

Shape and intracrystalline deformation analysis have been carried through EBSD in both metabasalts and metagabbros on the principal foliation-forming minerals. In the metabasalts, foliation-forming minerals have been recognised as actinolite, muscovite and chlorite, however, it was not possible to index either chlorite or muscovite grains because of their small grain size (less than 50 µm), hence only amphibole has been considered in intracrystalline deformation and fabric analyses. In the metagabbros, actinolite, epidote and albite have been analysed.

In the metabasalt, intracrystalline misorientation maps show that actinolite grains have relatively high degrees of misorientation, up to 8°, with the highest values localised in correspondence to fractures, at high angle with the grain boundaries. Locally, there is a variation in misorientation within the grains, oriented parallel to the grains long axes, which could be interpreted as subgrain boundaries and with some resembling subgrains (Fig. 7.7A,B). Actinolite shows relatively well developed SPO, where most of the grains with the highest aspect ratios are aligned along the lineation (Fig. 7.7D). LPO is well defined, with poles to (100) aligned sub-normal to foliation and <001> axes aligned with lineation (Fig. 7.7C).

In the metagabbros, intracrystalline misorientation angles are relatively high, up to 9 °, with the highest values located near fractures, at high angle with the grain boundaries, or at the edge of grains, resembling subgrains which are elongated parallel to the crystals long axes (Fig. 7.7E,F). To further check on the degree of internal misorientations, a misorientation profile on an actinolite grain with low degrees of misorientation was plotted (Fig. 7.8), showing that across the length of the crystal, misorientation angles increase up to 6 degrees. Actinolite grains so not have a well developed SPO, with only some of the grains with the highest aspect

ratios aligned with the lineation (Fig. 7.7H). LPO is well defined, with <001> axes parallel to the lineation and poles to (100) sub-normal to foliation (Fig. 7.7G). Epidote grains have internal misorientation angles up to 10 °, with the highest misorientation angles corresponding to fractures (Fig. 7.9A). Epidote LPO is not well-defined, with random distribution of both poles to (100) and <001> axes (Fig. 7.9B). Albite grains misorientation angles up to 5 °and relatively developed LPO, with poles to (100) at high angle to the foliation and <001> axes at an angle to the lineation (Fig. 7.9C,D).

7.4.1 Actinolite subgrain boundary analysis

To discern whether there is a systematic pattern of misorientations relating to fractures or crystal plastic deformation, actinolite grains were analysed with IPF maps. The resulting map shows how within some grains, there is a change in misorientation angles (from 1.5 to 10) around a line parallel to the grain long axis, which has been interpreted as a subgrain boundary.

The presence of inferred subgrain boundaries in actinolite grains, in both metabasalts and metagabbros, indicates that at least some of the deformation is guided by dislocation activity (Fig. 7.10A,B). Subgrain misorientation analysis in metagabbros show that subgrain boundaries exhibit <010> rotation axis, identified as the crystal axis where the intracrystalline misorientations are concentrated, (Fig.7.10D). A rotation axis on <010> identifies the correspondent slip system as either (100)<001> or (001)<100>, as slip direction is perpendicular to the rotation axis. Actinolite LPO patterns show poles to (100) subnormal to foliation and <001> axes aligned with lineation, hence identifying actinolite slip systems as (100)<001> (Fig. 7.10C). Subgrain boundary analysis (Fig. 7.10E) shows that the rotation axis <010> is contained within the inferred subgrain boundary plane, which is consistent with a tilt wall.

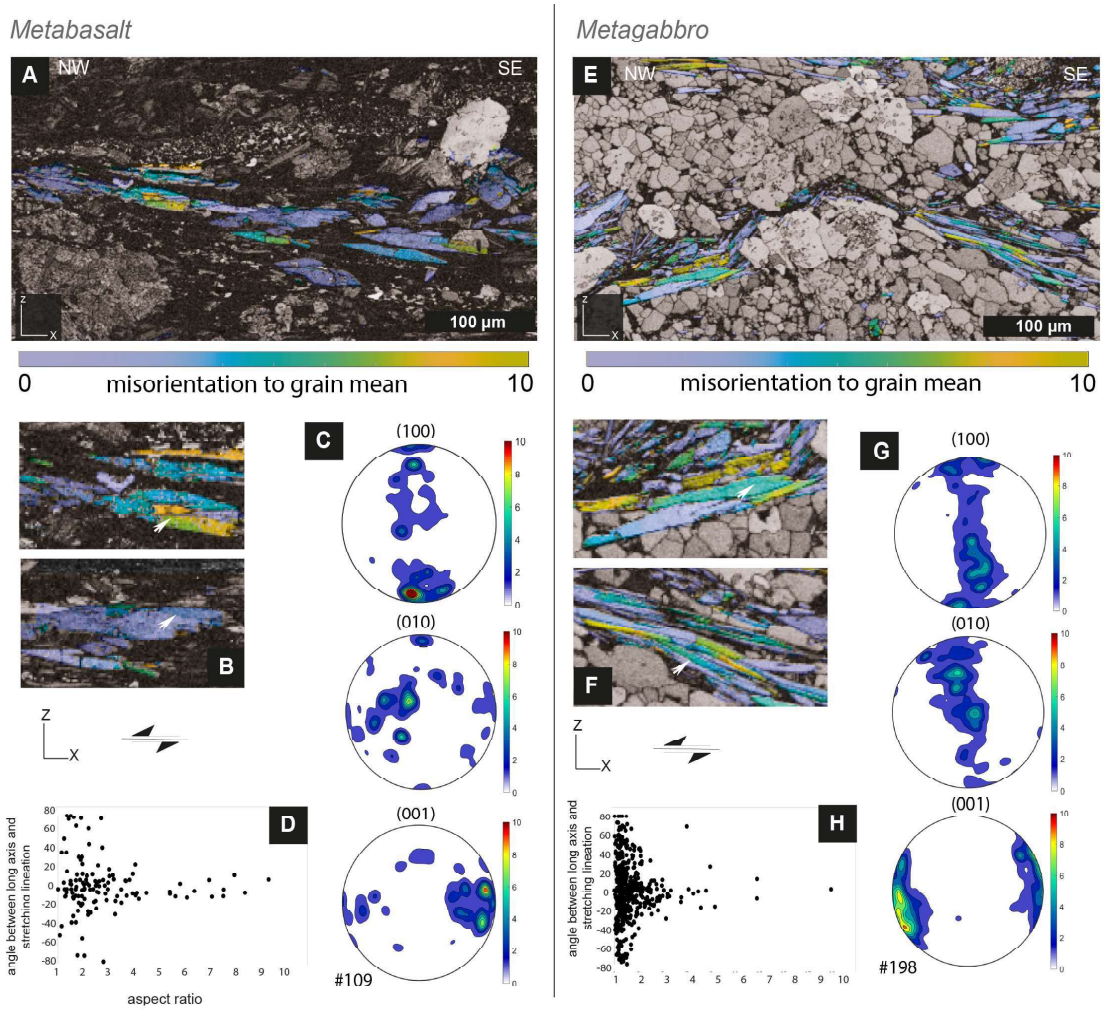

Figure 7.7: A) Misorientation map (mis2mean) of actinolite grains in the metabasites. Scale bar indicates the degree of internal misorientation within each grain. In B) zoom-in on some actinolite grains in metabasalts, white arrows indicate change in orientation resembling subgrain boundaries; C) LPO plots of actinolite, poles to (100) are aligned sub-normal to the foliation and <001> axes are aligned with the lineation; D) aspect ratio versus orientation to the foliation plot of actinolite grains showing the development of shape preferred orientation. (missing the axes labels; E) misorientation map (mis2mean) of actinolite grains in the metagabbros. Scale bar indicates the degree of internal misorientation within each grain; F) zoom in on some actinolite grains, white arrows indicate change in orientation resembling subgrain boundaries; G) LPO plots of actinolite, similar to C; H) aspect ratio versus angle to the foliation of actinolite grains. Most of the grains are not aligned with the foliation.

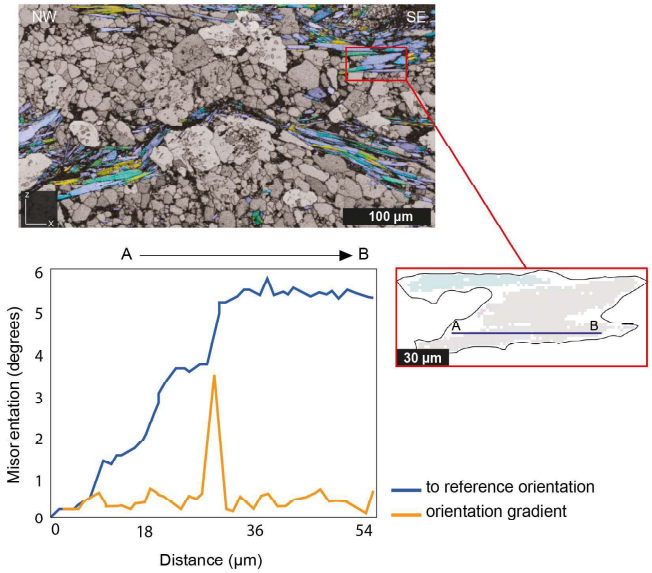

Figure 7.8: Misorientation profile of actinolite in metagabbro. The profile shows an increase of misorientation values up to 6 degrees from point A to B across the crystal length, even when misorientations on the mis2mean map are low.

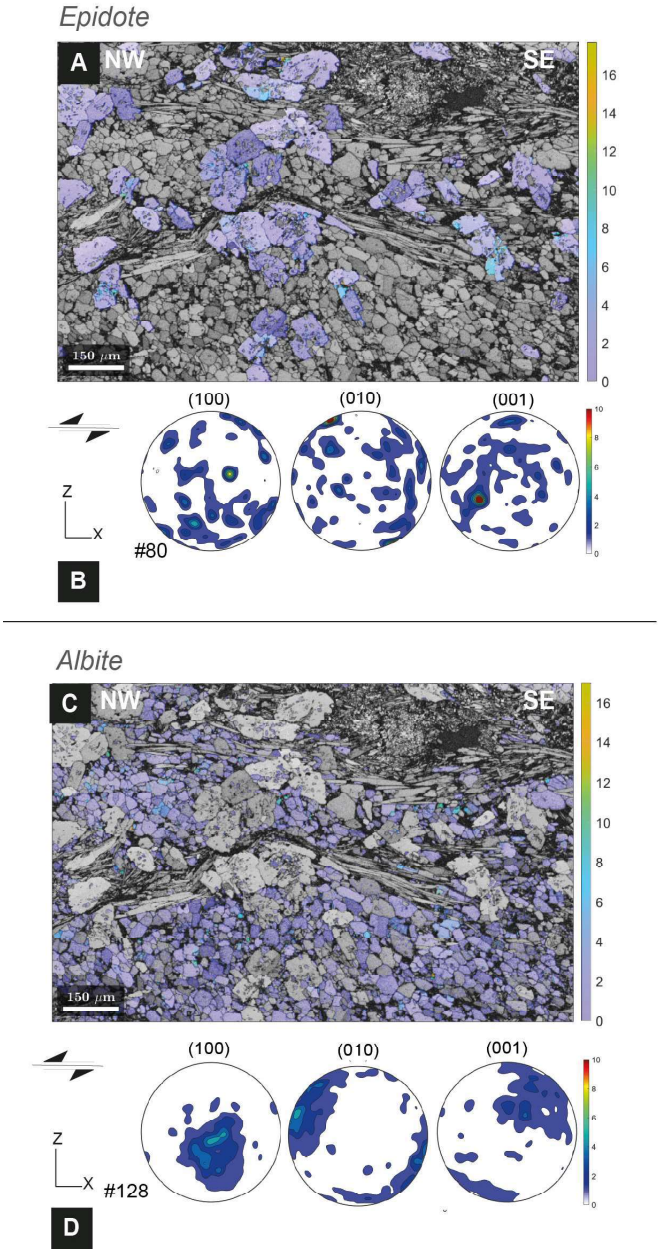

Figure 7.9: A) Misorientation map (mis2mean) of epidote grains in the metagabbros. The highest misorientations correspond to fractures; B) LPO plots of epidote grains, where no pattern is recognisable; C) Misorientation map (mis2mean) of albite grains in the metagabbros. All the grains show very small degrees of internal misorientations; D) LPO plots of albite grains, with poles to (100) subnormal to foliation and <001> axes at an angle to lineation.

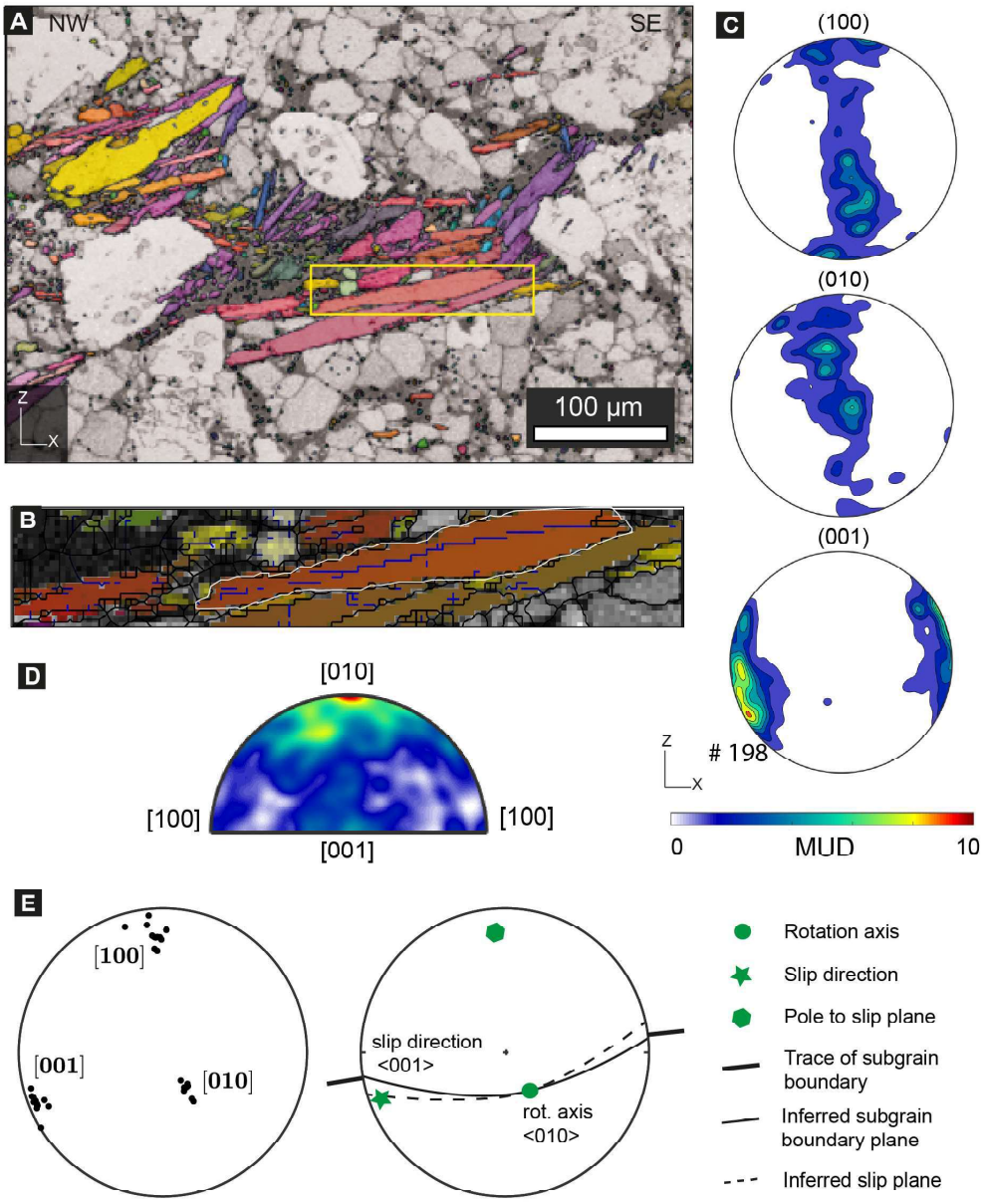

Figure 7.10: IPF – X map of actinolite grains in metagabbro, yellow rectangle is shown in B) Detail of actinolite grain used for subgrain trace boundary analysis. In blue, the trace of the subgrain boundary, parallel to the grain long axis; C) Actinolite LPO show <001> axes parallel to lineation; (D) Contour plot showing concentration of misorientation axes on <010>, which is identified as misorientation axis; E) Trace boundary analysis plot.

7.5 Discussion

7.5.1 Deformation mechanisms active in the Lento metabasites

Although it was not possible to collect fabric and intracrystalline deformation data on chlorite, its microstructure in the metabasalts allows to infer which deformation mechanisms were active during deformation. Chlorite grains have very small grain size and form along foliation, substituting amphibole, as a new phase, and in porphyroclasts strain shadow, with long axes parallel to foliation and lineation (Fig. 7.3C). Grain boundaries are commonly straight, however, when chlorite is close to the edge of large porphyroclasts, close to dissolution seams, it has irregular grain boundaries (Fig. 7.3E,F). This microstructure suggests that deformation of chlorite is guided by pressure solution in domains where the orientation is at an angle to the main foliation, whereas chlorite grains parallel to the foliation can deform by frictional sliding, as straight grain boundaries can favour slide on phyllosilicate foliae. These observations agree with previous literature, where chlorite has been described to deform by coupled pressure-solution and frictional sliding/glide (Bos and Spiers, 2002; Niemeijer and Spiers, 2005). The role of pressure solution is also evidenced by the presence of dissolution seams that contain abundant clay and some chlorite. In the metagabbros, small grain size of chlorite grains and their microstructural position, generally surrounding actinolite grains in discontinuous levels, does not allow to infer with specificity what deformation mechanisms were active, although we speculate that they might have been a combination of frictional sliding and pressure solution, in analogy with the metabasalts.

Actinolite microstructures vary within metabasalts and metagabbros. Actinolite grains can be found in porphyroclasts and epidote strain shadows with chlorite, with their long axis parallel to lineation and foliation (Fig. 7.3C). Locally, acti-

nolite grains are found at higher angle to the foliation, with chlorite rims, and the grain boundaries are cut by other minerals (Fig. 7.3D). These grains show straight boundaries and uniform extinction in cross polarised light. This type of microstructure can be related to deformation by pressure solution, which has been documented in previous literature as an effective mechanism guiding deformation of amphibole at greenschist to lower amphibolite facies conditions (Lee et al., 2022; Nishiyama et al., 2023; Tulley et al., 2020). In addition to that, locally, actinolite grains along the foliation have undulose extinction (Fig. 7.4B).

In both lithotypes, actinolite grains have high degrees of internal misorientations, up to 8°in the metabasalts and 9°in the metagabbros, with most of the high misorientation angles localised across fractures, commonly at high- and, locally, at low angle to the grain boundaries (Fig. 7.7A,E). Locally, areas of high internal misorientations resemble subgrains, typically parallel to the grain long axes (Fig. 7.10A). Subgrain analysis shows that subgrain formation is consistent with deformation by edge dislocations related to (100)<001> slip system, which is also consistent with actinolite LPO, where <001> is parallel to lineation, so that slip direction is aligned with lineation (Fig. 7.10). Deformation of amphibole by dislocation glide on (100)<001> has been documented through transmission electron studies (TEM) in naturally deformed samples of hornblende at amphibolite facies conditions (Biermann and Van Roermund, 1983) and in naturally deformed glaucophane at medium temperatures (550-600 ℃) (Reynard et al., 1989). Evidence of dislocation creep in naturally deformed actinolite is rare, although recently Hoover et al. (2022) showed evidence of dislocation creep active in actinolite grains in actinolite-bearing talcschists from a mélange zone deformed at conditions intermediate from epidote-amphibolite and lawsonite-blueschists. Through EBSD mapping, they documented high misorientation angles in the actinolite grains corresponding to subgrains developed along cleavage planes, paired with

a well-developed LPO, with <001> point maxima within foliation and lineation. This microstructure resembles the one in this study's samples.
In the Lento metabasites, crystal plasticity of actinolite likely accommodates part of the deformation, however contribution of dislocation creep to bulk deformation is relatively minor, compared to cataclasis and pressure solution, for which there is much more widespread evidence in the studied S2 shear zones.

In the metabasalts, albite deforms by distributed deformation by pressure solution. The grains do not show zoning, although, the presence of irregular grain boundaries and the inclusions of chlorite a suggests that there is some degree of mobility of the albite grains, likely accompanied by fluid flow, as the role of pressure solution is evident in these rocks (Fig. 7.4E). In the metagabbros, albite grains show very low internal misorientations (Fig. 7.9C), with LPO defined by <001> axes at a high angle with the lineation and poles to (100) at a high angle to the foliation. This pattern does not resemble dislocation by known slip systems active in albite, suggesting that dislocation creep is not an efficient deformation mechanism in these samples (Díaz-Azpiroz et al., 2011).

In metabasalts, therefore, pressure solution in an important mechanism guiding deformation, with dissolution-precipitation creep active in albite, epidote, and locally in actinolite. Pressure solution is coupled with cataclasis with minor dislocation creep of actinolite and frictional sliding on chlorite foliae. In the metagabbros there is evidence for pressure solution, although its role is not as preponderant as in the metabasalts in guiding bulk rock deformation. Evidence of pressure solution is in fact limited to albite grains, and although we can speculate that it could contribute to generate chlorite microstructure, there is not a significant amount of interconnected chlorite overall in these samples. The other foliation forming minerals, epidote and actinolite, show evidence for deformation mechanisms suggesting higher stress and lower strain conditions, with cataclasis of epidote and

cataclasis and minor dislocation creep of actinolite.

7.5.2 Rheological evolution during retrograde deformation

Chlorite is the most abundant foliation-forming mineral in the metabasalts of the Lento unit. Locally, the presence of glaucophane, actinolite and white mica preserved in the cores of chlorite grains suggests that at least some of the chlorite formed as replacement of amphibole and white mica. This replacement happened during deformation, as suggested by the microstructural position of chlorite grains, which are consistently oriented with the crystal long axes parallel to lineation and foliation. Locally, glaucophane grains with chlorite rims are preserved at a high angle to the main foliation, suggesting that chlorite formed as replacement of high-pressure minerals during the development of S2 foliation, in the early retrogression stage D2 (e.g., Levi et al., 2007).

Retrogressing a blueschist paragenesis into greenschist facies requires water as a reactant, through the reaction (Evans, 1990; Miyashiro, 1968):

$$25Gln \ + \ 6\ Czo \ + \ 7Qtz \ + \ 14H2O \ = \ 50\ Ab \ + \ 9\ Chl \ + \ 6\ Act \qquad (7.1)$$

Therefore, chlorite production requires fluids to be present in the system for retrogressive metamorphic reactions to take place. In the Lento metabasalts, lack of local fluid production means that external fluids must have been present in guiding the retrogression of amphibole and white mica composition to form chlorite, which grew into continuous layers along foliation, surrounding amphibole and white mica grains, and in porphyroclasts strain shadows. In the metagabbros, chlorite does not form interconnected layers, and it is only localised between amphibole grains. The difference in fabric and bulk deformation mechanisms between

the metabasalts and metagabbros suggests that fluids that aided retrogression and chlorite deformation were more active in the metabasalts than in the metagabbros, likely because of difference in grain size between metabasalts, fine-grained, and metagabbros, coarser-grained. Grain size is a factor determining rheology and thus strain distribution within shear zones, in particular, when deformation is guided by pressure solution, strain rate depends on grain size cube (e.g., McKlay, 1977; Rutter, 1983), thus small grain sizes favour higher strain rates and strain localisation. Therefore, strain localisation is more efficient in the metabasalts and likely less efficient in the metagabbros.

The crystallisation of chlorite from amphibole and white mica constitutes reaction softening (Hobbs et al., 2010; White and Knipe, 1978). The contiguity of chlorite layers and the orientation of chlorite grains, with their long axes parallel to lineation and along foliation, constitute textural softening (e.g., Wintsch et al., 1995) and influences the overall strength of the rocks, as with higher amount of phyllosilicates with consistent orientation parallel to foliation and in contiguity from layer to layer, the bulk strength of the rock is reduced (Shea and Kroenenberg, 1993). Textural weakening led to further strain localisation at the microscale, as the interconnected layers of chlorite in the metabasalts and the grains' strong alignment suggest that most strain is partitioned in the chlorite and that it thus controls the bulk rheology of the metabasalts (e.g., Handy, 1994). Chlorite microstructures are consistent with reduced rock bulk strength, as it deforms by coupled frictional sliding and pressure solution facilitated by the activity of external fluids. Actinolite microstructures are in contrast with low bulk strength, as dislocation creep in actinolite has been inferred to be active in dry conditions at high stress and strain rates (Bruckner and Trepmann, 2021; Hacker and Christie, 1990). These conditions could be potentially linked to a stress amplification effect in the discontinuous actinolite layers surrounded by high strain in the chlorite

layers (Beall et al., 2019; Hoover et al., 2022). The greenschist microstructure resembles the microstructures linked to frictional-viscous deformation. In these samples, viscous deformation is accommodated by pressure solution of chlorite, albite, actinolite, and epidote, with minor dislocation creep of actinolite while the frictional deformation is accomodated by cataclasis of actinolite and epidote and frictional sliding along chlorite foliae.

Both retrograde reactions and textural softening happened during early retrogression of the Lento unit at greenschist facies conditions, during D2 in a ductile, compressional regime (Levi et al., 2007). The common recognition of these softening processes in exhumed rocks indicates that reaction and textural softening are important processes in active fault zones, and they are likely to be important in limiting the magnitude of stress and allowing fault creep in shear zones (Fagereng and Diener, 2011; Schleicher et al., 2012), as such is oberved in deformation experiments where rocks characterised by interconnected layers of phyllosilicates have velocity-strengthening behaviour (ikari et al., 2011; Okamoto et al., 2019).

7.6 Conclusions

Metabasites from the Lento Unit show microstructures developed during the early exhumation stage (D2) guiding the evolution from blueschist facies to greenschist facies conditions. Metabasalts have a foliation formed by continuous levels of chlorite separating epidote, albite, actinolite, and muscovite. Metagabbros foliation is characterised by discontinuous layers of chlorite and actinolite separating more or less continuous layers of epidote and albite. In the Lento greenschist metabasites, bulk shearing flow is accommodated by frictional-viscous flow, where the frictional component is accommodated by cataclasis of epidote and actinolite and by sliding on chlorite foliae, and viscous deformation by pressure solution of chlorite, albite,

actinolite, epidote and minor dislocation creep of actinolite.

This retrogression required fluid circulation for metamorphic re-hydration reactions to take place. This is particularly evident in the metabasalts, which are well-foliated rock with a foliation rich in chlorite, whereas the metagabbros are poorly foliated, with chlorite present in only minor quantity. This difference in fabric could be the result of substantially different strain because of difference in grain size between metabasalts and metagabbros, given the assumed rheology of grain size sensitive frictional viscous flow (Niemeijer and Spears, 2005).

Fluids have effect on rock strength, as the nucleation of interconnected layers of chlorite during retrograde metamorphism is a mechanism of reaction and textural softening (e.g., Wintsch et al., 1995), as phyllosilicates are weaker mineral phases compared to the original reactants they derive from (in the case of Lento metabasites, amphibole), especially when they form interconnected layers (Handy, 1994). Reaction weakening can influence fault seismic style, as phyllonitisation could promote fault creep, as shown by experimental data where chlorite exhibits velocity strengthening behaviour (e.g., Belzer and French, 2022; Fagereng and Ikari, 2020; Okamoto et al, 2020; An et al., 2021).

Chapter 8

General Discussion

This thesis presents work conducted on an exhumed epidote-blueschist subduction complex exposed in the Ryukyu arc (Ishigaki Island, Southern Japan; Chapter 5 and 6) and on exhumed retrograde blueschists in the Lento Unit (Lento, Corsica; Chapter 7). In Ishigaki, block-in-matrix epidote-blueschists display structures indicative of deformation at convergent margins in a subduction setting. These rocks retain a prograde metamorphic mineral assemblage that evolved from greenschist to epidote-blueschist, and their structural heterogeneity, of block embedded in a matrix, is inferred to represent the analogue to rocks deforming on the plate interface. Metamorphic conditions of deformation of epidote blueschists are inferred at T∼400℃ and P ∼8-9 kbar (Ishizuka and Imaizumi, 1988). These P-T conditions are coincident to where deformation on the plate interface is governed by viscous creep downdip the seismogenic zone, as observed by microstructural analyses in Chapter 5 and 6. Therefore, the locus of deformation of Tomuru epidote-blueschists may be spatially coincident to where slow slip and tremor are inferred to occur along some active margins (e.g., Cascadia subduction zone, Luo and Liu, 2021, Nankai subduction zone, Kano et al., 2019). In Corsica, exhumed metabasites register deformation that guides exhumation from low-grade blueschist

to greenschist facies (peak metamorphic conditions at P= 8 ± 2 Kbar and T = 400 ± 50 ℃, Levi et al., 2007). Combined field observations and microstructural analyses allowed us to gain insights on the rheology of epidote-blueschists and the rheological effects of prograde (Tomuru block-in-matrix) and retrograde (Lento Unit) transitions between greenschists and epidote-blueschists.

The overall aim of this research was to understand what is the deformation style of epidote-blueschist rocks that deform at depth in subduction zones, at conditions similar to where ETS are described occur downdip the seismogenic zone, and what are the structures and fabrics resulting from exhumation. In particular, I address these questions:

Q1: Which structural fabrics (i.e., foliations, fractures, syn-tectonic veins) characterise epidote-blueschist rocks in subduction zones?
Q2: What guides rheology of epidote-blueschist in the subduction context?
Q3: How does the metamorphic path of epidote-blueschists in subduction zones affect rheology?
Below, findings from Chapter 5,6 and 7 are discussed to address these questions, with relative implications for active margins. Finally, conclusions summarise the main findings and include some suggestions for future work.

Q1: Which structural fabrics (i.e., foliations, syn-tectonic veins) characterise epidote-blueschist rocks in subduction zones?

Both prograde epidote-blueschists in Tomuru and retrograde blueschists in Lento are characterised by the coexistence of structural elements that form by continuous ductile shear, i.e., foliation and lineation, and discontinuous brittle shear, i.e., veins. This type of deformation is characteristic of exhumed subduction zones (Moore and Byrne, 1987; Shreve and Cloos, 1986), although, compared to other

well-documented exhumed subduction complexes, where veins are abundant and distributed with high frequency through the rock volume (Fagereng et al., 2017; Moore, 1989; Ujiie, 2002), in both Tomuru metabasites and Lento metabasites, the vein population is relatively scarce.

In Ishigaki, epidote-blueschists show a continuous, penetrative glaucophane-rich schistose foliation that wraps around greenschist facies blocks and is subparallel to the main contact with adjacent metasediments and their internal foliation (Chapter 6). Greenschist facies rocks have actinolite-rich foliation that is generally parallel to the epidote-blueschists foliation and shows some local variability, varying from a schistosity to being non-existent in some blocks. Foliation development shows some differences between block-in-matrix elements, in fact it is more developed in the epidote-blueschist matrix, where the glaucophane layers are well interconnected, than the epidote blueschist and greenschist blocks, which appear to be more competent elements within the block-in-matrix complex. In the epidote-blueschist blocks glaucophane layers are not interconnected, with grains edged between epidote and albite grains. In Lento, the foliation within metabasite blocks, which is subparallel to the one of the surrounding metasediments, shows different development between metabasalts and metagabbros. Metabasalts are characterised by a continuous, penetrative chlorite-rich foliation, whereas the metagabbros have a poorly developed foliation, defined by discontinuous levels of actinolite and chlorite (Chapter 7).

In Ishigaki, both epidote-blueschists and greenschists foliation strikes NW-SE to NNE-SSW with top-to-SE sense of shear (See Sections 5.4 and 6.3). Mineral extension lineation is defined by the elongation of amphibole and albite grains and is interpreted as stretching lineation, generally trending NNW/SSE. Both foliation and lineation are aligned with the direction of subduction of the Philippean Sea Plate, and the sense of shear indicators are consistent with present NW-directed

subduction under the Amurian Plate, which allows to interpret Tomuru block-in-matrix deformation as subduction related. Locally, top-to-N/NW sense of shear is preserved within the block-in-matrix, likely linked to post-subduction tectonic history of the Tomuru metabasalts and metasediments (Osozawa and Wakabayashi, 2013). In Corsica, Lento metabasites foliation strikes NW-SE, and the stretching lineation, defined by the elongation of amphibole and chlorite grains, generally trends NE/SW. Foliation shear sense indicators show top-to-NW sense of shear, consistent with deformation known to have accompanied early exhumation of the Lento Unit (D2, See Section 3.2; Levi et al., 2007).

In both settings, the principal brittle structures are foliation-parallel and foliation-oblique veins. In the prograde setting, foliation-parallel quartz-rich veins are interpreted to form during deformation at epidote-blueschist conditions, as suggested by their geometry, parallel to the foliation, and by their mineralogy, glaucophane-bearing (See Sections 6.3 and 6.5.2). Their boudinaged and locally dismembered appearance along foliation suggests that they were forming as the foliation was developing, or tentatively that they formed immediately before foliation development. These veins are unevenly distributed, as they tend to be more developed along the tectonic contact with the metasediments, the latter showing a well-developed system of foliation-parallel quartz-rich veins. Quartz veins have blocky texture, suggesting that they formed in a tensile regime, indicating that they likely did not accommodate significant deformation.

Epidote-rich veins occur exclusively in the epidote-blueschist matrix and blocks, and are also interpreted to form during deformation at epidote-blueschist conditions, as they occur either parallel to foliation or by forming intrafoliar folds and locally contain glaucophane grains (see Chapter 6, Section 6.5.2).

In the retrograde blueschists of the Lento unit, veins are characterised by quartz- and carbonate-rich mineralogy. They are typically at high angle to the

foliation and locally parallel to the main foliation (See Section 3.2). The foliation-parallel veins are commonly boudinaged along the foliation and folded with the foliation by later deformation stages, suggesting that their formation was penecontemporaneous to foliation forming. There is a possibility that these veins were already formed during prograde deformation in blueschist facies and then were pervasively overprinted and reoriented during exhumation, although at the moment there is no sufficient data to discern it.

Q2: What guides bulk rheology of epidote-blueschists in the subduction context?

In Tomuru epidote-blueschists, the glaucophane-rich foliation is interpreted to develop by diffusive mass transfer, as indicated by the principal foliation-forming mineral microstructures, which lack distinctive features of intracrystalline deformation by dislocations in glaucophane. Likewise, in the greenschist blocks, actinolite-rich foliation shows similar microstructures, with no evidence of dislocation creep, therefore it developed by the same deformation mechanisms of diffusive mass transfer (Section 6.5.3). The presence of epidote-rich veins in the epidote-blueschists suggest that, at least locally, diffusive mass transfer was fluid assisted. Bulk rheology in the Tomuru metabasites is therefore governed by viscous diffusive mass transfer which approximates linear-viscous behaviour at low stress and strain rate conditions. Studies on both laboratory and naturally deformed amphiboles have highlighted that diffusive mass transfer is a common mechanism guiding their deformation (commonly by dissolution-precipitation creep in the presence of an aqueous fluid) which is typical at low stress and strain rate conditions (Getsinger et al., 2014; Giuntoli et al., 2017; Imon et al., 2004; Lee et al. 2022; Stunitz et al., 2019). Some literature also highlights cataclasis and subsequent dissolution-precipitation creep (Imon et al., 2004) as well as dislocation creep (Biermann and

Van Roermund, 1983; Reynard et al., 1989). Specifically, at blueschist conditions, only limited literature is available on the deformation mechanisms governing glaucophane rheology. Available data on naturally deformed samples indicates that glaucophane can deform either by dissolution-precipitation creep or dislocation creep (Behr et al., 2018; Munoz-Monteciños et al., 2021; Kim et al., 2013).

In the Lento greenschists, chlorite-rich foliation is developed by the combined parallel processes of frictional sliding along phyllosilicate foliae and pressure solution (See Section 7.8.1). This has commonly been observed in phyllosilicate experiments (Bos and Spiers, 2005; Niemeijer and Spiers, 2005) and in naturally deformed samples (Braden and Behr, 2021; Leah et al., 2022; Phillips and White, 2017; Wallis et al., 2015).

What are the factors influencing this rheology of epidote-blueschists and retrograde blueschists?

Grain size

In Tomuru metabasites, grain size of amphibole is small (with average less than 20 µm, Section 6.5.3), which favours deformation by diffusive mass transfer, as small grain size has been parametrised to favour deformation by diffusion creep (Knipe, 1989; Tsenn and Carter, 1987, Section 2.6.2). In the Lento unit, amphibole grain sizes are much higher than the ones in Ishigaki (grain size up to 100 µm in Lento compared to 20 µm in Ishigaki), which would suggest that deformation by dislocations could be more likely to be effective in these rocks, although this is marginally speculative based on grain size alone, as there are no flow laws computed for amphiboles that could quantify this.

Anisotropy

Continuous fabrics (e.g. Wintsch et al., 1995) can lower the strength of the rock to

approximate the strength of a single grain. This is especially true when retrograde reactions take place to produce mineral assemblages that are weaker than the original rock (strain softening, e.g., White, 1980, see Section 2.X). In the Lento unit, at the microscale, the interconnected network of chlorite allows strain localisation in the phyllosilicate layers that deform around more competent grains, which do not form continuous layers (amphibole, albite, epidote). In the Tomuru metabasites the product of dehydration is not a weaker phase, but glaucophane, which is not considered a weak mineral (e.g., Getsinger and Hirth, 2014). However, the formation of interconnected layers of glaucophane in the matrix with strong anisotropy (well-developed LPO and SPO) seem to preferentially focus strain localisation in the matrix, which more easily deforms by distributed shear. The effect of structural evolution from blocks to matrix constitutes textural softening, where higher strain rates and lower stress conditions cause strain localisation in the epidote-blueschist matrix (White et al., 1980). The effect of fabric anisotropy in affecting strain localisation and rheology is particularly evident between epidote-blueschist blocks and matrix, where mineralogy is the same, but glaucophane fabric is different, with well-developed SPO and CPO in the matrix and poorly developed SPO and CPO in the blocks (See Chapter 5, Sections 5.6.2; 5.6.3).

Stress-strain rate

Quartz piezometry analysis on recrystallised quartz in foliation-parallel veins suggests low shear stress conditions at the time of deformation of the epidote-blueschists, with shear stress ranging 11-28 MPa (See Section 6.7). Low shear stress conditions favour distributed deformation by diffusive mass transfer (e.g., Knipe, 1989) which governs bulk rheology of the Tomuru block-in-matrix and deformation of quartz by grain boundary migration (see also Section 2.6.2), which characterises the quartz-rich veins in the Tomuru metabasites.

Fluids

Dehydration reactions that guide prograde metamorphism from greenschist to epidote-blueschist release fluids, with consequently leads to fluid pressure to increase. Fluid overpressure can promote embrittlement, by lowering effective normal stress, which leads to hydrofracturing and brittle deformation (e.g., Fagereng and Diener, 2011), however fluid flow can also promote deformation by diffusive mass transfer which allows deformation at relatively low viscosity and stress (e.g., Wassmann and Stöckhert, 2013 and references therein). In retrograde settings fluids are an essential component during deformation, as retrograde reactions involve parageneses that have likely been previously dehydrated, therefore water is a reactant necessary for mineral reactions to take place (e.g., Imber et al., 1997). Metamorphic retrograde reactions generally produce phyllosilicate-rich foliations, which lead strain localisation by reaction weakening.

Q3: How does the metamorphic path influence epidote-blueschist rheology?

In prograde settings, as rocks deform, water is available through metamorphic dehydration reactions as T and P increase. In particular, the reaction that guides metamorphic dehydration of greenschists into epidote-blueschists (Evans, 1990) is:

$$9Chl \ + \ 50Ab \ + \ 6Act \ = \ 25Gln \ + \ 6Ep \ + \ 7Qtz + \ 14H2O. \qquad (8.1)$$

Through metamorphic dehydration, there can be a significant quantity of fluids available in subduction zones during prograde deformation (Saffer and Tobin, 2011), and, as mentioned in the previous section, the consequent increase in fluid pressure has implications for rock rheology. Generally, fluid release from dehy-

dration can cause rising in fluid pressure, with consequence of lowering effective normal stress and the shear stress required for frictional sliding (e.g., Hubbert and Rubey, 1959). Fluid circulation also favours low stress activated deformation mechanisms such as diffusive mass transfer (diffusion creep and dissolution precipitation creep), which allow deformation at low effective viscosities at low stress and strain rates. Testament to this environment is the development of a penetrative foliation that forms through a combination of pressure solution and frictional sliding and systems of veins.

As analysed in Chapter 5 and 6, epidote-blueschists and greenschists of the Tomuru block-in-matrix metabasites bulk deformation is governed by diffusive mass transfer, with distribute diffusion creep and localised pressure solution within the epidote-blueschist matrix. Fluid is present in enough quantity to favour deformation by diffusive mass transfer and to form systems of syn-tectonic veins, although their frequency is limited, compared to most exhumed subduction complexes, where veining is typically a major feature. Likely, this is because deforming epidote-blueschist remain relatively permeable during deformation, with well-aligned grains of glaucophane guiding fluid flow and only locally generating overpressure that can lead to precipitation of material in veins.

In retrograde settings, rocks would have previously dehydrated during prograde metamorphism, so there is no mineral-bound water available in quantity to work as a reactant during metamorphism, and re-hydration is possible only if an external source of fluids is present (Giraud et al., 2001). In the Lento greenschists, fluid is present in enough quantity to allow the formation of retrograde mineral assemblages, where sodic amphibole destabilises in calcic amphibole and chlorite, but seemingly not enough to generate fluid overpressure that can produce significant veining. Fluids could come from dehydration occurring further down on the subduction interface, rising in the subduction zone along a permeability path, or

through shear zones that guides exhumation through tectonic extrusion (e.g., Saffer and Tobin, 2011). The consumption of fluids by retrograde reactions to form chlorite likely causes not significant overpressure to form, and by consequence, no significant amount of veins in the rock volume.

In conclusion, in prograde settings, fluid circulation via metamorphic dehydration reactions promotes diffusion creep of epidote-blueschists, thus favouring rheology guided by viscous creep. In retrograde blueschists, the metamorphic reactions guided by fluid influx generate a chlorite-rich paragenesis that is characteristically weaker than the original blueschist amphibole-rich rock. Here, deformation occurs by frictional-viscous flow, where combined pressure solution and frictional sliding on chlorite layers govern rheology. Localisation of strain in chlorite layers likely caused stress amplification in the amphiboles (Beall et al., 2019), which have distinct microstructures showing cataclasis and some evidence of crystal plastic deformation (See Section 7.6), unlike amphiboles in Tomuru rocks that have no evidence of intracrystalline plasticity.

Exhumation of blueschists

Without fluid presence, retrograde re-hydration reactions cannot happen, this leads to no strain localisation and no consequent reaction weakening. (e.g., White et al., 1980, weakened means more easily to deform at any imposed stress). So epidote-blueschists are likely preserved in Ishigaki because there is not the onset of fluid reactions that lead to retrograde shear zone formation that would destabilise epidote-blueschist assembages into greenschist assemblages (Evans, 1990, Selverstone and Barrientos, 1993) . We can speculate that if that were the case, Ishigaki blueschists would turn into greenschists similar to the ones in the Lento unit. It is unclear why fluid circulation was hindered during deformation that promoted exhumation in Ishigaki, given that literature is scarce, but the Ryukyu arc has not

undergone continental collision, unlike Corsica.

Implications for active margins

Tomuru epidote-blueschists deform at depths comparable to the source of ETS downdip the seismogenic zone (e.g., Cascadia). During deformation, progressive strain and diffusive mass transfer induces viscous softening into the matrix, where dehydration fluid causes distributed diffusion creep, and, in the presence of fluids, pressure solution which leads to epidote vein formation.

If we only look at the role of fluids in which Ishigaki rocks deforms, metamorphic dehydration of Ca-rich amphibole and (minor) chlorite generates fluids that likely favour diffusive mass transfer mechanisms (in the context of low shear stress conditions and small grain size as highlighted earlier in Q2). However, as lined up in Chapter 6, veining in the metabasites is not as abundant as usually found in exhumed plate boundary rocks, suggesting that fluid flow does not likely lead to fluid overpressure which is typically thought to happen at the source of ETS (Audet et al., 2009; Shelly et al., 2006). Moreover, the geological and structural heterogeneity observed might not be enough to initiate transients that can be linked to tremor, as the bulk rheology of both blocks and matrix is guided by interconnected layers of diffusively deforming amphiboles. The progressive deformation of greenschists into Tomuru epidote-blueschists seems therefore to represent deformation in creeping parts of the plate interface, downdip of the seismogenic zone. Observations of blueschist rocks at deeper, dryer conditions, where eclogites are stable, are likely to generate enough heterogeneity to host transients (Behr et al., 2018).

Viscous creep of the hydrated oceanic crust can therefore influence the bulk rheology and slip behaviour of the subduction thrust interface. Particularly, linear-viscous (Newtonian) rheology leads to deformation at low viscosity, which, linked with the measured low shear stresses in the epidote-blueschists, suggests that the

oceanic crust at epidote-blueschist conditions can be weak enough to control subduction megathrust rheology, and consequently control on the depth and degree of interseismic coupling. Moreover this negates the need for a continuous layer of lubricating sediments to explain the low viscosity plate interface at the base of the seismogenic zone. Finally, if the subducting oceanic crust is foliated and deforming by linear viscous rheology, it is likely that the low velocity seismic signals that are commonly interpreted as the sediment dominated megathrust (e.g., Abers et al., 2009) may also originate from the oceanic crust, similarly to what has been suggested by Audet and Schaffert (2018) in northern Cascadia and by Tulley et al. (2020) in Japan.

As discussed above, greenschists from the Lento unit require an external fluid source to explain both the mineralogy and the microstructures observed, requiring at least localised permeability, which in turn means that elevated fluid pressures are not likely to occur. Moreover, in this retrograde setting, rocks consume water by retrograde reactions, further reducing the possibility of fluid overpressure, which is also coherent with the limited amount of veining in the metabasites. There is just enough water to favour weakening by retrograde reactions, but not enough to create overpressure.

In Lento, fluid flow is essential to generate phyllosilicates, so in order to generate chlorite, fluid needs to flow and permeability paths need to present. Therefore, at the stage of S2 foliation formation, the amount of overpressure is not significantly high, partly because the high anisotropy of chlorite grains can allow fluid flow along foliation layers. The relatively scarce amount of veins strengthens the lack of significant fluid overpressure that could lead to stress transients linked to slow earthquake propagation (e.g., Kirkpatrick et al., 2021). Consequently, retrograde deformation during exhumation in the Lento unit is unlikely to happen with slow earthquake propagation. Speculatively, during subsequent deformation

stages after a chlorite-rich foliation is formed, the rock microstructure composed of a well-developed foliation formed by interconnected fine-grain size phyllosilicate grains can reduce rock permeability and therefore could lead to significant fluid overpressure (Collettini et al., 2019). In the case of Lento unit, further deformation stages linked to exhumation, like D3, where deformation is likely concentrated in shear zones deforming the accretionary prism (Levi et al., 2007), could likely lead to stress transients linked to slow earthquake propagation, as fluids flow in exhumation-related shear zones would be limited by an already established fine-grained chlorite foliation, where permeability is restricted by the well-developed network of fine grain-size chlorite. Consequently, the fluid overpressure generated could lead to lower effective normal stress (e.g., Hubbert and Rubey, 1959) and contribute to slow earthquake propagation.

8.1 Conclusions and future work

The aim of this thesis was to study the deformation style and bulk rheology of prograde epidote-blueschists (Tomuru block-in-matrix) and retrograde blueschists (Lento unit, Alpine Corsica). The main conclusions are:

- Tomuru block-in-matrix metabasites record prograde deformation on the plate interface, from greenschist to epidote-blueschist conditions, at T-P conditions similar to the ETS source in some subduction zones downdip of the seismogenic zone (e.g., Cascadia). Blocks have a greenschist and epidote-blueschist mineral assemblages while the matrix has epidote-blueschist assemblage. Blocks and matrix have similar bulk chemical composition (N-MORB metabasites); structural heterogeneity is the result of the complex interplay of grain size and strain influencing reaction kinetics at the time of

deformation.

- Both greenschists and epidote-blueschists rheology is governed by distributed diffusive mass transfer at low shear stress conditions, as highlighted by recrystallised quartz piezometry. The similar bulk deformation mechanisms in the block-in-matrix elements suggest that the viscosity contrast in the Tomuru block-in-matrix is relatively low, thus the structural heterogeneity does not set important mechanical heterogeneity that could lead to stress transients downdip of the seismogenic zone. The limited amount of syn-tectonic veins also suggests that fluid overpressure is likely not high enough to lower effective normal stress, therefore epidote-blueschists of the Ryukyu arc likely accommodate plate creep and not slow slip and tremor.

- Lento greenschist record retrograde deformation guiding exhumation from blueschist to greenschist facies conditions. Bulk rheology is guided by frictional sliding along chlorite foliae and pressure solution during frictional-viscous flow. Fluid flow is necessary for retrograde reactions to take place in destabilising the blueschist paragenesis into greenschist, leading to development of interconnected network of phyllosilicates, fine grained in size and well-aligned with the foliation. Vein population is scarce, suggesting that at the time of deformation there was not any significant overpressure that could lead to lower normal stress and to stress transients leading to slow earthquake development.

Future work

Through microstructural and EBSD analyses, it is possible to quantify foliation development and infer which deformation mechanisms are active in governing bulk rheology. Flow laws contribute to further quantify rheology parameters and

link grain size, stress and strain rate, to connect microstructure to the bigger picture of rock behaviour. In the late stages of writing this thesis, a flow law for sodic amphibole was published (Tokle et al., 2023). The flow law is restricted to modelling diffusion creep and microboudinage of amphiboles, not considering the field of pressure solution and dislocation creep. Given the importance of fluid-assisted deformation in subduction zones, we still need to consider a wider range of mechanisms and parameters to model subduction rheology for blueschist rocks.

Moreover, if microstructural studies constraining rheology of blueschists are scarce, isolate literature exists in trying to constrain mechanical properties of blueschists rocks. Sawai et al. (2016) did experiments on glaucophane to characterise the mineral mechanical response to deformation, in order to understand its behaviour in subduction zone settings. However the paper focuses on a sample taken from a naturally deformed lawsonite blueschist, limiting the mechanical properites to a specific structural level during deofrmaiton in subduciton zones. Widening the literature around blueschist, particularly blueschist microstructure and mechanics would significantly improve our understanding of rheology and fault behaviour at depth in subduction zones.

References

Abers, G. A., MacKenzie, L. S., Rondenay, S., Zhang, Z., Wech, A. G., and Creager, K. C. (2009). Imaging the source region of Cascadia tremor and intermediate-depth earthquakes. Geology, 37(12), 1119-1122.

An, M., Zhang, F., Min, K. B., Elsworth, D., Marone, C., and He, C. (2021). The potential for low-grade metamorphism to facilitate fault instability in a geothermal reservoir. Geophysical Research Letters, 48(11), e2021GL093552.

Arai, R., Takahashi, T., Kodaira, S., Kaiho, Y., Nakanishi, A., Fujie, G., Nakamura, Y., Yamamoto, Y., Ishihara, Y., Miura, S., Kaneda, Y., (2016). Structure of the tsunamigenic plate boundary and low-frequency earthquakes in the southern Ryukyu Trench. Nature Communications, 7: 12255.

Audet P., Bostock M.G., Christensesn N., Peacok S.M., (2009). Seismic evidence of overpressured subducted oceanic crust and megathrust fault sealing. Nature, 457, 76-78.

Audet, P., and Schaeffer, A. J. (2018). Fluid pressure and shear zone development over the locked to slow slip region in Cascadia. Science advances, 4(3), eaar2982.

Bachmann, F., Hielscher, R., Schaeben, H., (2010). Texture analysis with MTE-free and open source software toolbox. Solid State Phenomena 160, 63-68.

Barrientos X., Selverstone J., (1993). Infiltration vs. thermal overprinting of epidote blueschist, Ile de Groix, France. Geology, 21, 67-72.

Baziotis I, Mposkos E. (2011). Origin of metabasites from upper tectonic unit of the Lavrion area (SE Attica, Greece): Geochemical implications for dual origin with distinct provenance of blueschists and greenschists protoliths. Lithos, 126, 161-173.

Beall, A., Fagereng, Å., Ellis, S., (2019). Strength of Strained Two-Phase Mixtures: Application to Rapid Creep and Stress Amplification in Subduction Zone Mélange. Geophysical Research Letters 46(1), 169-178.

Beall, A., Fagereng, Å., Davies, J.H., Garel, F., and Davies, D. R. (2021). Influence of subduction zone dynamics on interface shear stress and potential relationship with seismogenic behavior. Geochemistry, Geophysics, Geosystems, 22, e2020GC009267.

Behr, W. M. and Platt, J. P. (2014). Brittle faults are weak, yet the ductile middle crust is strong: Implications for lithospheric mechanics. Geophysical Research Letters, 41(22), 8067-8075.

Behr, W. M., Gerya, T. V., Cannizzaro, C., and Blass, R. (2021). Transient slow slip characteristics of frictional-viscous subduction megathrust shear zones.

AGU Advances, 2(3), e2021AV000416.

Behr, W.M. and Bürgmann, R., (2021). What's down there? The structures, materials and environment of deep-seated slow slip and tremor. Philosophical Transactions of the Royal Society A 379, 20200218.

Behr, W.M., Kotowski, A.J., Ashley, K.T., (2018). Dehydration-induced rheological heterogeneity and the deep tremor source in warm subduction zones. Geology, 46, 475 – 478.

Belzer, B. D., and French, M. E. (2022). Frictional constitutive behavior of chlorite at low shearing rates and hydrothermal conditions. Tectonophysics, 837, 229435.

Berger A., Stünitz, H., (1996). Deformation mechanisms and reaction of hornblende: examples from the Bergell tonalite (Central Alps). Tectonophysics 257, 2-4, 149-174.

Beroza, G. C., and Ide, S. (2011). Slow earthquakes and nonvolcanic tremor. Annual review of Earth and planetary sciences, 39, 271-296.

Biermann, C., and Van Roermund, H. L. M. (1983). Defect structures in naturally deformed clinoamphiboles—a TEM study. Tectonophysics, 95(3-4), 267-278.

Blanpied, M. L., Lockner, D. A., and Byerlee, J. D. (1991). Fault stability inferred from granite sliding experiments at hydrothermal conditions. Geophysical Research Letters, 18(4), 609-612.

Blanpied, M. L., Lockner, D. A., and Byerlee, J. D. (1995). Frictional slip of granite at hydrothermal conditions. Journal of Geophysical Research: Solid Earth, 100(B7), 13045-13064.

Bos, B., and Spiers, C. J. (2002). Frictional-viscous flow of phyllosilicate-bearing fault rock: Microphysical model and implications for crustal strength profiles. Journal of Geophysical Research: Solid Earth, 107(B2), ECV-1.

Bousquet R., (2009). Metamorphic heterogeneities within a single HP unit: overprint effect or metamorphic mix? Lithos, 103, 46-69.

Brace, W. F., and Byerlee, J. D. (1966). Stick-slip as a mechanism for earthquakes. Science, 153(3739), 990-992.

Brace, W. F., and Kohlstedt, D. L. (1980). Limits on lithospheric stress imposed by laboratory experiments. Journal of Geophysical Research: Solid Earth, 85(B11), 6248-6252.

Braden, Z., and Behr, W. M. (2021). Weakening mechanisms in a basalt-hosted subduction megathrust fault segment, southern Alaska. Journal of Geophysical Research: Solid Earth, 126(9), e2021JB022039.

Bröcker, M. (1990). Blueschist-to-greenschist transition in metabasites from Tinos Island, Cyclades, Greece: Compositional control or fluid infiltration?. Lithos, 25(1-3), 25-39.

Brodie, K.H., Rutter E.H., (1985). On the relationship between deformation and metamorphism, with special reference to the behaviour of basic rocks. Advances in Physical Geochemistry, volume 4, Springer.

Brovarone, A. V., and Herwartz, D. (2013). Timing of HP metamorphism in the Schistes Lustrés of Alpine Corsica: New Lu–Hf garnet and lawsonite ages. Lithos, 172, 175-191.

Brovarone, A. V., Beyssac, O., Malavieille, J., Molli, G., Beltrando, M., and Compagnoni, R. (2013). Stacking and metamorphism of continuous segments of subducted lithosphere in a high-pressure wedge: the example of Alpine Corsica (France). Earth-Science Reviews, 116, 35-56.

Brovarone, A. V., Picatto, M., Beyssac, O., Lagabrielle, Y., and Castelli, D. (2014). The blueschist–eclogite transition in the Alpine chain: P–T paths and the role of slow-spreading extensional structures in the evolution of HP–LT mountain belts. Tectonophysics, 615, 96-121.

Brückner, L. M., and Trepmann, C. A. (2021). Stresses during pseudotachylyte formation-Evidence from deformed amphibole and quartz in fault rocks from the Silvretta basal thrust (Austria). Tectonophysics, 817, 229046.

Brunet, C., Monié, P., Jolivet, L., and Cadet, J. P. (2000). Migration of compression and extension in the Tyrrhenian Sea, insights from 40Ar/39Ar ages on micas along a transect from Corsica to Tuscany. Tectonophysics, 321(1), 127-155.

Bürgmann, R. (2018). The geophysics, geology and mechanics of slow fault

slip. Earth and Planetary Science Letters, 495, 112-134.

Bürgmann, R., and Dresen, G. (2008). Rheology of the lower crust and upper mantle: Evidence from rock mechanics, geodesy, and field observations. Annu. Rev. Earth Planet. Sci., 36, 531-567.

Byerlee, J. (1978). Friction of rocks. Rock friction and earthquake prediction, 615-626.

Byerlee, J. D. (1968). Brittle-ductile transition in rocks. Journal of Geophysical Research, 73(14), 4741-4750.

Chen, W. P., and Molnar, P. (1983). Focal depths of intracontinental and intraplate earthquakes and their implications for the thermal and mechanical properties of the lithosphere. Journal of Geophysical Research: Solid Earth, 88(B5), 4183-4214

Cloos, M., and Shreve, R. L. (1988). Subduction-channel model of prism accretion, melange formation, sediment subduction, and subduction erosion at convergent plate margins: 1. Background and description. Pure and Applied Geophysics, 128, 455-500.

Cloos, M., and Shreve, R. L. (1996). Shear-zone thickness and the seismicity of Chilean-and Marianas-type subduction zones. Geology, 24(2), 107-110.

Coble, R. L. (1963). A model for boundary diffusion controlled creep in polycrystalline materials. Journal of applied physics, 34(6), 1679-1682.

Collettini, C., and Holdsworth, R. E. (2004). Fault zone weakening and character of slip along low-angle normal faults: insights from the Zuccale fault, Elba, Italy. Journal of the Geological Society, 161(6), 1039-1051.

Collettini, C., Niemeijer, A., Viti, C., and Marone, C. (2009). Fault zone fabric and fault weakness. Nature, 462(7275), 907-910

Collettini, C., Niemeijer, A., Viti, C., Smith, S. A., and Marone, C. (2011). Fault structure, frictional properties and mixed-mode fault slip behavior. Earth and Planetary Science Letters, 311(3-4), 316-327.

Collettini, C., Tesei, T., Scuderi, M. M., Carpenter, B. M., and Viti, C. (2019). Beyond Byerlee friction, weak faults and implications for slip behavior. Earth and Planetary Science Letters, 519, 245-263.

Condit, C. B., and French, M. E. (2022). Geologic evidence of lithostatic pore fluid pressures at the base of the subduction seismogenic zone. Geophysical Research Letters, 49(12), e2022GL098862.

Condit, C.B., Mahan, K.H., (2018). Fracturing, fluid flow and shear zone development: Relationships between chemical and mechanical processes in Proterozoic mafic dykes from southwestern Montana, USA. Journal of Metamorphic Geology, 36 (2), 195-223.

Connolly, J. A. (2010). The mechanics of metamorphic fluid expulsion. Elements, 6(3), 165-172.

Cross, A. J., Prior, D. J., Stipp, M., and Kidder, S. (2017). The recrystallized grain size piezometer for quartz: An EBSD-based calibration. Geophysical Research Letters, 44(13), 6667-6674

Davis, E., Heesemann, M., and Wang, K. (2011). Evidence for episodic aseismic slip across the subduction seismogenic zone off Costa Rica: CORK borehole pressure observations at the subduction prism toe. Earth and Planetary Science Letters, 306(3-4), 299-305.

De Bresser, J., Ter Heege, J., and Spiers, C. (2001). Grain size reduction by dynamic recrystallization: can it result in major rheological weakening?. International Journal of Earth Sciences, 90, 28-45.

Di Rosa, M., Frassi, C., Meneghini, F., Marroni, M., Pandolfi, L., and De Giorgi, A. (2019). Tectono-metamorphic evolution of the European continental margin involved in the Alpine subduction: New insights from Alpine Corsica, France. Comptes Rendus Geoscience, 351(5), 384-394.

Díaz-Azpiroz, M., Lloyd, G. E., and Fernández, C. (2011). Deformation mechanisms of plagioclase and seismic anisotropy of the Acebuches metabasites (SW Iberian massif). Geological Society, London, Special Publications, 360(1), 79-95.

Dieterich, J. H. (1979). Modeling of rock friction: 1. Experimental results and constitutive equations. Journal of Geophysical Research, 84 (B5), 2161.

Dragert, H., Wang, K., and James, T. S. (2001). A silent slip event on the

deeper Cascadia subduction interface. Science, 292(5521), 1525-1528.

Duarte, J. C., W. P. Schellart, and A. R. Cruden (2015). How weak is the subduction zone interface?. Geophysical Research Letters, 42, 2664–2673.

Dungan M.A., Vance J.A., Blanchard D.P., (1983). Geochemistry of the Shuksan greenschists and blueschists, North Cascades, Washington: variably fractionated and altered metabasalts of oceanic affinity. Contributions to mineralogy and petrology, 82, 131-146.

Durand-Delga, M. (1984). Principaux traits de la Corse Alpine et correlations avec les Alpes Ligures. Memorie della Societi Geologica Italiana 28, 285–329.

Ernst W.G., (1988). Tectonic history of subduction zones inferred from retrograde. Blueschist P-T paths. Geology, 16, 1081-1084.

Ernst, W. G. (1973). Blueschist metamorphism and PT regimes in active subduction zones. Tectonophysics, 17(3), 255-272.

Etheridge, M. A., and Cooper, J. A. (1981). Rb/Sr isotopic and geochemical evolution of a recrystallized shear (mylonite) zone at Broken Hill. Contributions to Mineralogy and Petrology, 78, 74-84.

Etheridge, M. A., Wall, V. J., and Vernon, R. H. (1983). The role of the fluid phase during regional metamorphism and deformation. Journal of metamorphic Geology, 1(3), 205-226.

Evans, B. W. (1990). Phase relations of epidote-blueschists. Lithos, 25(1-3), 3-23.

Fagereng A., Diener J.F.A., Meneghini F., Harris C., Kvadsheim A., (2018). Quartz vein formation by local dehydration embrittlement along the deep, tremogenic subduction thrust interface. Geology, 46, 67-70.

Fagereng A., Hillary G.A., Diener J.F.A., (2014). Brittle-viscous deformation, slow slip, and tremor. Geophysical Research Letters, 4159 – 4167.

Fagereng, Å. and Diener, J.F., (2011). Non-volcanic tremor and discontinuous slab dehydration. Geophysical Research Letters, 38, L15302.

Fagereng, Å., and Den Hartog, S. A. (2017). Subduction megathrust creep governed by pressure solution and frictional–viscous flow. Nature Geoscience, 10(1), 51-57.

Fagereng, Å., and Sibson, R. H. (2010). Mélange rheology and seismic style. Geology, 38(8), 751-754

Fagereng, Å., Diener, J. F., Meneghini, F., Harris, C., and Kvadsheim, A. (2018). Quartz vein formation by local dehydration embrittlement along the deep, tremorgenic subduction thrust interface. Geology, 46(1), 67-70.

Fagereng, Å., Hillary, G.W. and Diener, J.F., (2014). Brittle-viscous deformation, slow slip, and tremor. Geophysical Research Letters 41, 4159-4167.

Fagereng, Å., Remitti, F. and Sibson, R.H., (2011). Incrementally developed slickenfibers—Geological record of repeating low stress-drop seismic events?. Tectonophysics 510, 381-386.

Faulkner, D. R., Jackson, C. A. L., Lunn, R. J., Schlische, R. W., Shipton, Z. K., Wibberley, C. A. J., and Withjack, M. O. (2010). A review of recent developments concerning the structure, mechanics and fluid flow properties of fault zones. Journal of Structural Geology, 32(11), 1557-1575

Faure, M., Monié, P., and Fabbri, O. (1988). Microtectonics and 39Ar-40Ar dating of high pressure metamorphic rocks of the south Ryukyu Arc and their bearings on the pre-Eocene geodynamic evolution of Eastern Asia. Tectonophysics, 156(1-2), 133-143.

Fisher, D., and Byrne, T. (1987). Structural evolution of underthrusted sediments, Kodiak Islands, Alaska. Tectonics, 6(6), 775-793

Frost, H. J., and M. F. Ashby (1982). Deformation Mechanism Maps, Pergamon Press, New York.

Getsinger, A.J. and Hirth, G., (2014). Amphibole fabric formation during diffusion creep and the rheology of shear zones. Geology 42(6) 535 – 538.

Giuntoli, F., Menegon, L., Warren, C. J., (2018). Replacement reaction and deformation by dissolution and precipitation processes in amphibolites. Journal of Metamorphic Geology 36, 1263 – 1286.

Grant J. A., 1986, The isocon diagram – a simple solution to Gresen's Equation for metasomatic alteration. Economic Geology, 81, 1976-1982.

Gratier, J. P., Dysthe, D. K., and Renard, F. (2013). The role of pressure solution creep in the ductility of the Earth's upper crust. Advances in geophysics, 54, 47-179.

Gratier, J. P., and Gamond, J. F. (1990). Transition between seismic and aseismic deformation in the upper crust. Geological Society, London, Special Publications, 54(1), 461-473.

Gresen R.L., 1967, Composition-volume relationships of metasomatism. Chem. Geology, 78,954-971.

Gueydan, F., Brun, J. P., Phillippon, M., and Noury, M. (2017). Sequential extension as a record of Corsica Rotation during Apennines slab roll-back. Tectonophysics, 710, 149-161.

Hacker, B. R., and Christie, J. M. (1990). Brittle/ductile and plastic/cataclastic transitions in experimentally deformed and metamorphosed amphibolite. The Brittle-Ductile Transition in Rocks, 56, 127-147.

Halama R. and Konrad-Schmolze M. (2015). Retrograde metasomatic effects on phase assemblages in an interalyerd blueschist-greenschist sequence (coastal Cordillera, Chile). Lithos, 216-217, 31-47.

Handy, M. R. (1990). The solid-state flow of polymineralic rocks. Journal of

Geophysical Research: Solid Earth, 95(B6), 8647-8661.

Handy, M. R. (1994). Flow laws for rocks containing two non-linear viscous phases: a phenomenological approach. Journal of structural Geology, 16(3), 287-301.

Hayman, N. W., and Lavier, L. L. (2014). The geologic record of deep episodic tremor and slip. Geology, 42(3), 195-198.

Hardebeck, J. L. and Loveless, J. P. (2018). Creeping subduction zones are weaker than locked subduction zones. Nature Geoscience, 11 (1), 60–64.

He, C., Wang, Z., and Yao, W. (2007). Frictional sliding of gabbro gouge under hydrothermal conditions. Tectonophysics, 445 (3-4), 353–362.

Heki, K. and Kataoka, T., (2008). On the biannually repeating slow-slip events at the Ryukyu Trench, southwestern Japan. Journal of Geophysical Research 113, B11402.

Hickman, S., Sibson, R., and Bruhn, R. (1995). Introduction to special section: Mechanical involvement of fluids in faulting. Journal of Geophysical Research: Solid Earth, 100(B7), 12831-12840.

Herring, C. (1950). Diffusional viscosity of a polycrystalline solid. Journal of applied physics, 21(5), 437-445.

Hikurangi subduction zone, New Zealand. Science, 352 (6286), 701–704.

Hirose, H., Hirahara, K., Kimata, F., Fujii, N., and Miyazaki, S. I. (1999). A slow thrust slip event following the two 1996 Hyuganada earthquakes beneath the Bungo Channel, southwest Japan. Geophysical Research Letters, 26(21), 3237-3240.

Hirth, G., and Tullis, J. A. N. (1992). Dislocation creep regimes in quartz aggregates. Journal of structural geology, 14(2), 145-159.

Hirth, G., Teyssier, C., and Dunlap, J. W. (2001). An evaluation of quartzite flow laws based on comparisons between experimentally and naturally deformed rocks. International Journal of Earth Sciences, 90, 77-87

Hobbs, B. E. (1968). Recrystallization of single crystals of quartz. Tectonophysics, 6(5), 353-401.

Hobbs, B. E., Ord, A., Spalla, M. I., Gosso, G., and Zucali, M. (2010). The interaction of deformation and metamorphic reactions. Geological Society, London, Special Publications, 332(1), 189-223.

Holdsworth, R. E., Van Diggelen, E. W. E., Spiers, C. J., De Bresser, J. H. P., Walker, R. J., and Bowen, L. (2011). Fault rocks from the SAFOD core samples: implications for weakening at shallow depths along the San Andreas Fault, California. Journal of Structural Geology, 33(2), 132-144.

Hoover, W. F., Condit, C. B., Lindquist, P. C., Moser, A. C., and Guevara, V. E. (2022). Episodic Slow Slip Hosted by Talc-Bearing Metasomatic Rocks: High

Strain Rates and Stress Amplification in a Chemically Reacting Shear Zone. Geophysical Research Letters, 49(21), e2022GL101083.

Hyndman, R. D., Yamano, M., and Oleskevich, D. A. (1997). The seismogenic zone of subduction thrust faults. Island Arc, 6(3), 244-260.

Hyndman, R.D., Yamano, M., Oleskevich, D.A., (1997). The seismogenic zone of subduction thrust faults. The Island Arc, 6, 244-260.

Ide, S., Beroza, G. C., Shelly, D. R., and Uchide, T. (2007). A scaling law for slow earthquakes. Nature, 447(7140), 76-79

Ikari, M. J., Marone, C., and Saffer, D. M. (2011). On the relation between fault strength and frictional stability. Geology, 39(1), 83-86.

Imber, J., Holdsworth, R. E., Butler, C. A., and Lloyd, G. E. (1997). Fault-zone weakening processes along the reactivated Outer Hebrides Fault Zone, Scotland. Journal of the Geological Society, 154(1), 105-109.

Imber, J., Holdsworth, R. E., Butler, C. A., and Strachan, R. A. (2001). A reappraisal of the Sibson-Scholz fault zone model: The nature of the frictional to viscous ("brittle-ductile") transition along a long-lived, crustal-scale fault, Outer Hebrides, Scotland. Tectonics, 20(5), 601-624.

Imon, R., Okudaira, T., Kanagawa, K., (2004). Development of shape- and lattice-preferred orientations of amphibole grains during initial cataclastic deformation and subsequent deformation by dissolution-precipitation creep in amphibo-

lites from the Ryoke metamorphic belt, SW Japan. Journal of Structural Geology 26, 793-805.

Ishizuka, H. and Imaizumi, M., (1988). Metamorphic aragonite from the Yaeyama metamorphic rocks on Ishigaki- jima, Southwest Ryukyu islands. Journal of the Geological Society of Japan 94 (9), 719 – 722.

Ito, Y., and Obara, K. (2006). Very low frequency earthquakes within accretionary prisms are very low stress-drop earthquakes. Geophysical Research Letters, 33(9).

Ito, Y., Obara, K., Shiomi, K., Sekine, S., and Hirose, H. (2007). Slow earthquakes coincident with episodic tremors and slow slip events. Science, 315(5811), 503-506

Jefferies, S. P., Holdsworth, R. E., Wibberley, C. A. J., Shimamoto, T., Spiers, C. J., Niemeijer, A. R., and Lloyd, G. E. (2006). The nature and importance of phyllonite development in crustal-scale fault cores: an example from the Median Tectonic Line, Japan. Journal of Structural Geology, 28(2), 220-235.

Kano, M., Fukuda, J., Miyazaki, S., Nakamura, M. (2018). Spatiotemporal evolution of recurrent slow slip events along the Southern Ryukyu Subduction zone, Japan, from 2010 to 2013. Journal of Geophysical Research: Solid Earth, 123, 7090–7107.

Kano, M., Kato, A., and Obara, K. (2019). Episodic tremor and slip silently invades strongly locked megathrust in the Nankai Trough. Scientific reports, 9(1),

9270.

Kennedy, B. M., Kharaka, Y. K., Evans, W. C., Ellwood, A., DePaolo, D. J., Thordsen, J., ... and Mariner, R. H. (1997). Mantle fluids in the San Andreas fault system, California. Science, 278(5341), 1278-1281.

Kerrich, R., and Allison, I. (1978). Flow mechanisms in rocks: microscopic and mesoscopic structures, and their relation to physical conditions of deformation in the crust. Geoscience Canada.

Kilian, R., Heilbronner, R., Stünitz, H., (2011). Quartz grain size reduction in a granitoid rock and the transition from dislocation to diffusion creep. Journal of Structural Geology 33(8), 1265-1284.

Kim, D., Katayama, I., Michibayashi, K., Tsujimori, T., (2013). Rheological contrast between glaucophane and lawsonite in naturally deformed blueschist from Diablo Range, California. Island Arc 22, 63 – 73.

Kimura, G., Yamaguchi, A., Hojo, M., Kitamura, Y., Kameda, J., Ujiie, K., Hamada, Y., Hamahashi M., Hina, S., (2012). Tectonic melange as fault rock of subduction plate boundary. Tectonophysics, 568 – 569, 25-38.

Kirkpatrick, J. D., Fagereng, Å., and Shelly, D. R. (2021). Geological constraints on the mechanisms of slow earthquakes. Nature Reviews Earth and Environment, 2(4), 285-301.

Kizaki, K., (1986). Geology and Tectonics of the Ryukyu Islands. Tectono-

physics 125, 193207.

Knipe, R. J. (1989). Deformation mechanisms—recognition from natural tectonites. Journal of Structural Geology, 11(1-2), 127-146.

Kodaira, S., Iidaka, T., Kato, A., Park, J. O., Iwasaki, T., and Kaneda, Y. (2004). High pore fluid pressure may cause silent slip in the Nankai Trough. Science, 304(5675), 1295-1298.

Kondo, H., Kimura, G., Masago, H., Ohmori-Ikehara, K., Kitamura, Y., Ikesawa, E., ... and Okamoto, S. Y. (2005). Deformation and fluid flow of a major out-of-sequence thrust located at seismogenic depth in an accretionary complex: Nobeoka Thrust in the Shimanto Belt, Kyushu, Japan. Tectonics, 24(6).

Kotowski, A., Behr, W.M., (2019). Length scales and types of heterogeneities along the deep subduction interface: Insights from exhumed rocks on Syros Island, Greece. Geosphere 15.

Kranjc, K., Z. Rouse, K. M. Flores, and P. Skemer (2016). Low-temperature plastic rheology of olivine determined by nanoindentation, Geophys. Res. Lett., 43, 176–184.

Lallemand, S., Liu, C., Dominguez, S., Schnurle, P., Malavielle, J., and ACT Scientific Crew, (1999). Trench-parallel stretching and folding of forearc basins and lateral migration of the accretionary wedge in the southern Ryukyus: A case of strain partition caused by oblique convergence. Tectonics 18(2), 231- 247.

Langdon, T. G. (2006). Grain boundary sliding revisited: Developments in sliding over four decades. Journal of Materials Science, 41, 597-609.

Leah, H., Fagereng, Å., Groome, N., Buchs, D., Eijsink, A., and Niemeijer, A. (2022). Heterogeneous subgreenschist deformation in an exhumed sediment-poor mélange. Journal of Geophysical Research. Solid Earth, 127(8).

Leake, B.E., Woolley, A.R., (1997). Nomenclature of amphiboles: report of the subcommittee on amphiboles of the international mineralogical association, commission on new minerals and mineral names. The Canadian mineralogist, 35, 219-246.

Lee, A., Stünitz, H., Soret, M., Ariel Battisti, M., (2022). Dissolution precipitation creep as a process for the strain localisation of mafic rocks. Journal of Structural Geology, 155, 104505.

Levi, N., Malasoma, A., Marroni, M., Pandolfi, L., and Paperini, M. (2007). Tectono-metamorphic history of the ophiolitic Lento unit (northern Corsica): evidences for the complexity of accretion-exhumation processes in a fossil subduction system. Geodinamica Acta, 20(1-2), 99-118

Li, S., Freymueller, J. and McCaffrey, R., (2016). Slow slip events and time-dependent variations in locking beneath Lower Cook Inlet of the Alaska-Aleutian subduction zone. Journal of Geophysical Research: Solid Earth, 121(2), pp.1060-1079.

Linde AT, Gladwin M, Johnston M, Gwyther R, Bilham R. 1996 A slow earth-

quake sequence on the San Andreas fault. Nature 383, 65–68. (doi:10.1038/383065a0)

Lloyd, G. E., and Freeman, B. (1994). Dynamic recrystallization of quartz under greenschist conditions. Journal of Structural Geology, 16(6), 867-881.

Lloyd, G. E., Farmer, A. B., and Mainprice, D. (1997). Misorientation analysis and the formation and orientation of subgrain and grain boundaries. Tectonophysics, 279(1-4), 55-78.

Lockner, D. A., Morrow, C., Moore, D., and Hickman, S. (2011). Low strength of deep San Andreas fault gouge from SAFOD core. Nature, 472(7341), 82-85.

Luo, Y., and Liu, Z. (2021). Fault zone heterogeneities explain depth-dependent pattern and evolution of slow earthquakes in Cascadia. Nature communications, 12(1), 1959.

Maekawa, H., Shozui, M., Ishli, T., Fryer, P., Pearce, J., (1993). Blueschist metamorphism in an active subduction zone. Nature, 364.

Malavieille, Chemenda, and Larroque. (1998). Evolutionary model for Alpine Corsica: Mechanism for ophiolite emplacement and exhumation of high-pressure rocks. Terra Nova, 10(6), 317-322.

Malvoisin, B. and Baumgartner, L.P., (2021). Mineral dissolution and precipitation under stress: model formulation and application to metamorphic reactions. Geochemistry, Geophysics, Geosystems 22(5).

Marroni, M., and Pandolfi, L. (2003). Deformation history of the ophiolite sequence from the Balagne Nappe, northern Corsica: insights in the tectonic evolution of Alpine Corsica. Geological Journal, 38(1), 67-83.

Marroni, M., and Pandolfi, L. (2007). The architecture of an incipient oceanic basin: a tentative reconstruction of the Jurassic Liguria-Piemonte basin along the Northern Apennines–Alpine Corsica transect. International Journal of Earth Sciences, 96, 1059-1078.

Marroni, M., Pandolfi, L., Meneghini, F., 2004. From accretion to exhumation in a fossil accretionary wedge: a case history from Gottero Unit (Northern Apennines, Italy). Geodin. Acta 17, 41e53.

Maruyama S., Cho M, Liou J.G., (1986). Experimental investigations of blueschist-greenschist transition equilibra: pressure dependence of Al2O3 contents in sodic amphiboles – a new geobarometer. In Evans, B.E., Brown ,E H.(eds.) Blueschists and Eclogites. Geological Society of America Memoir vol. 164, 1-16.

Matsubara, M., Obara, K., and Kasahara, K. (2009). High-VP/VS zone accompanying non-volcanic tremors and slow-slip events beneath southwestern Japan. Tectonophysics, 472(1-4), 6-17.

Matthews, A., and Schliestedt, M. (1984). Evolution of the blueschist and greenschist facies rocks of Sifnos, Cyclades, Greece: A stable isotope study of subduction-related metamorphism. Contributions to Mineralogy and Petrology, 88, 150-163.

McAleer, R. J., Bish, D. L., Kunk, M. J., Sicard, K. R., Valley, P. M., Walsh, G. J., ... and Wintsch, R. P. (2017). Reaction softening by dissolution–precipitation creep in a retrograde greenschist facies ductile shear zone, New Hampshire, USA. Journal of Metamorphic Geology, 35(1), 95-119.

McClay, K. R. (1977). Pressure solution and Coble creep in rocks and minerals: a review. Journal of the Geological Society, 134(1), 57-70.

Menegon, L., Fusseis, F., Stünitz, H., and Xiao, X. (2015). Creep cavitation bands control porosity and fluid flow in lower crustal shear zones. Geology, 43(3), 227-230.

Menegon, L., Pennacchioni, G., Heilbronner, R., and Pittarello, L. (2008). Evolution of quartz microstructure and c-axis crystallographic preferred orientation within ductilely deformed granitoids (Arolla unit, Western Alps). Journal of Structural Geology, 30(11), 1332-1347.

Misch, P., (1969). Paracrystalline microboudinage of zoned grains and other criteria for synkinematic growth of metamorphic minerals. American Journal of Science, 267, 43-63.

Miyashiro, A, (1961). Evolution of metamorphic belts. Journal of Petrology, 2(3), 277-311.

Molli, G., and Malavieille, J. (2011). Orogenic processes and the Corsica/Apennines geodynamic evolution: insights from Taiwan. International Journal of Earth Sciences, 100, 1207-1224.

Montési, L.G., Hirth, G., (2003). Grain size evolution and the rheology of ductile shear zones: from laboratory experiments to postseismic creep. Earth and Planetary Science Letters, 211(1-2), 97-110.

Moore, D.E., and Lockner, D.A., 2004. Crystallographic controls on the frictional behavior of dry and water-saturated sheet structure minerals. J. Geophys. Res. Solid Earth 109, B03401.

Moore, D. E., and Rymer, M. J. (2007). Talc-bearing serpentinite and the creeping section of the San Andreas fault. Nature, 448(7155), 795-797.

Moore, J. C., and Saffer, D. (2001). Updip limit of the seismogenic zone beneath the accretionary prism of southwest Japan: An effect of diagenetic to low-grade metamorphic processes and increasing effective stress. Geology, 29(2), 183-186.

Moore, J. C. and Vrolijk, P. (1992). Fluids in accretionary prisms. Reviews of Geophysics, 30 (2), 113.

Morrow, C.A., Moore, D.E., Lockner, D.A., 2000. The effect of mineral bond strength and adsorbed water on fault gouge frictional strength. Geophys. Res. Lett. 27, 815e818.

Muñoz-Montecinos J., Angiboust, S., Garcia-Casco, A., and Raimondo, T., (2023). Shattered veins elucidate brittle creep processes in the deep Slow Slip and Tremor region. Tectonics, 42, e2022TC007605.

Nabarro, F.R.N. (1948). Deformation of crystals by the motion of single ions, in Report of a conference on the strength of solids: Phys. Soc. London, Proc., 75.

Nakamura, C., Enami, M., (1994). Prograde amphiboles in hematite-bearing basic and quartz schists in the Sanbagawa belt, field gradient and P-T paths of individual rocks. Journal of Metamorphic Geology, 12, 841-852.

Nakamura, M., (2017). Distribution of low-frequency earthquakes accompanying the very low frequency earthquakes along the Ryukyu Trench. Earth Planets Space 69, 49. https://doi.org/10.1186/s40623-017-0632-4

Niemeijer, A. R., and Spiers, C. J. (2005). Influence of phyllosilicates on fault strength in the brittle-ductile transition: Insights from rock analogue experiments. Geological Society, London, Special Publications, 245(1), 303-327.

Nishiyama, N., Ujiie, K., Noro, K., Mori, Y., and Masuyama, H. (2023). Megathrust slip enhanced by metasomatic actinolite in the source region of deep slow slip. Lithos, 446, 107115.

Nuong, N.D., Itaya, T., Nishimura, Y., (2008). Age (K-Ar phengite)-temperature-structure relations: a case study from the Ishigaki high-pressure schist belt, southern Ryukyu Arc, Japan. Geological Magazine 145(5), 677 – 684.

Nyman, M.N., Law, R.D., Smelik, A., (1992). Cataclastic deformation mechanism for the development of core-mantle structures in amphiboles. Geology, 20, 455-458.

Obara, K., (2002). Nonvolcanic deep tremor associated with subduction in Southwest Japan. Science 296, 1679 – 1681.

Obara, K., Hirose, H., Yamamizu, F., and Kasahara, K. (2004). Episodic slow slip events accompanied by non-volcanic tremors in southwest Japan subduction zone. Geophysical Research Letters, 31(23).

Obara, K., and Ito, Y. (2005). Very low frequency earthquakes excited by the 2004 off the Kii peninsula earthquakes: A dynamic deformation process in the large accretionary prism. Earth, Planets and Space, 57(4), 321-326.

Obara, K., and Kato, A. (2016). Connecting slow earthquakes to huge earthquakes. Science, 353(6296), 253-257

Obara, K., Hirose, H., Yamamizu, F., Kasahara, K., (2004). Episodic slow slip events accompanied by non-volcanic tremors in southwest Japan subduction zone. Geophysical Research Letters, 31, L23602.

Obara, K., Kato, A., (2016). Connecting slow earthquakes to huge earthquakes. Science 353(6296), 253-257.

Ohta, Y., Freymueller, J.T., Hreinsdóttir, S. and Suito, H., (2006). A large slow slip event and the depth of the seismogenic zone in the south central Alaska subduction zone. Earth and Planetary Science Letters, 247(1-2), pp.108-116.

Okamoto, A. S., Niemeijer, A. R., Takeshita, T., Verberne, B. A., and Spiers,

C. J. (2020). Frictional properties of actinolite-chlorite gouge at hydrothermal conditions. Tectonophysics, 779, 228377.

Oncken, O., Angiboust, S., Dresen, G., (2022). Slow slip in subduction zones: Reconciling deformation fabrics with instrumental observations and laboratory results. Geosphere, 18(1), 104-129.

Osozawa, S., Wakabayashi, J., (2012). Exhumation of Triassic HP-LT rocks by upright extrusional domes and overlying detachment faults, Ishigaki-jima, Ryukyu islands. Journal of Asian Earth Sciences 59, 70 – 84.

Oxburgh, E. R., and Turcotte, D. L. (1971). Origin of paired metamorphic belts and crustal dilation in island arc regions. Journal of Geophysical Research, 76(5), 1315-1327.

Pacheco, J. F., Sykes, L. R., and Scholz, C. H. (1993). Nature of seismic coupling along simple plate boundaries of the subduction type. Journal of Geophysical Research: Solid Earth, 98(B8), 14133-14159

Passchier, C. W., Trouw R.A., (2005). Microtectonics. Springer Science and Business Media.

Paterson, M. (1973). Nonhydrostatic thermodynamics and its geologic applications. Reviews of Geophysics, 11 (2), 355-389.

Peacock, S. M. (1990). Fluid processes in subduction zones. Science, 248(4953), 329-337.

Peacock, S. M. (1992). Blueschist-facies metamorphism, shear heating, and P-T-t paths in subduction shear zones. Journal of Geophysical Research: Solid Earth, 97(B12), 17693-17707.

Peacock, S. M. (2009). Thermal and metamorphic environment of subduction zone episodic tremor and slip. Journal of Geophysical Research: Solid Earth, 114(B8).

Peacock, S. M., Christensen, N. I., Bostock, M. G., and Audet, P. (2011). High pore pressures and porosity at 35 km depth in the Cascadia subduction zone. Geology, 39(5), 471-474.

Pearce J., (1996). A User's guide to basalt discrimination diagrams in Wyman D.A¿ ed. Trace element geochemistry of volcanic rocks: applications for massive sulphide exploration. Geological Association of Canada, Short Course Notes, 12, 79-113.

Peng, Z., and Gomberg, J. (2010). An integrated perspective of the continuum between earthquakes and slow-slip phenomena. Nature geoscience, 3(9), 599-607.

Phillips, N. J., and White, J. C. (2017). Grain size-dependent strength of phyllosilicate-rich gouges in the shallow crust: Insights from the SAFOD site. Journal of Geophysical Research: Solid Earth, 122(7), 5789-5812.

Piazolo, S., and Jaconelli, P. (2014). Sillimanite deformation mechanisms within a Grt-Sil-Bt gneiss: effect of pre-deformation grain orientations and char-

acteristics on mechanism, slip-system activation and rheology. Geological Society, London, Special Publications, 394(1), 189-213.

Pognante U., Kienast J.R., (1987). Blueschist and eclogite transformations in Fe-Ti gabbros: a case from the Western Alps ophiolites. Journal of Petrology, 138, 114-126.

Poirier, J. P., and Guillopé, M. (1979). Deformation induced recrystallization of minerals. Bulletin de Mineralogie, 102(2), 67-74.

Prior, D. J., Wheeler, J., Peruzzo, L., Spiess, R., and Storey, C. (2002). Some garnet microstructures: an illustration of the potential of orientation maps and misorientation analysis in microstructural studies. Journal of Structural Geology, 24(6-7), 999-1011.

Reiner, M. (1964). The Deborah number. Physics today, 17 (1), 62.

Reynard, B., Gillet, P., (1989). Deformation mechanisms in naturally deformed glaucophanes – a Tem and Hrem study. European Journal of Mineralogy, 1, 611-624.

Ridley, J., and Dixon, J. E. (1984). Reaction pathways during the progressive deformation of a blueschist metabasite: the role of chemical disequilibrium and restricted range equilibrium. Journal of Metamorphic Geology, 2(2), 115-128

Rogers, G., and Dragert, H. (2003). Episodic tremor and slip on the Cascadia subduction zone: The chatter of silent slip. Science, 300(5627), 1942-1943.

Rowe, C. D., Meneghini, F., and Moore, J. C. (2011). Textural record of the seismic cycle: strain-rate variation in an ancient subduction thrust. Geological Society, London, Special Publications, 359(1), 77-95.

Rowe, C., Moore, J.C., Remitti, F., (2013). The thickness of subduction plate boundary faults from the seafloor into the seismogenic zone. Geology 41(9), 991-994.

Rubinstein, J. L., Shelly, D. R., and Ellsworth, W. L. (2010). Non-volcanic tremor: A window into the roots of fault zones. New Frontiers in Integrated Solid Earth Sciences, 287-314.

Ruina, A. (1983). Slip instability and state variable friction laws. Journal of Geophysical Research: Solid Earth, 88 (B12), 10359–10370.

Ruff, L. J. (1989). Do trench sediments affect great earthquake occurrence in subduction zones?. Subduction Zones Part II, 263-282.

Rutter, E. H. (1976). A discussion on natural strain and geological structure-the kinetics of rock deformation by pressure solution. Philosophical Transactions of the Royal Society of London. Series A, Mathematical and Physical Sciences, 283(1312), 203-219.

Rutter, E. H. (1983). Pressure solution in nature, theory and experiment. Journal of the Geological Society, 140(5), 725-740.

Rutter, E. H. (1986). On the nomenclature of mode of failure transitions in rocks. Tectonophysics, 122(3-4), 381-387

Rutter, E. H., and Brodie, K. H. (1988). The role of tectonic grain size reduction in the rheological stratification of the lithosphere. Geologische Rundschau, 77, 295-307.

Rutter, E.H., (1976). The kinetics of rock deformation by pressure solution. Transactions of the Royal Society of London 283, 203-219.

Rybacki, E., and Dresen, G. (2004). Deformation mechanism maps for feldspar rocks. Tectonophysics, 382(3-4), 173-187.

Saffer, D. M., and Tobin, H. J. (2011). Hydrogeology and mechanics of subduction zone forearcs: Fluid flow and pore pressure. Annual Review of Earth and Planetary Sciences, 39, 157-186.

Sawai, M., Niemeijer, A. R., Plümper, O., Hirose, T., and Spiers, C. J. (2016). Nucleation of frictional instability caused by fluid pressurization in subducted blueschist. Geophysical Research Letters, 43(6), 2543-2551.

Schleicher, A. M., Van Der Pluijm, B. A., and Warr, L. N. (2012). Chlorite-smectite clay minerals and fault behavior: New evidence from the San Andreas Fault Observatory at Depth (SAFOD) core. Lithosphere, 4(3), 209-220.

Schliestdt M., Matthews A., (1987). Transformation of blueschist to greenschist facies rocks as a consequence of fluid infiltration, Sifnos (Cyclades), Greece.

Contributions to mineralogy and petrology, 97,237-250.

Schmalzle, G., McCaffrey, R., Creager, K.C., (2014). Central Cascadia subduction zone creep. Geochemistry Geophysics Geosystems 15, 1515-1532.

Schmid, S. M. (1991). Towards a genetic classification of fault rocks: geological usage and tectonophysical implications. Controversies in modern geology.

Schmid, S. M., and Hsü, K. J. (1982). Microfabric studies as indicators of deformation mechanisms and flow laws operative in mountain building. a= a, 6, 4.

Scholz, C. H. (1988). The brittle-plastic transition and the depth of seismic faulting. Geologische Rundschau, 77, 319-328.

Scholz, C. H. (1998). Earthquakes and friction laws. Nature, 391(6662), 37-42.

Schumacher, J.C., (1997). The estimation of ferric iron in electron microprobe analysis of amphiboles. American Mineralogist, 82, 643-651.

Schwartz, S. Y., and Rokosky, J. M. (2007). Slow slip events and seismic tremor at circum-Pacific subduction zones. Reviews of Geophysics, 45(3).

Segall, P., and Rice, J. R. (1995). Dilatancy, compaction, and slip instability of a fluid-infiltrated fault. Journal of Geophysical Research: Solid Earth, 100(B11), 22155-22171.

Shea W.T and Kronenberg A.K., (1993). Strength and anisotropy of foliated rocks with varied mica contents. Journal of Structural Geology, 15, 1097-1121.

Shelly, D. R., Beroza, G. C., and Ide, S. (2007). Non-volcanic tremor and low-frequency earthquake swarms. Nature, 446(7133), 305-307.

Shelly, D. R., Beroza, G. C., Ide, S., and Nakamula, S. (2006). Low-frequency earthquakes in Shikoku, Japan, and their relationship to episodic tremor and slip. Nature, 442(7099), 188-191.

Shervais J.W., (1982). Ti-V plots and the petrogenesis of modern and ophiolitic lavas. Earth and Planetary Science Letters, 59, 101-118.

Shreve, R.L. and Cloos, M., (1986) Dynamics of sediment subduction, melange formation, and prism accretion. Journal of Geophysical Research 91(B10), 10229-10245.

Sibson, R. H. (1977). Fault rocks and fault mechanisms. Journal of the Geological Society, 133(3), 191-213.

Sibson, R. H. (1982). Fault zone models, heat flow, and the depth distribution of earthquakes in the continental crust of the United States. Bulletin of the Seismological Society of America, 72(1), 151-163.

Sibson, R. H. (1984). Roughness at the base of the seismogenic zone: contributing factors. Journal of Geophysical Research: Solid Earth, 89 (B7), 5791(5799)

Sibson, R. H. (1994). Crustal stress, faulting and fluid flow. Geological Society, London, Special Publications, 78(1), 69-84.

Skarbek, R. M., Rempel, A. W., and Schmidt, D. A. (2012). Geologic heterogeneity can produce aseismic slip transients. Geophysical Research Letters, 39(21).

Skemer, P., Katayama I., Jiang Z., Karato, S., (2005). The misorientation index: Development of a new method for calculating the strength of lattice-preferred orientation. Tectonophysics 411(1), 157–167.

Skrotzki, W., (1990). Microstructure in hornblende of a mylonitic amphibolite. Geological Society, London, Special Publications, 54, 321-325.

Stenvall, C., Fagereng, A., Diener, J.F.A., (2019). Weaker than weakest: On the strength of shear zones. Geophysical Research Letters 46, 7404 – 7413.

Stipp, M., Stünitz, H., Heilbronner, R., and Schmid, S. M. (2002). Dynamic recrystallization of quartz: correlation between natural and experimental conditions. Geological Society, London, Special Publications, 200(1), 171-190.

Stipp, M., Tullis, J., Scherwath, M., and Behrmann, J. H. (2010). A new perspective on paleopiezometry: Dynamically recrystallized grain size distributions indicate mechanism changes. Geology, 38(8), 759-762.

Suenaga, N., Yoshioka, S., Ji, Y., (2021). 3-D thermal regime and dehydration processes around the regions of slow earthquakes along the Ryukyu Trench. Sci Rep 11, 11251.

Takagi, R., Obara, K., and Maeda, T. (2016). Slow slip event within a gap between tremor and locked zones in the Nankai subduction zone. Geophysical Research Letters, 43(3), 1066-1074

Tichelaar, B. W., and Ruff, L. J. (1993). Depth of seismic coupling along subduction zones. Journal of Geophysical Research: Solid Earth, 98(B2), 2017-2037.

Tokle, L., Hufford, L. J., Behr, W. M., Morales, L. F. G., and Madonna, C. (2023). Diffusion creep of sodic amphibole-bearing blueschist limited by microboudinage. Journal of Geophysical Research: Solid Earth, 128, e2023JB026848

Tsenn, M.C., Carter, N.L., (1987). Upper limits of power law creep of rocks. Tectonophysics 13(1-2), 1 – 26.

Tulley, C. J., Fagereng, Å., and Ujiie, K. (2020). Hydrous oceanic crust hosts megathrust creep at low shear stresses. Science Advances, 6(22), eaba1529.

Tulley, C., Fagereng, A., Ujiie, K., (2020). Hydrous oceanic crust hosts megathrust creep at low shear zones. Science Advances 6, eaba1529.

Tulley, C.J., Fagereng, Å., Ujiie, K., Diener, J.F.A. and Harris, C., (2022). Embrittlement within viscous shear zones across the base of the subduction thrust seismogenic zone. Geochemistry, Geophysics, Geosystems 23, e2022GC010569.

Tullis, J., Yund, R.A., (1991). Diffusion creep in feldspar aggregates: experimental evidence. Journal of Structural Geology, 13(9), 987 – 1000.

Ujiie, K., Saishu, H., Fagereng, A., Nishiyama, N., Otsubo, M., Hiroyuki, K., (2018). An explanation for episodic tremor and slow slip constrained by crack-seal veins and viscous shear in subduction melange. Geophysical Research Letters, 45, 5371 – 5379.

Ujiie, K., Saishu, H., Fagereng, Å., Nishiyama, N., Otsubo, M., Masuyama, H., Kagi, H., (2018). An explanation for episodic tremor and slow slip constrained by crack-seal veins and viscous shear in subduction mélange. Geophysical Research Letters 45, 5371 – 5379.

Ujjie, K., Noro, K., Shigematsu, N., Fagereng, Å., Nishiyama, N., Tulley, C. J., Masuyama. H., Mori, Y., Kagi, H., (2022). Megathrust shear modulated by albite metasomatism in subduction mélanges. Geochemistry, Geophysics, Geosystems. 23, e2022GC010569.

Wallace, L. M., Webb, S. C., Ito, Y., Mochizuki, K., Hino, R., Henrys, S., ... and Sheehan, A. F. (2016). Slow slip near the trench at the Hikurangi subduction zone, New Zealand. Science, 352(6286), 701-704.

Wallis, D., Lloyd, G. E., Phillips, R. J., Parsons, A. J., and Walshaw, R. D. (2015). Low effective fault strength due to frictional-viscous flow in phyllonites, Karakoram Fault Zone, NW India. Journal of Structural Geology, 77, 45-61.

Wang, K., and Bilek, S. L. (2011). Do subducting seamounts generate or stop large earthquakes?. Geology, 39(9), 819-822.

Wang, S., Hsu, S., Yeh, Y., (2019). Earthquake-related structures beneath the Southernmost portion of the Ryukyu Arc and Forearc. Geophysical Research Letters, 46, 3717-3725.
Wassmann, S.and Stöckhert, B., (2013). Rheology of the plate interface – Dissolution precipitation creep in high pressure metamorphic rocks. Tectonophysics 608, 1 – 29.

Weertman, J., (1968). Dislocation climb theory of steady-state creep, Transactions of the American Society of Metals, 61, 681.
Wheeler, J., (1992). Importance of pressure solution and Coble creep in the deformation of polymineralic rocks. Journal of Geophysical Research 97, 4579–4586.

Wheeler, J., Prior, D., Jiang, Z., Spiess, R., and Trimby, P. (2001). The petrological significance of misorientations between grains. Contributions to mineralogy and petrology, 141, 109-124.

White, S. (1976). A Discussion on natural strain and geological structure-The effects of strain on the microstructures, fabrics, and deformation mechanisms in quartzites. Philosophical Transactions of the Royal Society of London. Series A, Mathematical and Physical Sciences, 283(1312), 69-86.

White, S. H., and Knipe, R. J. (1978). Microstructure and cleavage development in selected slates. Contributions to Mineralogy and Petrology, 66(2), 165-174.

White, S. H., Burrows, S. E., Carreras, J., Shaw, N. D., and Humphreys, F. J. (1980). On mylonites in ductile shear zones. Journal of structural geology, 2(1-2), 175-187.

Winchester J.A., Floyd P.A., (1978). Identification and discrimination of altered and metamorphosed volcanic rocks using immobile elements. Chemical Geology, 21, 211-218.

Wintsch, R.P., Christoffersen, R., Kroenenberg, A.K., (1995). Fluid-rock reaction weakening of fault zones. Journal of Geophysical Research, 100, 13021-13032.

Wintsch, R.P., Yeh, M., (2013). Oscillating brittle and viscous behavior through the earthquake cycle in the Red River Shear Zone: Monitoring flips between reaction and textural softening and hardening. Tectonophysics, 587,46-62.

Wintsch, R.P., Yi, K., (2002). Dissolution and replacement creep: a significant deformation mechanism in mid-crustal rocks. Journal of Structural Geology, 24, 1179-1193.

Wojtal, S., Blenkinsop, T., and Tikoff, B. (2022). An integrated framework for structural geology: kinematics, dynamics, and rheology of deformed rocks. John Wiley and Sons.